ABSTRACT

Title of Document:	ENHANCED GAS-LIQUID ABSORPTION UTILIZING MICRO-STRUCTURED SURFACES AND FLUID DELIVERY SYSTEMS
	Harish Ganapathy, Doctor of Philosophy, 2014
Directed By:	Professor Michael Ohadi, Mechanical Engineering

Despite intensive research and development efforts in renewable energy in recent years, more than 80% of the energy supply in the year 2040 is expected to come from fossil fuel-based sources. Increasing anthropogenic greenhouse gas emissions led the United States to legislatively limit domestic CO_2 emissions to between 1000-1100 lb/MWh for new fossil fuel-fired power plants, thus creating an urgent need for efficient gas separation (capture) processes. Meanwhile, the gradual replacement of coal with cleaner burning natural gas will introduce additional challenges of its own since nearly 40% of the world's gas reserves are sour due to high concentrations of corrosive and toxic H_2S and CO_2 gases, both of which are to be separated. Next-generation micro-structured reactors for industrial mass and heat transfer processes are a disruptive technology that could yield substantial process intensification, size reduction, increased process control and safety. This dissertation proposes a

transformative gas separation solution utilizing advanced micro-structured surfaces and gas delivery manifolds that serves to enhance gas separation processes. Experimental and numerical approaches have been used to achieve aggressive enhancements for a solvent-based CO_2 absorption process. A laboratory-scale microreactor was investigated to fundamentally understand the physics of multiphase fluid flow with chemical reactions at the length scales under consideration. Reactor design parameters that promote rapid gas separation were studied. Computational fluid dynamics was used to develop inexpensive stationary (fixed) interface models for incorporation with optimization engines, as well as high fidelity unsteady (deforming) interface models featuring universal flow regime predictive capabilities. Scalability was investigated by developing a multiport microreactor and a stacked multiport microreactor that represented one and two orders magnitude increase in throughput, respectively. The present reactors achieved mass transfer coefficients as high as 400 s^{-1}, which is between 2-4 orders of magnitude higher than conventional gas separation technologies and can be attributed to the impressive interfacial contact areas as high as 15,000 m^2/m^3 realized in this study through innovative design of the system. The substantial enhancement in performance achieved is indicative of the high level of process intensification that can be attained using the proposed micro-structured reactors for gas separation processes for diverse energy engineering applications. This dissertation is the first comprehensive work on the application of micro-structured surfaces and fluid delivery systems for gas separation and gas sweetening applications. More than ten refereed technical publications have resulted from this work, part of which has already been widely received by the community.

ENHANCED GAS-LIQUID ABSORPTION UTILIZING MICRO-STRUCTURED
SURFACES AND FLUID DELIVERY SYSTEMS

By

Harish Ganapathy

Dissertation submitted to the Faculty of the Graduate School of the
University of Maryland, College Park, in partial fulfillment
of the requirements for the degree of
Doctor of Philosophy
2014

Advisory Committee:
Professor Michael Ohadi, Chair
Professor Reinhard Radermacher
Professor Marino diMarzo
Assistant Professor Amir Riaz
Assistant Professor Mohamed Alshehhi
Professor Kyu Yong Choi (Dean's Representative Member)

Dedication

To my Gurudev and my Family.

Acknowledgements

Table of Contents

List of Tables

List of Figures

xv

xvii

xviii

Nomenclature

a	specific interfacial area (m^2/m^3)
b	empirical constants in Sh number correlation (-)
Bo	Bond number (-)
c	Chisholm parameter (-)
C	concentration (mol/m^3); courant number (-)
C^*	interfacial concentration (mol/m^3)
Ca	capillary number (-)
C_A	concentration of specie A (mol/m^3)
C_A^*	interfacial concentration of specie A (mol/m^3)
$C_{CO2,\,in}$	concentration of CO_2 in gas phase at channel inlet (mol/m^3)
$C_{CO2,\,out}$	concentration of CO_2 in gas phase at channel outlet (mol/m^3)
d	diffusivity (m^2/s)
D	hydraulic diameter or characteristic dimension (m)
E	energy per unit mass (J/kg); enhancement factor (-)
$E\ddot{o}$	Eötvös number (-)
F	force (N)
f	friction factor (-)
f_0	term representing bulk free energy density
f_{ext}	external free energy density (J/m^3)
f_{mix}	mixing energy density (J/m^3)
G	chemical potential (N/m^2); mass flux (kg/m^2s)
h	heat transfer coefficient (W/m^2K); ion-specific parameter (m^3/mol)
h'	height of channel in 3D geometry (m)
H	element size (m); Henry's constant (Pa m^3/mol)
h_{LV}	latent heat (J/kg)
i	ion
I	Ionic strength (mol/m^3); identity matrix
j	Mesh element size (m)
k	Reaction rate constant (m^3/mol s); thermal conductivity (W/mK)
k_{-1}	backward first-order reaction rate constant (1/s)
k_2	forward second-order reaction rate constant (m^3/mol s)
k_B	forward second-order reaction rate constant for base B (m^3/mol s)
k_L	liquid-side mass transfer coefficient (m/s)
$k_L a$	liquid-side volumetric mass transfer coefficient (1/s)
L	length (m)
MAE	mean absolute error (%)
n	Factor of domain resolution (-)
$\mathbf{N}$	normal vector

N	number of data points for calculating average
N_A	absorption flux of specie A(mol/m^2 s)
n_A	molar flow rate of specie A (mol/s)
n_{phase}	number of phases
Nu	Nusselt number (-)
p	partial pressure (Pa)
P	pressure (Pa)
Q	volumetric flow rate (m^3/s)
q''	heat flux (W/m^2)
R	reaction rate (mol/m^3 s)
Re	Reynolds number (-)
Sc	Schmidt number (-)
S_h	energy source term (kg/ms^3)
Sh	Sherwood number (-)
S_α	mass source term ($kg/m^3 s$)
T	temperature (K)
t	time (s)
T	transpose
U	velocity (m/s)
U	velocity vector
V	velocity (m/s); volume (m^3)
w'	width of channel in 3D geometry (m)
X	absorption fraction (%); Martinelli parameter (-)
x	gas mass fraction (-); vapor quality (-)
Y	vertical axis in Cartesian coordinates
Z	horizontal axis in Cartesian coordinates
z	Valence of ion i (-)

Greek Symbols

α	volume/void fraction (-)
β	volumetric flow ratio (-)
χ	mobility parameter (m s/kg)
δ	thickness of thin liquid film (m)
ε	volume/void fraction (-)
ϕ	phase-field variable (-)
ϕ	two-phase friction multiplier (-)
γ	time scale of Cahn-Hilliard diffusion (m^3 s/kg)
η_{abs}	absorption efficiency (%)

κ	mean curvature (m^{-1})
λ	magnitude of mixing energy (N), pressure drop parameter (-)
μ	dynamic viscosity (Pa s)
θ	contact angle (degrees, radians)
ρ	density (kg/m^3)
σ	surface tension (N/m)
τ	gas-liquid contact time (s)
ξ	interface thickness parameter (m)
ψ	phase-field help variable (-)

Subscripts and Superscripts

A	acceleration
B	bubble
eff	effective
F	friction
G	gas
g	gravity
i	denotes the ith phase
in	channel inlet
L	liquid
LO	liquid only
m	log-mean
out	channel outlet
res	residence
S	liquid slug
sat	saturation
ST	Surface tension
TP	two-phase
V	vapor
VO	vapor only
wall	channel wall

Chapter 1: Introduction

1.1 Motivation of Study

World energy consumption is expected to grow continuously over the forthcoming decades. The International Energy Outlook 2013 report by the U.S. Energy Information Administration projected a 56% increase in worldwide energy consumption between 2010 and 2040, thus indicating a rise from 542 quadrillion Btu in 2010 to 630 quadrillion Btu in 2020 and to 820 quadrillion Btu in 2040 (Figure 1.1).
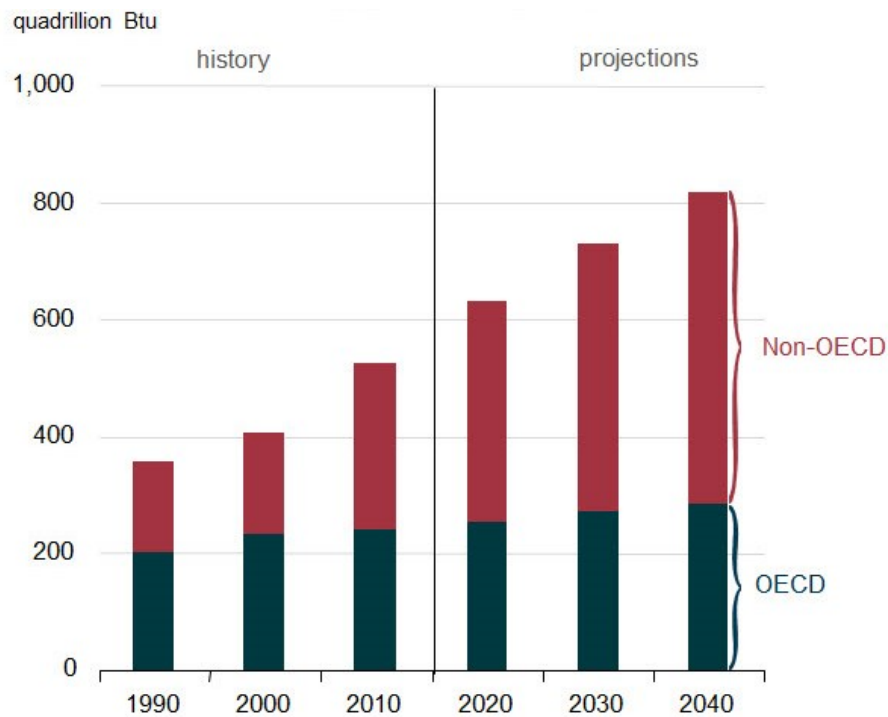
Figure 1.1: Past and projected future worldwide energy consumptions (adapted from U.S. EIA, 2013).

Over 50% of this energy will be consumed by the industrial sector. Despite the rapid

growth of renewable and nuclear energy sources at approximately 2.5% per year,

fossil fuels will continue to supply nearly 80% of the energy demand until 2040

(Figure 1.2).
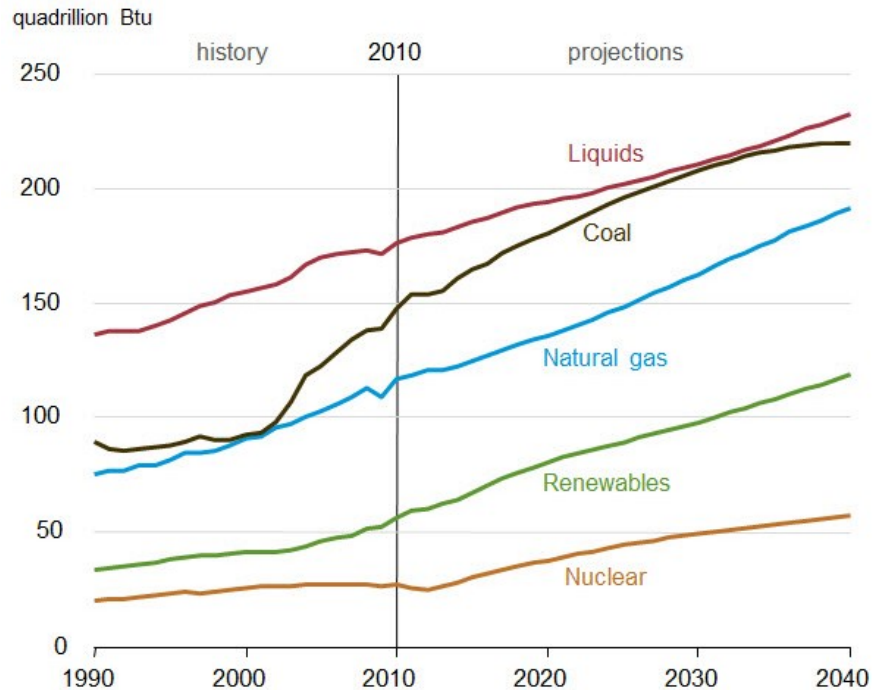
Figure 1.2: Past and projected future worldwide energy consumption by fuel type
(adapted from U.S. EIA, 2013).

Fossil fuels such as oil, natural gas, and coal have been the world's primary energy

source for several decades due to their competitive low prices (Ohadi et al., 2015).

Natural gas is projected to be the fastest growing fossil fuel with the average increase

in consumption amounting to 1.7% per year, from 113 trillion cubic feet in 2010 to

185 trillion cubic feet in 2040 (Figure 1.3). This increase is supported by increasing

supplies of tight gas, shale gas, and coal-bed methane. Enabling technologies in the

U.S. for increased natural gas production have included horizontal drilling and

hydraulic fracturing, which have resulted in a near doubling of the technically

recoverable natural gas reserve estimates. Natural gas is being seen as an optimum

fuel for the industrial and electric power sectors, which will account for 77% of the

projected increase on account of its lower carbon emissions in comparison to coal and

oil, its relatively low power plant capital costs, and favorable heat rates for natural gas

generation.
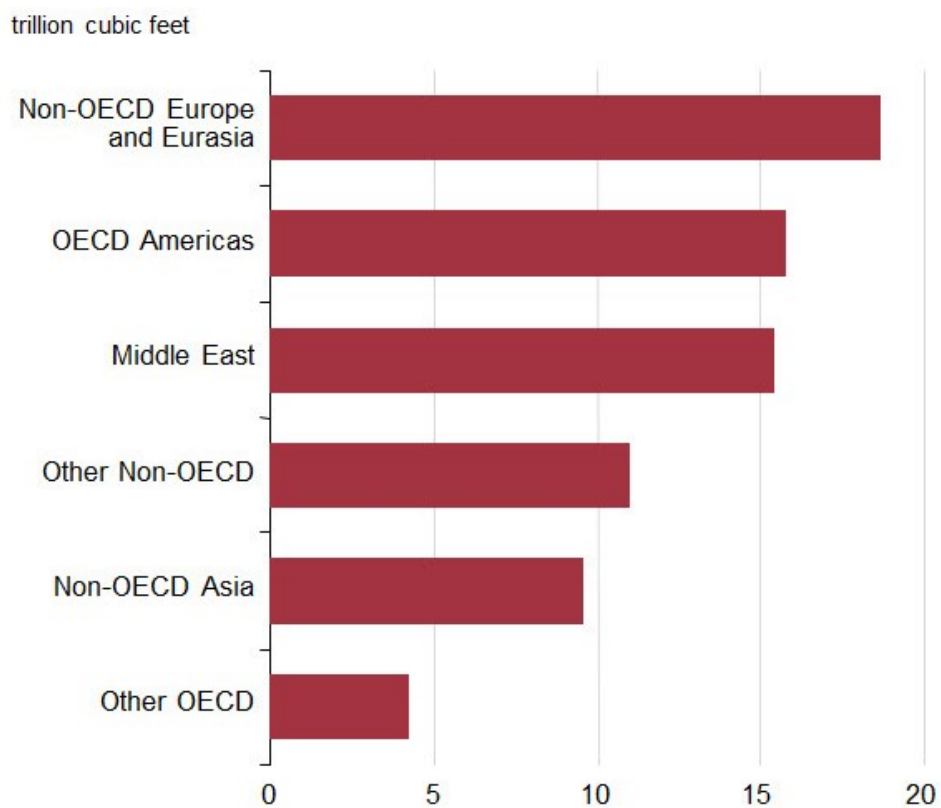
Figure 1.3: Worldwide increase in natural gas production by country grouping from
2010 to 2040 (adapted from U.S. EIA, 2013).

Coal is projected to continue to remain the second-largest energy source with its

consumption increasing on average by 1.3%, per year, from 147 quadrillion Btu in

2010 to 220 quadrillion Btu in 2040 (Figure 1.4). China, the U.S., and India account

for 47%, 14%, and 9% of the coal consumption, respectively. These three countries alone were responsible for 70% of the worldwide coal consumption in 2010 and are predicted to be responsible for 75% in 2040. It is worth noting that the fraction of coal as an energy source to meet worldwide demand is projected to gradually decline after 2025 from 40% in 2010 to 36% in 2040 on account of the environmental impacts associated with its mining and combustion.
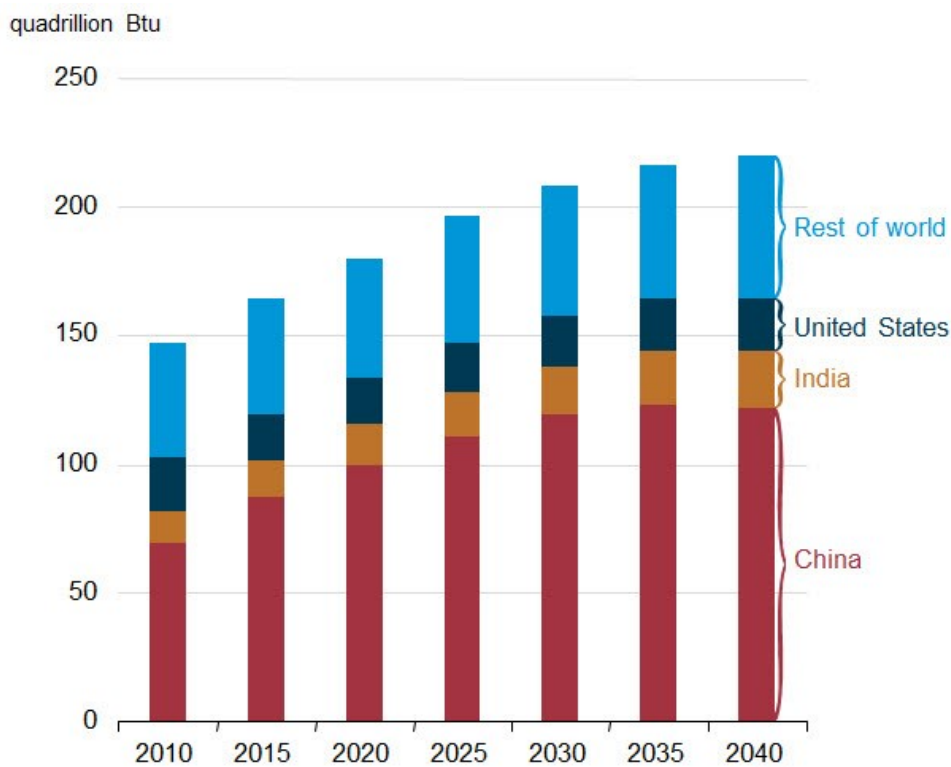
Figure 1.4: Past and projected future worldwide coal consumption by country grouping (adapted from U.S. EIA, 2013).

Meeting these present and future energy demands creates several engineering challenges pertaining to the availability of energy sources as well as the by-products of their usage. Some of these challenges are discussed here and subsequently addressed in this dissertation. First, let us consider the issue of carbon dioxide (CO_2)

emissions resulting from the combustion of hydrocarbon-based fossil fuels. As seen in Figure 1.2, fossil fuels will continue to account for a significant fraction of energy sources until 2040 at the earliest. CO_2 is a greenhouse gas and its increasing presence in the Earth's atmosphere can result in global warming and thus potentially lead to adverse climatic changes (Figure 1.5).

The greenhouse effect

3 ... most escapes to outer space, allowing the Earth to cool...

2 Infrared radiation (IR) is given off by the Earth...

4 ... but some infrared radiation is trapped by gases in the air (including CO_2), keeping the earth warm enough to sustain life.

1 Sunlight passes through the atmosphere and warms the earth.

5 ENHANCED GREENHOUSE EFFECT Increasing levels of CO_2 increase the amount of heat retained, causing the atmosphere and Earth's surface to heat up.

© CO2CRC

Figure 1.5: Schematic representation of the greenhouse effect caused by CO_2 emissions (CO2CRC, 2014).

In May 2013, one of the world's oldest observatories in Mauna Loa, Hawaii, involved in measuring atmospheric CO_2 concentration levels in real time since the year 1958 reported a daily average value that crossed a symbolic but nonetheless significant

threshold of 400 ppm for the first time (NOAA, 2013). Trends of the same are reported in Figure 1.6 and Figure 1.7.
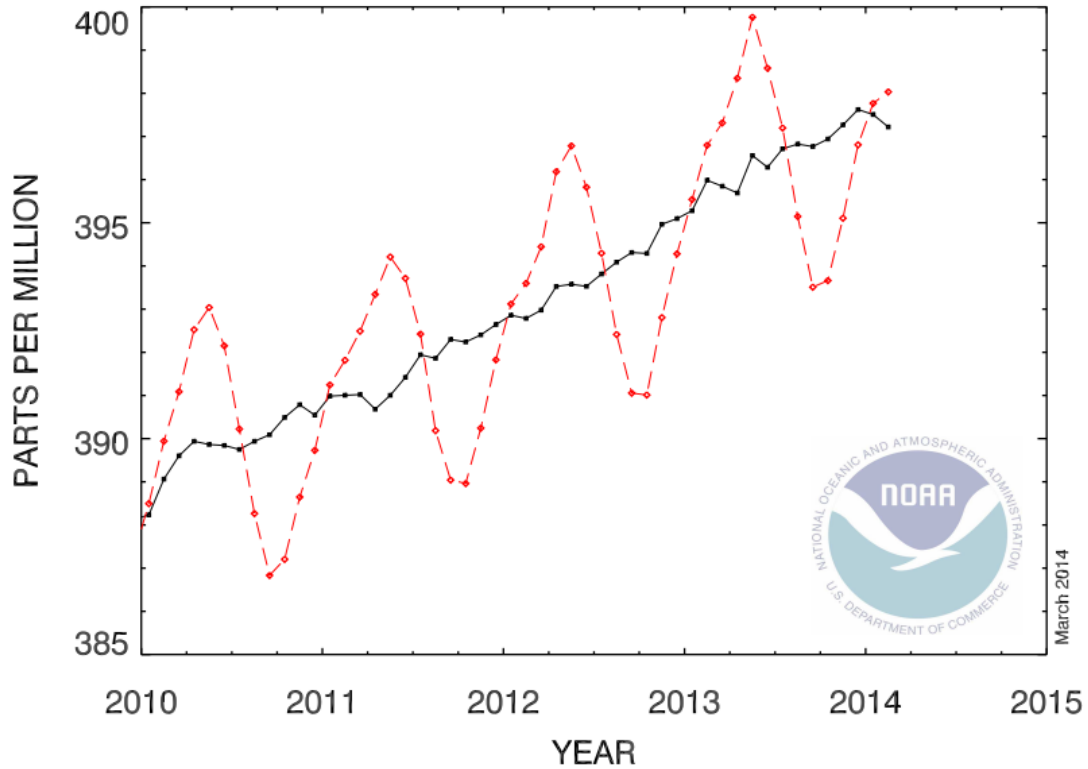
Figure 1.6: Recent monthly mean data of atmospheric CO_2 concentration measurements obtained at Mauna Loa Observatory, Hawaii (adapted from NOAA, 2014).

New technologies are rapidly emerging in the energy industry to reduce anthropogenic greenhouse gas emissions (Metz et al., 2005). Several investigations have shown that CO_2 emissions from power plants can be reduced by cost-effective carbon capture and storage/sequestration (CCS) (IEA, 2009; Aaron and Tsouris, 2005; Yang et al., 2008a; Pires et al., 2011; Kunze and Spliethoff, 2012; Rubin et al., 2012; Li et al., 2013). The U.S. Environmental Protection Agency (EPA) recently proposed greenhouse gas emission standards for various classes of new fossil fuel-

fired power plants that will limit emissions to between 1000-1100 pounds of CO_2 per MWh (454-499 kg CO_2/MWh) (U.S. EPA, 2014). Meeting these limits will definitely require the incorporation of some form of carbon capture technology.
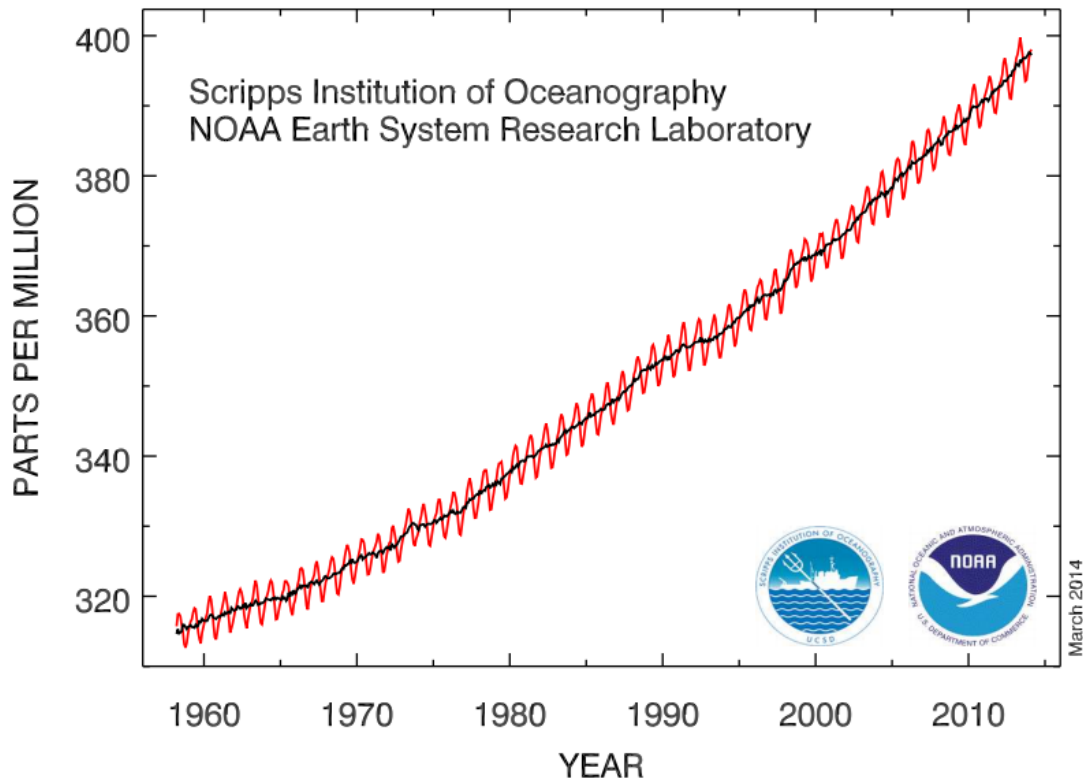
Figure 1.7: Complete history of measurements of atmospheric CO_2 concentration measurements at Mauna Loa Observatory, Hawaii (adapted from NOAA, 2014).

CO_2 can be separated from a gas stream by different approaches, including physical/chemical absorption (Rochelle, 2009; Bin et al., 2010, Mokhtar et al., 2012; Giuffrida et al., 2013), adsorption (Zhao et al., 2010; Akhtar et al., 2012; Cheung et al., 2013; Hedin et al., 2013; Jiang et al., 2013), membrane separation (Kovvali and Sirkar, 2002; Bounaceur et al., 2006; Ho et al., 2008; Merkel et al., 2010; Lv et al., 2012a, 2012b) and cryogenic distillation (Hart and Gnanendran, 2009; Tuinier et al.,

2010; Chiesa et al., 2011; Song et al., 2012a, 2012b). Three major techniques for CCS are post-combustion, pre-combustion, and oxy-combustion (or oxyfuel).

Schematic diagrams representing power generation in a fossil fuel-fired power plant and CO_2 capture technologies are shown in Figure 1.8. In post-combustion processes, CO_2 is separated from the flue gas after the plant's fuel has been combusted. In pre-combustion capture systems, separation occurs before combustion of the fuel. In the case of coal, this is done by gasification (partial oxidation) of coal to form syngas followed by reacting it with steam (shift reaction) to form a mixture of CO_2 and H_2. The CO_2 is separated from the stream following which H_2 gas is burned in the power plant. When natural gas is the fuel, a reforming process involving reactions with oxygen and steam converts it to syngas. The subsequent processes involving the shift reaction and CO_2 separation from H_2 are similar to the case of coal. The approach is known as an integrated gasification combined cycle (IGCC). In oxyfuel combustion, pure oxygen is used instead of air for the burning process, which significantly reduces the concentration of N_2 in flue gas. Instead, water vapor and CO_2 are the main components in addition to minor fractions of other pollutants like SO_2 and NOx.

The present work focuses on post-combustion CO_2 capture, among other applications. The concentration of CO_2 in the post-combustion flue gas stream varies depending upon several factors including the operating conditions and the nature of the fuel being used. Concentrations have been estimated to range between 12-14% for coal-fired boilers and integrated gasification combined cycles (IGCC), 11-13% for oil-fired boilers, 3-4% for gas turbines, and 7-10% for natural gas fired boilers (Metz et

al., 2005). Among the various stages in CCS, which include capture, compression, transportation and storage, it is the former that consumes the ~70% of the total cost (Figure 1.9). Hence, there is an acute need to develop highly efficient and low-cost capture technologies in order to facilitate the widespread adoption of CCS.
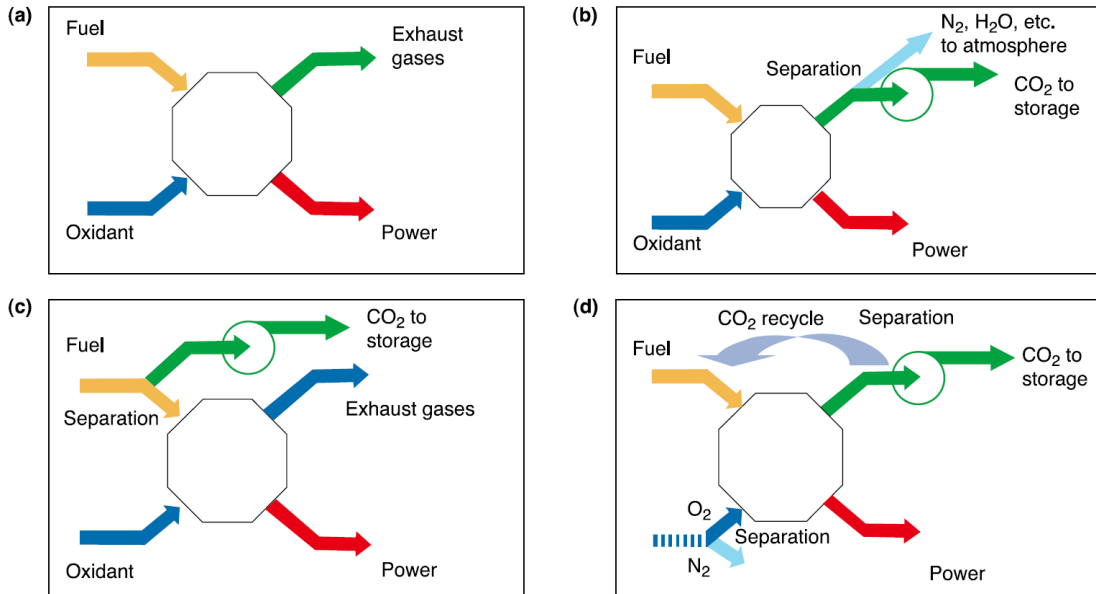
Figure 1.8: Schematic diagrams of (a) power generation in fossil fuel-fired electric power plant; (b) post-combustion carbon capture; (c) pre-combustion carbon capture; (d) oxyfuel combustion (Metz et al., 2005).

The captured CO_2, apart from storage/sequestration, can also be used for enhanced oil recovery (EOR) processes. Crude oil in reservoirs is developed in up to three phases. The primary phase utilizes the natural reservoir pressure, gravity, and/or artificial lift techniques such as pumping to bring the oil to the surface, which produces only ~10% of the original oil in place (OOIP) (U.S. DOE, 2014). The secondary phase injects water or gas to drive the oil into a production well, and results in capturing ~20-40% of the OOIP. Subsequently, one or many tertiary phases, which include

EOR, are employed to recover ~30-60% of the OOIP. Gas injection or miscible

flooding-based EOR accounts for ~60% of EOR-based oil production in the US. The

injection of a gas like pure CO_2 into a reservoir results in expanding the reservoir and

driving the oil to a production wellbore, while simultaneously lowering the oil

viscosity.
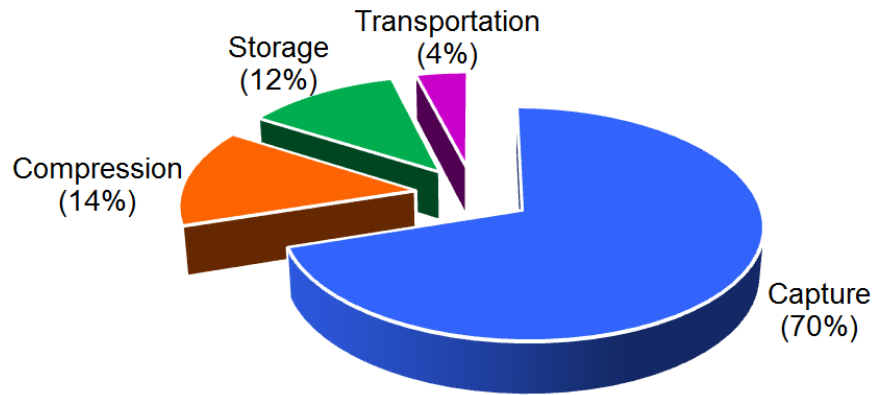
Figure 1.9: Costs of various stages of CCS (data from Rodosta, 2013).

A second application that we consider deals with the production of natural gas. Gas

which contains high concentrations of CO_2 and/or hydrogen sulfide (H_2S) is

characterized as sour. The yield from sour gas fields can typically contain as much as

8% CO_2 and 17% H_2S in addition to the major component of natural gas, which is

methane (Kohl and Nielson, 1997). Sour gas fields are challenging to develop on

account of the corrosive nature of CO_2 and H_2S, which can cause damage to pipelines

and equipment. Additionally, H_2S is highly toxic and can cause death at minute

concentrations of a few hundred ppm. Due to these reasons, the yield from sour gas

fields is subjected to a gas sweetening process based on gas-liquid absorption with

liquid solvents.

It has been estimated that nearly 40% of the world's gas reserves are sour (Total, 2007) and the increasing production of natural gas is expected to create a need for efficient gas sweetening facilities. Furthermore, the recent interest in developing certain extreme-sour fields will involve dealing with gas reserves containing high concentrations of CO_2 and H_2S. An example is the Shah gas field in Abu Dhabi, United Arab Emirates, wherein reserves have been estimated to comprise up to 23% H_2S and 10% CO_2 (Al Hosn Gas, 2012). Likewise, the Bab gas field, also in Abu Dhabi, comprises up to 33% H_2S and 10% CO_2 (Wood Mackenzie, 2013). One on hand, development of these gas reserves will undoubtedly require tremendous gas sweetening capacities associated with high capital and operating costs. On the other hand, with such high sour gas concentration levels, the yield of sweet natural gas from these fields, which is the primary output, is relatively low. Hence, these are substantial economic advantages to be gained by developing low-cost, high-performance technologies for efficient natural gas sweetening.

It is also worth noting the case of natural gas processing plants that integrate CO_2 separation along with sequestration. A recent example is the Gorgon Joint Venture located in Barrow Island, Australia, which involves the participation of several entities: Chevron Australia, Shell, ExxonMobil, Osaka Gas, Tokyo Gas, and Chubu Electric Power. This is a 15.6 million tonnes per annum (MTPA) liquefied natural gas (LNG) processing project involving a feed gas CO_2 molar concentration of 14% (Chevron Australia, 2014; Global CCS Institute, 2014). An image of one of its acid gas removal unit (AGRU) modules that weighs 5,500 tonnes, is 81 m long and 50 m tall, is shown in Figure 1.10. The separated CO_2 will be injected and stored in a deep

reservoir unit located 2 km beneath Barrow island, which is expected to reduce the project's greenhouse gas emissions by ~40%. Another example of a natural gas sweetening plant that stores CO_2 in a deep saline formation is the In Salah project in Algeria (Figure 1.11). The development of high-performance gas sweetening technologies is likely to benefit these types of projects.

Figure 1.10: An acid gas removal unit (AGRU) module for the Gorgon LNG project on Barrow Island (Chevron Corporation, 2013).

Figure 1.11: Amine-based CO_2-separation system for natural gas sweetening at BP plant in In Salah, Algeria (In Salah Gas, 2014).

1.2 Research concept

Microscale devices are quickly penetrating new application areas in diverse engineering applications due to their ability to intensify processes, improve process control, increase safety, and reduce the overall size (Ehrfeld et al., 2000; Guangwen et al., 2008; Ohadi et al., 2013). The inherent high surface area to volume ratio of these systems results in substantial enhancements of the heat and mass transfer performance. Optimized designs and geometries have been demonstrated to operate efficiently at modest pressure drops. A widely accepted classification system defines minichannels as having hydraulic diameters between 3 mm and 200 μm, and microchannels as those having hydraulic diameters between 200 μm and 10 μm (Kandlikar and Grande, 2003). The focus of this dissertation is on gas separation using a liquid solvent-based absorption process that can be potentially enhanced by using microreactor systems.

1.3 Research objectives

The main objectives of this dissertation are as follows.

1. To conduct an experimental investigation of a reactive gas-liquid absorption process in laboratory-scale single channel microreactors; study the effect of the channel geometrical dimensions and operating conditions on the hydrodynamics and mass transfer; characterize the reactor performance; visualize the prevalent two-phase flow regimes and their effect on mass transfer; compare the investigated performance parameters with available models; and compare the performance of the present microreactors with conventional absorption technologies to analyze the magnitude of enhancement that can be achieved.

2. To study the scaling up potential of the aforementioned single channel microreactor by designing and fabricating a multiple channel microreactor that is at least one order of magnitude larger than the single channel microreactor; conduct an experimental investigation of a reactive gas-liquid absorption process; study the effect of operating conditions on the hydrodynamics and mass transfer; and characterize the reactor performance and compare it with conventional absorption technologies.

3. To further study the scaling up potential of the aforementioned single and multiple channel microreactors by designing and fabricating a stacked multiple channel microreactor that is at least two orders of magnitude larger than the single channel microreactor; conduct an experimental investigation of a reactive gas-liquid absorption process; study the effect of operating conditions on the hydrodynamics

and mass transfer; and characterize the reactor performance and compare it with conventional absorption technologies.

4. To study the performance of a finite element method-based phase field model for simulating two-phase flows and to compare its performance with a finite volume method-based volume of fluid model for a case of adiabatic, non-interacting gas-liquid Taylor flow in microchannels. To perform a comprehensive analysis of the various hydrodynamic features of Taylor flow.

5. To develop a numerical formulation to model mass transfer during gas-liquid absorption for Taylor flow in microreactors by decoupling the hydrodynamics from the mass transfer; validate the model predictions with available experimental data; and perform parametric studies using the model to characterize the mass transfer performance of microreactors.

6. To develop a numerical formulation to model flow regimes, heat and mass transfer during two-phase flow in microchannels with a deforming (unsteady) interface simulation capability; validate the model predictions; and perform parametric studies using the model to characterize the performance of microscale systems.

1.4 Organization of dissertation

The present Chapter 1 provides an introduction to this dissertation. A review of the literature pertaining to the subsequent research reported in this dissertation is presented in Chapter 2. Chapter 3 reports an experimental investigation of a laboratory-scale single channel microreactor for gas-liquid absorption processes.

Subsequently, the efforts undertaken to model heat/mass transfer in these single channel systems are described in distinct stages. First, prior to modeling heat/mass transport phenomena in multiphase systems, a detailed analysis of numerical modeling techniques for simulating adiabatic, non-interacting two-phase flow using the phase field and volume of fluid models is reported in Chapter 4. Next, Chapter 5 reports a numerical model for mass transfer across non-deforming (fixed) interfaces. Subsequently, heat/mass transfer across deforming (unsteady) interfaces is reported in Chapter 6 wherein condensation phenomena are first modeled as a simpler precursor to the more complex problem of gas-liquid absorption with chemical reactions. Following this extensive experimental and numerical analysis involving single channel systems, Chapter 7 and Chapter 8 focus on scaling up of the laboratory-scale single channel reactor by one and two orders of magnitude, respectively. Lastly, conclusions from this dissertation and recommendations for future work are presented in Chapter 9.

Chapter 2: Background and Literature Survey

This chapter provides a background to the research objectives discussed in Chapter 1 as well a comprehensive review of the pertinent literature. Section 2.1 focuses on experimental analyses of gas-liquid absorption in various types of microreactors. Section 2.2 focuses on the modeling of adiabatic, non-interacting two-phase flow. Numerical modeling of heat and mass transfer in microchannels is discussed in Section 2.3.

2.1 Experimental study of gas-liquid mass transfer in microreactors

The published literature in gas-liquid mass transfer in microreactors largely comprises studies based on single channel systems, and limited works on scaled-up systems. Yue et al. (2007a) studied the reactive mass transfer characteristics between pure CO_2 and an aqueous solution of $NaHCO_3/Na_2CO_3$ in a 667 μm minichannel. The experimental two-phase frictional pressure drop was well predicted by the Lockhart-Martinelli approach (1949) with a modified expression for the Chisholm parameter, c, that was obtained by regression. The liquid-side mass transfer coefficient and specific interfacial area were estimated and shown to be at least one to two orders of magnitude higher than those observed in conventional gas-liquid absorption systems.

Niu et al. (2009) studied the absorption of CO_2 mixed with N_2 into piperazine-activated methyldiethanolamine (MDEA) solution in minichannels (0.5-2 mm). They reported an improvement in the absorption efficiency with decreasing channel

diameter. However, the reactor performance was not characterized in terms of mass transfer coefficient.

Shao (2010) and Shao et al. (2010) studied the absorption of CO_2 mixed with N_2 into aqueous NaOH in minichannels (345-816 μm). Different channel lengths were studied, which demonstrated that longer channels yield better absorption efficiencies. However, the effect of channel length on pressure drop and mass transfer coefficient was not discussed. Further, their work was limited to studying only the Taylor flow regime. Similar studies focusing on this regime were reported by Kundu et al. (2012) and Tan et al. (2012a, 2012b).

Su et al. (2010) studied the absorption of H_2S mixed with N_2 in aqueous MDEA in a minichannel (1 mm). High values of interfacial area and gas-side mass transfer coefficient were achieved, which were reported to be at least 1-2 orders of magnitude higher than those of conventional absorption technologies. Empirical correlations for the Sherwood number and the interfacial area, obtained by regression, were proposed.

Ye et al. (2012) tested the absorption of CO_2 mixed with N_2 in methylethanolamine (MEA) in a minichannel (408 μm). The system performance was analyzed while operating at both ambient pressure and an elevated pressure of 3 MPa, and enhanced transport phenomena were reported with the latter case.

Shooshtari et al. (2012) studied the absorption of pure CO_2 in aqueous diethanolamine (DEA) in a minichannel (750 μm). Different channel lengths were tested, and the reactor performance was reported in terms of absorption efficiency,

pressure drop and acid gas loading ratio. However, their study considered the absorption of pure CO_2 into the amine solution, while most practical applications involve relatively dilute mixtures, wherein the gas to be absorbed is usually present as a small fraction along with a dominant non-absorbable fraction.

While most published works are based on single channel systems, limited attempts have indeed been made to scale up the same. Zanfir et al. (2005) studied the absorption of CO_2 mixed with N_2 into aqueous NaOH in falling film reactors. The gas flow was guided by a chamber along the length of multiple parallel and rectangular channels. The high interfacial area to volume ratio and the presence of thin liquid films was reported to enhance the absorption performance. A two-dimensional numerical model was developed to simulate the performance of the falling film reactor, and the predictions were in good agreement with the experimental data for low liquid reactant concentrations. The poor agreement obtained at high reactant concentrations was attributed to the effects of maldistribution that were not considered while developing the model.

Yue et al. (2010) studied the absorption of CO_2 in water in a reactor comprising multiple minichannels fed by constructal distributors having a dichotomic tree structure. The reactor was stated to yield a high uniformity in the distribution of the gas and liquid phases at high gas-phase velocities, and the same was attributed to the presence of the distributers. However, maldistribution of the two-phase mixture occurred at low gas velocities. Further complex absorber designs involving mesh structures have been reported by Constantinou and Gavriilidis (2009), Chen et al.

(2011), Gao et al. (2011), and Constantinou et al. (2012). A summary of select studies

is reported in Table 2.1.

Table 2.1: Review of studies on gas-liquid absorption in single and multiple channel
microreactors.

Authors	Gas phase	Liquid phase	Characteristic dimension(s)	Cross-sectional geometry	Performance parameters[1]	Parametric studies[1]
Zanfir et al. (2005)	CO_2-N_2	NaOH	150, 600 μm	Rectangular	AE	D, Q, C
Yue et al. (2007a)	CO_2	Water, $NaHCO_3$/ Na_2CO_3	667 μm	Rectangular	ΔP, MTC, IA	Q
Niu et al. (2009)	CO_2-N_2	Piperazine-activated MDEA	0.5, 1, 2 mm	Circular	ΔP, AE	D, Q, C, T
Shao et al. (2010), Shao (2010)	CO_2-N_2	NaOH	345, 577, 816 μm	Trapezoidal	ΔP, AE, MTC	D, L, Q
Su et al. (2010)	H_2S-N_2	MDEA	1 mm	Circular	ΔP, AE, MTC, IA, Sh	Q
Yue et al. (2010)	CO_2	Water	667 μm	Rectangular	MTC	Q
Kundu et al. (2012)	CO_2-N_2	NaOH, DEA	6, 8, 10 mm	Circular	AE, AR, ACLR	D, Q,C
Shooshtari et al. (2012)	CO_2	DEA	750 μm	Circular	ΔP, AE, ACLR	L, Q,C
Tan et al. (2012a, 2012b)	CO_2-N_2	NaOH	444 μm	Rectangular	MTC, E	Q, C
Ye et al. (2012)	CO_2-N_2	MEA	408 μm	Rectangular	AE, MTC, E	Q, P, T

[1]Abbreviations- ΔP: pressure drop; AE: absorption efficiency; MTC: mass transfer coefficient; IA: interfacial area; E: enhancement factor; Sh: Sherwood number; AR: absorption rate; AGLR: acid gas loading ratio; Q: flow rate; C: reactant concentration; L: channel length; D: characteristic dimension; T: temperature; P: pressure

Based on the above review, the following points are inferred. First, only limited

works have investigated the effect of channel length (residence time). Moreover,

these have not been comprehensive in nature, and have not involved practical

systems. For instance, Shao et al. (2010) focused only on the Taylor flow regime,

while Shooshtari et al. (2012) considered the absorption of pure CO_2 as against a

more practical dilute gas mixture, such as CO_2 mixed with N_2. Clearly, a detailed

study is warranted in this area, since the channel length is a crucial design parameter

that influences both the pressure drop and mass transfer characteristics.

Second, there is a lack of comprehensive quantitative understanding on the effect of

hydraulic diameter on mass transfer coefficient, which is one of the most important

performance parameters used for evaluating and comparing different gas-liquid

absorption technologies. Only limited published works have studied the effect of

channel hydraulic diameter on the performance of the reactor (Niu et al., 2009; Shao

et al., 2010) and even these studies have not been comprehensive in nature. For

instance, Niu et al. (2009) did not analyze either the pressure drop or mass transfer

coefficient, while Shao et al. (2010) focused only on the slug flow regime.

Third, while various experimental works have reported the two-phase pressure drop, a

comparison of this with existing two-phase pressure drop models has not yet been

performed for amine solutions. This is believed to be essential, since available

empirical models for two-phase pressure drop have not considered amine solutions in

their source experimental data. With a higher amine concentration, there is a larger

increase in the viscosity ratio, as against the density ratio. This warrants assessing the

applicability of existing pressure drop models for these amine-based working fluids, since the availability of a validated pressure drop model for CO_2 absorption in amine solutions would greatly facilitate the design and optimization of a scaled-up microreactor. In addition to the frictional component of the total pressure drop, fluid flow during gas-liquid absorption is also associated with a negative acceleration pressure drop that requires consideration. Furthermore, there is a need to evaluate the predictive accuracy of available two-phase pressure drop models at small hydraulic diameters, as is the case with microreactors. This is believed to be essential given that smaller diameter channels are associated with higher pressure drop and hence increased pumping power requirements. These are key factors that require consideration during the design and optimization of a scaled-up microreactor.

Fourth, while numerous authors have performed comprehensive analyses of acid gas absorption in single channels, relatively few works have investigated multiple channel absorbers, and even these studies have not been comprehensive in nature. Two-phase pressure drop, an important performance parameter, was not considered by either Zanfir et al. (2005) or Yue et al. (2010). Furthermore, the latter considered a system involving only physical, non-reactive mass transfer. The predictive accuracy of pressure drop models also requires assessment in order to facilitate subsequent design and scaling of microreactors. Potentially occurring maldistribution under any or all operating conditions requires investigation because, unlike single channel absorbers that permit accurate feeding of the gas and liquid phase directly into the channel, an uneven phase distribution can occur when multiple channels are fed by a single inlet manifold, which can adversely impact the mass transfer performance.

2.2 Numerical modeling of adiabatic, non-interacting two-phase flow

2.2.1 Introduction

In order to accurately model multiphase heat and mass transport phenomena in microscale devices, the hydrodynamics of adiabatic, non-interacting multiphase flow must be accurately predicted. This is because the flow features at the microscale differ from those at larger length scales. For instance, two-phase flow in the latter case is largely in the form of stratified flow, whereas the phase distribution in microscale systems is highly variable depending upon the relative magnitudes of surface tension and inertial forces. It is obvious that accurate prediction of the flow field directly results in improved accuracy of the predicted heat/mass transport phenomena.

On the experimental front, there are many published works that have studied two-phase flow phenomena, starting from the early studies of Fairbrother and Stubbs (1935), Bretherton (1961) and Taylor (1961), to more recent studies that primarily focus on microscale flows. Comprehensive reviews of these works have been presented by Ghiaasiaan and Abdel-Khalik (2001), Kreutzer et al. (2005), Angeli and Gavriilidis (2008), Shao et al. (2009) and Gupta et al. (2010). In general, two-phase flow patterns can be classified into the surface tension dominated type, comprising Taylor (or slug) and bubbly flows; the transitional type, comprising churn and Taylor-annular flows; and the inertia dominated type, comprising dispersed and annular flows.

2.2.2   Multiphase flow models

Various models have been developed for multiphase systems and have been applied

towards two-phase flow in both minichannels and microchannels. The VOF method

(Hirt and Nichols, 1981), which has proven to be the most popular, and the level set

method (Osher and Sethian, 1988; Sussman et al., 1994), belong to the class of

diffuse-interface modeling approaches. They are primarily based on the

approximation of surface tension forces in the interfacial region as a body force, using

the continuum surface force (CSF) formulation of Brackbill et al. (1992). These

approaches have been implemented in numerous studies including Taha and Cui

(2004), Qian and Lawal (2006), Kumar et al. (2007), Carlson et al. (2008), Fang et al.

(2008), Lakhehal et al. (2008), Liu and Wang (2008), Chen et al. (2009), Gupta et al.

(2009), Krishnan et al. (2010), Santos and Kawaji (2010), Asadolahi et al. (2011,

2012). Likewise, the front tracking model by Unverdi and Tryggvason (1992) is also

a diffuse-interface formulation, wherein the center of the interface is marked by

following the advection of control points (Jacqmin, 1999). The surface tension forces

are estimated from the positions of the control points and fluid properties across the

interface varies over multiple cells.

Another relatively less investigated approach is the phase-field method that is studied

in detail in this dissertation. This approach also belongs to the class of diffuse

interface techniques but governs the interface based on the fluid free energy. The free

energy density is comprised of the gradient energy and the bulk energy density (van

der Waals, 1893). Cahn and Hilliard (1959) defined the phase-field variable, ϕ, which

is considered as a measure of phase. It assumes two distinct values in either phase and

undergoes a rapid smooth change across the interface. In the interfacial region, the two phases are considered to be mixed and are thereby associated with a mixing energy. An implementation of the phase field method was presented by Jacqmin (1999), following which several others have presented their modifications to deal with different types of systems. Among these, the work of Yue et al. (2004) is suitable for the present work and is therefore reviewed in the subsequent section.

2.2.3 Phase field method

Based on van der Waals' theory, the expression for mixing energy density is given by Eq. 2.1. By considering a double-well potential for $f_0(\phi)$, as given by Eq. 2.2, the Ginzburg-Landau form of mixing energy density is obtained (Eq. 2.3). This mixing energy adds to the total free energy density of the system. The first and second terms on the right side in Eq. 2.3 represent the gradient energy and bulk free energy density, respectively. λ is the magnitude of mixing energy and ξ scales with the thickness of the interface.

$$f_{mix}\left(\phi,\nabla\phi\right)=\lambda\left[\frac{1}{2}\left|\vec{\nabla}\psi\right|+J_0\left(\phi\right)\right] \tag{2.1}$$

$$f_0\left(\phi\right)=\frac{1}{4\xi^2}(\phi^2-1)^2 \tag{2.2}$$

$$f_{mix}\left(\phi,\nabla\phi\right)=\frac{1}{2}\lambda\left|\vec{\nabla}\psi\right|+\frac{\lambda}{4\xi^2}(\phi^2-1)^2 \tag{2.3}$$

The rate of change of free energy with respect to the phase field variable, ϕ, yields the chemical potential of the system, G, given by Eq. 2.4. The chemical potential is zero at an interface at equilibrium.

$$G = \frac{\partial f_{mix}}{\partial \phi} = \lambda \left[-\vec{\nabla} \psi + \frac{{}^2 - 1)}{\xi^2} \right] \tag{2.4}$$

By integrating Eq. 2.4 once, and in conjunction with the conditions specified by Eq. 2.5, we obtain Eq. 2.6. The solution of Eq. 2.6 gives the equilibrium profile for $\phi(x)$, which is reported by Eq. 2.7.

$$f_0(\pm\infty) = 0 \; ; \; \left. \frac{d\phi}{dx} \right|_{x=\pm\infty} = 0 \tag{2.5}$$

$$f_0(\phi) = \frac{1}{2}\left(\frac{d\phi}{dx} \right)^2 \tag{2.6}$$

$$\phi(x) = \tanh\left(\frac{x}{\sqrt{2}\xi} \right) \tag{2.7}$$

The diffuse mixing energy in the interfacial region must be equal to the traditional surface energy (Eq. 2.8). Eqs. 2.7 and 2.8 together result in the final expression for interfacial tension, given by Eq. 2.9, which corresponds to the sharp interface formulation while the limit of ξ tends to zero.

$$\sigma = \lambda \int_{-\infty}^{\infty} \left[\frac{1}{2}|\vec{\nabla}\psi| + J_0(\phi) \right] dx \tag{2.8}$$

$$\sigma = \frac{2\sqrt{2}\lambda}{3\xi} \tag{2.9}$$

Based on the above formulation, Yue et al. (2004) derived the following governing equations for the phase field approach to model multiphase flows.

$$\frac{\partial \phi}{\partial t} + \mathbf{U}.\nabla \phi = \nabla.\frac{\gamma \lambda}{\xi^2}\nabla \psi \qquad (2.10)$$

$$\psi = -\nabla.\xi^2 \nabla \phi + \left(\phi^2 - 1\right)\phi + \left(\frac{\xi^2}{\lambda}\right)\frac{\partial f_{ext}}{\partial \phi} \qquad (2.11)$$

As noted by Jacqmin (1999), the phase field governing equations are a function of the time scale of Cahn-Hilliard diffusion, γ.

$$\gamma = \chi \xi^2 \qquad (2.12)$$

As per the definition in Eq. 2.12, the functional dependence of γ on two user-defined parameters: mobility, χ, and interface thickness, ξ, posed difficulties on account of the absence of definitive guidelines on their selection which are to be taken into consideration while determining the element size, h. Subsequently, a criterion, $h \leq \xi$, was proposed by Yue et al. (2006), and further, the h/ξ ratio was varied from 0.5 to 1 in order to ensure that the region occupied by the interface would be sufficiently resolved with at least 7-10 elements, as recommended by Yue et al. (2004). However, it is more likely that the interface thickness parameter is merely a relative measure of interface thickness and does not represent an absolute value of length. Therefore, further investigation is warranted to understand the universal applicability of the criterion of Yue et al. (2006), particularly their specified range of values for the h/ξ ratio. Additionally, guidelines for selecting the value of mobility, χ, are quite necessary (Donaldson et al., 2011). While these have been addressed to a certain extent by Jacqmin (1999) and Yue et al. (2007b) by proposing scaling relations

between χ and ξ, careful consideration is required while implementing them, especially while utilizing the values of h/ξ ratio recommended in the literature.

2.2.4 Gas-liquid Taylor flow

Among the numerous flow patterns that occur in microscale systems, Taylor flow (Davies and Taylor, 1950) is characterized by several well-studied features that render it an optimum choice for assessing the performance of numerical modeling approaches. It consists of gas bubbles of length typically larger than the characteristic dimension of the channel and separated by liquid slugs. A thin film of liquid separates the gas bubble from the channel wall. Recirculating velocity components are present within the liquid slugs, as seen from the moving frame of reference. Taylor flow has also been a dominant research interest, especially for microchannel heat exchangers and reactors on account of enhanced convective mixing phenomena, as described by Salman et al. (2004). Certain aspects that are of interest to the modeling of Taylor flow are reviewed subsequently.

2.2.4.1 Bubble formation mechanisms

The dynamics of droplet flow and break-up in microscale and nanoscale flow domains, typically a channel having a T-junction inlet configuration (Thorsen et al., 2001), have been commonly studied by experimental means on account of the wide range of applications for such droplet generating devices in the biological and chemical industries. However, relatively few works have studied these dynamics by numerical methods, more specifically, by utilizing the phase field method. De Menech et al. (2008) utilized the phase field approach they proposed in an earlier

work (De Menech, 2006), wherein the phase field model coupled with the Navier-Stokes equation was used to govern the interface and hydrodynamics of the flow, respectively. An attempt was made to verify the mechanisms of droplet break-up proposed in an earlier experimental work by Garstecki et al. (2006). The pressure drop across the emerging discontinuous phase was verified to be the dominant break-up mechanism at low capillary number (Ca) flows by simultaneously tracking the bubble evolution and pressure at the channel inlet. While the break-up mechanism was verified to a satisfactory extent, a comment attributing sharp kinks in the pressure profile to the interactions between the emerging droplet and channel outlet is indeed interesting. Further investigation on this phenomenon is warranted and could be achieved by simply simulating a longer channel with multiple droplets present between the T-junction and channel exit.

2.2.4.2 Parasitic/spurious currents

Parasitic or spurious currents are the unphysical velocity components at the interface (Lafaurie et al., 1994). These currents are an important issue in the modeling of multiphase flow, especially while using the continuum surface force (CSF) approximation of Brackbill et al. (1992), which forms the basis for the VOF model. The currents are generated in the near-interface regions on account of local variations in the CSF body force, which is essentially an approximation of the surface tension forces in this region. At higher magnitudes, the parasitic currents could destroy the interface and thereby adversely affect the hydrodynamics of the flow.

Past works have demonstrated that phase field modeling can significantly reduce the magnitude of parasitic currents. De Menech (2006) demonstrated by means of a simple static droplet problem that the magnitude of spurious currents at the interface could be significantly reduced by up to 5% of the characteristic flow velocity by changing the grid resolution. His study utilized the phase-field model to govern the interface, coupled with the Navier-Stokes equation to govern the flow hydrodynamics.

Similar results were reported by He and Kasagi (2008) for a comparison of the CSF and the phase-field methods for modeling gas-liquid two-phase flow. Both models were first applied to a stationary bubble problem, the results of which indicated that the unbalanced surface tension forces in the CSF model resulted in parasitic currents. These were reduced to the level of machine accuracy using the phase-field model. The improved performance was attributed to the appropriate transfer of the initially generated energy due to the discretization error between the kinetic energy and the surface tension energy, which is further dissipated as viscosity. They further performed two-dimensional simulations of air-water two-phase flow in a minichannel for the Taylor and bubbly flow regimes. It was observed that the bubbles obtained using the CSF method for surface tension had additional circulations in the interior of the bubble, which was attributed to the accelerating effect produced by the parasitic flow components.

The advantages of the phase field method over alternate multiphase models have already been demonstrated to a fair extent in previous works. These advantages are verified here as well.

2.2.4.3 Wall adhesion

Liu and Zhang (2009) proposed the use of a lattice Boltzmann approach for modeling the hydrodynamics and a phase field approach for governing the interface. Findings on the influence of capillary number, flow conditions and fluid properties were discussed. The influence of wettability was studied by varying the specified contact angle: 110° to 180°. This was reported to affect the phase distribution in the flow domain at spatial scales in terms of the droplet shape and in temporal scales in terms of bubble generation (detachment) frequency. While the effect of wettability was dominant at low capillary number flows (typically less than 10^{-2}), even then, the specified values of static contact angle were not always replicated in the simulated flow patterns. While this was attributed to contact angle hysteresis, further investigation is required, given that alternative modeling approaches such as the VOF model (Qian and Lawal, 2006; Santos and Kawaji, 2010) have been reasonably successful at simulating accurate contact angles.

The following issues pertaining to modeling of wall adhesion are addressed in this dissertation. Phase field simulations considering wall adhesion for two multiphase systems have been performed. First is a spinodal decomposition problem that isolates the governing equations for hydrodynamics (Navier-Stokes) from those for interface tracking (phase field). This was aimed at simplifying the physics at hand in order to

31

obtain a better understanding. Second is the Taylor flow problem, which is more involved than the former. Additionally, a wider range of contact angles than those used by Liu and Zhang (2009) have been utilized for both problems.

2.2.4.4   Modeling of thin liquid film

Gas-liquid Taylor flow is generally characterized by the presence of a thin film of liquid phase between the gas bubble and the channel wall, which prevents the occurrence of a dry-out condition (region of wall being occupied entirely by gaseous phase; not to be confused with the dry-out associated with critical heat flux). Capturing this liquid film by numerical simulation has proven to be a significant challenge. A multitude of results has been reported in the literature, ranging from complete dry-out at the wall, to the existence of a temporary liquid film that subsequently dissipates downstream, to a stable liquid film surrounding the bubble.

Modeling studies that do not have a junction at the inlet, where two phases meet and impinge, have been relatively successful in capturing the liquid film. Shao et al. (2008) and Chen et al. (2009) attempted to simulate the experimental results of Salman et al. (2006), which had a nozzle-type inlet configuration. The former used a grid resolution of $D/50$ in an implementation of the VOF model, while the latter used grid resolutions ranging from $D/40$ to $D/80$ in an implementation of the level-set method. The notation D/n pertains to the mesh element size, where D is the characteristic dimension of the channel and n is the factor by which it is resolved. While both studies reported the presence of the liquid film, it is worth noting that this success in capturing the liquid film might have been aided by the absence of a mixing

junction at the inlet, as indicated by the use of a nozzle for injecting both phases (similar to an annular inlet). Gupta et al. (2009), who implemented the VOF model, reported the presence of a stable liquid film at grid resolutions of $D/200$ and higher, while at $D/100$ the initially obtained liquid film dissipated as the bubble progressed through the channel. Their study also used an annular inlet configuration. They indicated that the expression by Bretherton (1961) as given by Eq. 2.13 for film thickness could be used as a guideline for resolving the computational domain near the channel wall with typically at least five elements across the liquid film. Similar results that were able to capture the thin liquid film, were reported by Asadolahi et al. (2011, 2012), wherein the behavior of a periodic unit cell of Taylor flow was modeled with a computational domain that moved with the bubble velocity while the bubble was kept stationary in the domain. This moving domain approach was reported to require less computational time than that of Gupta et al. (2009).

$$\frac{2\delta}{D} = 1.34 \times \left[\frac{\mu_L (U_L + U_G)}{\sigma} \right]^{2/3} \tag{2.13}$$

Unlike the above studies, which lack a mixing region at the inlet, several works have modeled channels otherwise. Qian and Lawal (2006) applied the VOF model in channels having a T-junction inlet configuration. Their results indicated a dry-out condition at the channel wall. However, this may have been caused by the low domain resolution in their study (value of domain resolution not explicitly mentioned). Further, Krishnan et al. (2010), who also implemented the VOF method for channels with a cross-flow inlet configuration, remarked on the high

computational costs associated with extremely fine grids (like $D/100$ in Gupta et al., 2009) but nonetheless utilized a relatively high resolution of $D/35$. Their aim was to simulate an unstable liquid film (prone to subsequent dissipation) in the vicinity of the inlet mixing region. While the outcome of this strategy was not clearly indicated, the reported results do not indicate the presence of a stable liquid film.

Santos and Kawaji (2010) presented three-dimensional simulations (based on the VOF method) of Taylor flow in a channel having cross-flow inlet configuration. Their mesh spacing of 5.67 μm, though small, corresponds to a domain resolution of only $D/20$, which cannot be considered an adequately fine mesh. Despite modeling the third dimension and using a measured value of the static contact angle, their numerical predictions indicated a dry-out condition at the wall.

Using a fundamental lattice-Boltzmann based model, Yu et al. (2007) reported the occurrence of a liquid film for capillary numbers, typically of the order of 10^{-2}. For the lower values of capillary numbers wherein dry-out was predicted, the limited resolution of the domain (value not mentioned explicitly) was remarked to be the contributing factor.

The above review indicates that variant results have been obtained by different studies, though based on the same numerical model. In general, it can be inferred that the presence of an inlet mixing junction as compared to a co-injection configuration, results in a more complex numerical problem due to the different bubble formation mechanisms associated with these cases. The occurrence of the dry-out condition can be attributed to several factors as outlined by Santos and Kawaji (2010). Among

34

those, it is believed that insufficient grid resolution may not be a sole factor, since, even with relatively coarse grids, an unstable film (that dissipates later) is expected to be formed. Investigations on this are indeed a challenge due to computational power requirements, as indicated by the extremely long simulation times reported by Gupta et al. (2009). Further, adopting a block-structured discretization strategy for the computational domain is not feasible with all models, such as the present phase field method, since this would not maintain a constant resolution of the interface throughout. Inaccuracies in the defined values of the static contact angle and surface tension are not believed to be significantly dominant factors. Modeling of a dynamically varying contact angle at the channel wall also requires future investigation.

2.3 Numerical modeling of two-phase flow with heat/mass transfer

Gas-liquid mass transfer with chemical reactions is a complex process that can involve the transport of multiple species across the gas-liquid interface. On the other hand, condensation heat transfer involves only liquid and vapor phases without multiple species. In both processes, the void fraction of the gas/vapor phase decreases along the channel length, albeit due to different reasons. This section reviews those works that have conducted numerical modeling of condensation phenomena, and subsequently gas-liquid absorption in microchannels.

2.3.1   Modeling of condensation

Miniaturization of electronic devices has led to advances in various engineering fields, including space technology, defense systems, aerospace applications,

manufacturing technology, industrial processes and consumer electronics. Researchers in these fields are investigating novel methods to manage the thermal dissipation from electronic components in miniaturized devices, with the aim of guaranteeing the reliability and safety of the device during operation, and microscale and nanoscale technologies have played an important part in this effort (Wang et al., 2004; Baummer et al., 2008; Kim et al., 2008; Cetegen, 2010; David et al., 2011; Ganapathy et al., 2011d; Harirchian and Garimella, 2011; Harish et al., 2011; Krishna et al., 2011; Ganapathy and Sajith, 2013; Ohadi et al., 2013).

The use of microscale heat exchangers to manage this thermal dissipation has been widely studied since the pioneering work of Tuckerman and Pease (1981). Since then, the majority of literature has focused on characterizing the heat transfer coefficient and pressure drop for electronics cooling applications, as reported by Sobhan and Garimella (2001). While changes in simple channel geometries can yield significant enhancements in thermal performance, the improvements come at the expense of high pressure drops. However, this drawback is being actively mitigated by the development of advanced designs for microchannel heat exchangers, using innovative fluid feed systems (Ohadi et al., 2013).

A major advantage of numerical modeling of heat transfer over simpler empirical correlation-based approaches is that, the former, when appropriately validated with experimental data, may serve as an effective tool for the design and optimization of next-generation, compact heat exchangers utilizing complex geometries. While correlations are specific to the geometries for which they were originally developed,

numerical modeling, once validated, can be extended to non-conventional and more complicated geometries. Additionally, numerical modeling provides insight into the details of the flow field and transport phenomena.

Existing approaches for modeling phase change phenomena under steady state conditions include the formulation proposed by Wang and Rose (2005, 2006, 2011), who reported a fundamental approach for laminar film condensation based on the Nusselt approximations, which was subsequently applied to study different minichannel geometries. Similarly, Wu et al. (2009) reported a three-dimensional model for steady state annular condensation in rectangular microchannels.

While boiling heat transfer involves numerous, complex physical mechanisms, the physics governing evaporation, in addition to being simpler, also closely resembles that responsible for condensation heat transfer. From a modeling perspective, both these modes bear certain resemblances to the presently studied condensation heat transfer, and are therefore reviewed here. Heat transfer from thin films during evaporation comprises a meniscus region, an evaporating thin film region, and a nanoscale non-evaporating region. Wang et al. (2007a, 2007b) utilized a Young-Laplace approach coupled with kinetic theory-based expressions for modeling thin film evaporation in microchannels. Subsequently, Mandel et al. (2011) coupled the models of Wang et al. (2011) and Xu and Carey (1990) to obtain an improved formulation of the problem and therefore better accuracy. Modeling of similar problems using kinetic theory-based expressions in conjunction with commercial CFD codes was reported by Ranjan et al. (2011) for thin film evaporation in capillary

wicks and by Wang et al. (2011) for an evaporating meniscus in an open V-microgroove.

All of the above studies were based on steady-state analysis. In other words, a solution of the governing equations yielded the profile of the liquid-vapor interface, based on which, the two-phase heat transfer performance was estimated. An alternative approach is to continuously track the transient liquid-vapor interface. This results in a highly accurate prediction of the interfacial area in the microchannel, which in turn influences the phase change mass flux and heat transfer. The method generally involves including mass and energy source terms in the multiphase flow model, and implementations of the method for film boiling problems have been reported by several groups. Juric and Tryggvason (1998), Esmaeeli and Tryggvason (2004a, 2004b), and Tryggvason et al. (2005) implemented the front tracking model of Unverdi and Tryggvason (1992), Son and Dhir (1998) implemented the level set method of Sussman et al. (1994), and Welch and Wilson (2000) implemented the volume of fluid (VOF) method of Hirt and Nichols (1981).

Zhang et al. (2001) modeled condensation in a minichannel using the VOF model to govern the interface, and defined mass and energy source terms to model the phase change phenomena. A steady-state solution was obtained for the transient problem using a false transient method. The model was validated based on the liquid film thickness during Nusselt condensation on a vertical flat plate.

Mukherjee and Kandlikar (2005) modeled the growth of a single bubble due to evaporation during flow boiling in a microchannel. This was a fundamental study that

applied Fourier's law to estimate the heat flux at the liquid-vapor interface and determine the corresponding evaporation mass flux based on the latent heat. The level set method was implemented to govern the liquid-vapor interface. The results demonstrated the axial growth of a single bubble as it progressed through the channel and the results were qualitatively validated against the available experimental visualization data of Balasubramanian and Kandlikar (2004).

Wu et al. (2007b) and Yang et al. (2008b) modeled flow boiling in conventional channels having a serpentine structure using the Eulerian and the VOF models, respectively. The phase change was modeled following the approach of Lee (1980), which assumed a quasi-thermo equilibrium state at constant pressure, with the mass transfer being determined by the saturation temperature. Empirical coefficients were present in the expressions for the source terms, and appropriate values for the same were recommended in order to maintain the interfacial temperature reasonably close to the saturation temperature and to avoid divergence issues. The phase distribution in the channel was qualitatively compared with experimental visualization data.

Fang et al. (2010a) modeled flow boiling in a vapor-venting microchannel. The system was designed to locally vent the generated vapor phase into a separate secondary channel, thereby ensuring that the primary channel is predominantly occupied by the liquid phase. The interface was governed by the VOF model and their mass transfer formulation was similar to that of Yang et al. (2008b). The effect of the porous membrane that performed the venting action was also considered, and the associated flow patterns in these vapor-venting channels were compared with that

obtained using non-venting channels. The former was reported to yield reductions in pressure drop, dry-out and flow instabilities.

Jeon et al. (2011) studied the dynamics of a single condensing bubble during subcooled flow boiling in a conventional channel. The VOF method was used to govern the liquid-vapor interface. An empirical correlation derived by Kim and Park (2011) was used to quantify the interfacial heat and mass transfer. The predictions of time-variant bubble volume were favorably compared with transient experimental measurements.

Wang and Zhuan (2008) and Zhuan and Wang (2010, 2011, 2012) modeled flow boiling in mini/microchannels having various cross-sectional geometries. The various regimes of the boiling process were modeled using known empirical expressions for the heat flux in each regime. The bubble characteristics, boiling curves and flow regime transition lines for certain flow patterns, primarily intermittent liquid-vapor flow patterns, were reported and compared against experimental data.

A summary of select previous works is reported in Table 2.2. The above review indicates that majority of the studies on transient numerical simulation of phase change phenomena have focused on boiling and evaporation heat transfer, and relatively fewer works have modeled transient condensation in microchannel geometries. Further, the use of empirical expressions integrated with the numerical governing equations appears to be a common way to model the physics of the phase change phenomena. While such studies are indeed valuable for certain simple geometries, their potential for application to any other geometry is limited by the

40

availability of an empirical correlation for that particular geometry. Hence, it is essential to develop a purely theoretical and validated formulation that explicitly solves for the physics of the phenomena, which could be of use for the design of next-generation heat exchangers having complex, microscale geometries.

Table 2.2: Summary of select works on modeling of condensation.

Authors	Heat transfer phenomena	Computational domain	Nature of model	Multiphase model	Validation of model
Zhang et al. (2005)	Condensation	Minichannel (1.5 mm)	Theoretical	Volume of fluid	Quantitative: film thickness
Mukherjee and Kandlikar (2005)	Evaporation of single bubble during flow boiling	Microchannel (100 μm)	Theoretical	Level set	Qualitative: transient bubble profiles
Wu et al. (2007)	Flow boiling	Conventional channel (8 mm)	Theoretical	Eulerian	Qualitative: flow patterns
Yang et al. (2008b)	Flow boiling	Conventional channel (6 mm)	Theoretical	Volume of fluid	Qualitative: flow patterns
Fang et al. (2010a)	Flow boiling	Vapor venting microchannel (200 μm)	Theoretical	Volume of fluid	Qualitative: flow pattern; quantitative: liquid rise velocity in porous medium
Jeon et al. (2011)	Condensation of a single bubble during subcooled flow boiling	Conventional channel (15 mm)	Theoretical and empirical expressions	Volume of fluid	Qualitative: transient bubble profile; quantitative: transient bubble volume
Zhuan and Wang (2008)	Flow boiling	Microchannel (41, 48 μm)	Theoretical and empirical expressions	Volume of fluid	Quantitative: transient bubble diameter
Zhuan and Wang (2010)	Flow boiling	Minichannel (768 μm)	Theoretical and empirical expressions	Volume of fluid	Quantitative: transient bubble diameter
Zhuan and Wang (2011)	Subcooled flow boiling	Minichannel (200, 334 μm)	Theoretical and empirical expressions	Volume of fluid	Quantitative: void fraction, boiling curves
Zhuan and Wang (2012)	Flow boiling	Minichannel (500 μm)	Theoretical and empirical expressions	Volume of fluid	Quantitative: bubble departure diameter, location and frequency, flow regime transition lines

2.3.2   Modeling of mass transfer

Modeling of mass transfer in mini/microchannels has been conducted using empirical approaches as well as numerical formulations. Berčič and Pintar (1997) experimentally studied the absorption of methane in water during Taylor flow in minichannels and subsequently proposed an empirical correlation for the mass transfer coefficient. However, as has been reviewed and remarked upon in many subsequent works, the notable absence of any functional dependence on channel diameter in their correlation has led to a relatively poor predictive accuracy of the expression for alternative systems.

Fundamental approaches to predict the mass transfer coefficient were developed by Irandoust and Andersson (1989) by separately considering the various contributions to the overall mass transfer from the gas bubble through the liquid film to the channel wall, from the gas bubble to the liquid slugs through the bubble caps, and from the liquid slugs to the channel wall. Likewise, van Baten and Krishna (2004) modeled a single unit cell of Taylor flow in minichannels of varying diameters and accounted for the mass transfer contributions from the two bubble caps and the film region. Modifications to their model in order to consider long contact times (or large unit cell lengths) were suggested by Vandu et al. (2005) in order to match their predictions with experimental data for the absorption of oxygen into water, wherein the film contribution to mass transfer was shown to be the dominant factor.

Yue et al. (2007a) reported reactive mass transfer experiments in a rectangular minichannel and proposed an empirical correlation for the mass transfer coefficient.

Subsequently, Yue et al. (2009) reported another empirical correlation for non-reactive mass transfer in square minichannels to improve the inaccurate predictions obtained by using certain previous mass transfer correlations, such as that of van Baten and Krishna (2004), for their square minichannel application. Likewise, Su et al. (2010) and Tan et al. (2012a) have also proposed empirical expressions for Sherwood number and mass transfer coefficient, respectively.

It is worth noting from the above brief review of empirical approaches, that these methods are typically limited to specific systems only and are not universal in nature. For this reason, certain studies, including the present one, have focused on the development of numerical approaches, which are reviewed subsequently.

Salman et al. (2004) modeled a unit cell of the Taylor flow regime using a finite volume method-based code. An initial tracer concentration was applied to the cell, and changes to its concentration were tracked. The model was reported to be suitable for low Bodenstein numbers only, and a simplified analytical solution was proposed for higher Bodenstein numbers, typically greater than 10. A similar approach was presented by van Baten and Krishna (2004) considering only the liquid slug and treating the Taylor bubble as a void with a constant initial tracer concentration at the interface.

Raimondi et al. (2008) performed direct numerical simulation (DNS) of liquid-liquid mass transfer during Taylor flow in square microchannels. The hydrodynamics were obtained by the VOF method. The concentration field was governed using transformational parameters to modify the conventional convention-diffusion

equations in order to derive equations that were compatible with the one-fluid

approach used for predicting the hydrodynamics of the flow. It is worth noting that

Raimondi et al. (2008) decoupled the hydrodynamics from the mass transfer, and

therefore their method is accurate only when the transport of species negligibly

affects the hydrodynamics of the flow. In other words, interfacial deformations due to

mass transfer are assumed to be negligible here. These issues were outlined by Onea

et al. (2009), who reported a qualitative study of the mass transfer across deforming

interfaces. The model was based on the VOF approach and considered a continuous

numerical concentration across the interface by implementing Henry's law on one

side and a reference concentration on the other. The discontinuities in mass flux

across the interface were overcome by effecting appropriate modifications to the cell

face diffusivities.

Shao et al. (2010) noted that some previous modeling approaches are not well suited

for applications involving chemical reactions for which a highly accurate prediction

of the interfacial concentration is required. These include approaches that consider

only the bubble boundary and apply a tracer concentration at the interface. They

proposed a numerical model which considered both phases and simultaneously solved

for the concentration change in each phase. The gas concentration at the interface was

continuously updated in a method very similar to that of Onea et al. (2009), by using

Henry's law to obtain a continuous concentration profile. As in most previous studies,

the Taylor flow regime was modeled using the unit cell approach, with mass transfer

occurring across the interface to both the liquid slugs and the thin liquid film region

between the gas bubble and channel wall. They favorably compared their predictions

45

against experimental data while the disagreement with existing empirical correlations was noted.

Various other types of models have been proposed by Kececi et al. (2009), Bothe et al. (2011), Hassanvand and Hashemabadi (2011, 2012), Aboulhasanzadeh et al. (2012, 2013), Abiehv and Lavretsov (2012), Marschall et al. (2012), and Kuzmin et al. (2013).

2.4 Chapter Closure

A comprehensive survey of the literature pertaining to the topics discussed subsequently in this dissertation was provided in this Chapter and the deficiencies in published literature for these topics were identified. Section 2.1 focused on experimental analyses of gas-liquid absorption in various types of microreactors. Section 2.2 focused on the modeling of adiabatic, non-interacting two-phase flow. Numerical approaches for modeling of heat/mass transfer in microchannels were reviewed in Section 2.3. Subsequent chapters in this dissertation describe the presently undertaken research efforts and their outcomes.

Chapter 3: Experimental Study of Single Channel Microreactors

3.1 Introduction

This chapter reports an experimental analysis of the fluid flow and mass transfer characteristics during the absorption of CO_2 mixed with N_2 in aqueous DEA in single channel microreactors. A detailed description of the experiments is reported in Section 3.2. The performance is characterized with respect to the absorption efficiency, pressure drop, mass transfer coefficient, interfacial area, enhancement factor, and Sherwood number. Various two-phase flow regimes are visualized by high-speed imaging and their associated mass transfer performances are analyzed. An image-processing algorithm is developed to quantify the gas-liquid interfacial area. Parametric studies varying the flow rates of the gas and liquid phases, liquid phase reactant concentration, and gas phase concentration are conducted. The effect of residence time is studied by varying the channel length for a microreactor with hydraulic diameter of 762 μm (Section 3.3). The effect of hydraulic diameter is investigated for reactor hydraulic diameters of 762, 508 and 254 μm (Section 3.4). The single-phase and two-phase frictional pressure drop data is validated by comparison with available models. A modified approach is proposed for predicting the two-phase frictional pressure drop with amine-based working fluids. Lastly, empirical Sherwood number models are developed and compared with the presently obtained experimental data.

3.2 Description of experiments

3.2.1　Experimental setup

A schematic of the test setup is shown in Figure 3.1. The test section involved a minichannel having circular cross-sectional geometry and hydraulic diameters of 762, 508 and 254 μm. The channels were made of a polyphenylsulfone, a transparent polymer whose commercial name is Radel R (Idex Health & Science, USA). Three such channels having lengths of 0.5 m, 0.3 m and 0.1 m were investigated in this work.
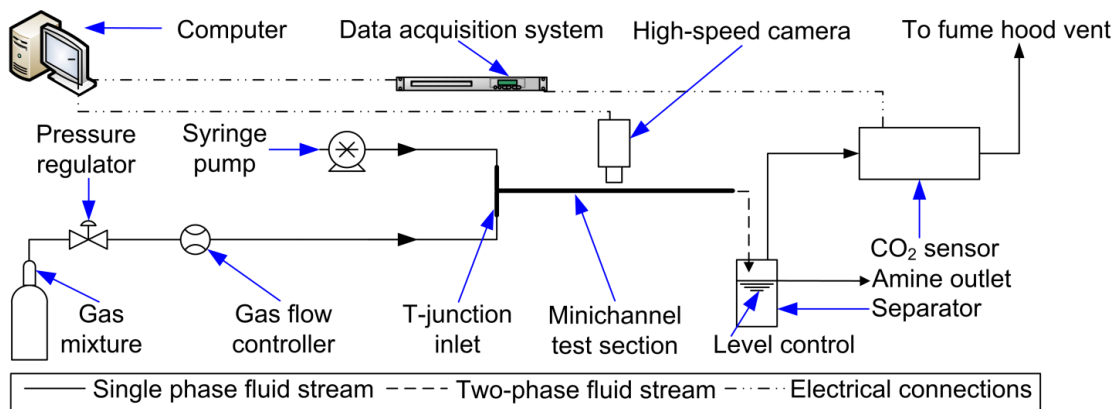
Figure 3.1: Schematic of experimental test setup.

A T-junction inlet configuration was used to inject the gas and liquid phases into the minichannel test section. A syringe pump (Harvard Apparatus, USA) was used to control the liquid flow rate. The pressurized gas mixture was present in a cylinder connected to a pressure regulator. A differential pressure-based mass flow controller (Cole-Parmer, USA) measured and controlled the flow rate of the gas phase. The gas flow rate controller also measured the absolute pressure, and since the outlet of the channel was exposed to the atmosphere, the differential pressure drop across the flow

48

loop could be determined. Two-phase flow patterns were visualized using a high-speed camera (Vision Research, USA) at a rate of 3000 frames per second. The two-phase mixture leaving the reactor entered a separator column that used gravity to separate the loaded amine solution from the unabsorbed gas stream. The column was constructed to have an internal diameter of 0.04 m, and a level control mechanism maintained a relatively constant level of liquid in the column by continuously removing the liquid amine solution. The design was such that a minimal quantity of liquid, approximately 6 mL, was present in the separator column during the experiments, ensuring that minimal absorption occurred outside of the minichannel test section. The concentration of CO_2 in the unabsorbed gas stream, $C_{CO_2,out}$, was measured by a non-dispersive infrared sensor (Vaisala Inc., USA). This value, in conjunction with the concentration of CO_2 at the inlet of the channel, $C_{CO_2,in}$, yielded the absorption efficiency (Eq. 3.1).

$$\eta_{abs} = \frac{C_{CO_2,in} - C_{CO_2,out}}{C_{CO_2,in}} \times 100\% \qquad (3.1)$$

3.2.2 Measurement of pressure drop

The two-phase pressure drop through the minichannel test section was determined by conducting two sets of experiments in order to account for the additional pressure drop across the remaining flow components. The first set of measurements was obtained with the entire length of the channel connected in the test setup. The second set was performed with a channel of similar diameter, but having a shorter length of 0.02 m, connected in the test loop. The difference between the measured values of

49

pressure drop from two sets of experiments performed at the same flow rate yielded the total experimental two-phase pressure drop, ΔP_{TP}. This quantity comprised the pressure drop due to the effects of friction and acceleration, as given by Eq. 3.2, in a single minichannel of known length. It is noted that the acceleration component, $\Delta P_{TP,A}$, was present only when gas-liquid absorption occurred in the reactor and for such cases, this component was quantified by Eq. 3.3 and subtracted from the measured pressure drop, ΔP_{TP}, to yield the two-phase frictional pressure drop, $\Delta P_{TP,F}$. For the present absorption experiments, $\Delta P_{TP,A}$ is a negative quantity.

$$\Delta P_{TP} = \Delta P_{TP,F} + \Delta P_{TP,A} \tag{3.2}$$

$$\Delta P_{TP,A} = G^2 \left[\left(\frac{x^2}{\rho_G \alpha} + \frac{(1-x)^2}{(1-\alpha)\rho_L} \right)_{out} - \left(\frac{x^2}{\rho_G \alpha} + \frac{(1-x)^2}{(1-\alpha)\rho_L} \right)_{in} \right] \tag{3.3}$$

Theoretical analysis of the two-phase frictional pressure drop requires knowledge of the single phase frictional pressure drop as well. For this purpose, separate experiments were conducted with the liquid phase flowing through the minichannel. The channel outlet was maintained at atmospheric pressure, and the pressure drop was measured by a differential transducer (Validyne Engineering Corp., USA). Water and aqueous amine solution (20% concentration by mass) were used as the working fluids. Contraction losses at the inlet were estimated using the loss coefficient, K_c, as given by Eq. 3.4. The head loss at the channel outlet due to sudden expansion was estimated with the loss coefficient, K_e, equaling unity since the channel outlet, for these single-phase measurements, was directly exposed to the atmosphere. By subtracting these losses from the experimentally measured pressure drop, ΔP_{SP}, the

single-phase frictional pressure drop, $\Delta P_{SP,F}$ was calculated (Eq. 3.5). Subsequently, the experimental Darcy friction factor, $f_{exp,F}$ was determined from Eq. 3.6.

$$K_c = 0.42\left[1-\left(\frac{D_1}{D_2}\right)^2\right]; \; D_1 < D_2 \tag{3.4}$$

$$\Delta P_{SP,F} = \Delta P_{SP} - \left(K_e\frac{\rho U^2}{2}\right) - \left(K_c\frac{\rho U^2}{2}\right) \tag{3.5}$$

$$f_{exp} = \frac{2\Delta P_{SP,F}D}{\rho L U^2} \tag{3.6}$$

3.2.3 Measurement of interfacial area

The flow patterns observed by high-speed visualization were analyzed to estimate the specific interfacial area, which is the surface area of the gas-liquid interface per unit volume of the reactor. The analysis was performed by an in-house MATLAB image processing code that is detailed as follows. First, the acquired image was converted into an 8-bit grayscale image comprised of 2^8 or 256 intensity levels. Second, following the recommendations of Ong and Thome (2011), a 3x3 averaging filter was applied to reduce the image noise. Third, the gradient of intensity across the channel width was calculated at a single axial location. Typical plots of the intensity gradient, obtained by following the above procedure, are reported in for a 762 μm channel, in which the inset images represent situations associated with a single-phase (Figure 3.2a) and two-phase mixture (Figure 3.2b) present in the channel, respectively. In both images, the internal and external boundaries of the top and bottom channel wall are visible. Additionally, the two-phase mixture shown in Figure 2b consists of a thin

51

film of liquid adjacent to the internal channel walls (both top and bottom) and a central gas core. These images represent a small segment of the acquired images and are composed of 20 pixels in the horizontal (X) direction (along the channel length). Both images correspond to the same axial location in the channel, and the reported profiles of intensity gradient were obtained at the axial center of the corresponding images. Fluid flow occurs along the positive X direction. Both the intensity gradient as well as pixel location data on the horizontal and vertical axes in Figure 3.2, respectively, are scaled from zero to unity for better presentation.
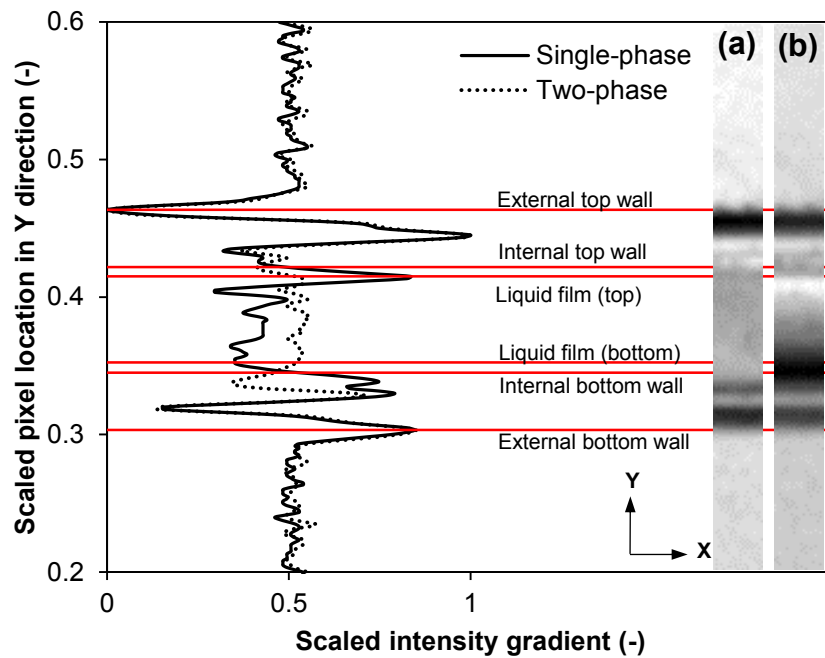
Figure 3.2: Variation of intensity gradient across channel width for (a) single phase (b) two-phase flow. Intensity gradient and pixel locations are scaled from zero to unity. Flow in the inset image is from left to right, along the positive X direction.

As seen in Figure 3.2, peaks are present in the intensity gradient data at locations corresponding to the external top and bottom channel walls. The distance between the

two peaks, in conjunction with the outer diameter of the channel (1587.5 μm) facilitated in calibrating the image processing code in order to convert pixel-based distances into a physical value of length. In the present work, an average of 96 pixels was present between the top and bottom external channel walls. Accordingly, each pixel represents a physical length of approximately 17 μm, and the inset images in Figure 3.2 correspond to a physical channel length of 340 μm. After the calibration process, the pixels corresponding to the top and bottom internal channel walls were estimated using the known value of channel wall thickness, calculated as (1587.5-762)/2 = 412.75 μm. In this way, the region corresponding to the interior of the channel was quantitatively estimated. Following the analysis procedure of Ong and Thome (2011), the first peak in the intensity gradient that occurred within the interior of the channel was considered to be representative of the boundary between the liquid and gas phases, thereby yielding the thickness of the liquid film both at the top and bottom of the channel. The above procedure was repeated at multiple axial locations in the channel, and the results were averaged.

Kawahara et al. (2002) remarked that flow visualization in circular channels could be adversely affected by the effects of optical distortion on account of the small radius of curvature of the channel wall. As a result, they stated that the observed film thickness in the acquired image could be significantly greater than the actual film thickness in the channel. While this is not of concern for qualitative analysis of flow patterns, Kawahara et al. (2002) recommended the use of a distortion correction factor for quantitative analyses of the acquired images. Likewise, Ong and Thome (2011) remarked that film thickness measurements conducted without accounting for the

effects of refraction would at best be qualitative in nature. Following the recommendations of these studies, the measured values of film thickness in the present work were multiplied by a distortion correction factor. In order to obtain this factor, we compared the gas void fraction, α, obtained from the visualization study, against the predictions of the expression by Armand and Treschev (1946), given by Eq. 3.7. The volumetric flow ratio, β, is defined by Eq. 3.8. Several studies have demonstrated that the gas void fraction in channels having the present range of dimensions can be accurately represented by this model (Zhao and Bi, 2001; Chung and Kawaji, 2004; Hayashi et al., 2007; Yue et al., 2008; Chapter 4; Chapter 5).

$$\alpha = 0.833\beta \tag{3.7}$$

$$\beta = \frac{U_G}{U_G + U_L} \tag{3.8}$$

With the objective of minimizing the discrepancy between the measured gas void fraction and that predicted by the Armand correlation, an optimum value for the distortion correction factor was obtained. A comparison between the experimental and predicted values of gas void fraction is reported in Figure 3.3 for gas and liquid phase superficial velocities ranging from 1.8-9.1 m/s and 0.04-0.4 m/s, respectively. The mean absolute error (MAE) is 7%.
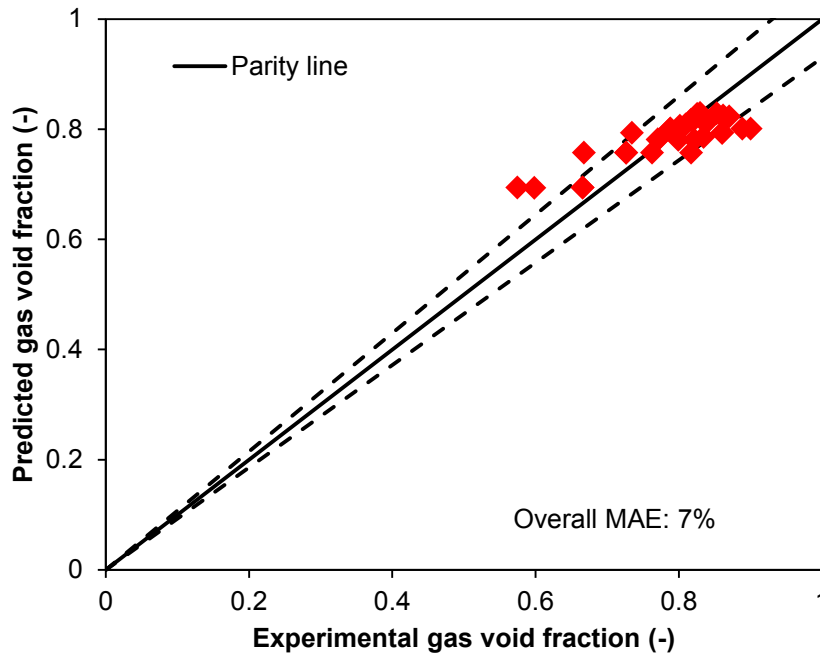
Figure 3.3: Comparison of experimental gas void fraction with expression by Armand and Treschev (1946).

3.2.4   Reaction system

The reaction kinetics between CO_2 and DEA (molecular formula: $(CH_2CH_2OH)_2NH$) follows the zwitterion mechanism (Versteeg and Oyevaar, 1989; Blauwhoff et al., 1984; Versteeg and van Swaaij, 1988), which can be described by the following reactions:

$$CO_2 + (CH_2CH_2OH)_2 NH \underset{k_{-1}}{\overset{k_1}{\rightleftharpoons}} \qquad (CH_2CH_2OH)_2 NH^+COO^- \qquad (3.9)$$

$$(CH_2CH_2OH)_2 NH^+COO^- + B \overset{k_B}{\rightarrow} (CH_2CH_2OH)_2 NCOO^- + BH^+ \qquad (3.10)$$
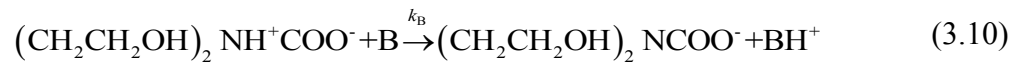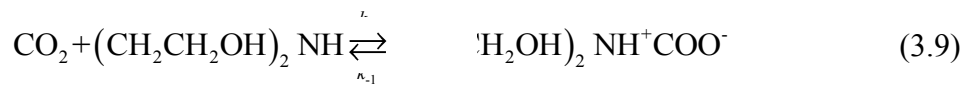
In the second step (Eq. 3.10), "B" represents the species (amine and water) that can deprotonate the zwitterion (molecular formula: $(CH_2CH_2OH)_2NH^+COO^-$). By

55

assuming a pseudo steady state for the zwitterion, the rate of the forward reaction is given by Eq. 3.11.

$$R_{CO_2} = \frac{\left[(CH_2CH_2OH)_2\,NH\right]\left[CO_2\right]}{\dfrac{1}{k_2} + \dfrac{k_{-1}}{k_2 k_{H_2O}\left[H_2O\right] + k_2 k_{(CH_2CH_2OH)_2\,NH}\left[(CH_2CH_2OH)_2\,NH\right]}} \tag{3.11}$$

For the present reaction system, the high diffusivity of the gas phase resulted in a negligible resistance to mass transfer on the gas side (Mills, 1995). Therefore, the dominant resistance to mass transfer was present on the liquid side, and the corresponding mass transfer coefficient was estimated as follows. The CO_2 absorption flux, N_{CO_2}, was determined from Eq. 3.12, wherein the term "a" denotes the specific interfacial area, and "V" is the volume of the reactor. The molar flow rate at the inlet and outlet, $n_{CO_2,in}$ and $n_{CO_2,out}$, respectively, were obtained from experimental measurements of CO_2 concentration and gas flow rate, while the specific interfacial area was determined from high-speed visualization and subsequent image processing-based analysis as detailed in Section 3.2.3.

$$N_{CO_2} = \frac{n_{CO_2,in} - n_{CO_2,out}}{aV} \tag{3.12}$$

The absorption flux is related to the liquid-side mass transfer coefficient, k_L, by Eq. 3.13. Here, the log-mean concentration, $\Delta C_{CO_2,m}$, is defined by Eq. 3.14 in terms of the interfacial concentrations of CO_2 at the inlet and outlet of the reactor. The liquid-side volumetric mass transfer coefficient, k_La, is defined by Eq. 3.15.

$$k_L = \frac{N_{CO_2}}{\Delta C_{CO_2,m}} \qquad (3.13)$$

$$\Delta C_{CO_2,m} = \frac{C^*_{CO_2,in} - C^*_{CO_2,out}}{\ln\left(C^*_{CO_2,in}/C^*_{CO_2,out}\right)} \qquad (3.14)$$

$$k_L a = \frac{n_{CO_2,in} - n_{CO_2,out}}{V \cdot \Delta C_{CO_2,m}} \qquad (3.15)$$

By applying Henry's law (Eq. 3.16), the log-mean concentration can be expressed in terms of the partial pressure of CO_2 (Eq. 3.17). The partial pressure at a given location was calculated based on the mole fraction and absolute pressure.

$$p_{CO_2} = H C^*_{CO_2} \qquad (3.16)$$

$$\Delta C_{CO_2,m} = \frac{1}{H}\left[\frac{p_{CO_2,in} - p_{CO_2,out}}{\ln\left(p_{CO_2,in}/p_{CO_2,out}\right)}\right] \qquad (3.17)$$

The liquid phase mass transfer coefficient for physical absorption was calculated from Eq. 3.18, which follows Higbie's penetration model (Danckwerts, 1970), wherein the gas-liquid contact time, τ, is defined by Eq. 3.19. Subsequently, the enhancement factor, E, which is the ratio of mass transfer coefficient due to the chemical reaction (Eq. 3.13) to that due to physical absorption (Eq. 3.18), was calculated (Eq. 3.20).

$$k_{L,physical} = 2\sqrt{\frac{d}{\pi\tau}} \qquad (3.18)$$

$$\tau = \frac{V}{Q_G + Q_L} \tag{3.19}$$

$$E = \frac{k_{L,\text{chemical}}}{k_{L,\text{physical}}} \tag{3.20}$$

The gas phase was represented by CO_2 mixed with N_2 at concentration levels of 5%, 10% and 18% by mass, and was of industrial grade purity. The liquid phase was aqueous amine solution prepared using laboratory grade DEA (99% purity). The amine was diluted with distilled water to concentration levels ranging from 5-20% by mass, and the corresponding properties are summarized in Table 3.1. The density of the aqueous amine solution was calculated based the mass fraction of its components. The viscosity of the solution was obtained from the data reported by Kohl and Nielsen (1997). The diffusivity of CO_2 and Henry's constant were both determined by the N_2O analogy in conjunction with the experimental data of Versteeg and van Swaaij (1988) and Browning and Weiland (1994), respectively. The solubility of CO_2 in aqueous DEA at various temperatures and partial pressures is shown in Figure 3.4.

All experiments were conducted at an ambient temperature of 298 K and at atmospheric pressure. The gas and liquid phase Reynolds numbers in the present work ranged from 92 to 490 and 18 to 257, respectively.

Table 3.1: Properties of aqueous diethanolamine at various concentrations.

Mass fraction (%)	Concentration (mol/m^3)	Density (kg/m^3)	Viscosity $(mPa\ s)$[1]	Density ratio[2] (-)	Viscosity ratio[3] (-)	CO_2 diffusivity[4] $(m^2/s)\ (x10^{-9})$	Henry's constant[5] $(Pa\ m^3/mol)$
0	0	997.10	0.89	1	1	1.91	3090.70
5	474.76	1001.31	1.09	1.004	1.224	1.64	3268.61
10	949.52	1005.56	1.23	1.008	1.381	1.46	3320.19
15	1424.29	1009.85	1.38	1.013	1.550	1.27	3371.76
20	1899.05	1014.17	1.53	1.017	1.718	1.08	3423.34

[1]data from (Kohl and Nielson, 1997); [2]ratio calculated as $\rho_{solution}/\rho_{water}$; [3]ratio calculated as $\mu_{solution}/\mu_{water}$; [4]determined from (Versteef and van Swaaij, 1988); [5]determined from (Browning and Weiland, 1994).
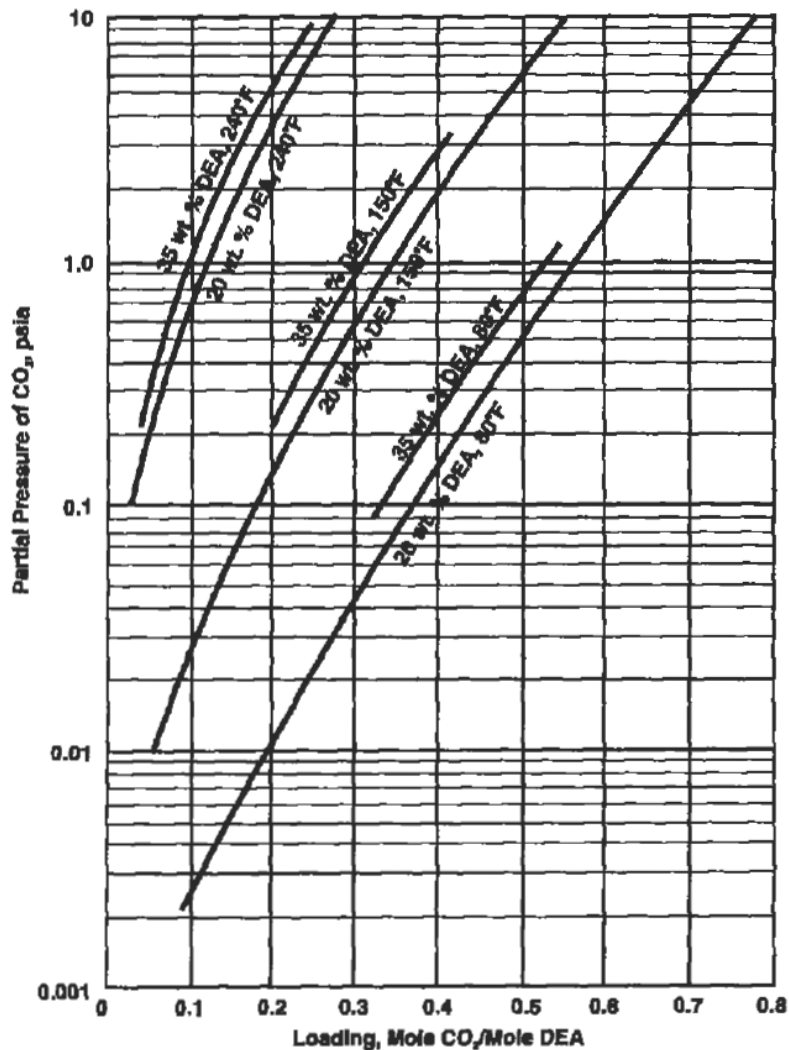
Figure 3.4: Solubility of CO_2 in aqueous DEA at various temperatures and partial pressures (Kohl and Nielsen, 1997).

The absorption of pure CO_2 in DEA is an exothermic reaction having a heat of reaction of 68.8 kJ/mol (Kohl and Nielson, 1997). Even with the assumption that all heat generated is transferred to the liquid phase, the average increase in the temperature of the aqueous amine solution was estimated to be less than 2 K. In reality, there is heat transfer to the gas phase as well as to the ambient environment which should result in a further smaller rise in temperature of the liquid phase. The low values are attributed to the relatively short residence times associated with microscale systems, and the low concentration of the gas phase in the present experiments (at most 18% of CO_2 in N_2 by mass). Accordingly, it was concluded that the rise in reactor temperature as a result of the absorption process could be neglected and hence, a cooling water loop was not required.

The range and limits of error for the various measurement devices are summarized in Table 3.2. The uncertainty in absorption efficiency and liquid-side volumetric mass transfer coefficient was estimated using the error propagation method which can be briefly described as follows. Consider a quantity of interest, Y, that is calculated as a function of i measured variables (Z_1, Z_2, …), as given by Eq. 3.21.

$$Y = f\{Z_1, Z_2, \ldots$$

(3.21)

The uncertainty in each measured variable, u_{Z_i}, contributes to the uncertainty of Y. The resulting uncertainty in Y is u_Y which is estimated as the square root of the sum of squares of individual uncertainties (Eq. 3.22).

$$u_Y = \left[\sum_i \left(\frac{\partial Y}{\partial Z_i} u_{Z_i} \right)^2 \right]^{0.5}$$

(3.22)

Accordingly, the average uncertainties in absorption efficiency and liquid-side volumetric mass transfer coefficient were determined to equal ±6.0% and ±13.9%, respectively, for the constant hydraulic diameter studies (Section 3.3), and ±5.3% and ±17.7%, respectively, for the varying hydraulic diameter studies (Section 3.4).

Table 3.2: Sensor range and limits of error for measurement variables.

Measurement variable	Sensor range	Limits of error
Gas flow rate	0 to 8.3x10^{-6} m^3/s	±(0.8% of reading + 0.2% of range)
Liquid flow rate	0 to 3.7x10^{-6} m^3/s	±0.35% of reading
Differential pressure	0 to 13.8 kPa	±0.25% of range
Absolute pressure	100-1100 kPa	±(0.8% of reading + 0.2% of range)
CO_2 concentration	0 to 20%	±(3% of reading + 1.5% of range)
Temperature	-200 to 350 °C	±1 °C

3.3 Results and discussion: constant hydraulic diameter studies

3.3.1 Two-phase frictional pressure drop

The two-phase pressure drop for N_2-water flow was obtained from experimental measurements following the procedure described in Section 3.2.2. The experimentally measured two-phase frictional pressure drop, $\Delta P_{TP,F}$, was used to calculate the two-phase friction multiplier, ϕ_L^2 using Eq. 3.23, wherein the single phase pressure drop, $\Delta P_{L,F}$, was estimated from Eq. 3.24 in conjunction with the definition for single phase friction factor given by Eq. 3.25 for fully developed laminar flow.

$$\Delta P_{TP,F} = \phi_L^2 \cdot \Delta P_{L,F} \tag{3.23}$$

$$\Delta P_{L,F} = \frac{f_L L \left[G(1-x) \right]^2}{2 \rho_L D} \tag{3.24}$$

$$f_L = \frac{64}{\text{Re}_L} = 64 \left[\frac{G(1-x)D}{\mu_L} \right]^{-1} \tag{3.25}$$

The validity of Eq. 3.25 for the present channel dimensions was verified through

separate experiments conducted to measure the single phase pressure drop across the

minichannel. As seen in Figure 3.5, Eq. 3.25 has a good predictive accuracy with

water as well as with aqueous amine (20% concentration by mass) as working fluids.

The overall MAE is 14.3%, justifying the use of Eq. 3.25 to analyze the two-phase

pressure drop. Likewise, the single-phase pressure drop in the gaseous phase is

defined by Eq. 3.26, and the associated friction factor given by Eq. 3.27. Eqs. 3.24

and 3.26 were used to determine the Martinelli parameter, X, given by Eq. 3.28.

$$\Delta P_{G,F} = \frac{f_G L (Gx)^2}{2 \rho_G D} \tag{3.26}$$

$$f_G = \frac{64}{\text{Re}_G} = 64 \left(\frac{GxD}{\mu_G} \right)^{-1} \tag{3.27}$$

$$X^2 = \Delta P_{L,F} / \Delta P_{G,F} = \phi_G^2 / \phi_L^2 \tag{3.28}$$
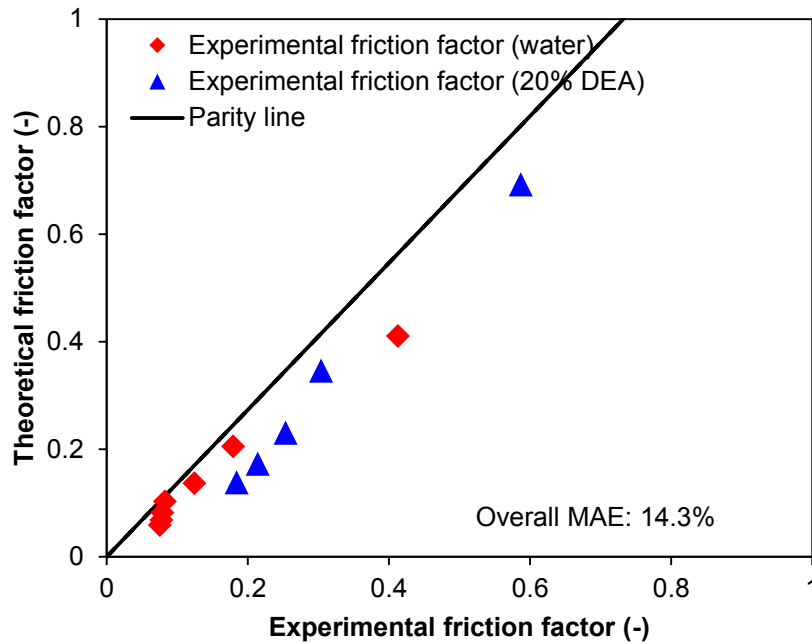
Figure 3.5: Comparison of experimental single phase friction factor with theoretical predictions.

The experimental value of ϕ_L^2 was compared against the predictions by the model of Li and Wu (2010) which is based on the Bond number (Eqs. 3.29-3.31). This model is based on a database of 769 data points obtained from the literature involving various working fluids and operating conditions and has been reported to yield reasonably accurate predictions in previous studies (Kim and Mudawar, 2012b; Park et al., 2012). The two-phase friction multiplier, ϕ_L^2, given by Eq. 3.30, is a function of the Martinelli parameter, X, and the Chisholm parameter, c (Eq. 3.31). For the present range of operating conditions, the Bond number equaled 0.02, which indicates that surface tension forces are dominant over inertial and viscous forces. A reasonably good agreement was obtained with an MAE of 15.1% with water as the working fluid (Figure 3.6a).

$$Bo = \frac{(\rho_L - \rho_G)gD^2}{\sigma} \qquad (3.29)$$

$$\phi_L^2 = 1 + \frac{c}{X} + \frac{1}{X^2} \qquad (3.30)$$

$$c = \begin{cases} Bo \leq 1.5 & 11.9Bo^{0.45} \\ 1.5 < Bo \leq 11 & 109.4\left(Bo\,\mathrm{Re}_L^{0.5}\right)^{-0.56} \end{cases} \qquad (3.31)$$

Subsequently, the same tests were repeated with N_2 as the gas phase and amine solutions as the liquid phase having concentrations of 5% and 20% by mass. The acceleration component of pressure drop was not present for the current experiments on account of the absence of any discernible absorption when the gas phase is N_2. A relatively poor agreement was obtained with MAE values of 37.2% and 59.7% for the 5% and 20% amine concentration cases, respectively (Figure 3.6a). Further, these results are indicative of increasingly higher MAE values with an increase in the amine concentration. The results also make it clear that the model of Li and Wu (2010), which yields good predictive accuracy with water, fails to accurately predict the pressure drop for a viscous liquid phase such as aqueous amine solutions. Hence, the presently obtained pressure drop data for 5% and 20% amine solutions was used to modify the expression for the Chisholm parameter by regression. The optimum expression for c, for use with aqueous amine solutions, is given by Eq. 3.32.

$$c = 14.81Bo^{0.25} \qquad (3.32)$$
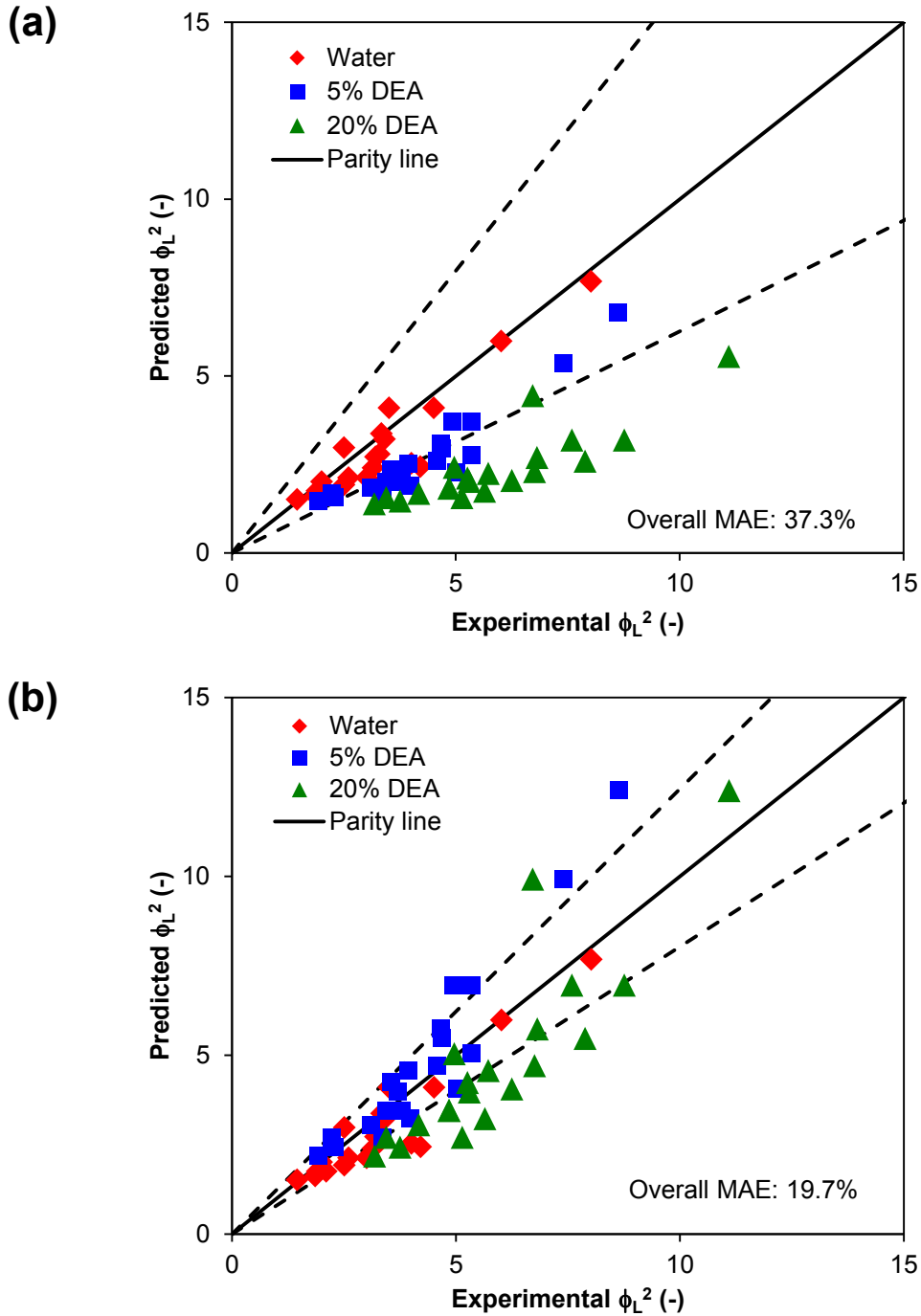
Figure 3.6: Validation of two-phase frictional pressure drop by comparing experimental two-phase friction multiplier with empirical model (a) Li and Wu (2010) model (Eq. 3.31) for water and amine solutions (b) Li and Wu (2010) model (Eq. 3.31) for water and modified Li and Wu model (Eq. 3.32) for aqueous amine solutions.

Figure 3.6b shows a parity plot that compares the experimental two-phase friction

multiplier with the predictions obtained using the modified model for aqueous

amines. A substantial increase in the predictive accuracy was observed with an overall

MAE of 19.7%. Based on these results, we conclude that the proposed model is more

suitable for predicting the pressure drop when viscous aqueous amine solution is the

liquid phase. It is noted that the above results in Figure 3.6 were obtained for two-

phase flow without mass transfer (gas phase is pure N_2). Subsequently, the presently

proposed model was applied for flows with mass transfer, wherein CO_2 mixed with

N_2 is the gas phase, and a reasonably good predictive accuracy was achieved. These

data points (65 in total; discussed later in Sections 3.3.3-3.3.6) yielded an MAE of

26.9% with the proposed model (Eq. 3.32), as against the higher MAE of 48.1%

obtained with the original Li and Wu (2010) model (Eq. 3.31).

3.3.2   Flow patterns

Various two-phase flow patterns were observed by the visualization study, of which

typical images are reported in Figure 3.7. These flow patterns have been mapped in

Figure 3.8 with respect to the gas and liquid phase superficial velocities, U_G and U_L,

respectively. At relatively low U_G and U_L, slug flow (Figure 3.7a) was observed. This

flow pattern is characterized by an alternating arrangement of elongated, cylindrical

gas bubbles and liquid slugs. The gas bubbles are typically longer than the hydraulic

diameter of the channel and are separated from the channel wall by a thin film of

liquid. Recirculating velocity components are present within the gas and liquid phases

that enhance mixing. The corresponding velocity vectors have been obtained

66

experimentally using particle image velocimetry (King et al., 2007; Malsch et al., 2008), and by numerical simulations (He and Kasagi, 2008; Chapter 4).
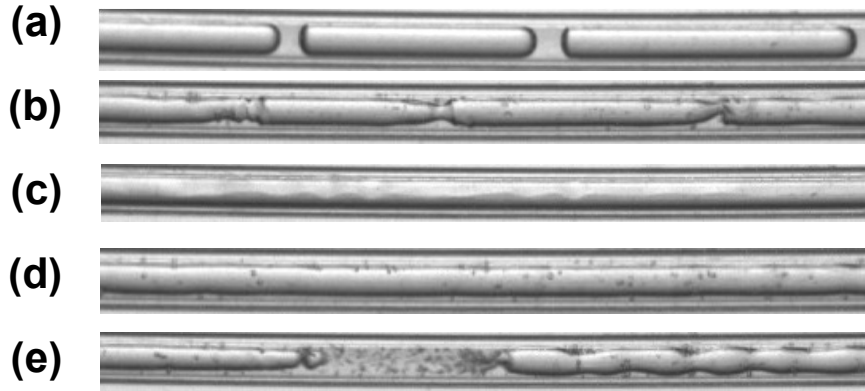
Figure 3.7: Flow patterns during absorption of 10% by mass of CO_2 in N_2 into 20% by mass of DEA in water (a) slug flow (U_L: 0.04 m/s; U_G: 1.8 m/s) (b) slug-annular flow (U_L: 0.1 m/s; U_G: 9.1 m/s) (c) annular flow (U_L: 0.01 m/s; U_G: 18.3 m/s) (d, e) churn flow (U_L: 0.4 m/s; U_G: 9.1 m/s).
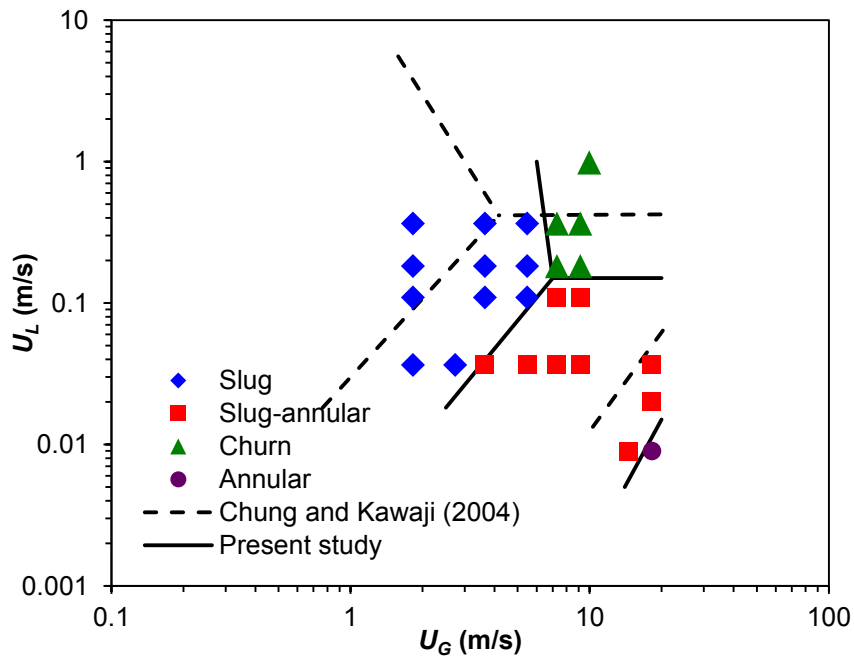
Figure 3.8: Flow pattern map for 762 μm channel.

With an increase in U_G, the mechanism behind the formation of alternative gas

bubbles and liquid slugs becomes less dominant, resulting in slug-annular flow

(Figure 3.7b). Here, the liquid phase does not neck into the gas phase and instead, a

continuous gas core surrounded by a liquid film having periodic interfacial waves was

observed. These interfacial waves become less dominant at higher gas flow rates

resulting in annular flow (Figure 3.7c), which is characterized by a relatively smooth

interface. At gas and liquid flow rates higher than those of both slug and slug-annular

flows, churn flow was observed (Figure 3.7d and Figure 3.7e). This was characterized

by a central gas core surrounded by a liquid film and having either a smooth

interfacial profile at certain instances of time as shown in Figure 3.7d, or a wavy

profile, as shown in Figure 3.7e. Further, the occurrence of periodic instabilities

resulted in disruptive phenomena that periodically broke the gas core and created a

region of intense mixing, as shown in Figure 3.7e.

The transition lines between the flow patterns are reported in Figure 3.8 and

compared against those reported previously by Chung and Kawaji (2004) for a 530

μm channel. In spite of certain differences in the transition lines between these two

studies, which could likely be attributed to the difference in hydraulic diameter (762

μm versus 530 μm), the overall trends are in reasonable agreement.

3.3.3   Effect of superficial velocity

U_G and U_L were varied between 1.8-9.1 m/s and 0.04-0.4 m/s, respectively. The

results reported here correspond to a channel length of 0.5 m, gas concentration of

10% by mass of CO_2 in N_2, and an aqueous amine concentration of 20% by mass of

DEA in water. First, the results of two-phase pressure drop are reported in Figure 3.9. As can be seen, an increase in pressure drop was observed with an increase in both U_G and U_L, which is consistent with the physics of fluid flow.
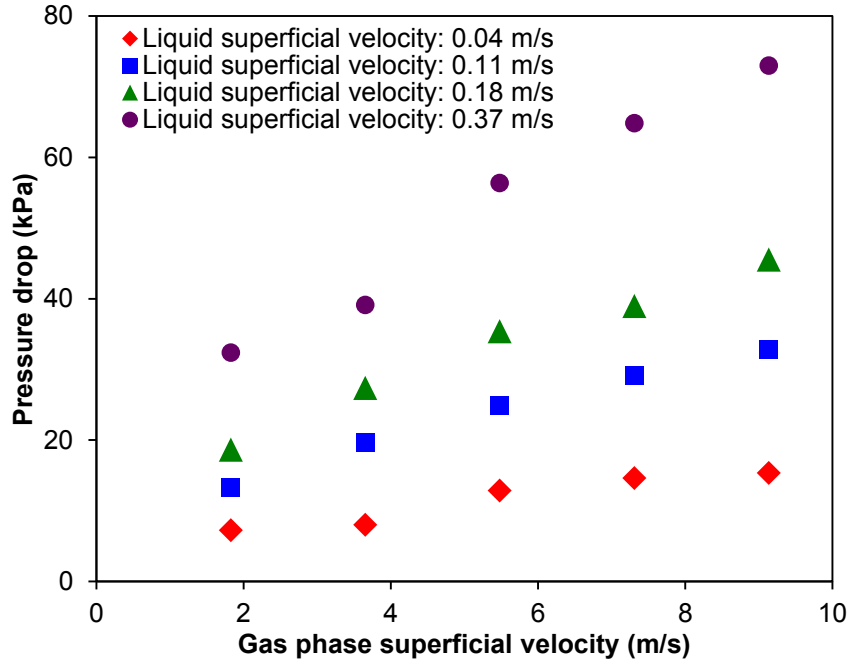
Figure 3.9: Effect of phase superficial velocity on pressure drop (C_{CO2}: 10% by mass of CO_2 in N_2; C_{DEA}: 20% by mass of DEA in water; L: 0.5 m).

The results of absorption efficiency are reported in Figure 3.10. An increase in U_G at constant U_L resulted in a decrease in the absorption efficiency. The reasons for this vary depending upon the prevalent flow pattern. In the slug flow regime, an increase in U_G resulted in a higher magnitude of recirculating velocity currents within the gas bubbles and a lower magnitude of these currents within the liquid slugs. Although this results in additional mixing within the gas phase, this mixing is not influential because the present mass transfer system has negligible resistance on the gas side. In contrast, the dominant resistance to mass transfer is on the liquid side, wherein the

69

magnitude of convective mixing currents is reduced. Here, the liquid reactant adjacent to the gas bubble becomes rapidly saturated, resulting in poorer absorption efficiencies.
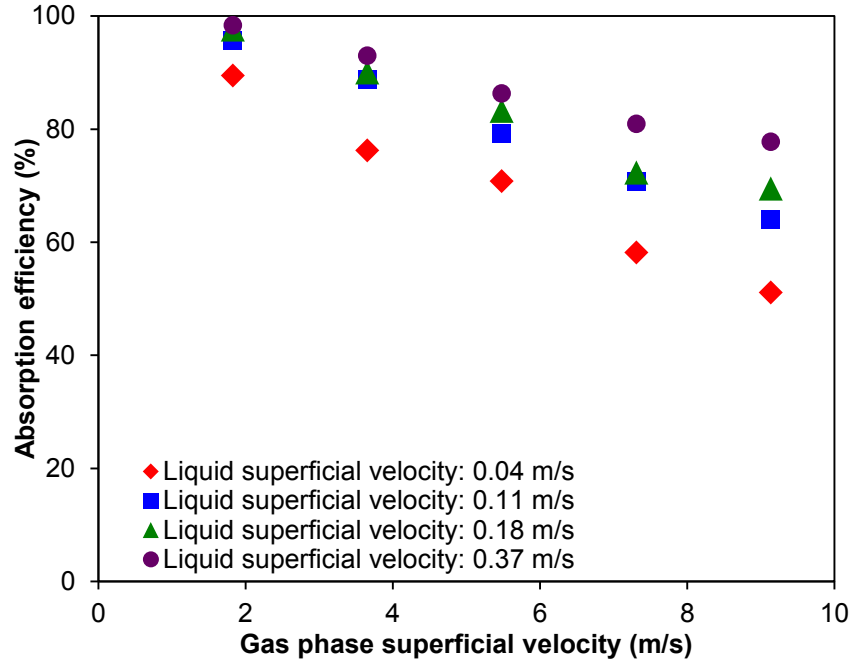
Figure 3.10: Effect of phase superficial velocity on absorption efficiency (C_{CO2}: 10% by mass of CO_2 in N_2; C_{DEA}: 20% by mass of DEA in water; L: 0.5 m).

During slug-annular and churn flow regimes, an increase in U_G leads to a higher gas void fraction and therefore a less thick liquid film. Consequently, the liquid reactant was more easily saturated and reduced absorption was observed to occur. Additionally, the periodic troughs in slug-annular flow (Figure 3.7b), and the intermittent regions of intense mixing in churn flow (Figure 3.7e), are supposed to be locations in the channel associated with high levels of mass transfer. However, with increasing U_G the frequency of occurrence of these regions is expected to decrease. For instance, the transition from slug to slug-annular flow is due to the lack of

sufficient liquid momentum to completely neck into the gas phase and cause bubble detachment to occur. This partial bubble formation mechanism results in the occurrence of troughs and a wavy interfacial profile. Ultimately, at higher gas velocities, annular flow characterized by a smooth interface is observed.

Next, the effect of U_L is discussed. As can be seen in Figure 3.10, for a constant U_G, higher absorption efficiencies were achieved at larger values of U_L. For slug flow, this can be attributed to the increased convective mixing within the liquid phase that delays saturation of the liquid reactant adjacent to the gas-liquid interface. For slug-annular and churn flows, an increase in the liquid film thickness is expected, and the previously discussed regions associated with high mass transfer are expected to occur more frequently. The presently observed trends pertaining to the effect of phase flow rate on absorption efficiency are in agreement with earlier findings by Niu et al. (2009) and Su et al. (2010).

The effect of phase superficial velocity on $k_L a$ is reported in Figure 3.11. It is noted that the expression for $k_L a$ indicates no direct functional dependence on U_L. Clearly, for a constant U_G, the molar flow rate of CO_2 at the inlet of the channel, $n_{CO_2,in}$, does not vary with U_L (Figure 3.12). Therefore, the observed increase in $k_L a$ with an increase in U_L, for a constant U_G, can be attributed to the improvement in absorption efficiency observed in Figure 3.10 that results in a decrease in the molar flow rate of CO_2 at the outlet of the channel, $n_{CO_2,out}$ (Figure 3.12). Hence, Δn_{CO_2} increases, leading to higher values of $k_L a$.
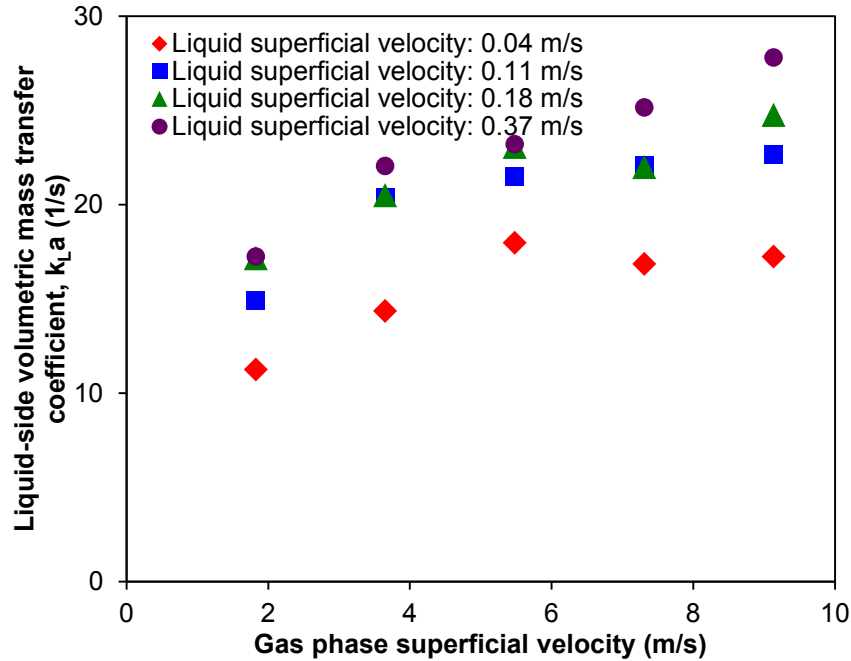
Figure 3.11: Effect of phase superficial velocity on liquid-side volumetric mass transfer coefficient (C_{CO2}: 10% by mass of CO_2 in N_2; C_{DEA}: 20% by mass of DEA in water; L: 0.5 m).

Next, the effect of U_G for a constant U_L is discussed. Obviously, with increasing U_G, there is an increase in $n_{CO_2,in}$ and accordingly, higher values of $n_{CO_2,out}$ were observed. Ultimately, the difference in molar flow rate, Δn_{CO_2}, is higher, as a result of which k_La increases. Similar trends have been reported elsewhere (Yue et al., 2007a; Tan et al., 2012b).

An interesting result was observed for the lowest value of liquid velocity (U_L: 0.04 m/s). Here, with increasing U_G, the value of k_La first increased in the slug flow regime, appeared to reach a peak, and then decreased slightly in the slug-annular flow regime. This can be attributed to a decrease in the liquid film thickness with increasing U_G, due to which the liquid phase becomes saturated faster. Hence the

mass transfer is reduced in comparison to that which could have occurred with a thicker and possibly less saturated liquid film. It is expected that a similar situation would occur at the higher liquid flow rates studied in the present work, provided the gas flow rates are increased beyond the present ranges. However, such extreme operating conditions were not tested on account of excessively high pressure drop. Among previous works on systems dominated by liquid-side mass transfer resistances, the above trend consisting of a peak in $k_L a$ was also reported by Luo and Ghiaasiaan (1997) for larger channel diameters, and more recently by Yue et al. (2007a) for certain liquid flow rates.
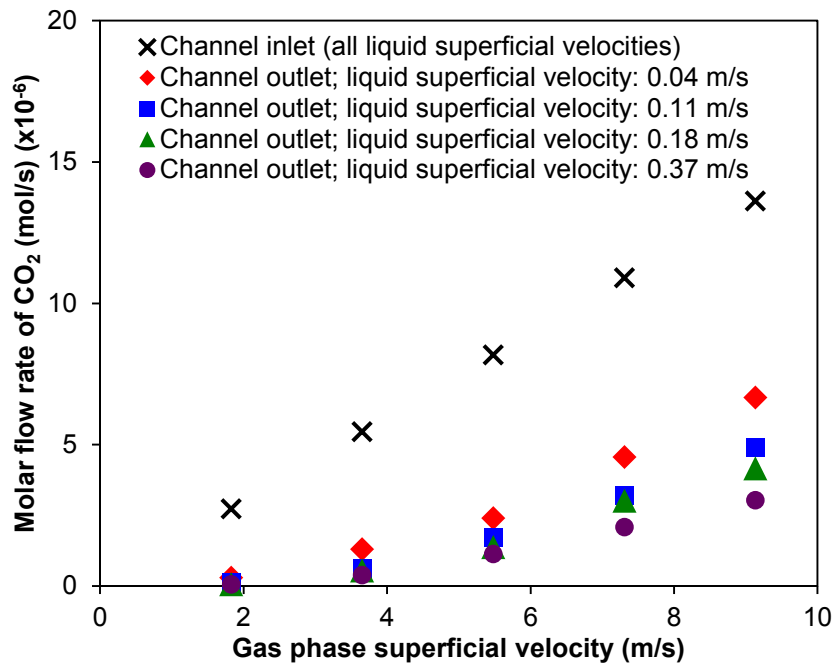
Figure 3.12: Effect of phase superficial velocity on molar flow rate of CO_2 (C_{CO2}: 10% by mass of CO_2 in N_2; C_{DEA}: 20% by mass of DEA in water; L: 0.5 m).

The specific interfacial area was determined from the visualization study and subsequent image processing analysis. The data reported in Figure 3.13 ranges

between 4000 and 4900 m^2/m^3. The highest values of interfacial area were mainly

achieved with slug-annular and churn flow regimes, wherein there is a minimal effect

of phase flow rate. With the slug flow regime, the effect of U_G was relatively

negligible. However, higher interfacial areas were achieved at lower U_L on account of

the longer gas bubbles and shorter liquid slugs associated with this case.
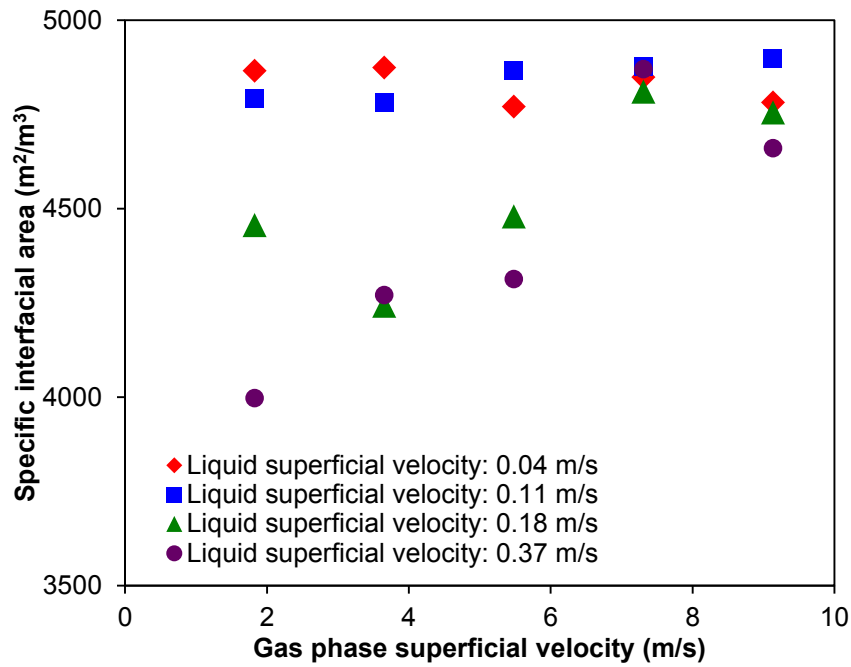
Figure 3.13: Effect of phase superficial velocity on specific interfacial area (C_{CO2}: 10% by mass of CO_2 in N_2; C_{DEA}: 20% by mass of DEA in water; L: 0.5 m).

With the data reported in Figure 3.11 and Figure 3.13, liquid-side mass transfer

coefficient, k_L, and subsequently, the enhancement factor, E, were calculated. The

trends reported in Figure 3.14 indicate a higher value of enhancement factor observed

at larger liquid flow rates and lesser gas flow rates, which is in agreement with Ye et

al. (2012). k_L in dimensionless form can be represented by the Sherwood number (Eq.

3.33), which is a common means of characterizing the mass transfer performance in

74

gas-liquid absorption systems similar to that studied in the present work. Empirical expressions of the form given by Eq. 3.34 have been commonly utilized in the literature, wherein the Schmidt number, *Sc*, is defined by Eq. 3.35.

$$Sh_L = \frac{k_L D}{d} \tag{3.33}$$

$$Sh_L = b_1 \, Re_G^{b_2} \, Re_L^{b_3} \, Sc_L^{b_4} \tag{3.34}$$

$$Sc_L = \frac{\mu_L}{\rho_L d} \tag{3.35}$$
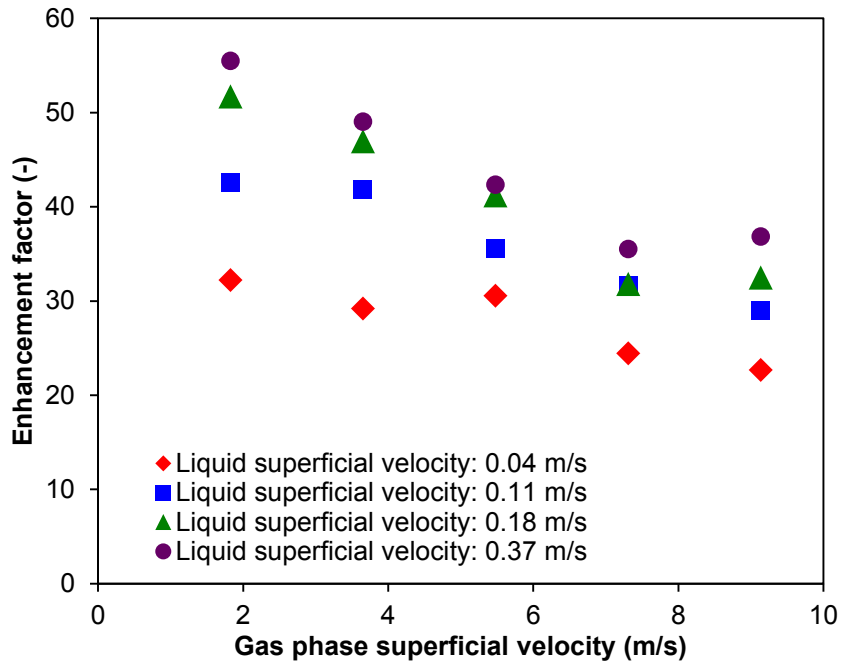
Figure 3.14: Effect of phase superficial velocity on enhancement factor (C_{CO2}: 10% by mass of CO_2 in N_2; C_{DEA}: 20% by mass of DEA in water; L: 0.5 m).

With the experimental data collected in the present work, the empirical constants in Eq. 3.34 were determined by regression. A comprehensive review by Akanksha et al.

(2008) suggested that the constant b_4, which determines the relationship between Sh and Sc, is system invariant, and takes a constant value of 0.5. Their work was based on reviewing conventional gas-liquid absorption systems. Likewise, a similar conclusion was drawn by Su et al. (2010) for a minichannel reactor. The dependency was currently verified for the present minichannel reactor and was found to hold true. With values of $b_1 = 10.201$, $b_2 = 0.206$, $b_3 = 0.218$ and $b_4 = 0.5$, the presently obtained data was predicted within an MAE of 5.2% (Figure 3.15).
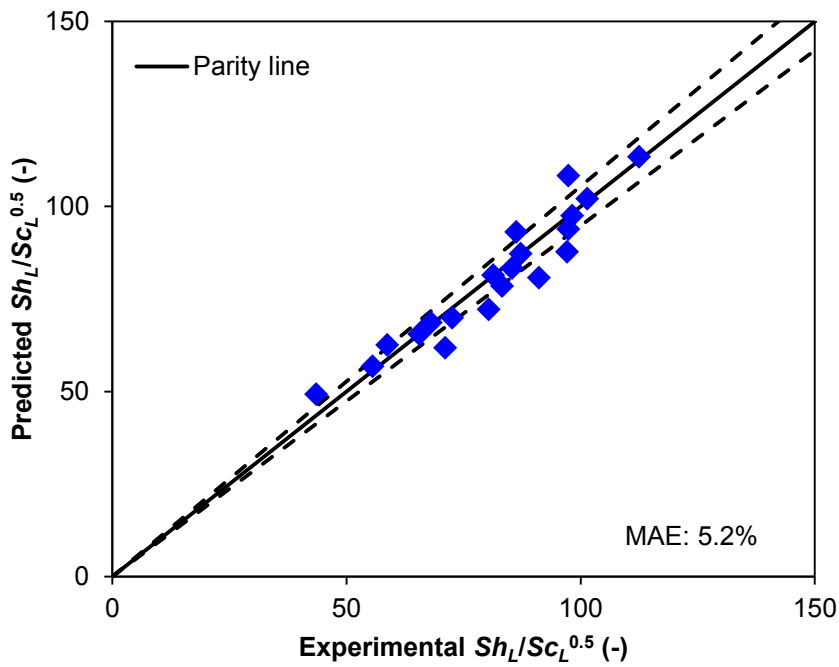
Figure 3.15: Comparison of experimental $Sh_L/Sc_L^{0.5}$ with predictions from Eq. 3.34 (C_{CO2}: 10% by mass of CO_2 in N_2; C_{DEA}: 20% by mass of DEA in water; L: 0.5 m).

3.3.4   Effect of channel length/residence time

Figure 3.11 indicates that the highest values of mass transfer coefficients were achieved when U_L equaled 0.4 m/s, which is the highest velocity within the range considered in the present work. Further, this case also yielded relatively high levels of

absorption efficiency (Figure 8b). Hence, for this value of liquid velocity, different channel lengths of 0.5 m, 0.3 m and 0.1 m were tested, the results of which are reported subsequently for various values of U_G. The results correspond to a gas phase concentration of 10% by mass of CO_2 in N_2, and an aqueous amine concentration of 20% by mass of DEA in water. The reduction in pressure drop with shorter channel lengths (Figure 3.16) is consistent with the physics of fluid flow.
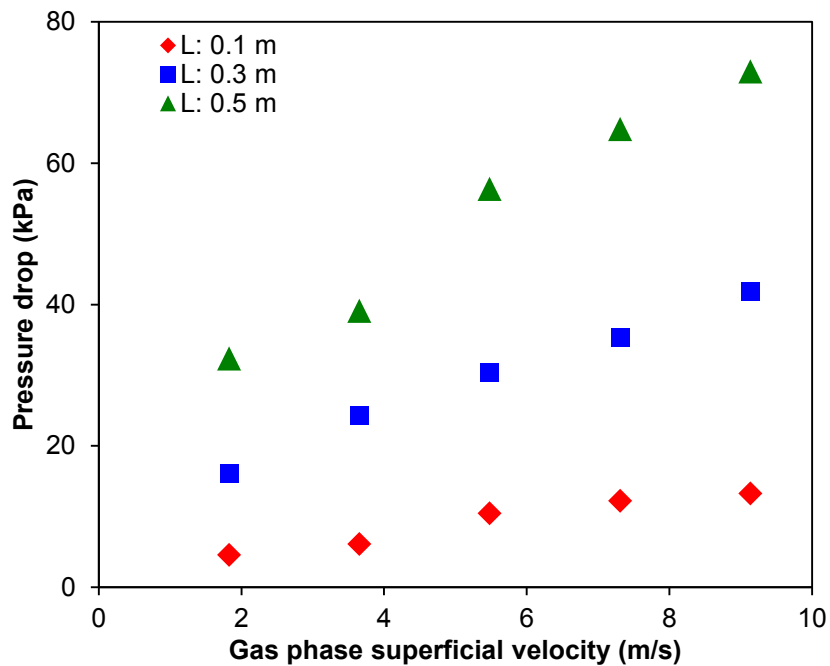
Figure 3.16: Effect of channel length on two-phase pressure drop (C_{CO2}: 10% by mass of CO_2 in N_2; C_{DEA}: 20% by mass of DEA in water; U_L: 0.4 m/s).

As can be seen in Figure 3.17, the absorption fraction decreases with shorter channel lengths on account of the reduced residence time of the gas and liquid phase reactants in shorter channels, which is similar to the findings of Shao et al. (2010). Since the molar flow rate of CO_2 at the channel inlet is constant for all channel lengths, the

reduced contacting time in shorter channels resulted in a higher molar flow rate of CO_2 at the channel outlet (Figure 3.18).
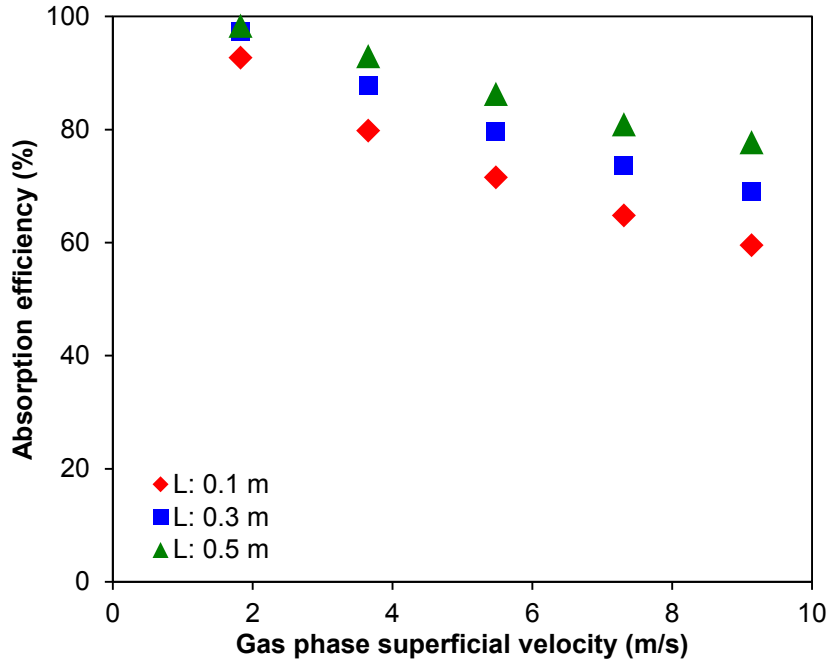
Figure 3.17: Effect of channel length on absorption efficiency (C_{CO2}: 10% by mass of CO_2 in N_2; C_{DEA}: 20% by mass of DEA in water; U_L: 0.4 m/s).

Based on this fact alone, it was expected that shorter channels having low residence times should result in lower values of $k_L a$. But on the contrary, the opposite was observed in the present experiments, as can be seen in Figure 3.19 . In comparison to the 0.5 m long channel, the mass transfer coefficients for the 0.3 m and 0.1 m channels were higher on average by 52% and 290%, respectively. This was attributed to the improved utilization of the absorption capacity of the amine solution for a given reactor volume. Short channel lengths prevent localized interfacial saturation of the liquid reactant, thereby yielding higher values of mass transfer coefficient.
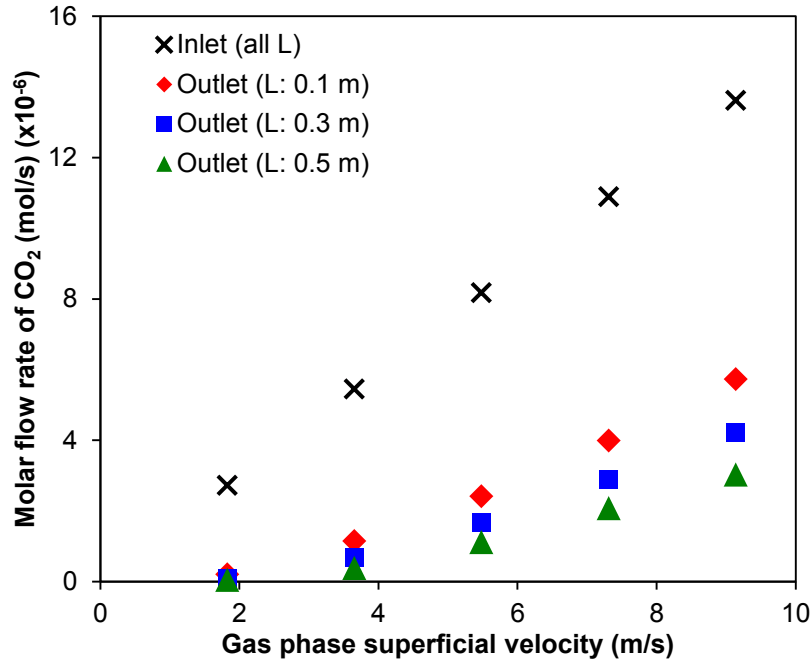
Figure 3.18: Effect of channel length on molar flow rate of CO_2 (C_{CO2}: 10% by mass of CO_2 in N_2; C_{DEA}: 20% by mass of DEA in water; U_L: 0.4 m/s).
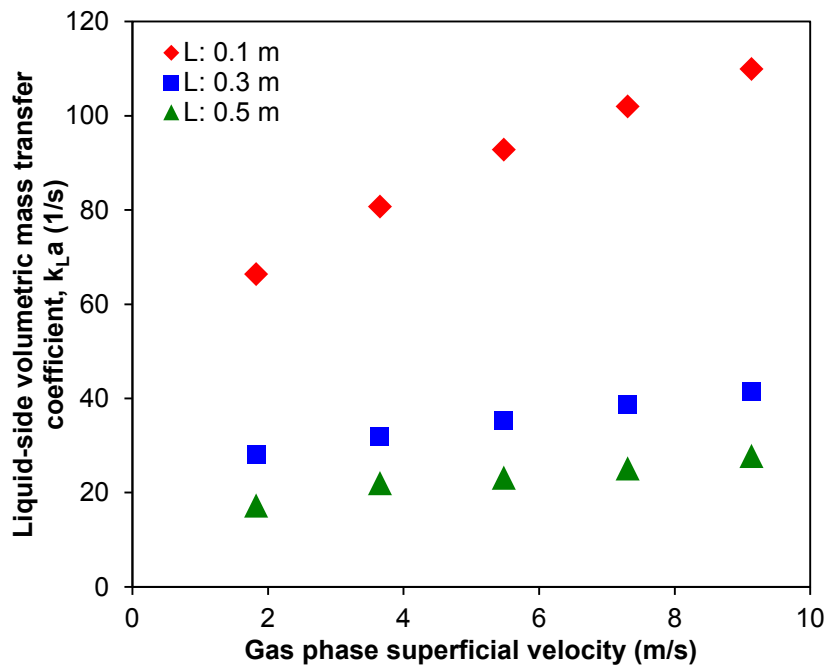
Figure 3.19: Effect of channel length on liquid-side volumetric mass transfer coefficient (C_{CO2}: 10% by mass of CO_2 in N_2; C_{DEA}: 20% by mass of DEA in water; U_L: 0.4 m/s).

3.3.5   Effect of liquid reactant concentration

This section discusses the effect of the concentration of the liquid and gaseous phases on the absorption performance. For the same reasons noted in Section 3.3.4, U_L was maintained at a constant value of 0.4 m/s while U_G was varied between 1.8-9.1 m/s. The highest values of mass transfer coefficient were achieved with a channel length of 0.1 m (Figure 3.19), and hence this length was used subsequently. The concentration of the aqueous amine solution was varied between 5-20% by mass of DEA in water. The gas phase concentration was a constant value of 10% by mass of CO_2 in N_2.

The pressure drop was observed to slightly increase with increasing amine concentration (Figure 3.20). In comparison to the 5% concentration case, the pressure drops for the 10%, 15% and 20% cases were higher on an average by 6%, 13% and 17%, respectively. Two factors play a role in explaining this trend. First is the increased viscosity of higher concentration solutions (Table 3.1) which results in a higher friction factor and therefore higher pressure drop. Second is the increased level of absorption that occurs with a more concentrated liquid reactant, thereby resulting in a higher value of acceleration pressure drop. This is one component of the experimentally measured total two-phase pressure drop that occurs in flows involving a varying void fraction. In this case, it is a negative quantity since a fraction of the gas phase is being absorbed into the liquid phase, thereby creating a decelerating effect. This results in a lower two-phase pressure drop than that in a two-phase flow system involving the same working fluids but no mass transfer (constant void fraction). The results in Figure 3.20 indicate that the effects of acceleration pressure drop are clearly

overcome by the effects of increased viscosity of the amine solution, and thus a larger

pressure drop is observed with more concentrated amine solutions.
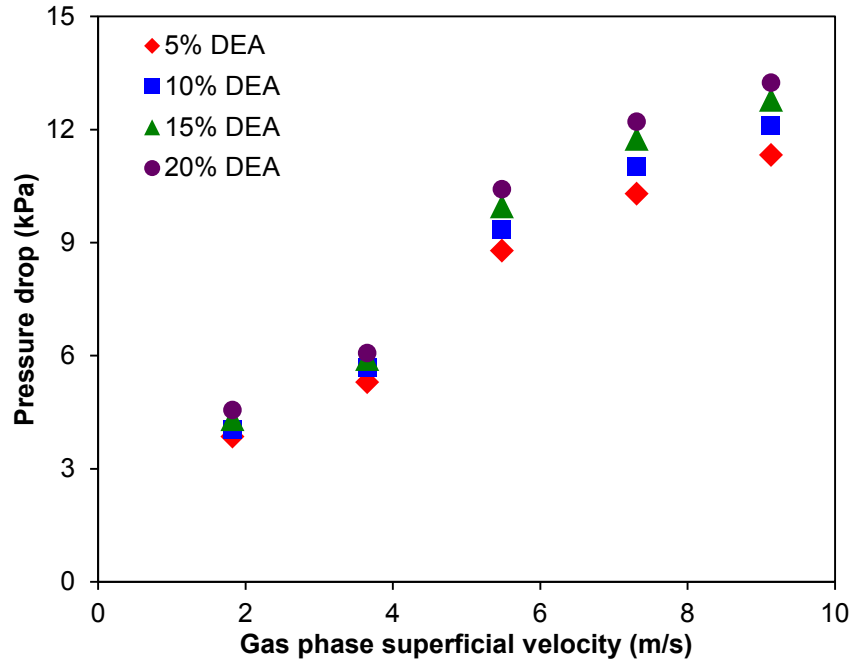
Figure 3.20: Effect of liquid reactant concentration on two-phase pressure drop (C_{CO2}: 10% by mass of CO_2 in N_2; U_L: 0.4 m/s; L: 0.1 m).

The results reported in Figure 3.21 indicate that the absorption efficiency is enhanced

with increasing amine concentration. This result can be attributed to the reaction

kinetics discussed in Section 3.2.4. Figure 3.22 shows an increase in the mass transfer

coefficient with an increase in amine concentration due to the enhanced mass transfer.

In comparison to the 5% concentration case, the average enhancement in $k_L a$ with the

10%, 15% and 20% concentration cases were 39%, 73% and 75%, respectively. It is

noted that there was a negligible improvement between the results obtained for the

15% and 20% concentration cases, which matches the results of absorption
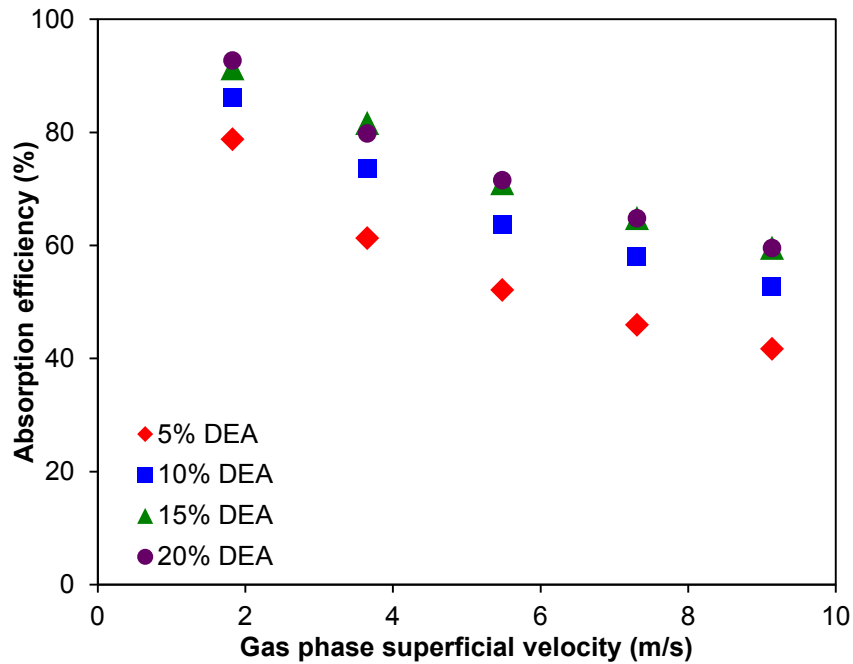
efficiency.

Figure 3.21: Effect of liquid reactant concentration on absorption efficiency (C_{CO2}: 10% by mass of CO_2 in N_2; U_L: 0.4 m/s; L: 0.1 m).
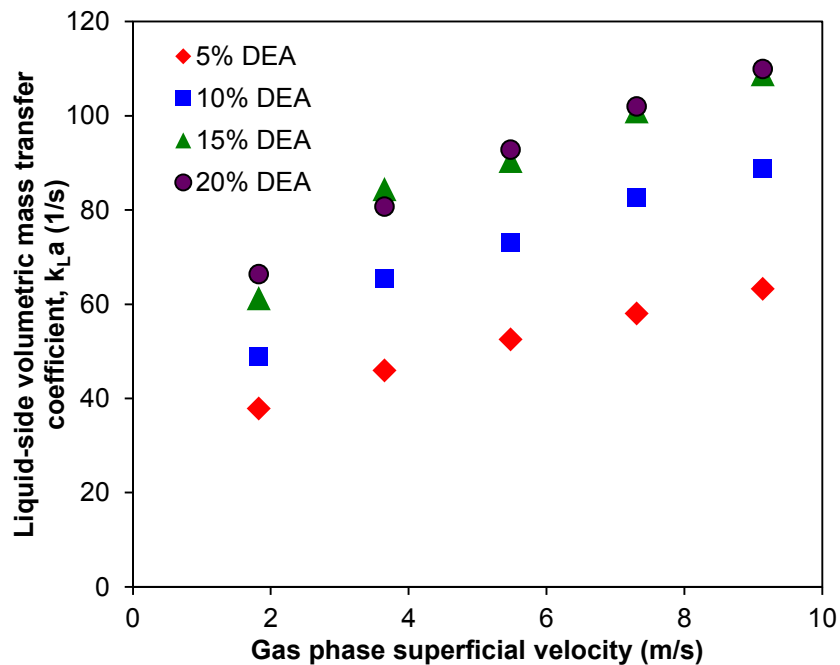
Figure 3.22: Effect of liquid reactant concentration on liquid-side volumetric mass transfer coefficient (C_{CO2}: 10% by mass of CO_2 in N_2; U_L: 0.4 m/s; L: 0.1 m).

3.3.6 Effect of gas phase concentration

The effect of gas phase concentration on the absorption performance was investigated for U_L equaling 0.4 m/s, U_G ranging from 1.8-9.1 m/s, and channel length of 0.1 m. Since different amine concentration levels are associated with varying absorption performance, tests involving 5% and 20% concentration of amine by mass were conducted for gas phase concentrations ranging from 5% to 18% of CO_2 in N_2 by mass. The results are reported and discussed below.

For a given amine concentration, negligible differences in the two-phase pressure drop were observed (Figure 3.23), which verifies our earlier conclusion pertaining to the negligible effect of acceleration pressure drop under the present operating conditions. Figure 3.24 indicates that the effect of gas phase concentration on absorption efficiency is more dominant for the 5% amine concentration cases as compared to the 20% amine concentration cases. A decrease in the gas phase concentration resulted in an increase in absorption efficiency, which in turn led to higher mass transfer coefficients (Figure 3.25). In comparison to the 18% CO_2 concentration results obtained with the dilute amine solution (5% DEA concentration), the mass transfer coefficient increased on an average by 11% and 26% for 10% and 5% CO_2 concentration levels, respectively. However, with 20% amine concentration, the above enhancement factors equaled 5% and 12%. This indicates that the enhancement in mass transfer with decreasing gas phase concentration is more dominant with the dilute amine solutions.
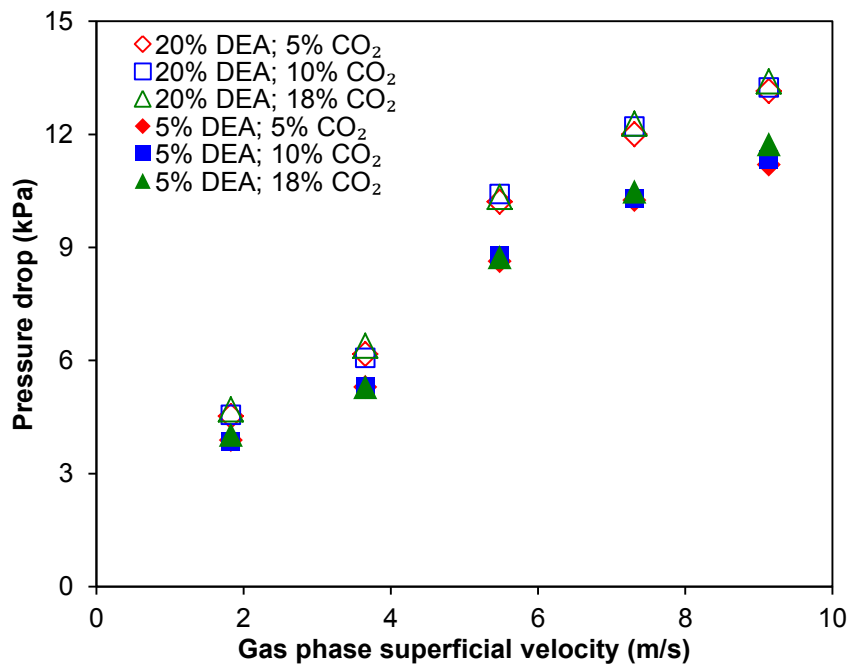
Figure 3.23: Effect of gas phase concentration on two-phase pressure drop (U_L: 0.4 m/s; L: 0.1 m).
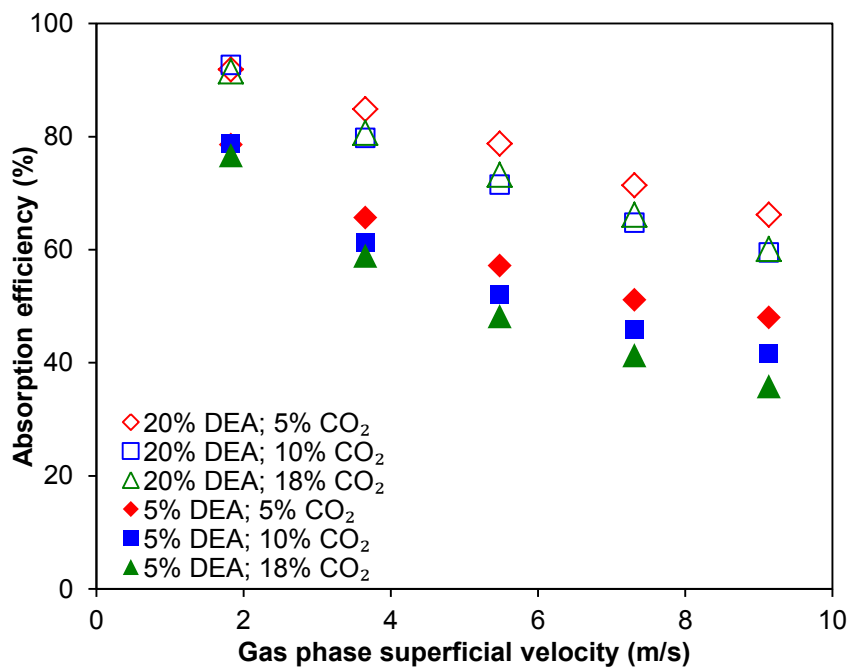
Figure 3.24: Effect of gas phase concentration on absorption efficiency (U_L: 0.4 m/s; L: 0.1 m).
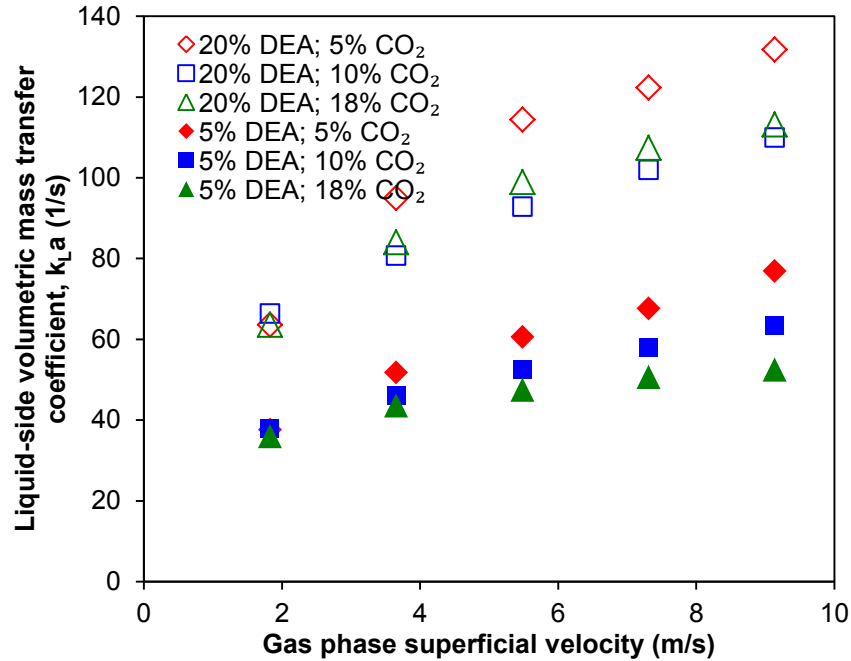
Figure 3.25: Effect of gas phase concentration on liquid-side volumetric mass transfer coefficient (U_L: 0.4 m/s; L: 0.1 m).

3.4 Results and discussion: varying hydraulic diameter studies

3.4.1 Pressure drop

The experimentally measured single-phase pressure drop with the liquid phase was measured and the associated friction factor was calculated. The same was compared against the theoretical predictions from Eq. 3.36 for laminar flow in circular channels. Water and aqueous amine (20% concentration by mass) were the working fluids for these measurements. As seen in Figure 3.26, Eq. 3.36 has good predictive accuracy with an MAE of 14.6%, and this justifies its use in subsequent analyses of the two-phase pressure drop.

$$f_{th} = \frac{64}{\text{Re}}$$ (3.36)
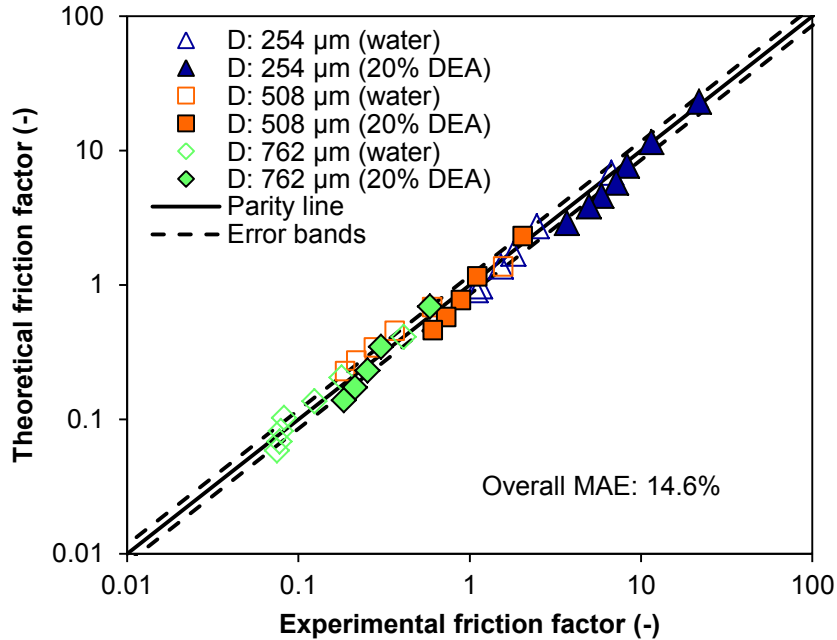
Figure 3.26: Comparison of experimental single phase friction factor with theoretical predictions at different channel diameters and with water and 20% DEA as the working fluids.

The two-phase pressure drop for N_2-water flow and N_2-DEA flow was obtained from the experimental measurements following the procedure described in Section 3.2.2. Amine concentration levels of 5% and 20% by mass were considered for these measurements. The acceleration component of pressure drop was not present for the current experiments on account of the absence of any discernible level of absorption when the gas phase is nitrogen. The experimental value of $\phi_L{}^2$ was compared against the predictions of the model proposed in Section 3.3.1 which is summarized below.

$$\phi_L^2 = 1 + \frac{c}{X} + \frac{1}{X^2}$$ (3.37)

86

$$c = \begin{cases} 11.9Bo^{0.45} & \text{water} \\ 14.81Bo^{0.25} & \text{amine} \end{cases} \tag{3.38}$$

$$Bo = \frac{(\rho_L - \rho_G)gD^2}{\sigma} \tag{3.39}$$

This model was proposed to specifically address the lack of empirical models for two-phase pressure drop that have considered aqueous amine solutions in their source data. Accordingly, pressure drop data was obtained with aqueous amine solutions at various concentration levels, in a 762 μm channel. Here, this model is applied to channels having smaller hydraulic diameters as well. As reported in Figure 3.27, the model yields reasonably good predictive accuracy with an MAE of 23.1% for all the working fluids considered.
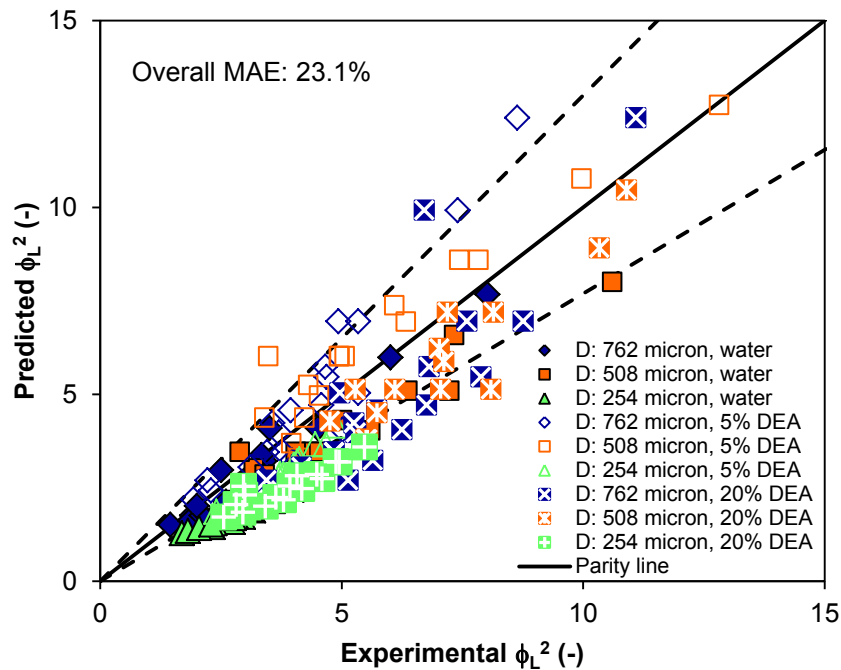
Figure 3.27: Comparison of experimental two-phase friction multiplier with predictions of empirical model at different channel diameters and with nitrogen as the gas phase. Water, 5% DEA and 20% DEA were considered as the liquid phase.

Given that the above pressure drop model was demonstrated to have good predictive accuracy for the present range of hydraulic diameters during two-phase flow without mass transfer, the same model was subsequently applied for flows with mass transfer, wherein CO_2 mixed with N_2 is the gas phase. From the parametric studies reported subsequently, a total of 120 data points were obtained for a range of operating conditions. These results included the effects of both friction and acceleration, and the latter was eliminated using Eq. 3.3. The results reported in Figure 3.28 indicate reasonably good agreement with an MAE of 17%.
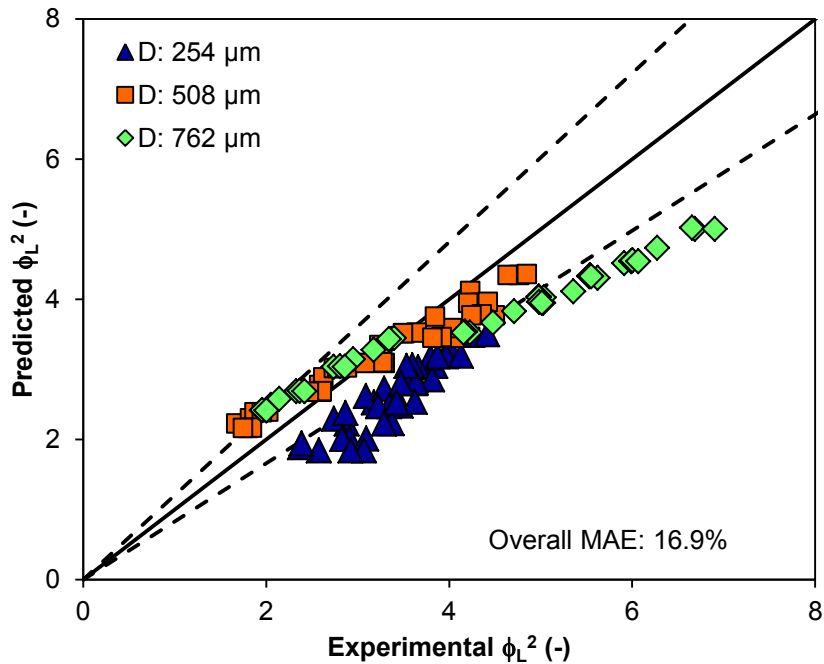
Figure 3.28: Comparison of two-phase frictional pressure drop during absorption process with empirical model. Data reported for all 120 data points obtained from present experiments wherein the varying parameters are channel diameter, liquid reactant concentration and gas phase concentration.

3.4.2 Effect of channel diameter

The effect of channel diameter on the mass transfer characteristics was studied for a gas phase concentration of 10% by mass of CO_2 in N_2 and an aqueous amine concentration of 5% by mass of DEA in water. The gas phase velocity varied between 1.8-9.1 m/s for all channel diameters and the liquid phase velocity was constant and equaled 0.4 m/s.

Figure 3.29 reports the two-phase pressure drop for various channel diameters. As can be seen, a decrease in channel diameter resulted in an increase in pressure drop. In comparison to the 762 μm diameter channel, the pressure drop for the 508 and 254 μm diameter channels was on average higher by 1.7 and 7.7 times, respectively. An increase in the gas phase superficial velocity also resulted in a higher pressure drop and both of these observations are consistent with the physics of fluid flow. Next, the mass transfer performance was studied.

Figure 3.30 reports the variation of absorption efficiency with gas flow rate for the three channel diameters under consideration. As can be seen, a decrease in channel diameter resulted in substantial enhancement in the absorption performance and this can be attributed to the higher gas-liquid interfacial area associated with smaller diameter channels.
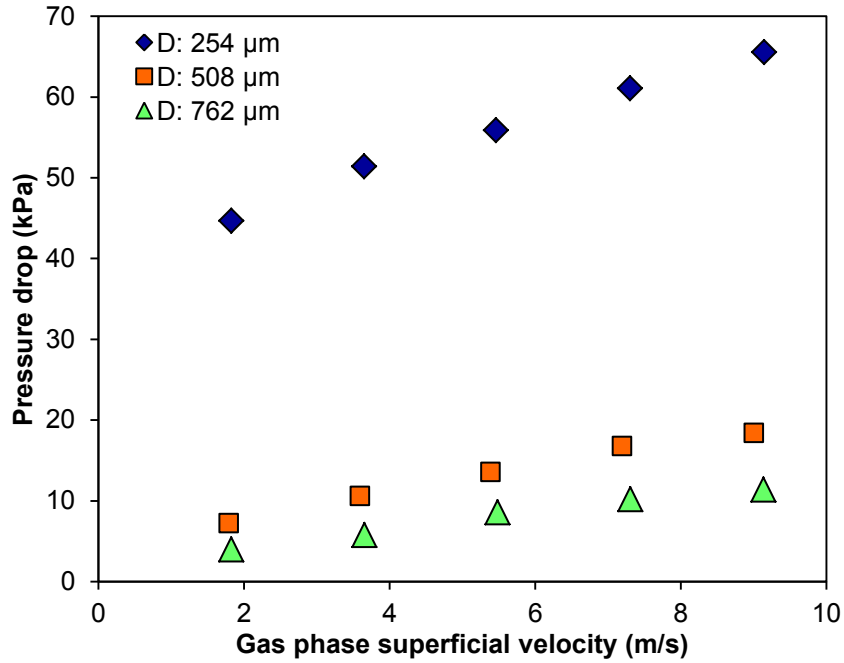
Figure 3.29: Effect of channel hydraulic diameter on pressure drop (C_{CO2}: 10% by mass of CO_2 in N_2; C_{DEA}: 5% by mass of DEA in water; U_L: 0.4 m/s; U_G: 1.8-9.1 m/s).
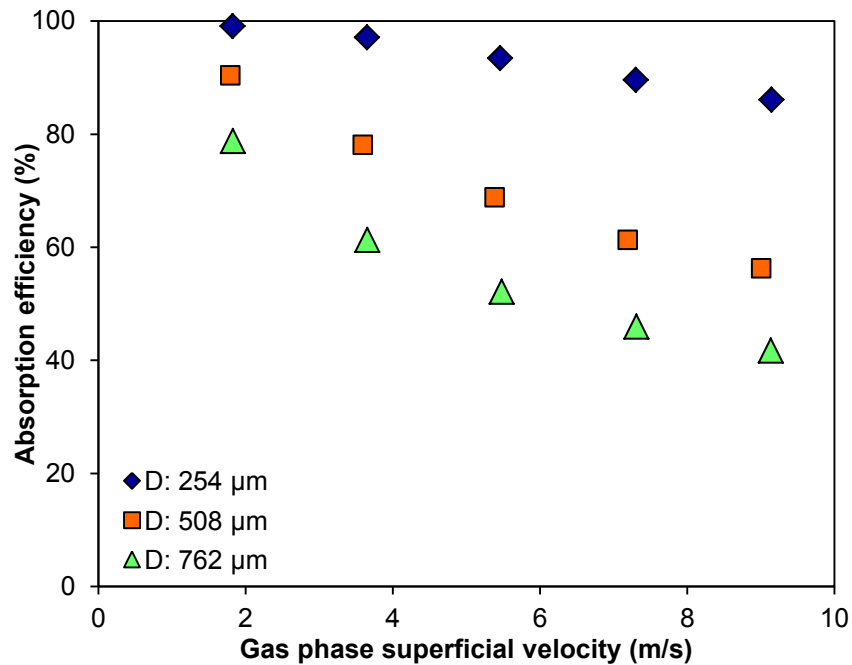

Figure 3.30: Effect of channel hydraulic diameter on absorption efficiency (C_{CO2}: 10% by mass of CO_2 in N_2; C_{DEA}: 5% by mass of DEA in water; U_L: 0.4 m/s; U_G: 1.8-9.1 m/s).

For the same reason, the liquid-side volumetric mass transfer coefficients, reported in Figure 3.31, were also observed to be higher with smaller diameter channels. On average, the $k_L a$ values obtained for the 254 and 508 μm diameter channels were 256% and 53% higher, respectively, than that obtained with the 762 μm channel. In order to verify the above reasoning, the gas-liquid interfacial area was estimated and the results are reported in Figure 3.32. As can be seen, the specific interfacial area for the 254 and 508 μm channels are on an average 183% and 50% higher, respectively, than that of the 762 μm channel.
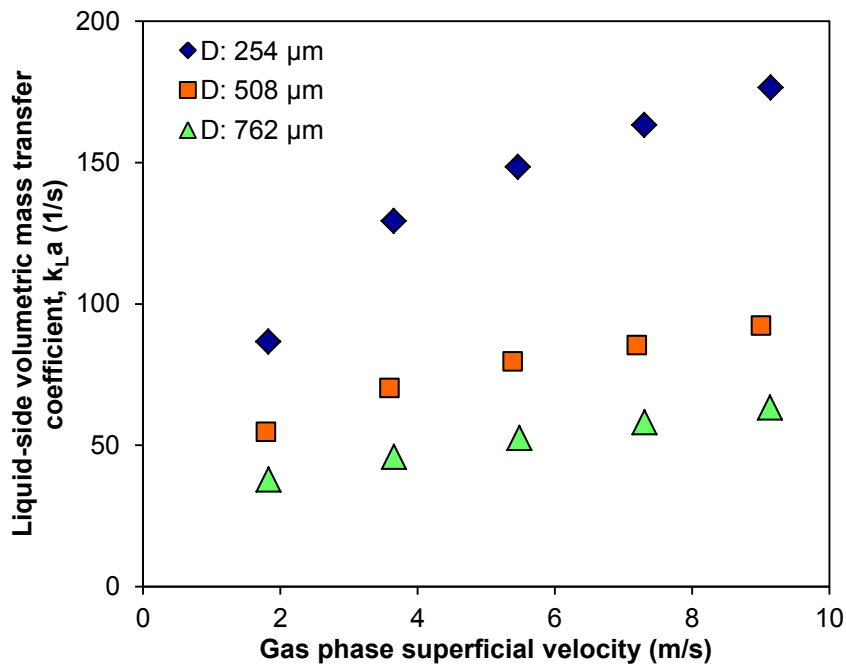
Figure 3.31: Effect of channel hydraulic diameter on liquid-side volumetric mass transfer coefficient (C_{CO2}: 10% by mass of CO_2 in N_2; C_{DEA}: 5% by mass of DEA in water; U_L: 0.4 m/s; U_G: 1.8-9.1 m/s).
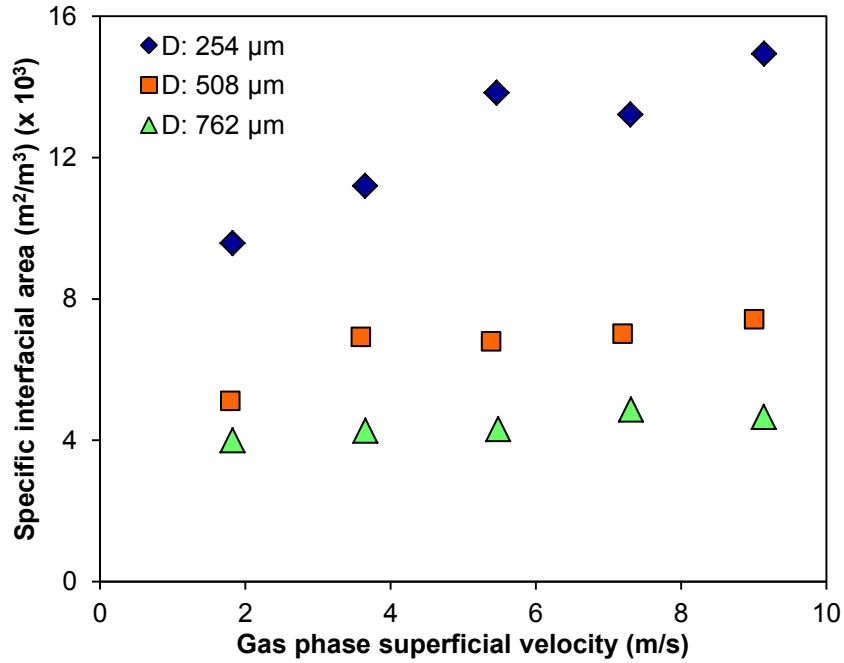
Figure 3.32: Effect of channel hydraulic diameter on specific interfacial area (C_{CO2}: 10% by mass of CO_2 in N_2; C_{DEA}: 5% by mass of DEA in water; U_L: 0.4 m/s; U_G: 1.8-9.1 m/s).

Having obtained an estimate of the specific interfacial area, it was possible to calculate the liquid-side mass transfer coefficient, k_L, and subsequently the enhancement factor, E. The results reported in Figure 3.33 are in agreement with those previously reported by Ye et al. (2012). k_L in represented in dimensionless form by the Sherwood number (Eq. 3.40) in Figure 3.34.

$$Sh_L = \frac{k_L D}{d} \qquad (3.40)$$
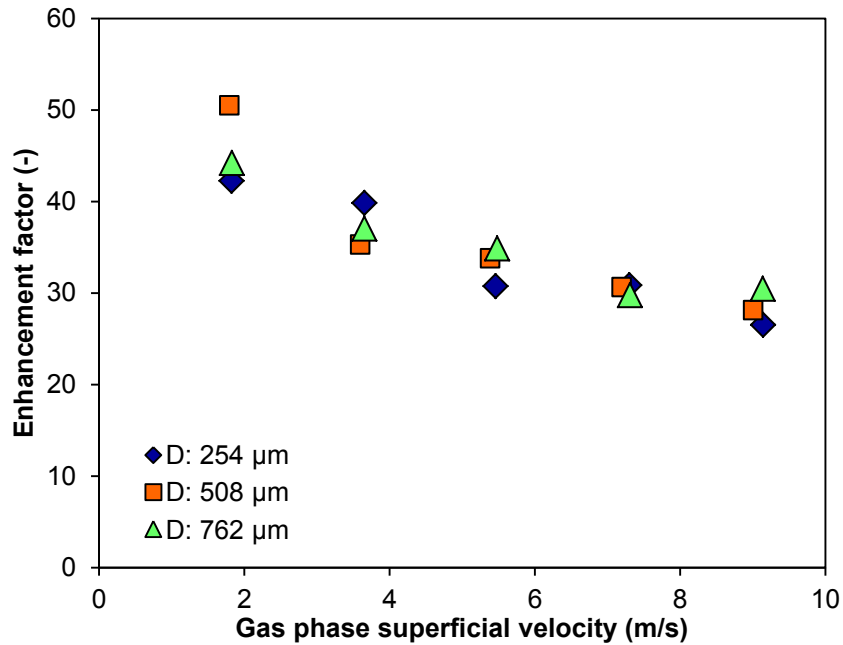
Figure 3.33: Effect of channel hydraulic diameter on enhancement factor (C_{CO2}: 10% by mass of CO_2 in N_2; C_{DEA}: 5% by mass of DEA in water; U_L: 0.4 m/s; U_G: 1.8-9.1 m/s).
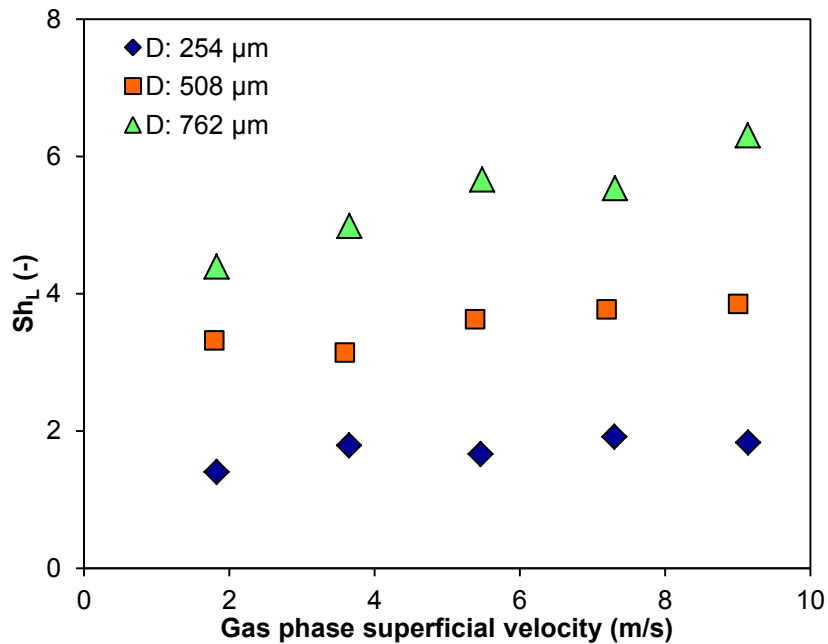
Figure 3.34: Effect of channel hydraulic diameter on Sherwood number (C_{CO2}: 10% by mass of CO_2 in N_2; C_{DEA}: 5% by mass of DEA in water; U_L: 0.4 m/s; U_G: 1.8-9.1 m/s).

In addition to the above analysis pertaining to channel diameter, a brief discussion is warranted on the effect of gas phase superficial velocity on two-phase flow regimes and mass transfer (Figure 3.35).
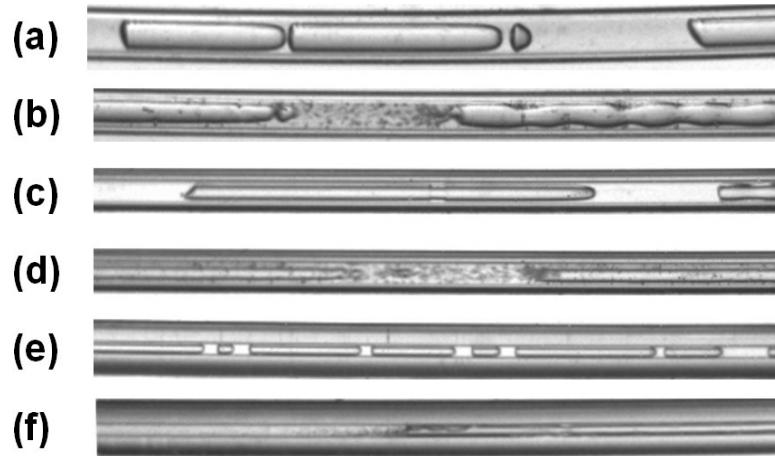
Figure 3.35: Two-phase flow regimes (a) slug flow (D: 762 μm; U_L: 0.4 m/s; U_G: 1.8 m/s) (b) churn flow (D: 762 μm; U_L: 0.4 m/s; U_G: 9.1 m/s) (c) slug flow (D: 508 μm; U_L: 0.4 m/s; U_G: 1.8 m/s) (d) churn flow (D: 508 μm; U_L: 0.4 m/s; U_G: 9.1 m/s) (e) slug flow (D: 254 μm; U_L: 0.4 m/s; U_G: 1.8 m/s) (f) churn flow (D: 254 μm; U_L: 0.4 m/s; U_G: 9.1 m/s).

Under the present operating conditions, slug and churn flow regimes were dominant in occurrence. At gas phase superficial velocities less than ~6.4 m/s, slug flow was the dominant for all three channel diameters (Figure 3.35a, Figure 3.35c, Figure 3.35e). This regime was characterized by an alternating arrangement of elongated, cylindrical gas bubbles and liquid slugs, with a thin film of liquid present between the bubble and channel wall. Convective mixing was enhanced by recirculating velocity currents present within the both phases. At gas velocities greater than ~6.4 m/s (Figure 3.35b, Figure 3.35d, Figure 3.35f), churn flow was dominant. This regime was characterized by a central gas core surrounded by a liquid film, and with

periodically occurring instabilities that disrupted the gas core creating regions of intense mixing. It is noted that the presently observed transition between these two flow patterns is in reasonable agreement with previously proposed transition criteria in the literature (Chung and Kawaji, 2004).

An increase in gas velocity resulted in a decrease in the absorption efficiency. In the slug flow regime, this can be attributed to a higher magnitude of recirculating velocity currents within the gas bubbles and a lower magnitude of these currents within the liquid slugs. Although, this results in additional mixing within the gas phase, this mixing is hardly dominant since the present reaction system is characterized by negligible resistance to mass transfer on the gas side. On the other hand, the dominant mass transfer resistance is present on the liquid side, wherein the magnitude of mixing currents is reduced. Here, the liquid reactant adjacent to the gas bubble becomes rapidly saturated, resulting in poorer absorption efficiencies. During the churn flow regime, an increase in gas velocity leads to a higher gas void fraction and therefore a less thick liquid film. Consequently, the liquid reactant in the film was more easily saturated and thus reduced absorption was observed to occur. Additionally, with increasing gas velocity in the churn flow regime, the frequency of occurrence of interfacial waves and the intermittent intense mixing zones was also reduced, and this is also a contributing factor towards lower absorption efficiencies. Despite the lower absorption efficiencies observed with increasing gas flow velocities, there is a net increase in the differential molar flow rate of CO_2, Δn_{CO_2}, as a result of which $k_L a$ increases. Similar trends have been reported elsewhere (Yue et al., 2007a; Kundu et al., 2012).

3.4.3   Effect of liquid and gas phase concentration

The effect of the liquid reactant concentration on the absorption performance was studied for amine concentration levels ranging from 5-20% by mass of DEA in water, and for the previously reported range of flow velocities. The gas phase concentration was 10% by mass of CO_2 in N_2.

The trends of absorption efficiency reported in Figure 3.36 indicates that a higher level of mass transfer occurs with a more concentrated reactant solution, at all channel diameters under consideration. This can be attributed to the reaction kinetics of the present system. As a result of the improved absorption, the liquid-side volumetric mass transfer coefficient (Figure 3.37) was also enhanced. The average increase in $k_L a$ between the 5% and 20% concentration cases equaled 77%, 102% and 78%, with the 762, 508 and 254 μm channels, respectively. Further, the increased viscosity of higher concentration amine solution resulted in a discernible rise in the pressure drop (Figure 3.38). With the 762, 508 and 254 μm channels, the average increase in pressure drop between the 5% and 20% concentration cases equaled 17%, 33% and 25%, respectively.
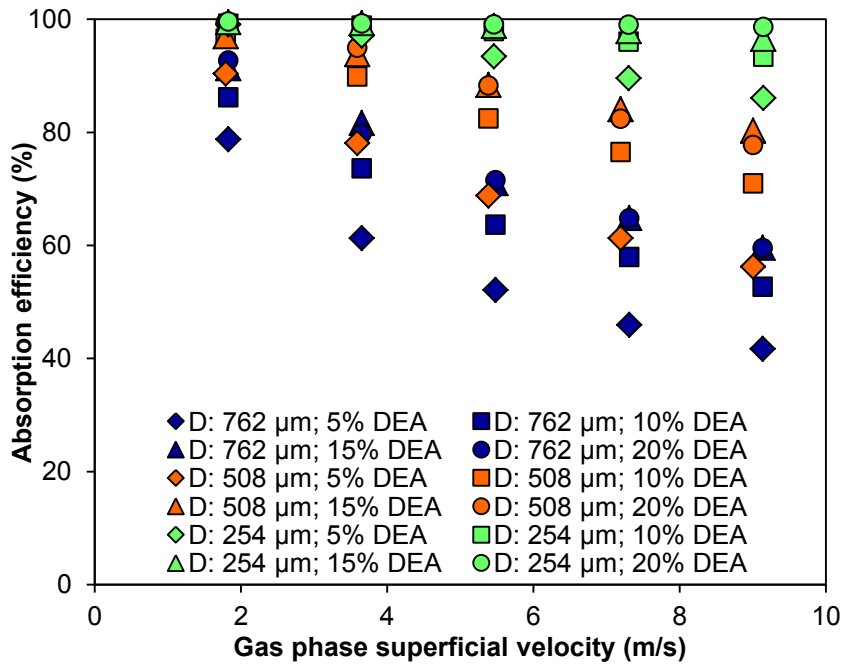
Figure 3.36: Effect of liquid reactant concentration on absorption efficiency at different channel diameters (C_{CO2}: 10% by mass of CO_2 in N_2; U_L: 0.4 m/s; U_G: 1.8-9.1 m/s).
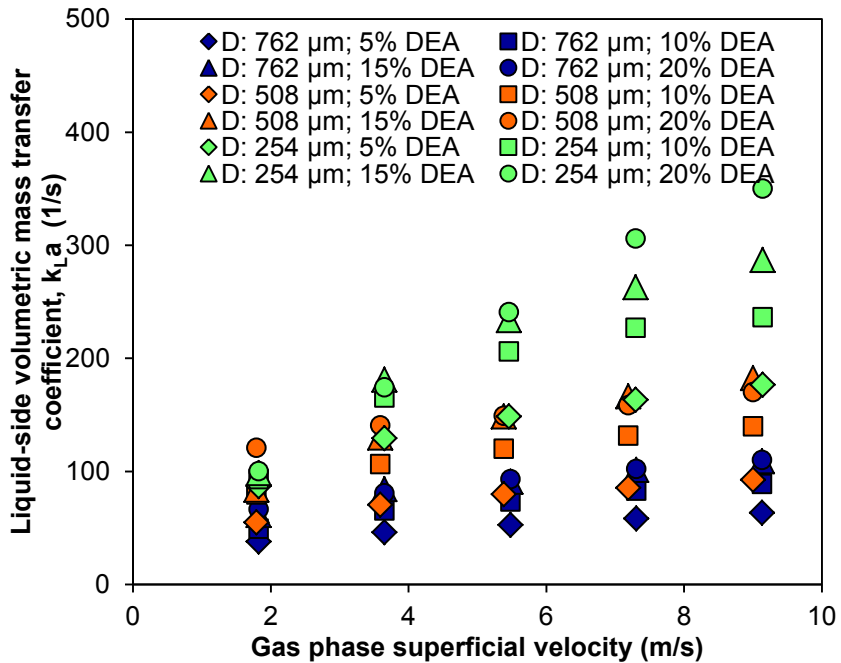
Figure 3.37: Effect of liquid reactant concentration on liquid-side volumetric mass transfer coefficient at different channel diameters (C_{CO2}: 10% by mass of CO_2 in N_2; U_L: 0.4 m/s; U_G: 1.8-9.1 m/s).

97
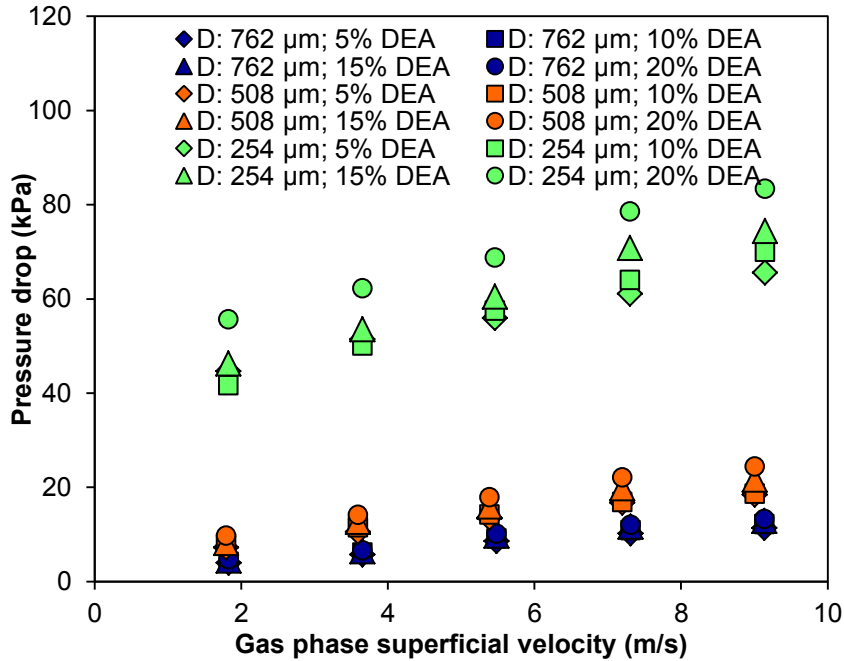
Figure 3.38: Effect of liquid reactant concentration on two-phase pressure drop at different channel diameters (C_{CO2}: 10% by mass of CO_2 in N_2; U_L: 0.4 m/s; U_G: 1.8-9.1 m/s).

The effect of CO_2 concentration in the gas phase was investigated for a range of 5-18% by mass. The liquid flow velocity was 0.4 m/s and the gas flow velocities ranged between 1.8-9.1 m/s. Tests involving amine concentration levels of 5% and 20% were performed and the former is discussed first. Figure 3.39 indicates that the effect of gas phase concentration on absorption efficiency is more dominant with larger diameter channels. As a result, the mass transfer coefficients between the 5% and 18% CO_2 concentration cases differed on an average by 20%, 7%, and 3% with the 762, 508, and 254 μm channels, respectively (Figure 3.40). The negligible effect of gas phase concentration in smaller diameter channels can be attributed to their correspondingly high interfacial areas. As can be seen in Figure 3.41, the pressure drop data at different gas phase concentration levels varied minimally. This was considered an

98

indication that the effect of negative acceleration due to gas-liquid absorption, on the total pressure drop, is relatively negligible, under the present operating conditions. Next, the above tests were repeated with an amine concentration of 20% by mass of DEA in water, and the results are reported in Figure 3.42, Figure 3.43, and Figure 3.44. While the overall trends were largely similar, the effect of gas phase concentration was less dominant. With the largest 762 µm channel, there was only a 10% average difference in mass transfer coefficient between the 5% and 18% CO_2 cases.
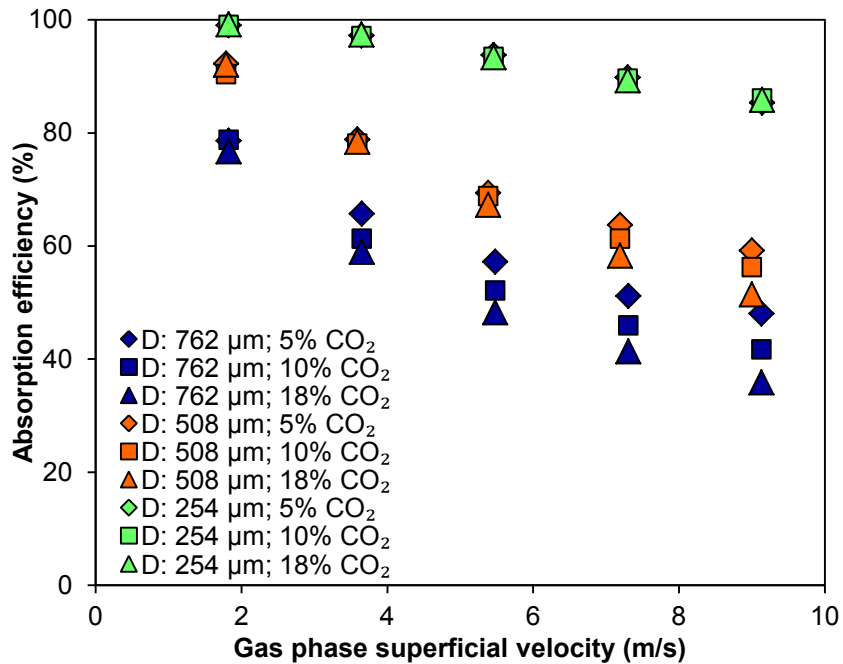
Figure 3.39: Effect of gas phase concentration on absorption efficiency (C_{DEA}: 5% by mass of DEA in water; U_L: 0.4 m/s; U_G: 1.8-9.1 m/s).
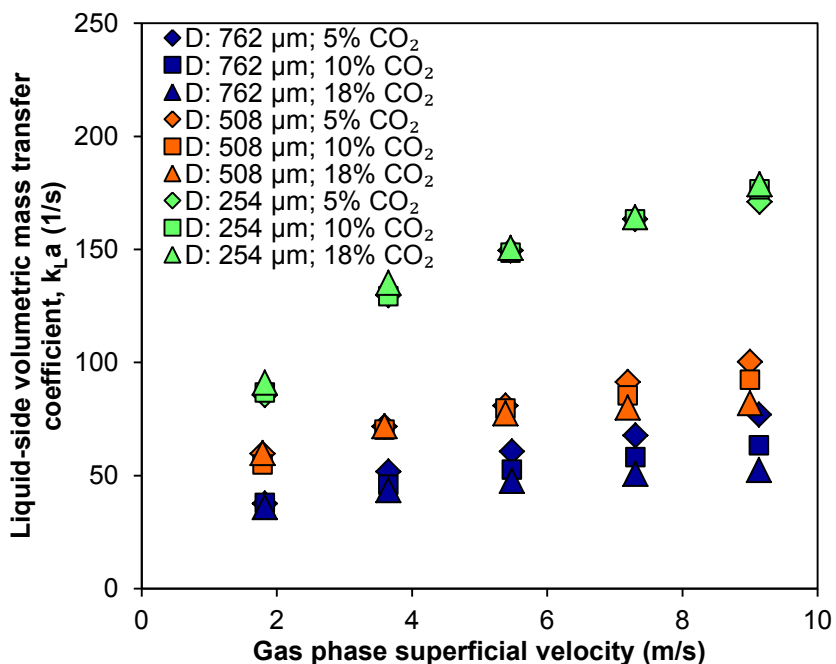
Figure 3.40: Effect of gas phase concentration on liquid-side volumetric mass transfer coefficient (C_{DEA}: 5% by mass of DEA in water; U_L: 0.4 m/s; U_G: 1.8-9.1 m/s).
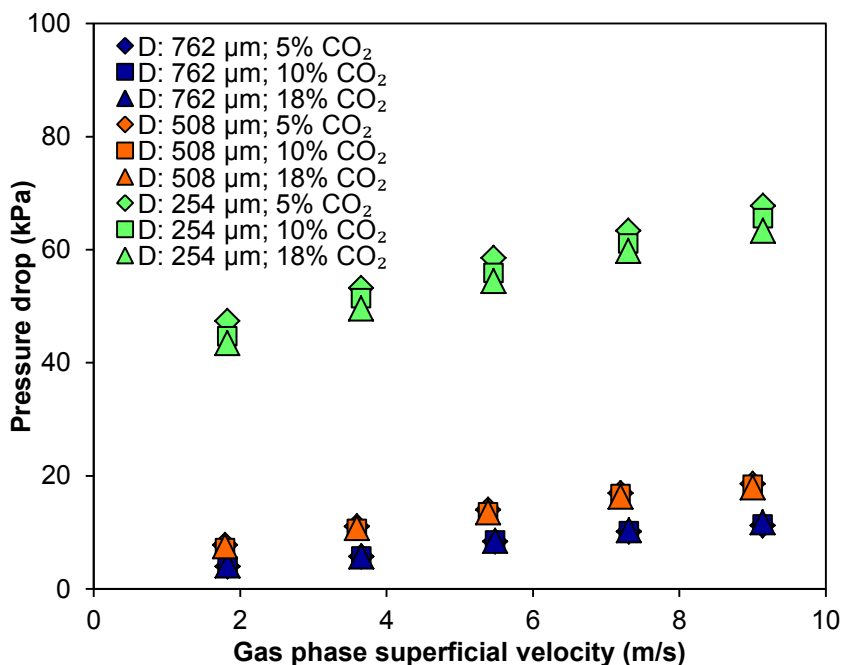
Figure 3.41: Effect of gas phase concentration on two-phase pressure drop (C_{DEA}: 5% by mass of DEA in water; U_L: 0.4 m/s; U_G: 1.8-9.1 m/s).

100
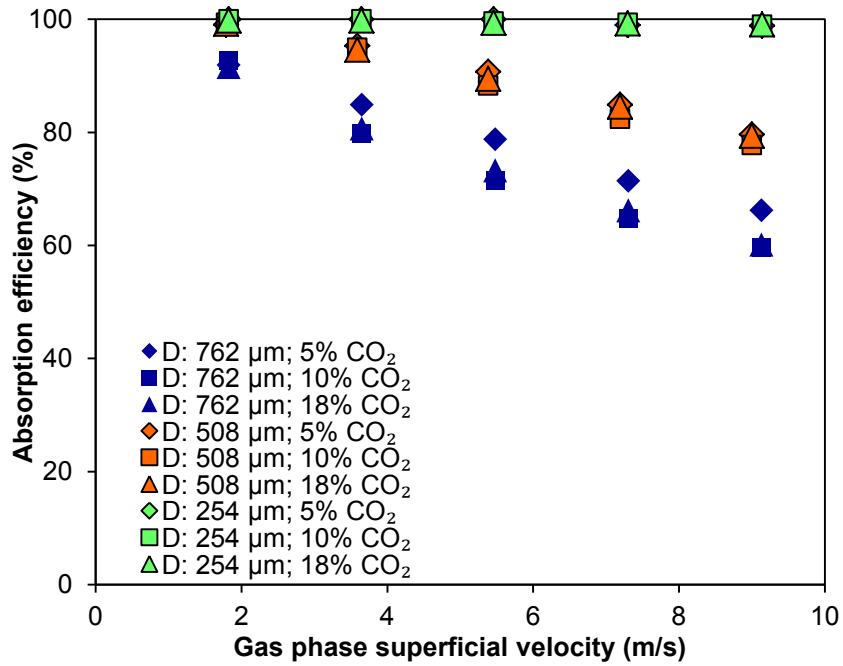
Figure 3.42: Effect of gas phase concentration on absorption efficiency (C_{DEA}: 20% by mass of DEA in water; U_L: 0.4 m/s; U_G: 1.8-9.1 m/s).
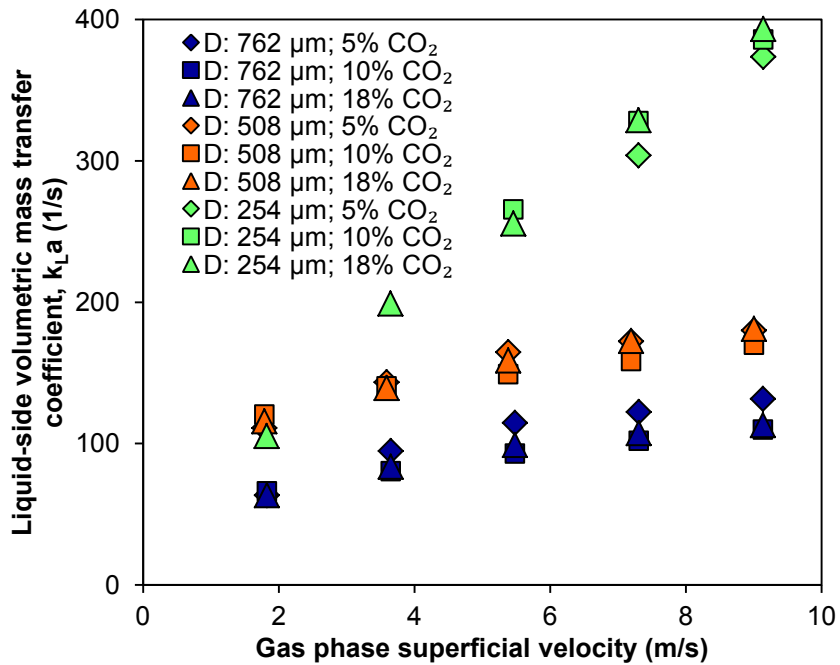
Figure 3.43: Effect of gas phase concentration on liquid-side volumetric mass transfer coefficient (C_{DEA}: 20% by mass of DEA in water; U_L: 0.4 m/s; U_G: 1.8-9.1 m/s).
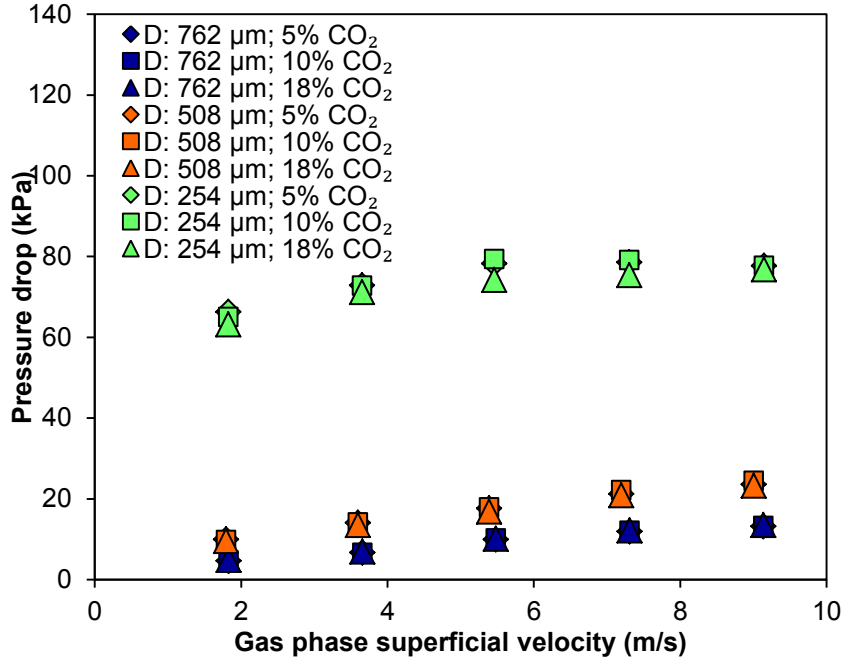
Figure 3.44: Effect of gas phase concentration on two-phase pressure drop (C_{DEA}: 20% by mass of DEA in water; U_L: 0.4 m/s; U_G: 1.8-9.1 m/s).

3.4.4 Empirical expression for Sh_L

The Sherwood number, Sh, is a common means of characterizing the mass transfer performance in gas-liquid absorption systems similar to that studied in the present work (Akanksha et al., 2008). Expressions of the form given by Eq. 3.41 have been successfully used for characterizing the Sherwood number in similar gas-liquid absorption applications, both in conventional systems as reviewed by Akanksha et al. (2008), as well as mini/microchannel systems (Su et al., 2010).

$$Sh_L = b_1 \, Re_G^{b_2} \, Re_L^{b_3} \, Sc_L^{b_4} \tag{3.41}$$

$$Sc_L = \frac{\mu_L}{\rho_L d} \tag{3.42}$$

A total of 117 data points for gas-liquid absorption were obtained in the present study with different channels and various operating conditions. With the objective of minimizing the discrepancy between the experimental Sherwood number and that predicted by Eq. 3.41, the constants were obtained as follows: $b_1 = 1.689 \times 10^{-4}$, $b_2 = 0.223$, $b_3 = 0.829$, and $b_4 = 1.766$. For the above values, the Sherwood number was predicted within an MAE of 10.1% and the results are reported in Figure 3.45.
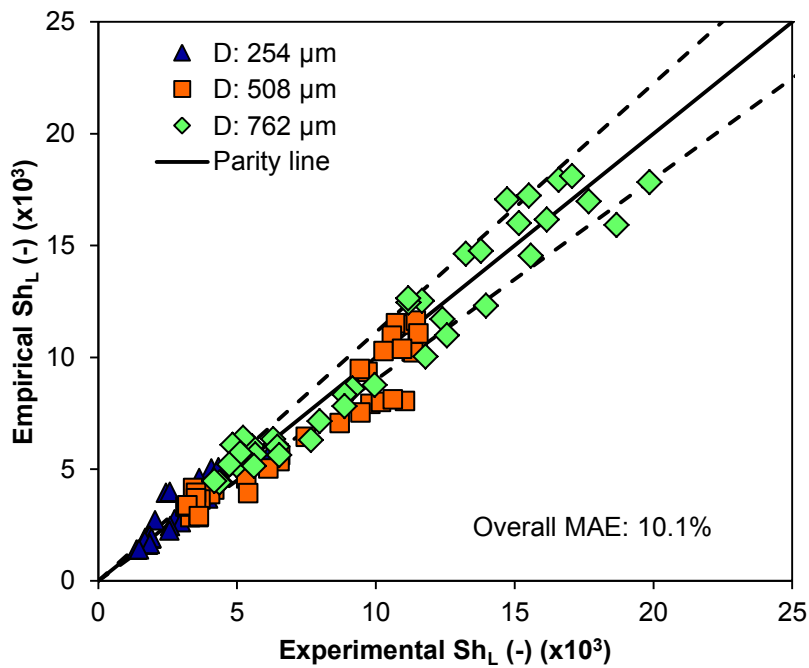
Figure 3.45: Comparison of experimental Sherwood number, Sh_L, with predictions from empirical model. Data reported for all 117 data points obtained from present experiments wherein the varying parameters are channel diameter, liquid reactant concentration and gas phase concentration.

3.5 Comparison with conventional reactors

It is essential to compare the performance of microreactor systems with that of conventional absorption technologies in order to perceive the magnitude of process

intensification that can be achieved. Table 3.3 reports the ranges of the performance

parameters achieved in the present work along with typical ranges of the same for

various types of conventional absorbers as obtained from Charpentier (1981). Similar

comparisons involving microreactors have been previously reported in the literature

(Yue et al., 2007a; Su et al., 2010) and select results from these works have also been

included. As can be seen, the presently achieved liquid-side mass transfer

coefficients, k_L, and interfacial areas, a, are higher than those of conventional systems

by 1-2 orders of magnitude. Furthermore, the liquid-side volumetric mass transfer

coefficient, $k_L a$, is higher by 2-4 orders of magnitude. These results, reported in

graphical form in Figure 3.46, are an indication of the substantial level of process

intensification that can be achieved by the use of microreactors.
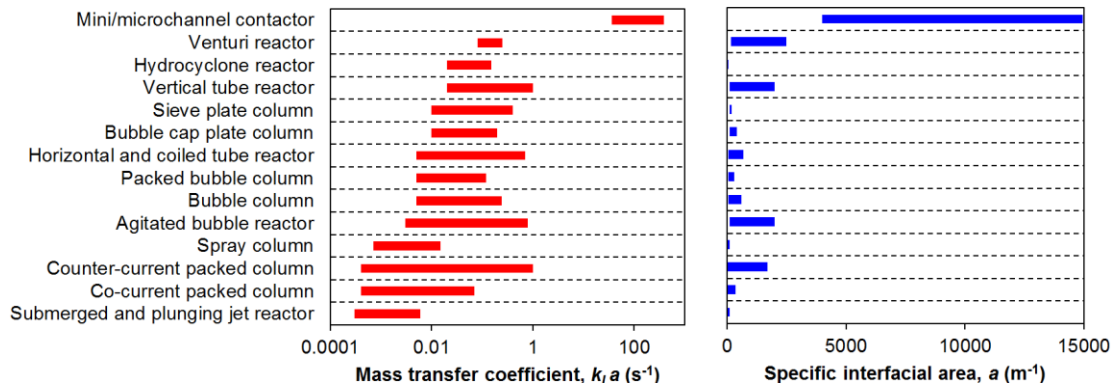
Figure 3.46: Comparison of mass transfer performance parameters of various
technologies.

Table 3.3: Comparison of mass transfer coefficients and interfacial area achieved using present microscale reactors with that reported using conventional gas-liquid absorption systems by Charpentier et al. (1981).

Type of system	k_L (x10^{-5}) (m/s)	a (m^2/m^3)	$k_L a$ (x10^{-2}) (1/s)
Countercurrent packed columns	4-20	10-350	0.04-7
Co-current packed columns	4-60	10-1700	0.04-102
Bubble cap plate columns	10-50	100-400	1-20
Sieve plate columns	10-200	100-200	1-40
Bubble columns	10-40	50-600	0.5-24
Packed bubble columns	10-40	50-300	0.5-12
Horizontal and coiled tube reactors	10-100	100-2000	0.5-70
Vertical tube reactors	20-50	10-100	2-100
Spray columns	7-15	100-2000	0.07-1.5
Mechanically agitated bubble reactors	3-40	20-120	0.3-80
Submerged and plunging jet reactors	1.5-5	20-50	0.03-0.6
Hydro cyclone reactors	100-300	100-2000	2-15
Venturi reactors	50-100	160-2500	8-25
Minichannel reactor (Yue et al., 2007a)	40-160	3400-9000	30-2100
Presently developed microreactors	231-2826	4000-14941	1100-39342

3.6 Chapter conclusions

This chapter reported an experimental investigation of the gas-liquid absorption of CO_2 into aqueous DEA in microreactors. Single channel reactors having hydraulic diameters of 762, 508 and 254 μm, and circular cross-sectional geometry, were tested. The performance of the reactor was studied with respect to the absorption efficiency, mass transfer coefficient, interfacial area, Sherwood number and two-phase pressure drop. Parametric studies investigating the effects of phase superficial velocity, liquid phase concentration, and CO_2 concentration in the gas phase were

performed and discussed. High levels of absorption efficiency, close to 100%, were observed under certain operating conditions. The mass transfer coefficient was found to be higher with short residence times, which was attributed to improved utilization of the absorption capacity of the amine solution for a given reactor volume. Parametric studies were conducted varying the liquid and gas phase concentrations. Enhanced mass transfer characteristics were obtained at higher liquid phase concentration levels, and an increase in the pressure drop was observed on account of the increase in the viscosity of the solution. The average increase in mass transfer coefficient between the 5% and 20% concentration cases was as high as 102%, while the associated increase in pressure drop equaled 33%. Higher gas phase concentrations yielded poorer mass transfer characteristics, particularly with dilute amine solutions and at larger channel diameters, while the effect of the same on pressure drop was relatively negligible. Based on the large data set obtained from the present experiments, empirical Sherwood number models were developed and favorably compared with the presently obtained experimental data. Measurements of single-phase and two-phase pressure drop were obtained and compared against available models. A two-phase pressure drop model that yielded good predictive accuracy with water as the working fluid failed to accurately predict the pressure drop with amine-based working fluids. Subsequently, a modified pressure drop model was proposed for aqueous amine solutions and verified against a dataset comprising 65 data points obtained from the parametric studies. This model was subsequently applied to a larger data set comprising 120 data points and a reasonably good agreement was obtained for all channel diameters. High-speed visualization of the

106

fluid flow was performed, with the observed two-phase flow patterns including slug, slug-annular, annular and churn flow. These flow patterns were mapped with respect to gas- and liquid-phase superficial velocities, and the transition lines were compared with the literature. Image-processing analysis of the acquired flow patterns was conducted to determine the specific interfacial area. The specific interfacial area for the 254 and 508 μm channels was on an average 183% and 50% higher than that of the 762 μm channel. This enhancement resulted in improved mass transfer characteristics, as was observed with respect to the absorption efficiency. Likewise, the liquid-side volumetric mass transfer coefficient values obtained for the 254 and 508 μm channels were on an average 256% and 53% higher than that obtained with the 762 μm channel. Specific interfacial areas and liquid-side volumetric mass transfer coefficients close to 15000 m^{-1} and 400 s^{-1}, respectively, were achieved in the present work. These values are between 1-4 orders of magnitude higher than that reported using most conventional gas-liquid absorption systems, which was considered an indication of the high level of process intensification and enhancement that can be achieved by using microreactors.

Chapter 4: CFD Modeling of Adiabatic Non-Interacting Gas-Liquid Taylor Flow in Microreactors

4.1 Introduction

Microreactors can offer substantial enhancement of transport phenomena for diverse engineering applications, as was demonstrated in Chapter 3 for laboratory-scale systems. Subsequent design, optimization and scaling-up are to be conducted and the availability of validated numerical modeling tools can greatly aid in this process. The accurate numerical modeling of multiphase flow with heat/mass transfer in microscale systems first requires accurate prediction of the hydrodynamics of adiabatic, non-interacting multiphase flow. Since flow features at the microscale different from those at larger length scales, there is a need to assess the performance of multiphase flow models for their accuracy when implemented for microscale systems. This chapter investigates the application of a relatively less investigated phase field model for modeling two-phase flow in microchannels and compares it with the popular volume of fluid approach. Both these approaches have been utilized in subsequent chapters in this dissertation. The Taylor or slug flow regime is characterized by several well studied features (reviewed in Section 2.2) that renders it an optimum choice for assessing the performance of numerical modeling approaches. Furthermore, it has also been a dominant research interest for microreactors and heat exchangers on account of enhanced convective mixing phenomena due to recirculating velocity currents. This chapter presents an analysis of the effects of the phase field parameters on Taylor bubble length and gas void fraction. A detailed

analysis of gas void fraction trends is conducted and comparison with those reported in the literature. The effects of wall adhesion and modeling of the thin liquid film between the Taylor bubble and the channel wall, flow field, pressure distribution and influence of channel inlet configuration have been investigated.

4.2 Numerical model

4.2.1   Governing equations

The hydrodynamics of two-phase flow are governed by the equation for continuity (Eq. 4.1) and incompressible Navier-Stokes equation (Eq. 4.2).

$$\nabla . \mathbf{U} = 0 \tag{4.1}$$

$$\rho \frac{\partial \mathbf{U}}{\partial t} + \rho (\mathbf{U}.\nabla)\mathbf{U} = \nabla . \left[-P\mathbf{I} + \mu \left(\nabla \mathbf{U} + \nabla \mathbf{U}^{T} \right) \right] + \mathbf{F_g} + \mathbf{F_{ST}} \tag{4.2}$$

The Eötvös number (or Bond number) criterion of Brauner and Moalem-Maron (1992): Eö $< (2\pi)^2$ was utilized to verify that under any selected simulation conditions, the surface tension forces were indeed dominant over gravitational forces, and hence the latter could be neglected.

Interface tracking was done by the phase-field method using the formulation of Yue et al. (2004), from which two second-order partial differential equations are obtained (Eqs. 2.10 and 2.11). As a convention, in the present study, the phase field variable, ϕ, was chosen to equal -1 in the pure gas phase and +1 in the pure liquid phase. A scaling relation, Eq. 4.3, which takes values from 0 to 1, was used to obtain the volume fraction of either phase. The effective fluid properties such as density and

viscosity were computed as the average value of the two phases weighted by their

respective volume fractions, as obtained from Eq. 4.3.

$$\varepsilon = \begin{cases} \dfrac{1-\phi}{2} & : \quad Gas \\[2ex] \dfrac{1+\phi}{2} & : \quad Liquid \end{cases} \qquad (4.3)$$

The time scale of the Cahn-Hilliard diffusion, γ, as defined by Eq. 2.12, is a function

of two user-defined parameters: mobility, χ, and interface thickness, ξ. Suitable

values for the mobility and interface thickness parameters, χ and ξ respectively, were

chosen to obtain a suitable time scale of diffusion that did not excessively dampen the

convective motion and yet retained a constant interfacial thickness (Jacqmin, 1999).

Likewise, sufficient diffusion was recommended to be present to resist straining flows

that thin or thicken the interface.

The effect of surface tension was modeled as a body force, F_{ST}, in Eq. 4.4. It was

computed as the product of the chemical potential of the system, G, and the gradient

of the phase-field variable.

$$F_{ST} = G.\nabla\phi \qquad (4.4)$$

4.2.2   Computational domain

Channels having characteristic dimensions ranging from 100 to 500 μm were

modeled using a two-dimensional planar computational domain. A cross-flow inlet

configuration was utilized for all cases, and a schematic is presented in Figure 4.1.

110

The entire domain was discretized with a homogeneous unstructured grid consisting of triangular elements with size $D/10$, where D denotes the characteristic dimension of the channel. To maintain a constant resolution of the gas-liquid interface throughout the channel, the entire domain was discretized using a constant element size. Hence, block-structuring to obtain a high resolution near the channel walls was not possible. Grid independency was verified in conjunction with the interface thickness parameter, ξ, by means of the h/ξ ratio.
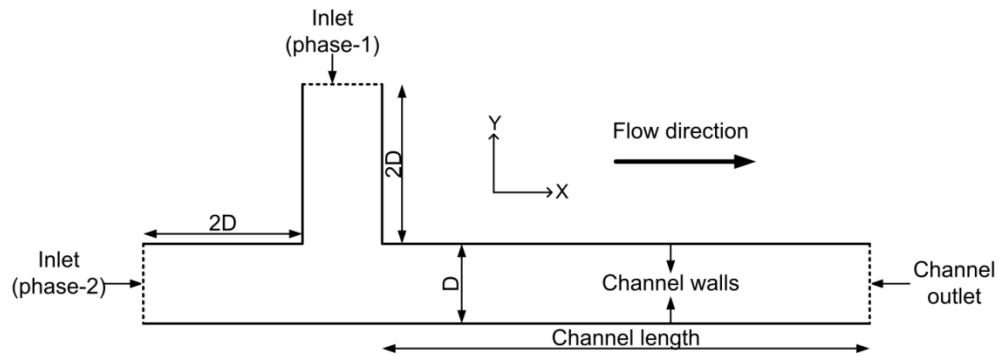
Figure 4.1: Schematic of computational domain.

It is worth noting that several studies exist in the literature on the numerical simulation of Taylor flow. These have been based on two-dimensional planar, two-dimensional axisymmetric, and three dimensional domains. Even between studies that use the same multiphase flow formulation, the results differ based on various factors including the choice of type of computational domain, resolution of the domain, and the methodology implemented to model the wetting behavior. These differences have been duly highlighted while discussing the various features of Taylor flow in their respective sections.

111

4.2.3 Boundary conditions

A constant velocity boundary condition was specified at the inlets with a single phase being admitted through each inlet. The flow pattern maps reported by Chung and Kawaji (2004) were used as a guideline to select the velocity ranges for the gas and liquid phases in order to simulate Taylor flow. A pressure-based outflow boundary condition was specified at the channel outlet, which applied a Dirichlet condition on the pressure. It is worth noting that a Hagen-Poiseuille velocity boundary condition for the channel was utilized by Chen et al. (2009) with the level-set method which specified a Hagen-Poiseuille velocity profile at the channel outlet with a mean velocity that equaled the inlet velocity. This was reported to yield results similar to those obtained with the use of a pressure-based boundary condition. A remark of concern on their study is the requirement for the bubble interface to be sufficiently far away from the outlet, which seems unreasonable given that the interface is always likely to be affected by the conditions at the outlet in developed two-phase flow. Nevertheless, the velocity-based condition was also tested in our study, but it did not yield a converged solution with the phase field method and hence it was not used. Consequently, it is recommended that phase field modeling of two-phase flow use a pressure-based boundary condition and not a velocity-based condition at the channel outlet.

For the channel walls, either no-slip or wetted-wall conditions were applicable. The wetted-wall condition specifies no-slip at the channel wall and alters the interface normal at the channel wall based on the value of contact angle specified in the boundary condition given by Eq. 4.5. For the no-slip case, the interface is assumed to

be normal to the channel wall and hence for θ equaling 90°, the right-hand side of

Eq. 4.5 becomes zero.

$$\mathbf{n}.\xi^2\nabla\phi = \xi^2 \ \tan\left(\frac{\pi}{2}-\theta\right)\times\left|\nabla\phi-(\mathbf{n}.\nabla\phi)\mathbf{n}\right| \tag{4.5}$$

4.2.4   Simulation conditions

Throughout this work, nitrogen and water were used as the gas and liquid phases,

respectively and the physical properties of the same, at 25 °C, are reported in Table

4.1. Exceptions to the above conditions include section 4.3.9, wherein the predicted

flow field was validated by comparing with available experimental data for liquid-

liquid Taylor flow involving water and FC-40 in a 762 μm channel. Additionally, the

channels having different inlet configurations have been discussed in Sections 4.3.11

and 4.3.12.

Table 4.1: Physical properties of fluids at 25 °C.

Phase	Property	Value
Gas phase (nitrogen)	Density	1.145 kg/m^3
	Dynamic viscosity	1.78x10^{-5} Pa s
Liquid phase (water)	Density	997.1 kg/m^3
	Dynamic viscosity	8.91x10^{-4} Pa s
Two-phase	Surface tension	7.19x10^{-2} N/m

4.2.5   Solver settings

The numerical model was implemented using a commercial CFD code, COMSOL Multiphysics (COMSOL Inc., Burlington, MA), version 3.5a, which is based on the finite-element method. An implicit time-stepping algorithm was used with residual tolerance levels of 10^{-4}. This was verified to be sufficient since similar solutions were obtained at lower tolerance levels. The phase-field variables were initialized by selectively solving for ϕ and ψ. This transient initialization run was used to define the initial interface. Since the channel was assumed to be initially filled with quiescent gaseous phase, the initial interface was formed at the liquid inlet. It was ensured for every simulation that the interface created by the initialization procedure was monotonic i.e. the phase field variable, ϕ, varied monotonically across the interface within the allowed range of -1 to +1. Subsequently, the transient simulation was performed starting from the above obtained initial solution.

All simulations were carried out on a workstation comprised of two Intel Xeon processors with eight cores and 4 GB of RAM.

4.2.6   VOF model

While the primary focus of the present study was the phase field formulation, select simulations were performed using an alternative approach, the VOF model, for comparison purposes. Hence, important details pertaining to its implementation have been briefly reported here.

114

The VOF model was implemented in the CFD code FLUENT, version 6.3.26

(ANSYS, Inc., Canonsburg, PA). It is based on the CSF model for surface tension

(Brackbill et al., 1992). Interface reconstruction was performed using the explicit

piecewise-linear interface construction (PLIC) scheme of Youngs (1982). A pressure-

based solver with an unsteady first order implicit formulation was used with the

SIMPLE algorithm for the pressure-velocity coupling and the PRESTO (pressure

staggering option) scheme. Following the recommendations of Krishnan et al. (2010),

based on a detailed assessment on the performance of various numerical schemes for

similar applications, a first-order upwind scheme for discretizing the momentum

equation, and a Green-Gauss node-based scheme for calculating the gradients of

scalar variables, was utilized. A grid independence analysis was performed with the

VOF model by analyzing bubble lengths at different levels of domain resolution. The

results obtained with element sizes $D/10$ and $D/20$ varied only by 4.2%, which was

considered to be acceptable. Further, as noted in section 4.2.2, the phase field-based

results were also grid independent with an element size of $D/10$. Therefore,

subsequent simulations performed with the VOF model for comparison against the

phase field-based results, have been obtained using the same element size for both

models ($D/10$). Further, select simulations reported have been performed with a

substantially finer mesh having an element size of $D/250$, in order to assess the

potential of the VOF model to capture the thin liquid film between the gas bubble and

the channel wall.

4.3 Results and discussion

4.3.1   Analysis of domain discretization

The sensitivity of the solution to the domain discretization in terms of the spatial

mesh element size and type was studied by monitoring characteristic features of

Taylor flow. It is noted that the issue pertaining to domain discretization and the

capture of the thin liquid film between the Taylor bubble and channel wall is

considered separately.

4.3.1.1   Element type

Krishnan et al. (2010) recommended the use of square grids for numerical modeling

of multiphase flow because they are better able to handle surface tension forces.

However, these quadrilateral grids were recommended for the finite-volume

implementation of the VOF method and hence their validity was analyzed for the

present finite-element implementation of the phase-field method which is based on

free energy.

The global flow features in terms of the phase distribution/bubble profiles indicated

no apparent discrepancy between results obtained using triangular and quadrilateral

elements. Further, the surface tension forces that act on the interface at the channel

wall were compared. The interface exists at the channel wall due to the absence of a

liquid film. A typical result at t=0.1 s is shown in Figure 4.2, wherein the

characteristic dimension of the channel is 500 μm and the gas and liquid phase

superficial velocities are 0.1 m/s. The results were found to be completely

independent of the element type. While the computational efforts for meshing were

comparable, the triangular elements resulted in a reduction in the computational time required by the solver by nearly 20% as compared to the quadrilateral elements, and hence they were the preferred choice in this study. The difference in computational time could possibly be attributed to the fact that the maximum element skewness for the quadrilateral cells was 0.13 which was slightly higher than that for the triangular cells at 0.08. Highly skewed meshes were avoided in order to maintain a constant resolution of the interface throughout the computational domain.
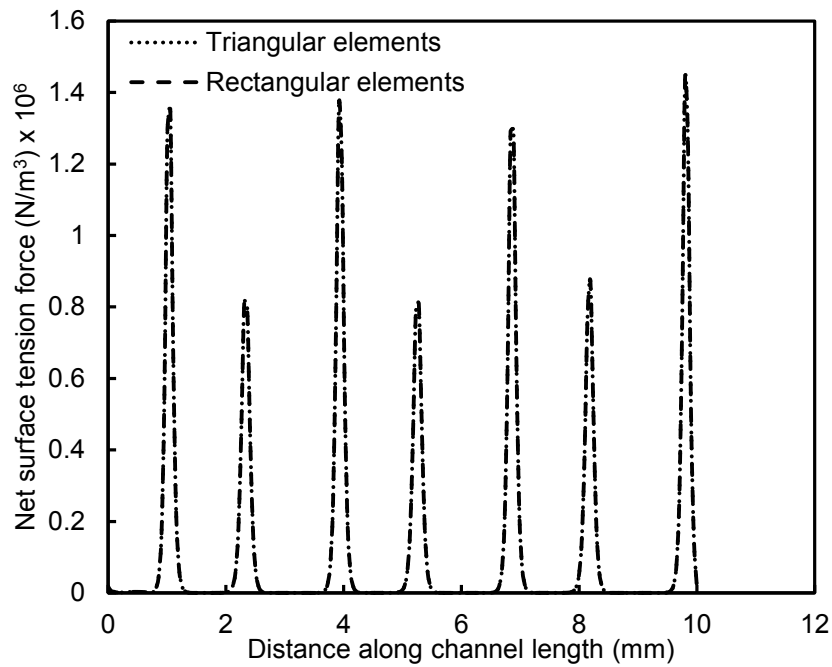
Figure 4.2: Comparison of numerically predicted surface tension force along channel length with triangular and rectangular mesh elements.

4.3.1.2 Element size

Given the lack of understanding on whether ξ represents an absolute or relative measure of interfacial width, the range of values for the h/ξ ratio, suggested by Yue et

al. (2006) to be between 0.5 to 1, was not directly utilized in this study. Instead, h/ξ values ranging from unity until two were investigated as two extreme cases. Here, the lower limit of unity was determined by the availability of computational memory to store larger factorization matrices in the finite-element method; i.e., smaller values of the h/ξ ratio represent more highly resolved domains. This is quite unlike the finite-volume method where solutions are generally obtainable at the cost of higher computational time overheads, as demonstrated by Gupta et al. (2009).

The region within 0.996 volume fraction of gaseous phase (0.004 volume fraction of liquid phase) was defined as the "interfacial region" for this study. For an h/ξ ratio of unity, it was found to be resolved by more than 15 elements, while for a ratio value of 2, it was just under 10 elements. Although both these cases lie within the recommendations of Yue et al. (2004), better grid independence was obtained with a value of unity for the h/ξ ratio (the higher resolution case) as compared to a value of 2, as seen in Figure 4.3. Therefore this condition was applied towards domain discretization in all further simulations. This finding also indicates that the interface thickness parameter serves as a relative and not absolute measure of interface thickness, and hence the guidelines of Yue et al. (2004, 2006) cannot be universally applied. Rather, it is always essential to verify grid-independence for the chosen values of interface thickness parameter and the resulting number of interfacial mesh elements.
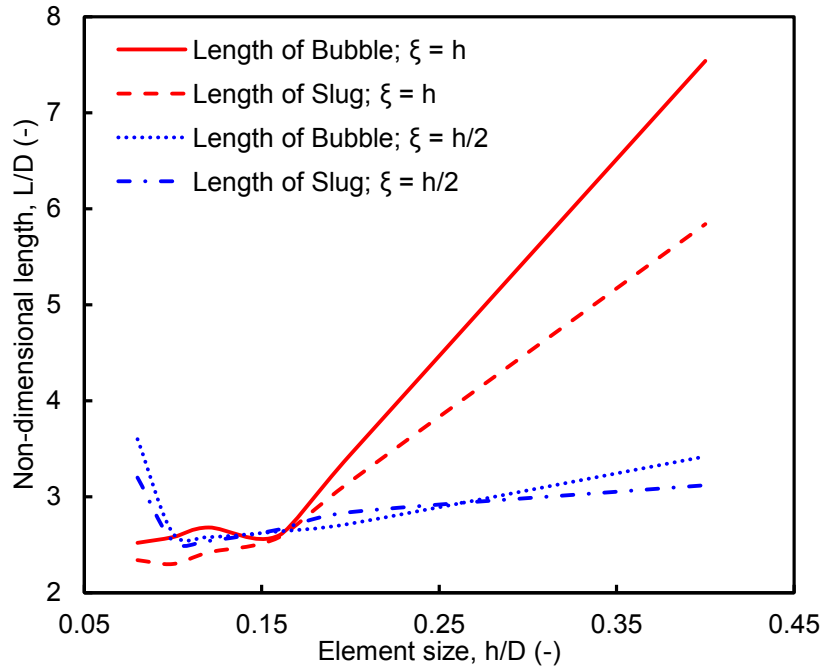
Figure 4.3: Variation of bubble/slug length with element size for h/ξ equaling unity and 2.

4.3.2   Analysis of Taylor bubble formation

In the Taylor flow regime, the bubble evolution and breakup can occur by different mechanisms. These were first described by Garstecki et al. (2006) and subsequently by Yue et al. (2008) and Santos and Kawaji (2010). A partial verification of these proposed theories using numerical methods was reported by De Menech et al. (2008). In the present study, an attempt was made to numerically simulate the phase distribution during bubble formation and compare the detachment mechanism with the theories proposed in literature based on the predicted flow features.

4.3.2.1 Dripping mechanism

Figure 4.4 corresponds to Taylor bubble formation by the dripping mechanism (or breaking-slug mechanism as in Santos and Kawaji, 2010) which occurs at high capillary number flows, typically greater than 10^{-2}. In this case, it is the shear stress that plays a dominant role in the bubble detachment. The effect of the build-up in pressure in the liquid phase is not dominant here since the evolving gas bubble occupies only a fraction of the channel width and the entire channel is not blocked by the phase. In order to verify this, the pressure at the liquid inlet was monitored over a single bubble formation cycle. The pressure is expressed as a ratio of the peak pressure over the time considered in order to facilitate comparison with alternative bubble formation mechanisms. As seen in Figure 4c, the pressure ratio is relatively constant as indicated by its proximity to unity throughout the bubble formation cycle.

4.3.2.2 Squeezing mechanism

Figure 4.5 corresponds to Taylor bubble formation by the squeezing mechanism (or snapping-slug mechanism as in Santos and Kawaji, 2010) which occurs at low capillary numbers, typically less than 10^{-2}. In Figure 4.5a and Figure 4.5b, the evolving gas bubble occupies the entire channel width, leading to an increase in the liquid phase pressure, upstream of the bubble. This leads to a squeezing of the gas neck and results in detachment of the bubble. The variation in pressure in the liquid inlet over a single bubble formation cycle is shown in Figure 4.5c, in which a wide variation in the pressure ratio is observed. This is quite unlike the numerical findings of De Menech et al. (2008), also based on the phase field model. In their study, the

squeezing mechanism was characterized by an initial rise in pressure, while the

evolving bubble (discontinuous phase) occupied increasing fractions of the channel

width followed by a drop in pressure while the liquid phase (continuous phase)

necked into the emerging gaseous phase. The rapid fluctuations in Figure 4.5c are

believed to be a more prominent representation of the "sharp kinks" described by De

Menech et al. (2008). While the fluctuations were previously attributed to the

interactions between the emerging droplet and the channel outlet, this is clearly not an

issue in the present simulations, since we have modeled longer channels containing

additional bubbles between the emerging bubble and channel outlet.
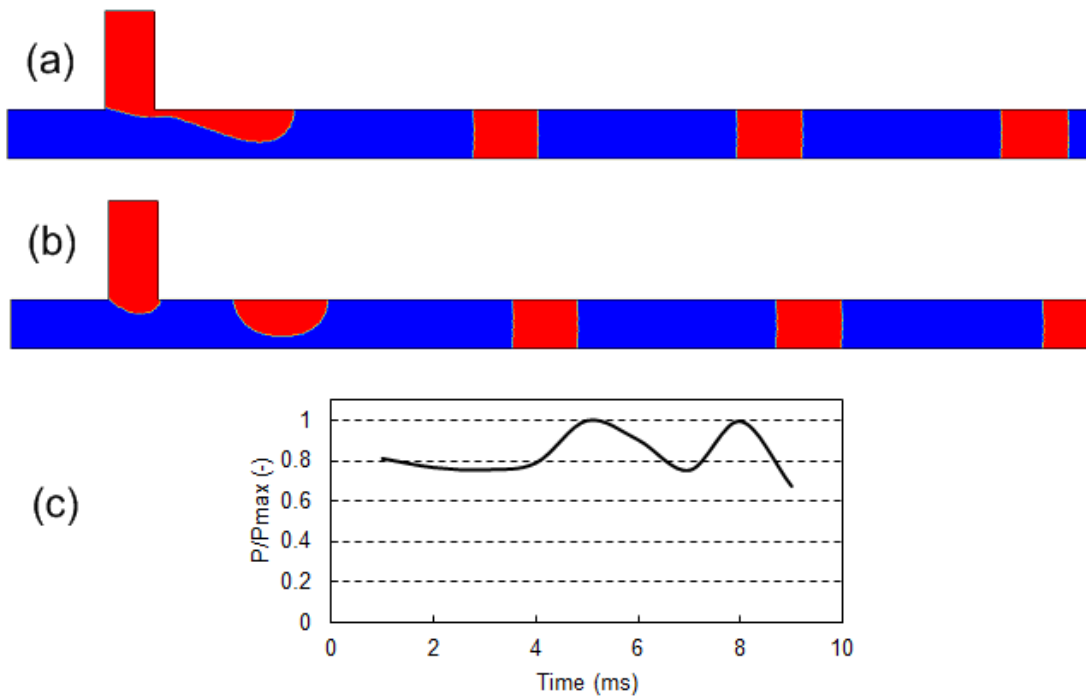
Figure 4.4: Bubble formation by dripping regime (a, b) contours of gas phase void faction (red), (c) transient variation of pressure ratio at liquid inlet.

121
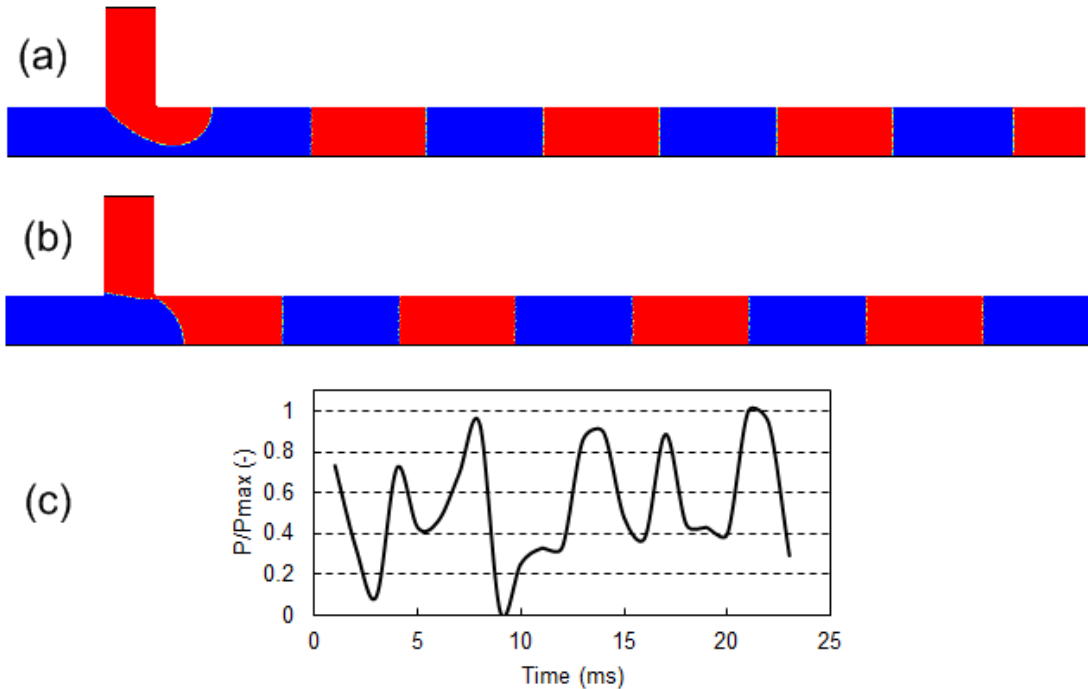
Figure 4.5: Bubble formation by squeezing regime (a, b) contours of gas phase void faction (red), (c) transient variation of pressure ratio at liquid inlet.

A plausible theory would be to consider Taylor bubble formation by the squeezing regime as not being associated with a singular rise in pressure followed by a drop over one bubble formation cycle. That is, building upon a remark by Yue et al. (2008), the liquid phase alone is not responsible for bubble detachment. Rather, as the gas stream continuously enters the liquid phase, increasing fractions of the channel width are continuously occupied by the emerging gaseous phase, leading to a build-up in pressure in the liquid phase. Simultaneously, this pressure build-up causes the liquid stream to neck into the gas stream, resulting in a drop in pressure. As understood from Figure 4.5, both these phenomena seem to occur simultaneously and hence yield a pressure profile with an alternating rise and drop pattern.

4.3.2.3   Jetting-slug mechanism

A third type of Taylor bubble formation, the jetting-slug mechanism, which occurs at further higher capillary number flows, typically greater than 0.02, was described by Santos and Kawaji (2010) as similar to the instability propagation of droplets from jets. A similar observation was reported by Yue et al. (2008) (refer to their Figure 9c) but was classified as the dripping regime since it was observed at capillary numbers higher than those for the squeezing regime. This is a three-dimensional pattern since the gas stream is flanked on both sides by the liquid phase-a situation that could not be captured with the present two-dimensional geometry on account of the absence of wall continuity from top to bottom. On the contrary, fluid flow in a three-dimensional domain is enclosed by a continuous wall, as is the case in a circular pipe or duct. Hence, we believe that three-dimensional modeling is essential for capturing the above bubble formation mechanism. Additionally, it would also provide an understanding of the actual physics behind this mechanism since experimental analysis is often limited to visual classification only and rarely provides a direct means to comprehend the prevalent force fields.

Lastly, it is worth noting that although Salman et al. (2006) reported that the initial phase present in the channel could affect the observed mechanism, the inlet configuration used in the present study, which is different from the nozzle geometry in their study, did not face this issue. Furthermore, when sufficient transient simulation time (or channel residence time) was solved for, the ensuing results

appeared independent of the initial phase present in the channel, irrespective of inlet configuration.

4.3.2.4 Bubble formation time

The Taylor bubble formation time was studied for gas and liquid superficial velocities ranging from 0.1 to 1 m/s in channels having characteristic dimensions of 500 and 250 μm, as shown in Figure 4.6.

For a constant gas-phase superficial velocity, bubble formation times were shorter with increasing liquid-phase velocity since the bubble lengths were correspondingly lesser. Likewise, with an increase in the gas-phase superficial velocity with constant liquid-phase superficial velocity, shorter bubble formation times were predicted, although the bubble lengths were higher. In addition, for the same flow conditions, bubble formation times were shorter for the 250 μm channel than for the 500 μm channel. While a similar trend was reported by Salman et al. (2006), the fluctuations in the bubble formation time observed in their experiments (attributed to exit effects) were not present. In general, in the present study, uniformity existed between all bubble generation cycles with variations of at most ±0.5 ms (indicated in Figure 4.6 by vertical bars), which is indeed less than the 4 ms variations reported by Salman et al. (2006).
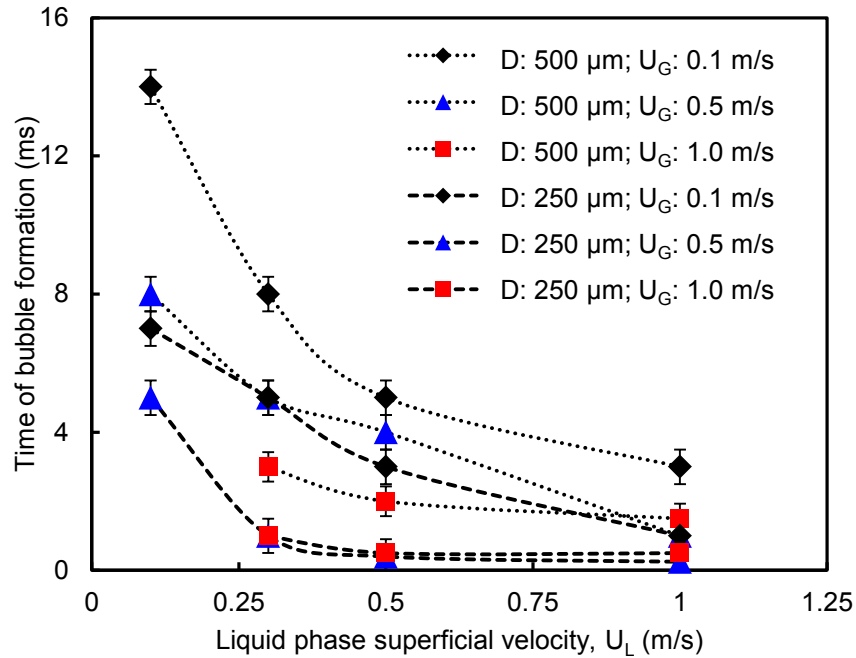
Figure 4.6: Time for bubble formation with varying gas and liquid phase superficial velocities.

4.3.3 Analysis of phase field parameters

The governing equations of the phase field method involve a term, γ, which is a function of the mobility parameter, χ, and the interface thickness parameter, ξ, as defined in Eq. 2.12. These parameters were found to affect the hydrodynamics of the flow and hence were studied systematically for flow in a channel having a characteristic dimension of 500 μm. The superficial velocities of the gas and liquid phases were both 0.1 m/s. Several simulations were performed by sequentially increasing this factor to range over several orders of magnitude. This was accomplished first by varying only the mobility parameter, χ, and keeping the interface thickness parameter, ξ, constant, and subsequently by halving the interface

thickness parameter for the same values of mobility parameter. In effect, the ranges

investigated were $10^{-8} < \gamma < 10^{-4}$.

4.3.3.1   Mobility parameter

A large data set was obtained from the ranges of the term γ from which it was

observed that for the lowest values of mobility, the solution did not converge, and

thereby the solver did not complete the transient simulation run. As the mobility was

increased, stratified flow was obtained, which was classified as an unphysical

solution, given that the expected regime is Taylor flow. At higher values of mobility,

the flow transitioned into Taylor flow with bubble formation first by the dripping

regime and at further higher mobility by the squeezing regime. These observations

were interpreted as follows.

Very low values of mobility result in thin-interfacial straining flows that lack

convective motion (Jacqmin, 1999). Hence, these flows are believed to have created

numerical difficulties that prevented convergence of the solution for these cases.

Subsequently, at higher values of mobility, during the development of stratified flow,

i.e. during the initial time-steps of the transient run, the leading edge of the liquid

phase stream that progressed through the channel length (filled initially with

quiescent gas phase) was characterized by a rounded, frontal nose. After the frontal

nose progressed through the channel length and reached the outlet, the phase

distribution then resembled that of stratified flow, which inherently appears to be at

steady state. However, at further higher values of mobility, the frontal nose did not

merely progress through the channel. Rather, it necked into the gaseous phase and

126

completely blocked the gas stream. This occurred in an alternating and repetitive fashion resulting in the generation of a Taylor flow pattern. Since the flow rate was maintained constant between the cases with low and high values of mobility (which yielded stratified flow and Taylor flow, respectively) the difference in flow pattern was hypothesized to be due to the predicted surface tension force field. This was verified by means of plots of the net surface tension force vectors superimposed on the contours of the gas void fraction as shown in Figure 4.7.
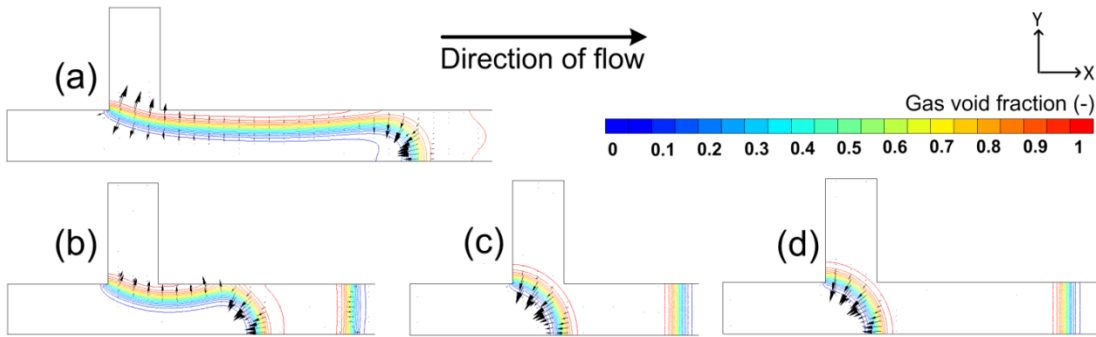
Figure 4.7: Predicted surface tension force vectors at channel inlet superimposed on contours of gas void fraction (mobility increases from a to d).

Figure 4.7a corresponds to stratified flow, obtained at the lowest value of mobility among the four cases. Figure 4.7b, Figure 4.7c, and Figure 4.7d correspond to Taylor flow simulated with increasing values of mobility leading to increasingly higher bubble lengths in each case. These results were obtained at the last time-step prior to the detachment of the Taylor bubble. The cases in Figure 4.7a and Figure 4.7b represent the transition from stratified flow to Taylor flow, in which the interfacial surface tension forces are represented by uniformly scaled vectors. At the frontal nose of the liquid thread, these forces act in an upstream direction, into the liquid phase.

This observation is in concordance with the theory proposed by Garstecki et al. (2006) pertaining to interfacial stresses in which these forces were approximated to have a magnitude $-\sigma(2/w' + 2/h')$ wherein the negative sign explains the upstream direction of forces indicated in Figure 6b. Further, the forces upstream of the tip were approximated to have a magnitude $+\sigma(1/w' + 2/h')$ wherein the positive sign explains the downstream direction of forces (directed into the gaseous phase) indicated in Figure 4.7b. The stabilizing effect of these opposing interfacial forces acts in addition to the shear stress and pressure drop forces described in Section 4.3.2. Consequently, we believe that for the stratified flow (Figure 4.7a), the surface tension forces and hence the stabilizing effect were over-predicted on account of the low mobility. As a result, the net surface tension force vectors upstream of the frontal nose were comparable in magnitude and were opposite in direction on either side of the interface. This balanced system of forces is believed to have prevented bubble detachment from occurring and thereby resulting in a stratified flow. In contrast, for Taylor flow shown in Figure 4.7b, these forces were oriented towards the upper channel wall only, which could have possibly aided the liquid thread to neck in to the gaseous phase and completely block the channel leading to subsequent bubble detachment.

As the mobility is increased, the Taylor bubble length increased as shown in Figure 4.7b, Figure 4.7c and Figure 4.7d. This is because the partially balanced surface tension force field in Figure 4.7b was increasingly unbalanced for the subsequent cases, with the presence of dominant forces acting in only one direction, i.e. into the liquid phase, in an upstream direction. This is believed to have prevented the liquid

phase from necking into the gaseous phase and thereby resulting in increasing amounts of the gaseous stream entering the channel and contributing to the formation of a longer Taylor bubble. It is interesting to note that even with increasing Taylor bubble lengths, the gas void fraction for all cases remained nearly constant. This observation, shown for a typical case in Figure 4.8, indicates the agreement between the present multiphase flow model with the physics of homogeneous two-phase flow (refer to Eq. 4.9) and implies that for a constant flow condition, the gas void fraction is unlikely to be altered, even though the bubble/slug lengths may vary due to surface tension effects.
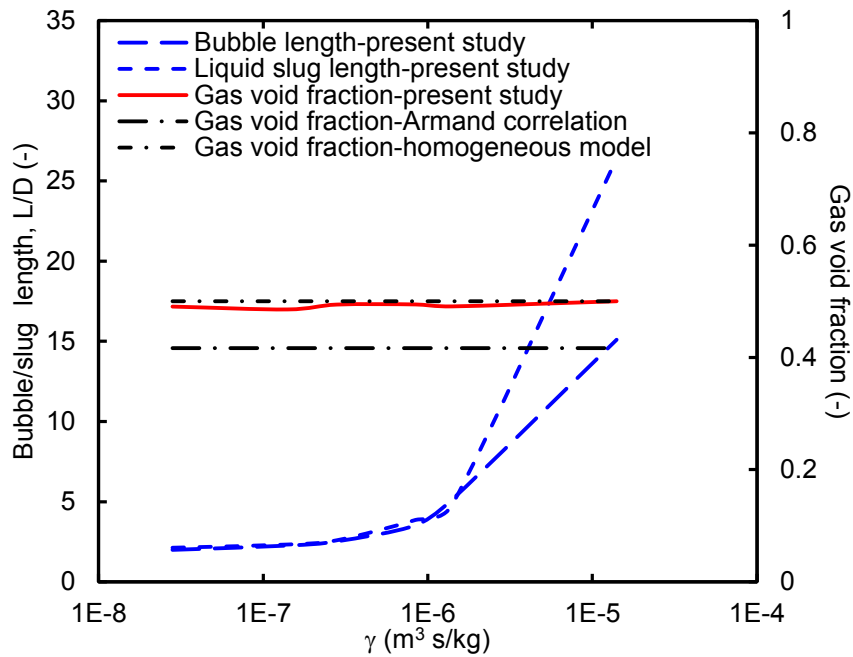
Figure 4.8: Variation of bubble/slug length and gas void fraction with mobility.

4.3.3.2 Interface thickness parameter

In the above cases, the interface thickness parameter, ξ, was maintained a constant, while the mobility parameter, χ, was varied to effect a net change in the time scale of Cahn-Hilliard diffusion, γ. In order to study the isolated influence of the interface thickness parameter, an alternative set of simulations was performed with the same values of χ and a lower, constant value of interface thickness parameter, ξ. As a test case, the interface thickness parameter was halved from its previous value since larger changes to the value would be associated with excessively coarse/fine mesh resolutions in order to maintain the same value of the h/ξ ratio. The results did not indicate any discernible changes for the Taylor flow cases. For the unphysical stratified flow case, an oscillating interface was observed (Figure 4.9) as against the relatively stationary interface obtained in the previous case. Given that this case was not of interest, it was not analyzed further.
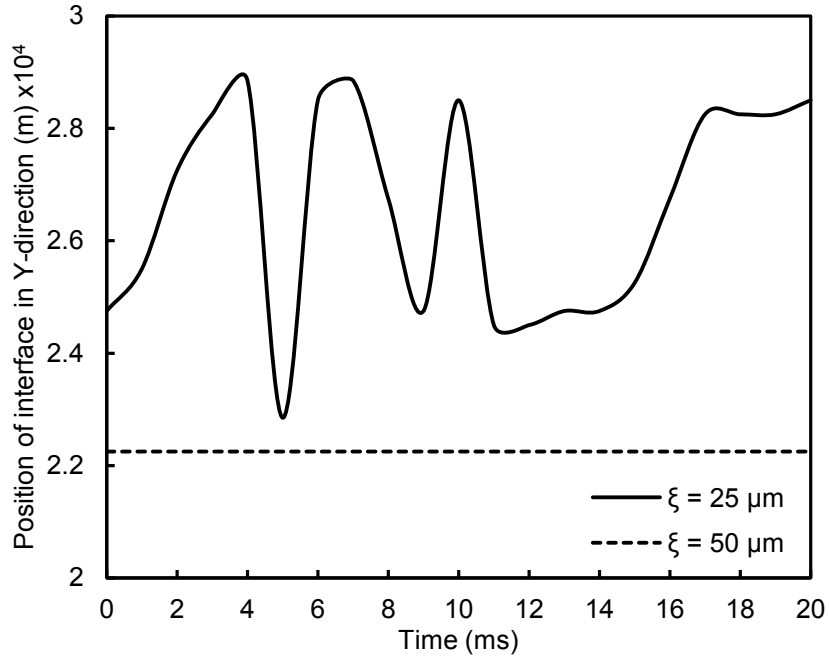
Figure 4.9: Variation of interface position with time for $\xi = 25$, 50 μm.

4.3.4 Analysis of Taylor bubble length

4.3.4.1 Comparison with empirical correlations

The literature presents several correlations for predicting the bubble/slug length, including Kreutzer (2003), Garstecki et al. (2006) and Qian and Lawal (2006). These are given by Eqs. 4.6, 4.7 and 4.8, respectively, re-written from their originally presented form to uniformly represent non-dimensional gas bubble lengths.

$$\frac{L_B}{D} = \left(\frac{\varepsilon_L}{-0.00141 - 1.556(\varepsilon_L)^2 \ln(\varepsilon_L)} \right) \times \left(\frac{\varepsilon_G}{1 - \varepsilon_G} \right) \qquad (4.6)$$

$$\frac{L_B}{D} = \left(1 + \alpha \frac{U_G}{U_L} \right) \qquad (4.7)$$

131

$$\frac{L_B}{D} = 1.637 \varepsilon_G^{0.107} \left(1 - \varepsilon_G\right)^{-1.05} \mathrm{Re}_B^{-0.075} Ca^{-0.0687} \tag{4.8}$$

The bubble lengths predicted by these relations are presented in Figure 4.10 for a characteristic case with gas phase superficial velocity of 0.1 m/s and liquid phase superficial velocities ranging from 0.1 to 1 m/s in a channel having a characteristic dimension of 500 μm. The empirical predictions are compared here with that of the phase field and VOF models.

As seen in Figure 4.10, bubble lengths vary between the different correlations, possibly indicating deviations between experimentally measured values. Further, the proposed correlations consider limited physical parameters only. A useful numerical model is required to make it possible to simulate different bubble lengths in order to yield compatibility with any specific condition that an experiment may demand. The phase-field method is better for this purpose than conventional multiphase flow models such as the VOF method. The extensively discussed mobility, χ, was previously shown to alter the predicted surface tension force-field and thereby the bubble and slug lengths. With an increase in this parameter, *ceteris paribus*, any higher bubble length could be predicted above the minimum length. The minimum possible length of a bubble exists because further reductions in mobility do not permit bubble detachment from occurring. In contrast to this, the VOF-based simulation results yield only a constant bubble length that generally lies in the range predicted by some correlations.
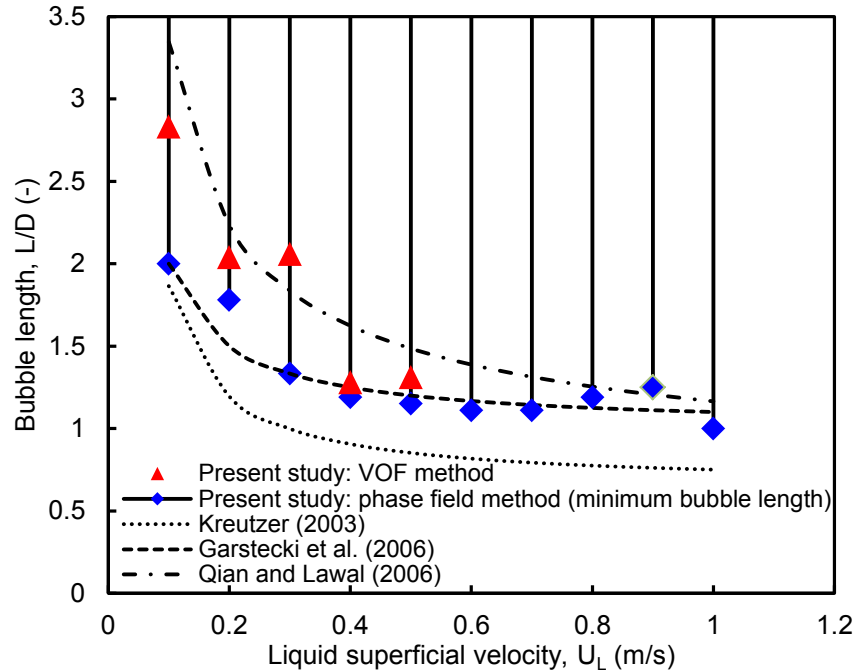
Figure 4.10: Comparison of numerically predicted bubble lengths with correlations in the literature.

The expressions presented by Laborie et al. (1999), Liu et al. (2005), and Akbar and Ghiaasiaan (2006) typically yield bubble lengths that are at least an order of magnitude higher than the remaining correlations, as is evident from the comparative plot reported by Shao et al. (2008). Hypothetically, infinite mobility is expected to yield an infinitely long bubble on account of the highly unbalanced surface tension forces acting on the liquid phase in an upstream direction. Hence, this would prevent the liquid from necking into the gas phase and thereby would continuously delay bubble detachment. Clearly, this requires very long channel lengths, greater than the already long bubbles, in order to sufficiently isolate the bubbles being generated from the channel outlet. Such cases were associated with a very large number of mesh

133

elements and hence the computational domain could not be discretized on account of the lack of memory available to store the large factorization matrices.

4.3.4.2 Comparison with experimental data

The present phase field formulation was implemented to model the experimental data of Santos and Kawaji (2010) in order to compare their experimentally obtained bubble lengths with the phase field predictions. Additionally, their VOF-based numerical results were also included for comparison. The channel had a characteristic dimension of 113 μm and cross-flow inlet configuration. The working fluids were air and water. Figure 4.11a reports the variation of the bubble lengths for different values of gas and liquid phase superficial velocity. The observed trends from both experiments as well as modeling indicate a decrease in the gas bubble length with a decrease in the gas phase superficial velocity. Likewise, shorter bubbles were formed at higher liquid phase superficial velocities. These trends are consistent with the physics of the phenomena. Figure 4.11b reports a parity plot comparing the numerical predictions with experimental data.

A mean absolute error (MAE) of 21.1% was obtained with the phase field approach as against a higher MAE of 45.1% with the VOF model. Although the phase field model yielded better predictive accuracy as compared to the VOF model, it is worth noting that both values of MAE are relatively high, primarily on account of the data point associated with the highest value of U_G/U_L equaling 7.6. For this case, both phase field and VOF models yielded relatively similar predictions with the L_B/D values equaling 17.3 and 16.6, respectively. However, both of these predictions were

highly inaccurate as compared to the experimental non-dimensional bubble length

equaling 6.6. The corresponding error for this data point alone is 160.9% and 149.1%

with the phase field and VOF models, respectively. However, when this data point

was neglected, the accuracy of both the phase field improved to 5.6% and that of the

VOF models was 33.5%. Based on the above analyses, it is concluded that while the

phase field method can yield better predictive accuracy as compared to the VOF

model, neither of the two approaches yield accurate predictions for high values of

U_G/U_L which are associated with high velocity slip (Santos and Kawaji, 2010). The

numerical models do not capture the effects of the same on account of the dry-out at

the channel wall.
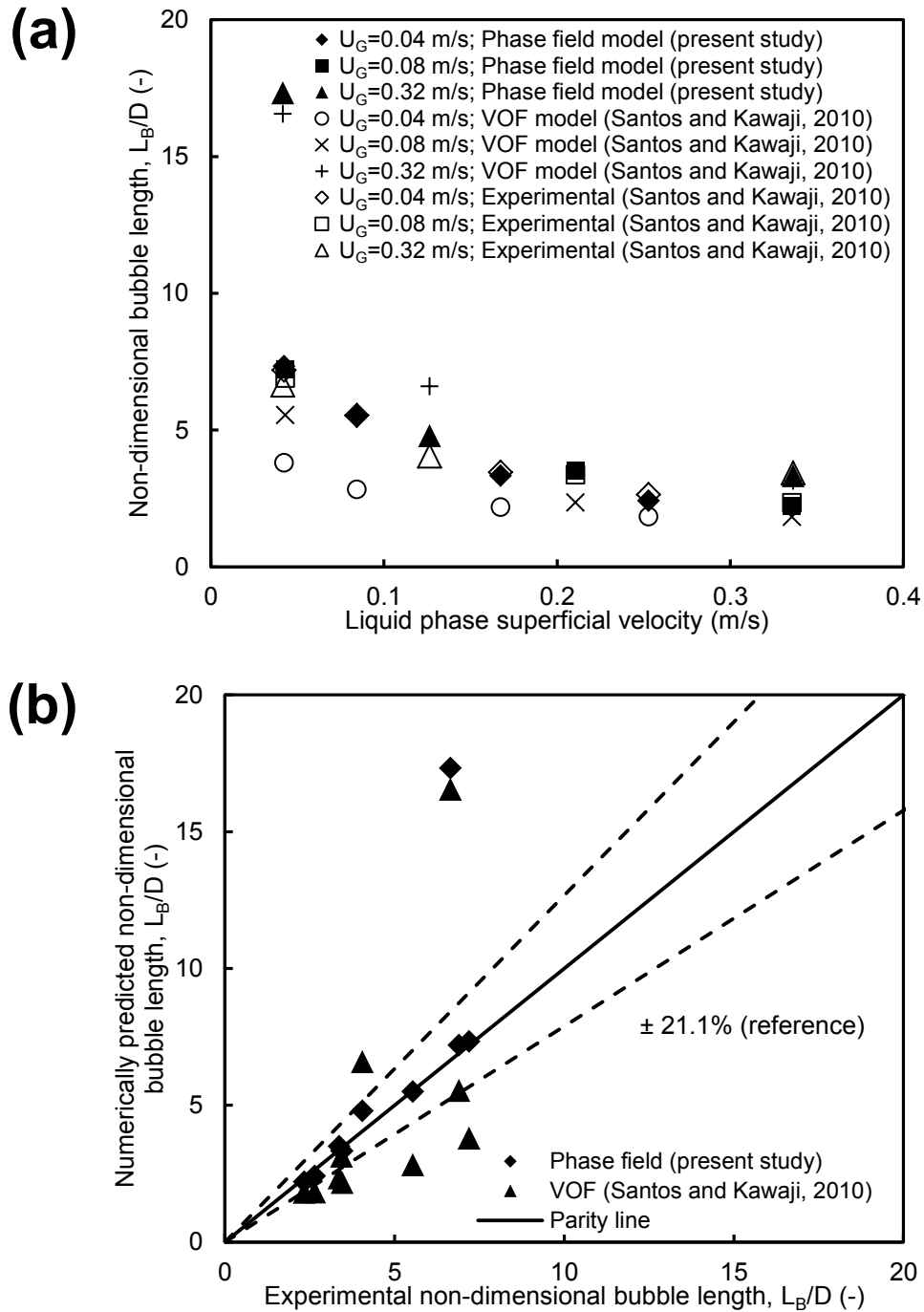
Figure 4.11: Comparison of non-dimensional bubble length predicted by the phase field method with experimental/modeling data of Santos and Kawaji (2010) (a) variation of non-dimensional bubble length with gas and liquid phase superficial velocity (b) parity plot.

4.3.5   Analysis of gas void fraction

In the present study, the gas void fraction, ε_G, was estimated from the numerically predicted flow patterns. Previous works in the literature have analyzed the variation of gas void fraction with respect to the volumetric flow ratio, β_G, and the trends have been reported to be either linear or non-linear in nature. A linear variation of ε_G with respect to β_G is typically comparable to the homogeneous flow model (Eq. 4.9) or the Armand correlation (Armand and Treschev, 1946; Eq. 4.10), while Eq. 4.11 (Kawahara et al., 2002), has been commonly used to represent a non-linear variation.

$$\varepsilon_G = \beta_G = \frac{U_G}{U_G + U_L} \tag{4.9}$$

$$\varepsilon_G = 0.833\beta_G \tag{4.10}$$

$$\varepsilon_G = \frac{0.03\beta_G^{0.5}}{1 - 0.97\beta_G^{0.5}} \tag{4.11}$$

The present phase field-based predictions are reported in Figure 4.12a for channels having a characteristic dimension of 250 and 500 μm, and in Figure 4.12b for a 100 μm channel. In general, the predicted gas void fraction varied linearly with the volumetric flow ratio, at all channel dimensions, and this is in better agreement with the linear equations given by Eqs. 4.9 and 4.10, as against the non-linear trend predicted by Eq. 4.11. A comparison of the predicted results against available experimental data is reported and discussed below.

137

4.3.5.1 Characteristic dimension ≥ 250 μm

The present phase field-based results for 500 and 250 μm channels have been
compared against the experimental works of Zhao and Bi (2001) (packed mesh inlet
with air and water; D=866 μm), Chung and Kawaji (2004) (reducer inlet with N_2 and
water; D=250, 530 μm), Hayashi et al. (2007) (annular inlet with N_2 and water;
D=600 μm), and Yue et al. (2008) (flow-focusing inlet with CO_2 and water; D=200,
400 μm), have been reported in Figure 4.12a. As can be seen, the linear variation of
gas void fraction with respect to volumetric flow ratio predicted by the present model
is in agreement with the trends reported by experimental works as well. It is worth
noting that although these works have utilized different inlet configurations, the trend
is always linear for the present range of characteristic dimensions.

4.3.5.2 Characteristic dimension < 250 μm

The trends of gas void fraction versus volumetric flow ratio for characteristic
dimensions smaller than 250 μm are compared in Figure 4.12b. The phase field
predictions for a 100 μm channel indicate a linear variation of gas void fraction with
volumetric flow ratio and this trend is in agreement with the experimental data of
Warnier et al. (2008) and Kawaji et al. (2009), and also with the VOF-based data of
Santos and Kawaji (2010). However, Figure 4.12b also indicates that there is
considerable disagreement between the presently considered studies for the current
range of characteristic dimensions and this was analyzed in more detail.

First, studies utilizing a reducer inlet configuration, wherein the gas and liquid phases are mixed in a region having a larger characteristic dimension than that of the mini/microchannel test section, were considered. Among these works, Kawahara et al. (2002) (N_2-water flow; D=100 μm) and Chung and Kawaji (2004) (N_2-water flow; D=50 μm) have reported a non-linear variation of ε_G with respect to β_G, while Serizawa et al. (2002) (air-water flow; D=20 μm) reported a linear variation, as shown in Figure 4.12b. While the use of a reducer inlet configuration can result in high velocity slip and therefore a lower void fraction (non-linear trend), the reasons for the above-mentioned discrepancy between the different experimental works are unclear. Additional experimental studies are warranted in order to resolve the same. Furthermore, details on the length of each step in the reducer inlet, a key design parameter that was not mentioned in any of the above works, is also required in order to facilitate a direct comparison of experimental results with numerical predictions.

Next, studies that have utilized a constant width flow domain were considered. Warnier et al. (2009) (flow-focusing inlet with N_2 and water; D=100 μm) and Kawaji et al. (2009) (cross-flow inlet with N_2 and water; D=100 μm) have reported a linear variation of ε_G with respect to β_G, while Santos and Kawaji (2010) (cross-flow inlet with air and water; D=113 μm) reported a linear trend for U_G/U_L less than unity and a non-linear trend otherwise. Further, their VOF-based modeling could not predict such a trend and a linear variation was predicted throughout, as was the case with the present phase field results too.

Based on the above discussion, it is clear that there is no consensus among available experimental works. Further, neither the phase field nor the VOF model predicts a non-linear variation of ε_G with respect to β_G. Santos and Kawaji (2010) noted that experimental factors such as the pressurization at the gas inlet (observed in their experiment and not predicted by their VOF incompressible fluid model) may require consideration. Likewise, while modeling deficiencies such as the inability to model a dynamic contact angle and prediction of dry-out at the channel wall could also be responsible factors, it may be premature to discuss the drawbacks of present-day multiphase flow models, given that additional experimental analyses are warranted for the present range of channel dimensions in order to obtain a better understanding of this aspect of Taylor flow.
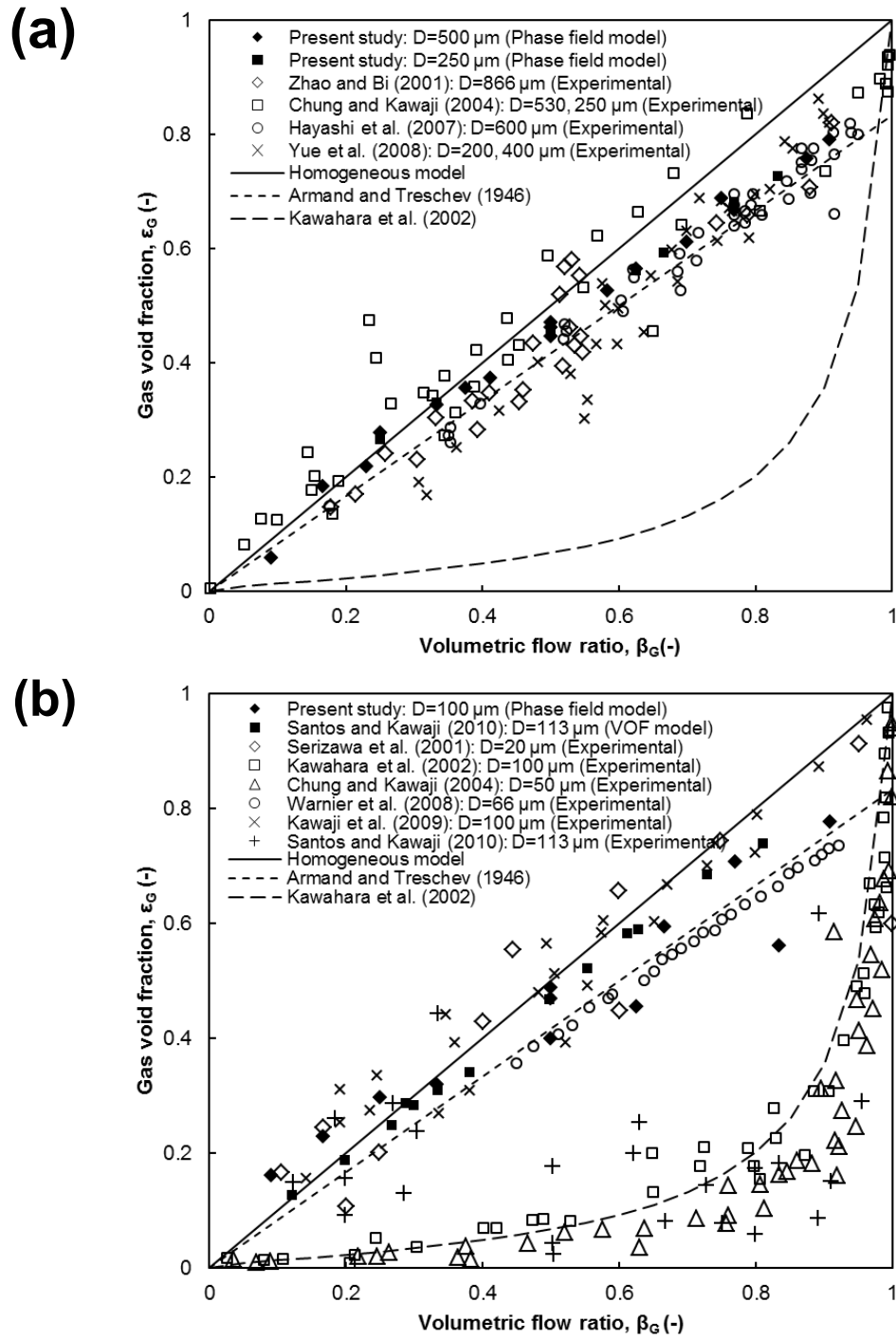
Figure 4.12: Variation of gas void fraction with respect to volumetric flow ratio and comparison with experimental data for (a) characteristic dimension greater than 250 μm (b) characteristic dimension lesser than 250 μm.

4.3.6 Pre-assessment of wall adhesion modeling by phase field method

As a precursor to modeling wall adhesion for two-phase flow in minichannels, a relatively simpler problem of spinodal decomposition (spontaneous separation of two immiscible phases into pure components) was performed to assess the predictive accuracy of the phase field method in obtaining an accurate contact angle at the channel wall. This step was deemed necessary in view of the shortcomings of the work of Liu and Zhang (2009) as reviewed in Section 2.2, since the phase field equations are now isolated from the equations for hydrodynamics (Navier-Stokes in the present study, lattice-Boltzmann in Liu and Zhang, 2009) with this simpler problem. The contact angle is specified as a boundary condition that follows Eq. 4.5, which alters the interface normal at the channel wall based on the specified value of contact angle. Additionally, this condition specifies no-slip (zero velocity) at the wall. The present study simulated the separation of two completely mixed phases with a random initial perturbation at t=0. These simulated cases used a wetted-wall boundary condition at all domain boundaries for which contact angles ranging from 0° to 180° were studied. As shown in Figure 4.13, most cases showed close agreement with the specified value of contact angle. Likewise, a clear distinction was observed between 60° and 120°, as shown in Figure 4.13b and Figure 4.13d, respectively. However, for 30° and 150° (Figure 4.13a and Figure 4.13e), the phase field method demonstrated relatively poor accuracy, since the phase distribution after separation did not conform to the specified contact angle. For all highly wetting and least wetting conditions (that is, angles typically lower than 30° and greater than 150°, respectively) convergence was not attained. Further, an increase in the mobility to create additional diffusion did

142

not resolve this issue. For this reason, the extreme cases of wetting/non-wetting behavior were not modeled in this study.
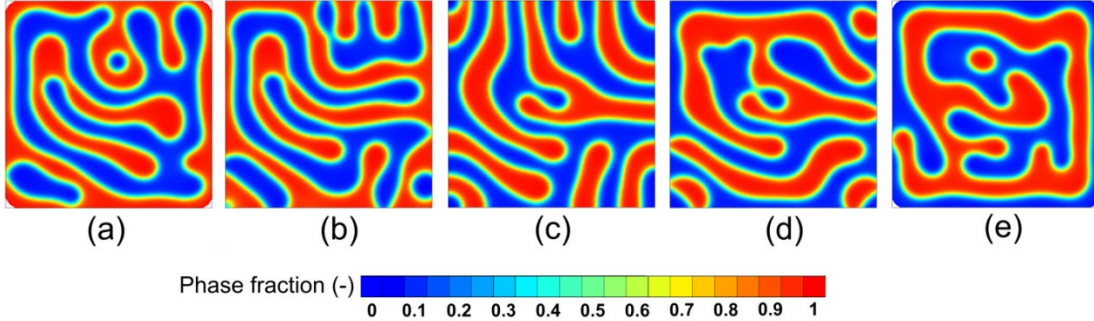
Figure 4.13: Spontaneous phase separation (spinodal decomposition) at t=20 s for contact angles (a) 30° (b) 60° (c) 90° (d) 120° (e) 150°.

At this point, it is not possible to ascribe with certainty a reason for the failure of the formulation of Liu and Zhang (2009) to simulate accurate contact angles (refer to Section 2.2), given that the present results did not face this issue. It is possible that their hybrid approach combining the lattice-Boltzmann and the phase field models had different limits for modeling the extreme wetting cases and hence further studies based on their approach with a larger range of contact angles are warranted.

4.3.7   Phase distribution and bubble profiles

Taylor flow in minichannels was investigated with no-slip and wetted-wall boundary conditions (refer to Section 4.2.3). Both of these cases are associated with a zero velocity at the channel wall and this is generally valid at the length scales under consideration in the present work. Additionally, for the no-slip case, the interface is assumed to be normal to the channel wall and hence for θ equaling 90°, the right-hand side of Eq. 4.5 becomes zero. The global phase distribution was similar for all

the simulated cases, apart from the differences in the bubble cap profiles due to a specific contact angle (90° or otherwise). Typical results shown in Figure 4.14 for gas and liquid phase superficial velocities of 0.1 m/s indicate that the current phase field-based results were indeed able to simulate the specified value of static contact angle accurately. These results verify the wetted-wall boundary condition specified in the present phase field formulation and the results are an improvement over that of Liu and Zhang (2009), as discussed in the preceding section.
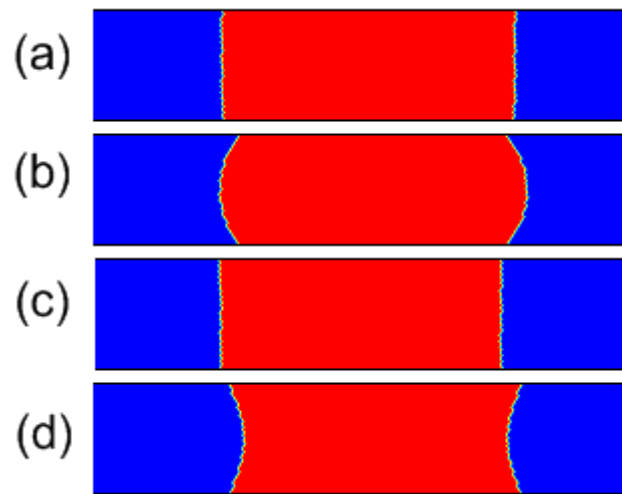
Figure 4.14: Bubble profiles predicted by the phase field method with different boundary conditions (a) no-slip (b) wetted wall- 60° (c) wetted wall- 90° (d) wetted wall- 120°; contours of gas void fraction (red).

The predicted gas void fraction varied by less than 0.8% for all cases reported in Figure 4.14. Further, the gas bubble/liquid slug lengths were altered only negligibly. This is in agreement with the remark by Gupta et al. (2009) that any difference induced by the contact angle would be purely numerical in nature. In addition, our results are also comparable to the VOF-based predictions of Qian and Lawal (2006), wherein contact angles ranging from 0° to 180° yielded a concave interface on the

liquid side for the fully wetting case and transitioned to a convex interface on the liquid side for the fully non-wetting case. However, since the extreme wetting cases were not modeled on account of the convergence issues mentioned in the preceding section, the bubble profiles described by Qian and Lawal (2006) for a contact angle of 0° (complete wetting at the channel wall) or 180° (complete dry-out at the channel wall) were not obtained.

Santos and Kawaji (2010) performed VOF-based simulations of Taylor flow in which an experimentally determined accurate value of contact angle was utilized. They reported that a computationally expensive three-dimensional model was essential because the two-dimensional modeling results lacked sufficient Laplace pressure to yield spherical bubble shapes. While this has not been an issue in most alternative studies based on the VOF method (Akbar and Ghiaasiaan, 2006; Qian and Lawal, 2006; Gupta et al., 2009 and Krishnan et al., 2010), nevertheless, the present phase-field method implemented in a two-dimensional domain was indeed able to obtain a realistic bubble profile.

4.3.8 Simulation of thin liquid film

Taylor bubbles are generally separated from the channel wall by a thin film of liquid having thickness of the order of a few micrometers. A review of previous efforts to capture this liquid film indicated an absence of studies in this area based on the phase field method and hence is investigated here.

As shown in Figure 4.14, at the current grid resolution of D/10, the phase field method predicted a dry-out condition at the channel wall for all values of contact

angle investigated (that is, in the cases modeled considering wall adhesion) and for the no-slip case. High mesh resolutions which could potentially capture the thin film were not feasible due to the high memory requirements of finite element method-based solvers as compared to finite volume method-based solvers. The finite element method typically requires larger amounts of memory to store large factorization matrices and hence is unable to handle highly resolved domains. This is quite unlike the finite volume method where solutions are generally obtainable at the cost of higher computational time overheads, as successfully demonstrated by Gupta et al. (2009).

In order to perform a similar study for comparative purposes, the VOF model was implemented for the same computational domain used in the phase field model. Domain discretization was performed with rectangular elements of sizes $D/10$ and $D/250$. The former corresponds to a resolution similar to that of the phase field model, while the latter corresponds to an element size of 2 μm, which is comparable to the mesh element size recommended by the criterion proposed by Gupta et al. (2009) based on the expression for film thickness (Eq. 2.13) given by Bretherton (1961). Both these cases are reported in Figure 4.15. In the highly resolved case (Figure 4.15b and Figure 4.15c) the liquid film that was formed during bubble formation subsequently dissipated, leading to dry-out.
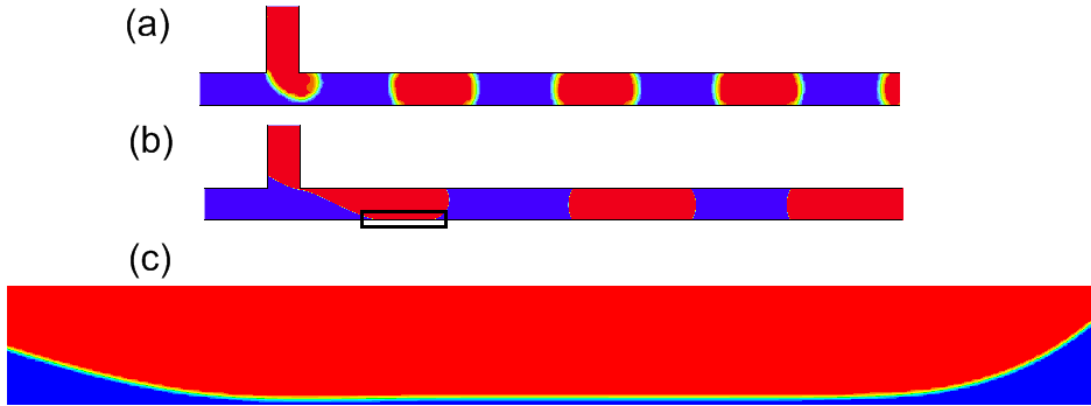
Figure 4.15: Contours of gas void fraction (red) obtained from VOF model for (a) coarse mesh (D/10) (b) fine mesh (D/250) (c) thin-film region shown in (b).

The absence of liquid film at the top channel wall is justified due to the two-dimensional nature of the present simulation which lacks wall continuity from the top to bottom. Fluid flow in a three-dimensional domain is enclosed by a continuous wall, as is the case in a circular pipe or duct. This was also explained by Krishnan et al. (2010) as the reason they did not obtain three-dimensional flow patterns such as churn flow, Taylor-annular flow, and annular flow by two-dimensional modeling. The inlet configuration is believed to play a significant role with respect to this point. Cross-flow and T-junction inlets are not best represented in two dimensions. The flow-focusing inlet is slightly better under some conditions in terms of its ability to simulate the liquid film (Yu et al., 2007). Likewise, the annular inlet in the study of Gupta et al. (2009) provides for the presence of a liquid phase above the gas bubble at the inlet itself, and this is probably the reason for its ability to capture the liquid film.

From the foregoing discussions, it is clear that a high resolution grid is essential for capturing the liquid film. Given the success of Gupta et al. (2009) in capturing the liquid film with a highly resolved two-dimensional domain for their annular inlet

configuration, it is quite likely that a highly resolved three-dimensional domain should be able to capture the liquid film with the present cross-flow inlet configuration. Additionally, modeling of a dynamically varying contact angle at the channel wall, and near wall flow models such as that developed by Thomas et al. (2010) using the front tracking method, requires further investigation with respect to the present Taylor flow problem. Studies based on such conditions are warranted for future works. Subsequent sections in this work based on the phase field method have carefully considered the possibility that the predicted results could be adversely affected by the unphysical dry-out at the channel wall.

4.3.9 Flow field in channel

4.3.9.1 Numerical predictions

The profiles of non-dimensional velocity across the channel width, U/U_{max}, extracted at an axial position corresponding to the center of the bubble, are reported in Figure 4.16. The superficial velocities of the gas and liquid phases were both 0.1 m/s. The velocity profiles obtained from the phase field model with both no-slip and wetted-wall (60°) boundary conditions were parabolic and characterized by a peak velocity at the exact center of the channel width i.e. Y/D=0.5. A similar result was obtained with the VOF model using a coarse mesh and wetted wall (60°) boundary condition. It is noted that all of the above cases were modeled using an element size of $D/10$ and the corresponding vectors of relative velocity are reported in Figure 4.17. Here, relative velocity was calculated as the difference between the magnitude of velocity, U, and the two-phase velocity, U_{TP}, wherein the latter was defined as the sum of the

superficial velocities of the liquid and gas phases (Liu et al., 2005). The results for all

three cases are similar and generally symmetric about the centerline. Two strong

recirculations were observed in the center of the bubble having anti-clockwise and

clockwise directions in the top and bottom half of the bubble, respectively. This

matches the findings of He and Kasagi (2008), who attributed it to the shear forces at

the wall which act in a direction against the flow. In addition, weaker recirculations

were observed at the frontal and rear ends of the bubble and the same can be

attributed to the weaker viscous forces. The bubble velocity, U_B, was calculated as the

velocity at the tip of the bubble nose, as suggested by Gupta et al. (2009) for

simulations that yielded a curved interface, and at the corresponding center-point with

a straight interface. The predicted bubble velocity for all cases was in close agreement

with the theoretical estimate from Eq. 4.12. This agreement, as suggested by Gupta et

al. (2009), indicated that the flow had close to a fully developed condition.

$$U_B = \frac{U_G}{\varepsilon_G} \tag{4.12}$$
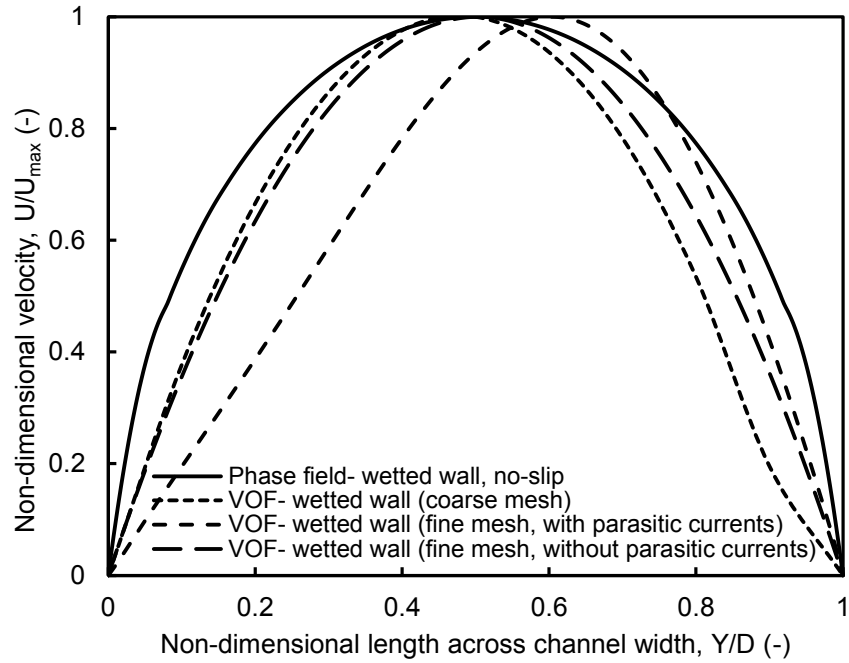
Figure 4.16: Variation of non-dimensional velocity across channel width with phase field and VOF models.
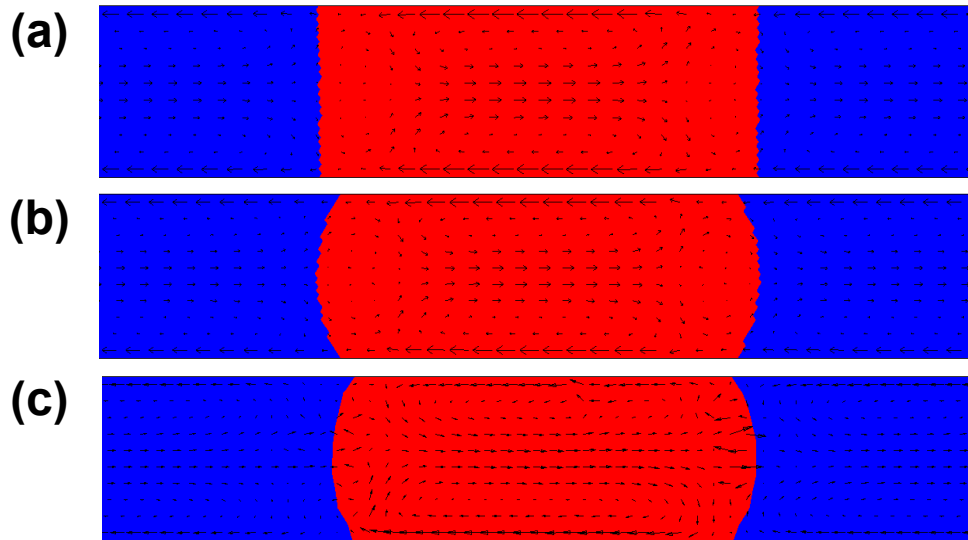
Figure 4.17: Vector of relative velocity superimposed on contours of gas void fraction (red) for results obtained with an element size of $D/10$ with (a) phase field model- no slip boundary condition (b) phase field model- wetted wall (60°) boundary condition (c) VOF model- wetted wall (60°) boundary condition (uniform scaling of vectors for all cases).

While the above results obtained with an element size of D/10 indicate the absence of any unphysical parasitic currents, this was not the case for the VOF-based results obtained with an element size of D/250 since unphysical recirculations were observed at certain instances of time. The two velocity profiles reported in Figure 4.16 obtained with the fine mesh were extracted at the axial center of the same bubble, and separated by a time interval of 2.1 ms. The case adversely affected by parasitic currents was characterized by an asymmetric velocity profile with a peak velocity at Y/D=0.6. The reason for this unphysical asymmetry was understood from the plot of relative velocity vectors in Figure 4.18a, wherein a strong recirculation was observed to be present towards the frontal end of the bubble and a weak recirculation was present in the center of the bubble, both of which are unphysical flow features. On the contrary, with the absence of parasitic currents, the relative velocity vectors reported in Figure 4.18b have physically realistic characteristics that are similar to those reported in Figure 4.17. It is worth noting that the CSF-based results of He and Kawagi (2008) were also characterized by unphysical parasitic currents resulting in additional recirculations within the gas bubble, while their phase field results were free of any unphysical flow features.
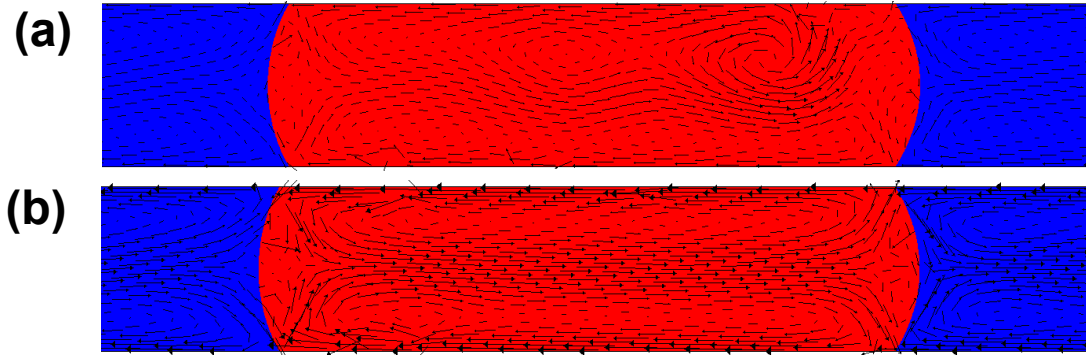
Figure 4.18: Vector of relative velocity superimposed on contours of gas void fraction (red) for results obtained with an element size of *D*/250 with VOF model for cases (a) with parasitic currents (b) without parasitic currents (uniform scaling of vectors for both cases; time interval of 2.1 ms between a and b).

4.3.9.2   Comparison with experimental data

The numerically predicted velocity profiles were compared with the experimental micro particle image velocimetry-based data of King et al. (2007). The available experimental data was for liquid-liquid Taylor flow involving water and FC-40 in a 762 μm channel, and hence the predicted results reported in Figure 4.19 were obtained with the above working fluids. King et al. (2007) demonstrated that the velocity gradients which result in a parabolic velocity profile during Taylor flow, as seen in Figure 4.16, are dominant only under certain conditions. Specifically, flows associated with low bulk velocity and short plug length, are characterized by minimal velocity gradients. Figure 4.19 compares the experimental and numerical velocity profiles for three cases. First, with a plug length of 7 mm and a high bulk velocity of 0.05 m/s, the experimental profile indicates the presence of strong velocity gradients which results in a parabolic profile. For this case, a reasonably good agreement was obtained between the experimental and numerically predicted profiles. For the same plug length (7 mm) and a lower bulk velocity of 0.005 m/s, the experimental velocity

profile indicates a marginal reduction in the gradient. Further, with a shorter plug

having a length of 2.5 mm and bulk velocity of 0.02 m/s, the gradients are

substantially lower, since U/U_{max} is close to unity throughout the channel width. For

both of the above cases, the numerical model was unable to predict a flow field with

reduced gradients. Instead, a parabolic profile was obtained for all cases. King et al.

(2007) remarked that the development of velocity gradients with short plugs and low

bulk velocities was restricted by the presence of the thin liquid film. According to

their study, under certain operating conditions, the presence of the thin film adjacent

to the channel wall could facilitate in the occurrence of a low velocity gradient within

the plug, thereby enabling the plug to behave like a 'solid body' moving along the

channel length. Consequently, it is clear that the dry-out predicted by the present

model is responsible for the failure to predict a flow field with low velocity gradients.
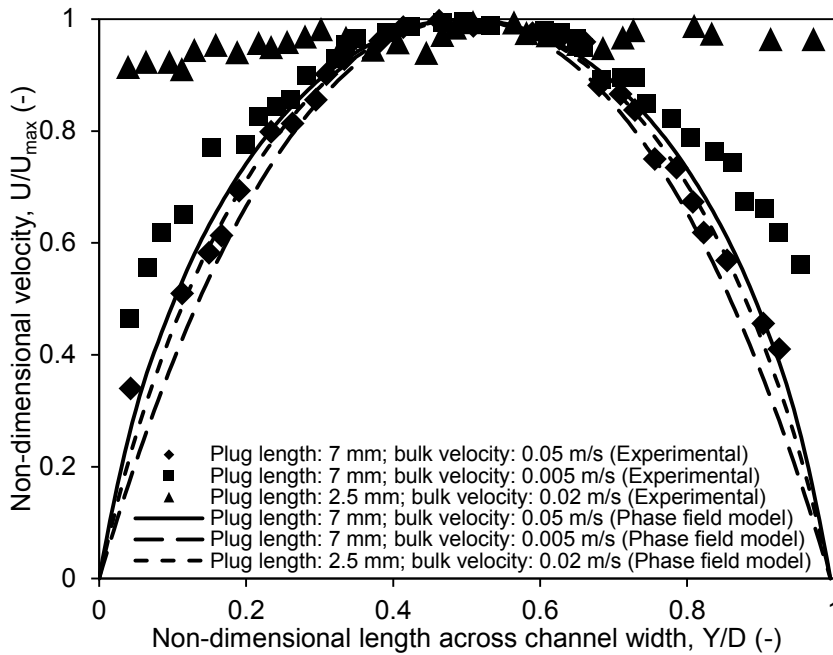
Figure 4.19: Comparison of profiles of non-dimensional velocity with experimental micro particle image velocimetry data of King et al. (2007).

4.3.10 Analysis of axial pressure profile

Numerically predicted axial pressure profiles obtained by the phase field method using different boundary conditions for the channel wall are reported in Figure 4.20 for gas and liquid phase superficial velocities of 0.1 m/s. Additionally, the profiles obtained with coarse and fine grid resolutions for the VOF model are reported. Unlike the previous section, wherein the flow field predicted by the VOF model with the fine grid (D/250) contained unphysical recirculations at certain instances of time (Figure 4.18), the associated pressure distribution for both the cases reported in Figure 7 did not involve any such anomalous differences. The cases modeled with no-slip and wetted-wall conditions yielded a negligible pressure drop per unit length in the gaseous phase (on account of its lower density) and a nearly constant pressure drop

per unit length in the liquid phase. These observations are consistent with the physics

of the flow. The numerically predicted pressure drop per unit length in the liquid

phase was higher than the Hagen-Poiseuille pressure drop for fully developed flow by

nearly 20%. Although an agreement on this has been reported in literature by

Kreutzer et al. (2005), this was clearly not the case in the present study and is

attributed to the presence of interfacial effects even in regions away from the

interface on account of the alternating gas and liquid phase pattern. Likewise, the

agreement in Kreutzer et al. (2005) could possibly be due to their use of a unit cell-

based computational domain in their study which typically considers only one gas

bubble and two liquid slugs.
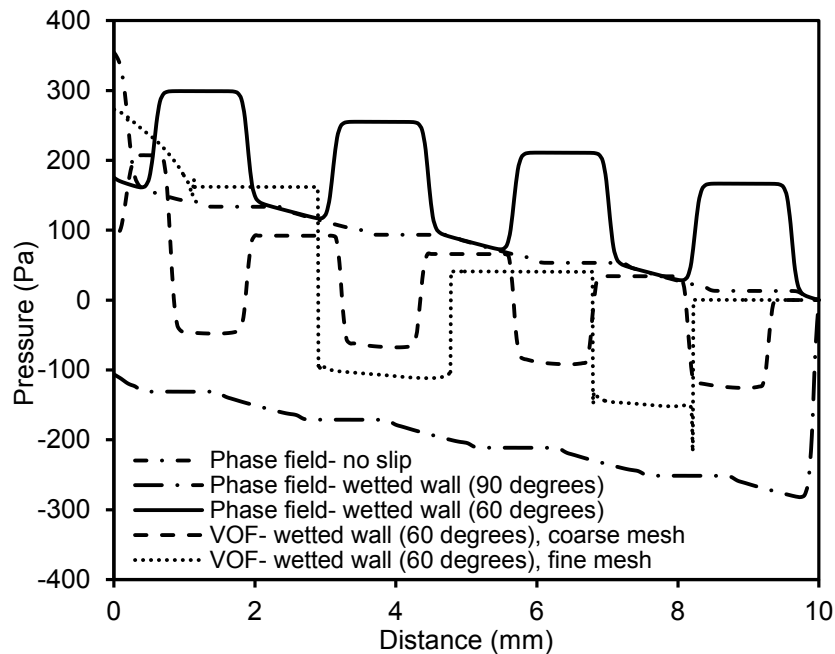
Figure 4.20: Variation of pressure (centerline) along length of channel with phase field and VOF models.

4.3.10.1 Laplace pressure

The Laplace pressure drop across the interface was found to be dependent on the curvature of the interface and hence a function of the defined contact angle. Consequently, the no-slip and wetted-wall with 90° contact angle cases, both characterized by minimal change in curvature across the interface, failed to predict both the jump and drop in pressure at the rear and frontal ends of the bubble, respectively. Although this failure can be explained by the small change in mean curvature, κ, across the interface for these cases, the net result, a lack of Laplace pressure drop, is clearly unrealistic in nature. Subsequently, increasing Laplace pressure drops were predicted for lower contact angles depending on the value of mean curvature, κ, for the respective case. As understood from the Youngs-Laplace equation (Eq. 4.13), it is this Laplace pressure drop that is responsible for the spherical nose curvature of a Taylor bubble.

$$\Delta P_{Laplace} = 2\sigma\kappa \qquad (4.13)$$

A comparison of the numerically predicted Laplace pressure difference across the interface with the corresponding results of the Youngs-Laplace equation, in which the effective mean curvature was considered to equal the minimum in curvature across the interface, indicated good agreement as shown in Figure 4.21. The compared cases are for different values of wall contact angle.
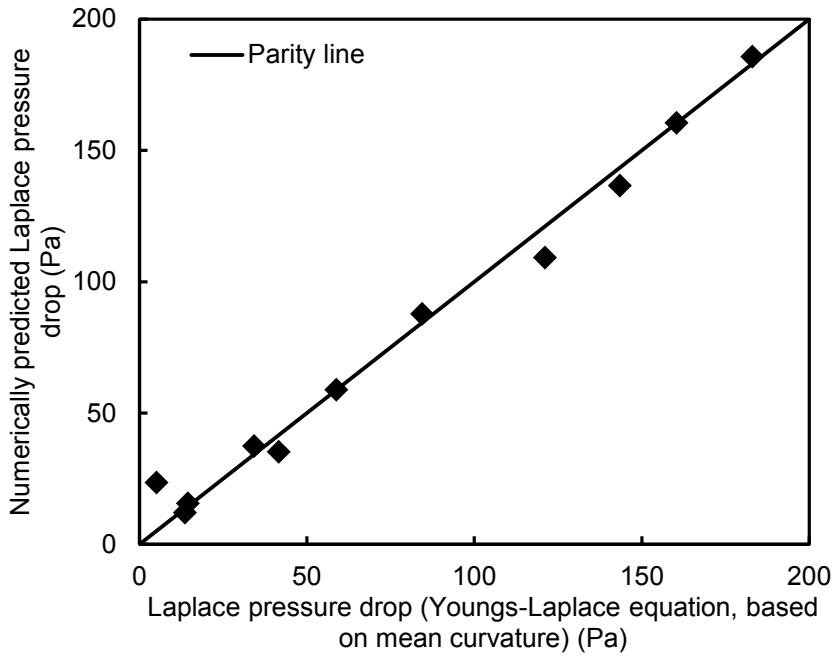
Figure 4.21: Comparison between numerically predicted Laplace pressure drop with that of Youngs-Laplace equation.

4.3.10.2 Pressure drop across unit cell

Using the Stokes-flow lubrication solution, Kreutzer et al. (2005) gave a modified form of Bretherton's expression for friction factor, Eq. 4.14, from which the pressure drop was estimated.

$$f = \frac{16}{\text{Re}}\left[1 + \lambda^*\left(\frac{D}{L_{slug}}\right)\left(\frac{\text{Re}}{\text{Ca}}\right)^{1/3}\right] \tag{4.14}$$

In the present study, the pressure drop across a unit cell was best represented by Eq. 4.14 with λ^* estimated by regression to equal 0.01. The literature contains varying values for λ^*, which are summarized in Table 4.2. Simulation-based values are generally lower than their experimental counterparts, and this has been attributed to

Marangoni effects on account of impurities that could be present in an experimental flow domain but generally remain unaccounted for in a numerical model. The value of λ^* obtained from the present simulations was of order of magnitude of 0.01. This is close to the value of 0.07 obtained from the simulations by Kreutzer et al. (2005) and Gupta et al. (2009). The slightly lower value obtained in the current work is believed to be a direct consequence of the dry-out condition at the channel wall as against both earlier modeling works in literature (Kreutzer et al., 2005 and Gupta et al., 2009), wherein the liquid film was also modeled.

Table 4.2: Summary of values of parameter λ^*.

Study	Description	Value of λ^*	Remarks on the value of λ^*
Kreutzer et al. (2005)	Experimental	0.17	Higher experimental based value attributed to interfacial impurities.
	Simulation (only liquid phase modeled)	0.07	
Walsh et al. (2009)	Experimental	0.12	Coincidentally, the average between experimental and simulation based values of Kreutzer et al. (2005).
Fries and von Rohr (2009)	Experimental	0.23, 0.21	Decrease of λ^* for increasing channel width was attributed to wall effects.
Gupta et al. (2009)	Simulation (VOF)	0.07	Agreement with simulation based value of Kreutzer et al. (2005).
Present work	Simulation (Phase field)	0.01	Similar order of magnitude as in the simulations of Kreutzer et al. (2005) and Gupta et al. (2009). The slightly lower value obtained in the present work than that reported in the above studies is attributed to dry-out at channel wall.

4.3.10.3 Oscillations in axial pressure profile

The axial pressure profiles shown in Figure 4.20 obtained by the phase field method indicate smooth changes in pressure at interfaces marked by the absence of any oscillations, apart from the physical Laplace pressure-based variations. The comparative VOF-based results indicate oscillations only with the fine mesh. While the literature presents varied findings in this regard, they are based primarily on numerical modeling and not verified through experimental data, which imposes a limit on their level of confidence. It is noted that with the VOF method, the cell-based gradient scheme has been shown to yield increased oscillations in pressure as compared to a node-based gradient scheme for the scalar variables (Gupta et al., 2009; Krishnan et al., 2010), and hence the latter was used in the present study.

First, the study by Gupta et al. (2009) based on the VOF model (they utilized high grid resolutions of at least $D/200$ and successfully captured the liquid film) reported oscillations in pressure at the interfaces. Second, the work of Krishnan et al. (2010), also based on the VOF model (they utilized less fine grids as compared to Gupta et al. (2009) having a resolution of $D/35$), and reported to have captured an unstable liquid film) reported oscillations in pressure at the interfaces. Third, Qian and Lawal (2006), again with the VOF model (they utilized relatively coarse grids and were unable to capture the liquid film) did not report oscillations in pressure at the interface. Our VOF model which was unable to capture a stable liquid film at low and high grid resolutions resulted in oscillations only with the latter case and this agrees with the reports in the literature as well. *Prima facie*, the logical explanation seems to be that

the grid-resolution rather than the liquid film determined the occurrence of these oscillations in pressure. However, Chen et al. (2009) with an alternative interface tracking model, the level-set method, and with grid resolutions of similar order of magnitude as that of Gupta et al. (2009), were able to capture the liquid film. Interestingly, their result for the pressure profile indicates minimal discontinuities at the interface.

Based on the above discussion, we conclude that reasoning based on factors such as grid resolution and the presence of the liquid film do not yield a universal agreement. An alternative factor that has not been considered above is the parasitic velocity currents. Depending on the magnitude, spurious velocity components can potentially result in unphysical instabilities and even destroy the interface (He and Kasagi, 2008). Hence, it would be reasonable to conclude that the absence of interfacial pressure oscillations in the present phase field-based results and in the level-set method-based results of Chen et al. (2009) could be a resulting effect of the reduced spurious velocity components of these two models. This would suggest that the phase field method, like the level-set method, would be an improvement over the VOF model. Nonetheless, future work reporting high resolution simulations of the phase field approach is warranted for a complete closure.

4.3.11 Effect of channel inlet configuration

There is limited understanding on the effect of inlet configuration in channels, in which the inlet has the same width as the main channel, since relatively few experimental studies have been reported considering different inlet designs. In the

present work, simulations were performed for various types of inlet configurations, as shown in Figure 4.22. The superficial velocities of the gas and liquid phases were both 0.1 m/s. For the cases involving multiple inlets for either phase (Figure 4.22c-f), the inlet velocity of that particular phase was halved in order to have equal net flow rates between all cases. This was justified since in a practical experiment a single manifold could supply the phase to both inlets, thereby halving the effective flow rate to either inlet. Further, it was assumed that a uniform distribution occurs between the two inlets, and hence any effects of maldistribution were neglected.
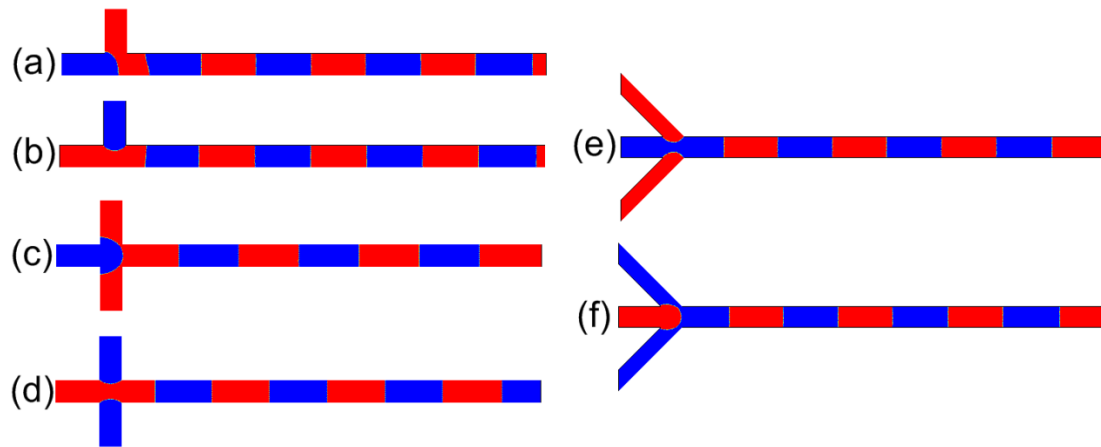
Figure 4.22: Bubble formation in microchannel having (a, b) cross flow inlet, (c, d) Flow focusing 90° inlet (e, f) flow focusing 60° inlet; (a, c, e) liquid phase inlet along main channel (b, d, f) gas phase inlet along main channel; contours of gas phase void fraction (red).

The non-dimensional bubble lengths (based on channel width) were compared. Between the two types of cross-flow inlet, i.e., liquid and gas phases along the main channel, respectively, the bubble length varied by less than 2%, as shown in Figure 4.22a and Figure 4.22b. However, Qian and Lawal (2006), from their simulations by the VOF method, reported an increase in the bubble and slug lengths of around 100%.

161

They hypothesized that in channels with the gas inlet along the main channel, the slug experiences difficulty in detaching from the inlet flow due to a smoother stream at the inlet mixing section.

We explain the discrepancy between the present study and Qian and Lawal (2006) as follows. The dominant mechanism responsible for bubble detachment was similar in both cases of the cross-flow inlet with gas or liquid along the main channel: the build-up of pressure in the liquid phase when a newly evolved gas bubble occupies the entire channel cross section and subsequently detaches. A volumetric flow ratio of unity was used in a channel having characteristic dimension of 500 μm, which is similar to the conditions of Qian and Lawal (2006). Figure 4.23 shows the pressure variation at the liquid phase inlet, which was observed to be discontinuous. There is a peak in pressure when the bubble evolves and occupies increasing fractions of the channel width followed by a drop in pressure when the liquid phase contributes to the necking process. This is in agreement with the theory described by Yue et al. (2008), indicating that the liquid phase alone is not responsible for Taylor bubble detachment. Thus, it can be hypothesized that, in the transient simulation, the rises in pressure are observed at times when the gas phase contribution is dominant, and the drops in pressure are observed at times when the liquid phase necking plays a dominant role. Similar trends were seen for the other inlet configurations as well.
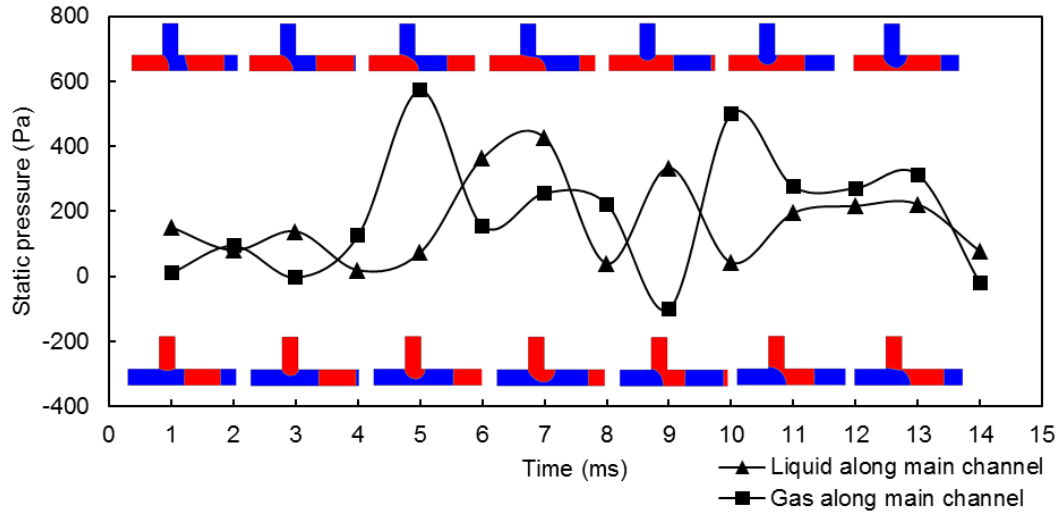
Figure 4.23: Transient variation of pressure at the liquid phase inlet for cross flow inlet with liquid and gas phase along the main channel; contours of gas void fraction (red).

Between the different inlet configurations, with only a change in the phase being injected along the main channel, i.e. Figure 4.22a, Figure 4.22c, Figure 4.22e and Figure 4.22b, Figure 4.22d, Figure 4.22f, small variations of up to 8% were seen. This matches with the experimental findings of Shao et al. (2008), which indicated that for constant inlet dimensions (with varying configurations) the bubble lengths were nearly constant. Their work compares with the cases in Figure 4.22d and Figure 4.22f in the present study.

The present flow ratio of unity was chosen due to its similarity to Qian and Lawal (2006) and resulted in nearly equal gas bubble and liquid slug lengths. As a check, the study was further extended to alternative flow ratios of 0.5 and 2 (U_L=0.2 m/s, U_G=0.1 m/s and U_L=0.05 m/s, U_G=0.1 m/s), from which it is concluded that all configurations result in very similar flow characteristics in terms of bubble/slug lengths and bubble formation times.

163

4.3.12 Effect of inlet width

The width of the inlet was varied from 0.5 to 2 times the channel width for a T-junction inlet configuration (similar to the study by Qian and Lawal, 2006). The superficial velocities of the gas and liquid phases were both 0.1 m/s. As reported in their study, the variation in simulated bubble lengths observed in Figure 4.24 is due to the altered flow field at the inlet, particularly with respect to larger velocity gradients (referred to in their study as toroidal velocity) in smaller inlet to channel width ratios.
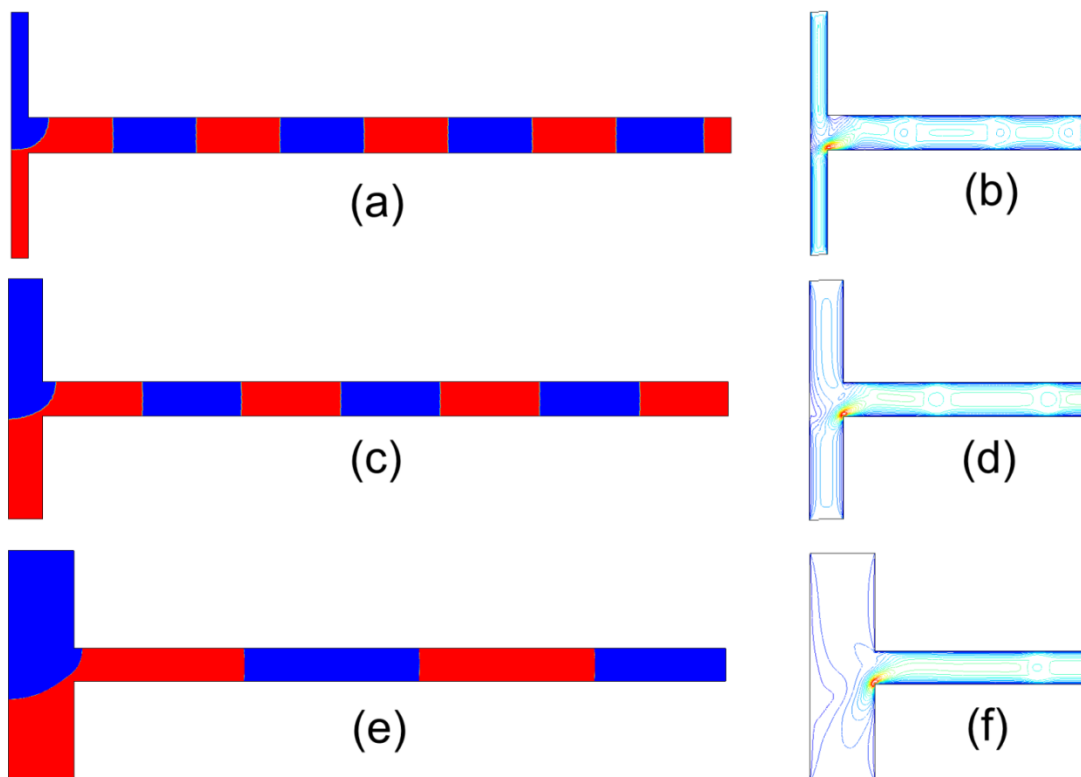
Figure 4.24: Variation of bubble length with inlet size (a, b) D/2 (c, d) D (e, f) 2D; contours of gas phase void fraction (red); streamlines of velocity field (uniform leveling in each case).

4.4 Chapter conclusions

This chapter presented CFD simulations of Taylor flow in mini/microchannels by the phase field method. Channels having characteristic dimensions ranging from 100 to 500 μm were modeled with a cross-flow inlet configuration. Taylor bubble formation was studied in order to identify the dominant mechanisms responsible for bubble detachment. The dripping regime was found to be characterized by marginal pressure forces and stronger shear forces, which agreed favorably with the literature. For the squeezing regime, an agreement with the literature was reached on pressure being the dominant factor responsible for bubble detachment. However, rather than a singular rise in pressure followed by a drop, multiple pressure fluctuations were observed, based on which a modified theory was proposed.

The dependence of the solution on the user-defined mobility and interface thickness parameters present in the phase field governing equations was analyzed with respect to characteristic features of the Taylor flow regime. The spatial discretization of the domain was given due consideration to ensure that the interface was sufficiently resolved for the chosen value of the interface thickness parameter. A sequential increase in the value of mobility indicated that the Taylor bubble formation mechanism was initially through the dripping mechanism and later through the squeezing mechanism. With increasing mobility, the surface tension force field was found to be suitably altered to yield increasingly longer bubbles. This was reported to be an advantage of the phase field method over alternate approaches, such as the VOF model, in terms of the ability to simulate multiple bubble lengths under constant flow

conditions while conforming to the physics of homogeneous two-phase flow. The numerically predicted bubble lengths were compared against empirical correlations as well as available experimental data in the literature.

The gas void fraction was compared against results reported in multiple experimental studies. The present phase field results indicated a linear variation of gas void fraction with respect to volumetric flow ratio, for all channel dimensions considered, and this is in agreement to some of works in the literature. Additional experimental work was recommended in order to provide a complete understanding of this aspect of Taylor flow. Modeling of the effects of adhesion at the channel wall was investigated in detail. The phase field method yielded bubble profiles that were consistent with the specified value of wall contact angle. This is an improvement over previous studies reported based on a similar phase field approach and conforms with results from alternate models as well.

An actively pursued objective in Taylor flow simulation is capturing the thin liquid film between the bubble and the channel wall. The varying results reported in the literature were reviewed in detail. The present phase field simulations as well as high-resolution VOF-based simulations were both found to be unsuccessful in this regard. It was inferred from the current findings that a highly resolved, three-dimensional domain may be the most successful method for capturing the liquid film. The numerically predicted flow field from the phase field model was found to be free of unphysical parasitic currents, while the VOF-based results obtained with the highly resolved domain were adversely affected by unphysical recirculations with the gas

166

bubble. The velocity profiles across the channel width were compared with available micro particle image velocimetry data from the literature. The predicted parabolic profile was in good agreement with the experimental data for the cases associated with strong velocity gradients. However, the phase field model failed to accurately capture the flow field associated with low bulk velocities and short plug lengths, which are characterized by minimal velocity gradients, on account of the dry-out at the channel wall. The pressure distribution in the channel predicted by the phase field model did not involve any unphysical interfacial oscillations in pressure that were shown to be present with the VOF model. Lastly, studies relating to bubble formation and the effect of the channel inlet were reported and discussed. Subsequent chapters in this thesis have utilized the presently investigated phase field and volume of fluid models to simulate heat/mass transfer in microscale two-phase flow systems.

Chapter 5: Decoupled Numerical Formulation for Modeling Reactive Mass Transfer across Non-Deforming (Fixed) Interfaces during Taylor Flow in Microreactors

5.1 Introduction

Gas-liquid absorption can be substantially enhanced using microreactors. Certain mass transfer applications such as carbon capture which are associated with relatively low gas phase concentration levels result in minimal changes to the gas-liquid interfacial profile as a result of the transport phenomena. For instance, during Taylor flow involving such systems, the bubble volume would change by a negligible amount, thus enabling the decoupling of the governing equations for the flow hydrodynamics from those for mass transfer to reduce the computational cost. This chapter proposes a decoupled numerical approach to simulate gas-liquid mass transfer with chemical reactions during Taylor flow in mini/microchannel reactors. In this approach, the hydrodynamics of the flow are decoupled from the mass transport phenomena. The modeling methodology that governs the hydrodynamics of two-phase flow and the mass transfer phenomena is based on purely theoretical (non-empirical) approaches. The computational domain considers an entire microreactor that includes the channel length as well as the inlet mixing region in order to investigate the contribution of the inlet mixing region to the overall mass transfer. The numerical predictions are validated with experimental and theoretical data

reported in the literature. Parametric studies varying the phase concentration, channel size, wall contact angle and temperature are performed and discussed.

5.2 Numerical model

The presently proposed approach decouples the hydrodynamics of two-phase flow from the mass transfer phenomena. Accordingly, the governing equations for each process were separately solved. A diffuse interface model, the phase field method, was used to simulate the fluid flow, as reported in Section 5.2.1. For the reaction system detailed in Section 5.2.2, the mass transfer across the interface of the Taylor bubbles was simulated using the formulation reported in Section 5.2.3.

5.2.1 Modeling of two-phase flow

Various models have been developed for multiphase systems and have been applied towards two-phase flow in both minichannels and microchannels. The VOF method (Hirt and Nichols, 1981), which has proven to be the most popular, and the level set method (Osher and Sethian, 1988; Sussman et al., 1994), belong to the class of diffuse-interface modeling approaches. They are primarily based on the approximation of surface tension forces in the interfacial region as a body force, using the continuum surface force (CSF) formulation of Brackbill et al. (1992). These approaches have been implemented in numerous studies including Taha and Cui (2004), Qian and Lawal (2006), Liu and Wang (2008), Kumar et al. (2007), Carlson et al. (2008), Fang et al. (2008), Lakhehal et al. (2008), Chen et al. (2009), Gupta et al. (2009), Krishnan et al. (2010), Santos and Kawaji (2010), Asadolahi et al. (2011, 2012. The phase-field method also belongs to the class of diffuse interface techniques

but governs the interface based on the fluid free energy. The free energy density is comprised of the gradient energy and the bulk energy density (van der Waals, 1893). Cahn and Hilliard (1959) defined the phase-field variable, ϕ, which is considered as a measure of phase. It assumes two distinct values in either phase and undergoes a rapid smooth change across the interface. In the interfacial region, the two phases are considered to be mixed and are thereby associated with a mixing energy.

Parasitic or spurious currents are the unphysical velocity components at the interface (Lafaurie et al., 1994). These currents are an important issue in the modeling of multiphase flow, especially while using the CSF formulation which forms the basis for the VOF model. The currents are generated in the near-interface regions on account of local variations in the CSF body force, which is essentially an approximation of the surface tension forces in this region. At higher magnitudes, the parasitic currents can potentially destroy the interface and thereby adversely affect the hydrodynamics of the flow. Recent works by De Menech (2006) and He and Kasagi (2008) have demonstrated that phase field modeling can significantly reduce the magnitude of parasitic currents. This has been attributed to the appropriate transfer of the initially generated energy due to the discretization error, between the kinetic energy and the surface tension energy, which is further dissipated as viscosity. On account of this improved accuracy, the phase field model has been utilized in the present work for modeling two-phase flow and the governing equations for the same, as derived by Yue et al. (2004), are reviewed below.

The hydrodynamics of two-phase flow are described by the equation for continuity (Eq. 5.1) and incompressible Navier-Stokes equation (Eq. 5.2).

$$\nabla \cdot \mathbf{U} = 0 \tag{5.1}$$

$$\rho \frac{\partial \mathbf{U}}{\partial t} + \rho(\mathbf{U}.\nabla)\mathbf{U} = \nabla.\left[-P\mathbf{I} + \mu\left(\nabla\mathbf{U} + \nabla\mathbf{U}'\right)\right] + \mathbf{F}_g + \mathbf{F}_{ST} \tag{5.2}$$

The Eötvös number criterion of Brauner and Moalem-Maron (1992), Eö $< (2\pi)^2$, was used to verify that for any given condition, the surface tension forces were indeed dominant over gravitational forces and hence the latter could be neglected. Surface tension was modeled as a body force (F_{ST}) in the momentum equation. Two second-order partial differential equations are given by Eqs. 5.3 and 5.4, wherein ϕ is the phase field variable that governs the interface. As a convention, in the present study ϕ was chosen to equal -1 in the pure gas phase and +1 in pure liquid phase.

$$\frac{\partial \phi}{\partial t} + \mathbf{U}.\nabla\phi = \nabla.\frac{\gamma\lambda}{\xi^2}\nabla\psi \tag{5.3}$$

$$\psi = -\nabla.\xi^2\nabla\phi + \left(\phi^2 - 1\right)\phi + \left(\frac{\xi^2}{\lambda}\right)\frac{\partial f_{ext}}{\partial\phi} \tag{5.4}$$

In the above equations, λ is the magnitude of mixing energy and ξ scales with the thickness of the interface. The time scale of the Cahn-Hilliard diffusion is determined by γ as defined by Eq. 5.5. It is a function of two user-defined parameters: mobility, χ, and interface thickness, ξ.

$$\gamma = \chi\xi^2 \tag{5.5}$$

Suitable values for the mobility and interface thickness parameters, χ and ξ, respectively, were chosen to obtain a suitable time scale of diffusion that did not excessively damp the convective motion and yet retained a constant interfacial thickness (Jacqmin, 1999). Likewise, sufficient diffusion was recommended to be present to resist straining flows that thin or thicken the interface.

The effect of surface tension was modeled as a body force, F_{ST}, in the equation for conservation of momentum (Eq. 5.2). It was computed as the product of the chemical potential of the system, G, and the gradient of the phase-field variable, ϕ.

$$F_{ST} = G.\nabla\phi \tag{5.6}$$

$$G = \lambda\left[-\nabla^2\phi + \frac{\phi(\phi^2-1)}{\xi^2}\right] \tag{5.7}$$

The scaling relation given by Eq. 5.8 was used to obtain the volume fraction of either phase, which takes values from 0 to 1. The effective fluid properties such as density and viscosity were computed as the average value of the two phases weighed by their respective volume fractions obtained from Eq. 5.8.

$$\varepsilon = \begin{cases} \dfrac{1-\phi}{2} & : \text{Gas phase} \\[2mm] \dfrac{1+\phi}{2} & : \text{Liquid phase} \end{cases} \tag{5.8}$$

A schematic of the computational domain is reported in Figure 5.1. A 2-D geometry was used in the present study on account of its reduced computational cost as compared to a 3-D geometry, and the same is justified as follows. Qian and Lawal (2006) compared Taylor flow simulations obtained using 2-D and 3-D domains. The gas bubble and liquid slug lengths were compared and negligible differences were reported. Subsequently, Krishnan et al. (2010) also utilized 2-D domains in their simulations of Taylor flow. However, 3-D computational domains yield improved accuracy, particularly with respect to the pressure and velocity distribution in the channel which influences the heat/mass transport phenomena. For instance, the Laplace pressure drop is higher in 3-D domain-based results, as compared to 2-D domain-based results on account of the different radii of curvature. However, this was not an issue in the present mass transfer results since the hydrodynamics were decoupled from the mass transfer.
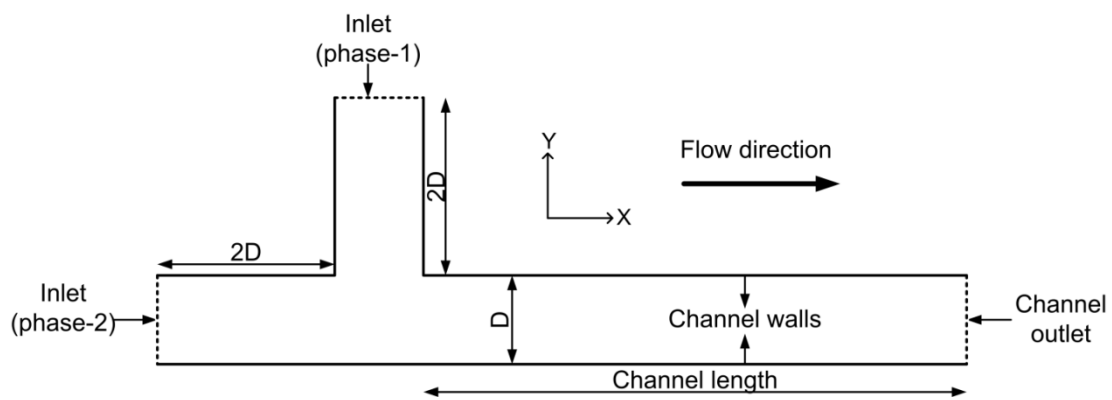
Figure 5.1: Schematic of computational domain.

The entire 2-D domain was discretized with a homogeneous unstructured grid consisting of triangular elements. To maintain a constant resolution of the interface

173

throughout the channel, the entire domain was discretized using the similar sized elements making it impossible to use block-structuring to obtain a high resolution near the channel walls. By monitoring the gas bubble and liquid slug lengths, a non-dimensional element size of $D/10$, wherein D is the characteristic dimension of the channel, was found to yield grid-independent results. It is noted that grid-independence analysis with the phase field method requires consideration of the element size, j, and the interface thickness parameter, ξ. This was investigated for a similar case of Taylor flow, based on the j/ξ ratio (Chapter 4). A value of unity for this ratio was found to yield grid independent results and accordingly, the same has been used in the present chapter as well.

The inlets were modeled with a constant velocity boundary condition with a single phase being admitted through each inlet. A pressure-based outflow boundary condition was specified at the channel outlet, which applied a Dirichlet condition on the pressure. A no-slip condition was specified on the channel walls. Additionally, the effect of contact angle was studied in Section 5.3.5 by specifying an angle, θ, in Eq. 5.9 which alters the interface normal at the channel wall based on the value of contact angle specified in the boundary condition.

$$\mathbf{n}.\xi^2\nabla\phi = \xi^2\,\tan\left(\frac{\pi}{2} - \theta\right) \times \left|\nabla\phi - (\mathbf{n}.\nabla\phi)\mathbf{n}\right| \tag{5.9}$$

The wetted-wall condition given by Eq. 5.9 specifies no-slip (zero velocity) at the wall. For those simulation runs where the wetting behavior was not modeled, the

interface was assumed to be normal to the channel wall and hence for θ equaling 90°, the right-hand side of Eq. 5.9 becomes zero.

5.2.2 Chemical reaction system

The chemical reactions considered are between a gaseous mixture of CO_2 and N_2 with an aqueous solution of NaOH and follow the following steps.

$$CO_{2(G)} \leftrightarrow CO_{2(L)} \tag{5.10}$$

$$CO_{2(L)} + OH^- \leftrightarrow HCO_3^- \tag{5.11}$$

$$HCO_3^- + OH^- \leftrightarrow CO_3^{2-} + H_2O \tag{5.12}$$
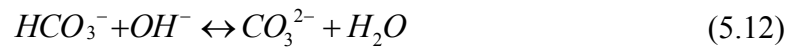
The overall reaction for the above system is given as:

$$CO_2 + 2NaOH \rightarrow Na_2CO_3 + H_2O \tag{5.13}$$
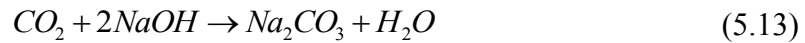
Modeling of the mass transfer in the above system requires the expression for the rate of the reaction to be determined from the reaction kinetics. While the major points are outlined here, the reader is referred to Zanfir et al. (2005) for a complete description. The first step, the dissolution of gaseous CO_2 into the liquid solution, has a high process rate and hence the equilibrium at the interface is described by Henry's law (Danckwerts, 1970). The value of Henry's constant in Eq. 5.14 pertains to the solubility of CO_2 in aqueous NaOH solution. It is obtained from Eq. 5.15 which relates the Henry's law constant in the solution to that in water at the same temperature. The summation in Eq. 5.15 is over all the ions, i, present in the solution.

The parameters h_i and h_G refer to the ions and the absorbed gas in the liquid phase respectively and their values, as given by Schumpe (1993), are reported in Table 5.1. The equilibrium solubility of CO_2 in water was reported by Crovetto (1991).

$$C^*_{CO_{2(L)}} = H \cdot p_{CO_2} \qquad (5.14)$$

$$\log_{10}\left(\frac{H}{H_{water}}\right) = -\sum_i (h_i + h_G)C_i \qquad (5.15)$$

Table 5.1: Values of parameters in Eq. 5.15 (Schumpe, 1993).

i	Component	h_i (m³/mol) (x10⁻³)
1	Na^+	0.1171
2	OH^-	0.0756
3	HCO_3^-	0.1372
4	CO_3^{2-}	0.1666
G	$CO_{2(L)}$	-0.0183

In the above reaction system, Eq. 5.10 is almost instantaneous, and Eq. 5.12, an ionic reaction, also has a significantly high rate of reaction. Thus, the overall rate of reaction is governed by Eq. 5.11 and follows second-order kinetics. The rate equation for the process is given by Eq. 5.16, in which the equilibrium constant k_{OH^-}, as given by Pohorecki and Moniuk (1988), is given by Eq. 5.17. The ionic strength of the solution, I, is given by Eq. 5.18 and is obtained by considering the concentration and valence of the various ions present in the solution.

$$R = k_{OH^-}C_{OH^-}C_{CO_2} \qquad (5.16)$$

$$\log_{10}\left(k_{OH^-}\right) = 11.916 - \frac{2382}{T} + \left(0.221 \times I\right) - \left(0.016 \times I^2\right) \tag{5.17}$$

$$I = 0.5 \sum_i C_i z_i^2 \tag{5.18}$$

The reaction rate was obtained by solving Eqs. 5.14-5.18 simultaneously (Zanfir et al., 2005; Shao et al., 2010).

5.2.3 Mass transfer model

The numerical model considered the mass transfer occurring between the gas bubble and the liquid slug. The study by Tan et al. (2012a) which reported transient measurements of gas bubble length and volume indicated a decrease in these quantities over time as a result of the absorption process. However, the present model did not account for interfacial deformations due to mass transfer. In other words, the change in bubble volume was assumed to be negligible, as suggested by Shao et al. (2010). The assumption is justified only in mass transfer systems involving a small fraction of the gas being transferred out of the bubble, across the interface, into the liquid phase. This limits the application of the present model to processes involving low gas phase concentrations, some of which are reviewed subsequently.

Sweetening of natural gas is a process that involves the absorption of CO_2 and H_2S from a sour gas mixture, and the concentration of the above components depends upon the source of the gas. The CO_2 concentration in natural gas from most common gas fields can range between 0.7-8% (Kohl and Nielson, 1997), 8.3% (Leal et al., 1996), 13% (Alonso, 2010), and 5% (Socolow et al., 2010), while the H_2S

concentration can commonly range between 2.1-16.5% (Kohl and Nielson, 1997), and 10% (ConocoPhillips, 2012). Post-combustion capture systems involve the absorption of CO_2 from flue gas streams produced by the burning of fossil fuels. The CO_2 concentration in the gas stream varies depending upon various factors including the operating conditions and the nature of the fuel being used. This has been estimated to range between 12-14% for coal fired boilers and integrated gasification combined cycle, 11-13% for oil fired boilers, 3-4% for gas turbines, and 7-10% for natural gas fired boilers (Metz et al., 2005). Likewise, Katzer et al. (2007) and Socolow et al. (2011) estimated that between 10-15% CO_2 is present in flue gas produced by the combustion of coal. Natural gas is a relatively cleaner fuel for which the CO_2 concentration in the flue gas is between 3-5% (Socolow et al., 2011). Direct capture of carbon dioxide from air is associated with a low gas concentration of about 0.04% (Socolow et al., 2010).

Several industrial gas streams require processing to remove volatile organic compounds (VOCs) and other polluting gases that are present in relatively low, yet harmful concentrations. Examples include benzene, carbon tetrachloride, methanol, and toluene, each ranging between 0.05-0.5% concentration (Ozturk and Yilmaz, 2006), H_2S or mercaptans ranging between 0.006-0.01% concentration (Blaszczak et al., 1995), and NO_X ranging between 0.02-0.2% concentration (Yasuda et al., 2011). Lastly, the direct fluorination of aromatic compounds such as toluene is often performed using low concentrations of fluorine gas mixed with nitrogen at levels ranging from 1-10% (de Mas et al., 2001) and 10% (Chambers et al., 2001), in order to control the highly exothermic nature of the reaction.

The above processes, under certain conditions, can serve as potential applications for the presently developed numerical model. However, it must be noted that the ranges reported here serve merely as reference levels. Individual instances may involve higher or lower levels of gas phase concentration, and the present modeling assumption becomes less valid for higher gas concentrations. For this reason, relatively low CO_2 concentration levels ranging from 1-10% were used in the parametric studies (Sections 5.3.2-5.3.6). Likewise, Shao et al. (2010) utilized a CO_2 concentration of 5% in their parametric studies as well. Hence, the modeling assumption that the hydrodynamics of the flow is negligibly affected by the mass transfer process is justified for such cases.

The computational domain for the mass transfer was obtained by the following procedure. First, the exact location of the interface was obtained from the two-phase flow patterns simulated in Section 5.2.1. The interface was fixed at a phase volume fraction of 0.5, as suggested by He and Kasagi (2008). The flow pattern was processed based on the phase field variable, ϕ, to create separate regions (sub-domains) for each phase. The boundary between the two regions was the interface, and the mass transfer was modeled to occur across this boundary line. Since the two-phase flow model did not accurately capture the thin liquid film between the gas bubble and channel wall, the channel boundary was slightly offset from the gas bubble in order to create this thin film. The offset was quantified such that the resulting film thickness was in accordance with the expression by Aussilous and Quere (2000), given by Eq. 5.19. The resulting change in the reactor volume was negligible since the thickness of the liquid film was of the order of only a few

micrometers in length. A schematic of the Taylor flow results obtained from the phase field method is reported in Figure 5.2a, wherein there is no liquid film at the channel wall. Subsequently, Figure 5.2b reports the result obtained after implementing the channel wall offset to create the liquid film. It is noted that this offset procedure does not alter the angle θ.

$$\delta = \frac{0.66Ca^{2/3}}{1+3.33Ca^{2/3}}D \tag{5.19}$$

The above-described procedure, when implemented, resulted in a computational domain for modeling the mass transfer. The domain consisted of an entire channel, including the inlet mixing region, with several gas bubbles and liquid slugs at intermittent intervals. Having obtained fully formed Taylor bubbles, as well as emerging Taylor bubbles in the inlet region, we modeled the mass transfer following an approach similar to Shao et al. (2010) which is described below.
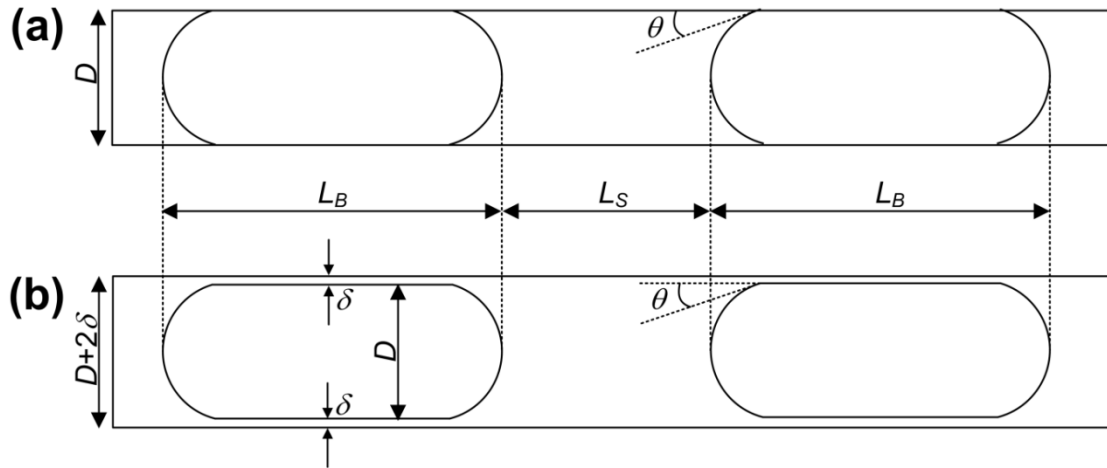
Figure 5.2: Schematic diagram of Taylor flow (a) phase field simulation result without thin liquid film (b) computational domain for mass transfer after implementing channel wall offset to account for thickness of liquid film, δ.

The convection-diffusion mass transfer equations following the general form given by Eq. 5.20 was solved for both phases for the reactants CO_2 and OH^-.

$$\frac{\partial C}{\partial t} + \nabla.\left(-d.\nabla C\right) = R - U.\nabla C \qquad (5.20)$$

The boundary conditions applied for the two reacting species, CO_2 and OH^-, were different. For CO_2, at the interface in the gas bubbles, the concentration of the gas as obtained at each time step was specified. In the liquid slugs, Henry's law was applied, which accounted for the discontinuous concentrations of CO_2 in the gas and liquid phases (Shao et al., 2010). For OH^-, a convective flux boundary condition was assumed along the interface in both the gas and liquid phase, which assumed that the mass flux of this specie due to diffusion is zero. The wall was insulated from the transport of species.

Domain discretization was performed using an unstructured grid consisting of triangular elements. Successive levels of mesh refinement indicated that the mass transfer characteristics were less sensitive to element size in the interiors of the liquid slugs and gas bubbles, as compared to the interfacial regions. Grid independent results were obtained by resolving the interior regions with non-dimensional element sizes of $D/10$ wherein D refers to the characteristic dimension of the channel. However, the interfacial regions required resolution levels between $D/100$ to $D/200$, which is at least an order of magnitude higher than the rest of the computational domain. Similar high interfacial grid resolutions were also reported by Shao et al. (2010) for their unit cell model.

181

It is worth noting that the mass transfer model did not involve an interface tracking algorithm and as a result, it was possible to use varying element sizes in the channel and therefore minimize the computational time. This is believed to be a primary advantage of developing decoupled approaches that separate the hydrodynamics of the multiphase flow from the mass transfer because the use of interface tracking algorithms necessitates the use of a constant element size in order to maintain a constant interface resolution throughout the computational domain. In other words, the currently proposed modeling methodology is a computationally inexpensive, purely theoretical (non-empirical) approach for simulating reactive mass transfer characteristics in microchannel geometries.

5.2.4   Solver settings

The numerical model was implemented using a commercial CFD code, COMSOL Multiphysics (COMSOL Inc., Burlington, MA), version 3.5a, which is based on the finite element method. An implicit time-stepping algorithm was used with residual tolerance levels of 10^{-4}. This was verified to be sufficient, since like solutions were obtained at lower tolerance levels too. All simulations were carried out on a Dell workstation comprising two Intel Xeon processors with eight cores and 4 GB of RAM.

For modeling of the two-phase flow, the phase-field variables were initialized by selectively solving for ϕ and ψ. This transient initialization run was used to define the initial interface. Since the channel was assumed to be initially filled with quiescent gaseous phase, the initial interface was formed at the liquid inlet. It was ensured for

182

every simulation that the interface created by the initialization procedure was monotonic and the phase field variable, ϕ, was always within the allowed range of -1 to $+1$. The final transient simulation was solved for all the governing equations using the initial values obtained above.

For modeling the mass transfer phenomena, the governing equations for both phases were solved simultaneously as suggested by Shao et al. (2010). This continuously updated the species concentration at the interface and resulted in a realistic prediction of the mass transfer.

5.3 RESULTS AND DISCUSSION

5.3.1 Validation of model

The modeling methodology adopted in the present study tied the predictive accuracy of the mass transfer model to that of the two-phase flow model. Both were validated as described below.

Two-phase flow simulations of Taylor flow were performed with nitrogen as the gas phase and water as the liquid phase. The gas void fraction averaged over an entire bubble formation cycle was estimated for channels having a characteristic dimension of 100, 250 and 500 μm. The same was compared with the predictions of the homogeneous model (Eq. 5.21) and the Armand correlation (Eq. 5.22) (Armand and Treschev, 1946).

$$\varepsilon_G = \beta_G = \frac{U_G}{U_G + U_L} \qquad (5.21)$$

$$\varepsilon_G = 0.833\beta_G \qquad (5.22)$$

The results of gas void fraction are reported in Figure 5.3 and a good agreement was obtained with the homogeneous flow model and the Armand and Treschev (1946) expression. Similar findings have been reported in numerous earlier works as well (Zhao and Bi, 2001; Serizawa et al., 2002; Chung and Kawaji, 2004; He and Kasagi, 2008; and Yue et al., 2008).
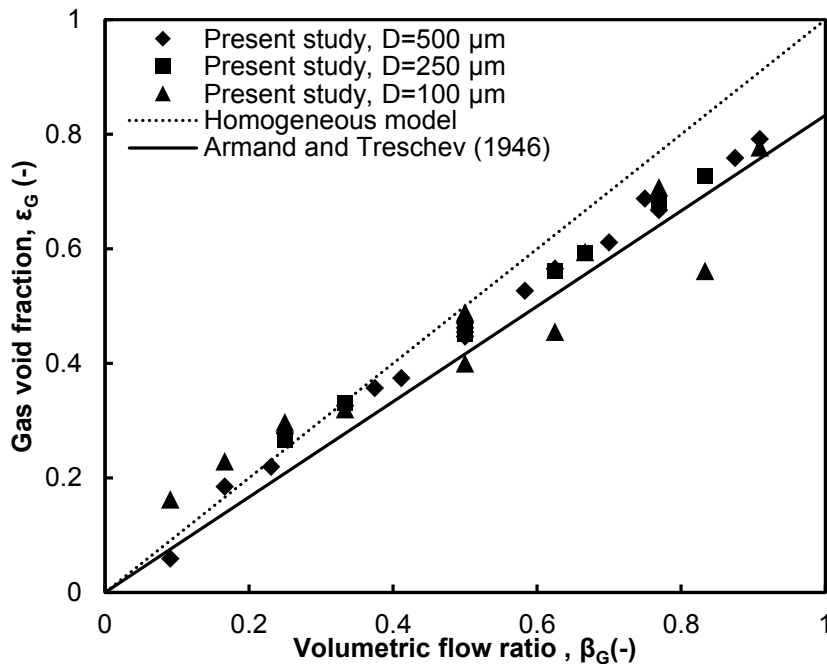
Figure 5.3: Comparison of numerically predicted gas void fraction with correlations in the literature for nitrogen-water Taylor flow (D: 100, 250 and 500 μm).

The results of the mass transfer model were validated using the experimental data of Shao et al. (2010) for a similar system and the predictions of their unit cell model.

The inlet mixing region was modified from the cross-flow configuration shown in Figure 5.1 to a flow-focusing inlet configuration, as used by Shao et al. (2010), wherein a single gas phase inlet was smoothly flanked between two liquid phase inlets. The gas phase was comprised of CO_2 gas at a concentration of 23% by volume in a mixture with nitrogen and the liquid phase was 0.2 M NaOH.

The comparison was made with respect to the gas absorption fraction, as defined by Eq. 5.23. Further, the residence time defined by Eq. 5.24 is related to the length of the channel, L, and bubble velocity, U_B. The latter was obtained from Eq. 5.25 (Liu et al., 2005). Clearly, for the same flow conditions, a longer channel is associated with a larger residence time.

$$X = \frac{C_{CO_2,in} - C_{CO_2,out}}{C_{CO_2,out}} \times 100\% \tag{5.23}$$

$$t_{res} = \frac{L}{U_B} \tag{5.24}$$

$$U_B = U_{TP} \frac{1}{1 - 0.61 Ca^{0.33}} \tag{5.25}$$

As shown in Figure 5.4, the numerical predictions from the current model had a mean absolute error of 11.9% which was considered a strong indicator of its predictive accuracy. It is worth noting that the present predictions of absorption fraction could be slightly higher than the experimental data which was obtained with a CO_2 concentration of 23%. This is due to the nature of the present modeling methodology which assumes negligible decrease in the bubble volume, and thereby the interfacial area, over the residence time. As previously noted in Section 2.3, the validity of this

assumption decreases at higher gas phase concentration levels and accordingly, interpretations of the numerical predictions should consider this aspect.
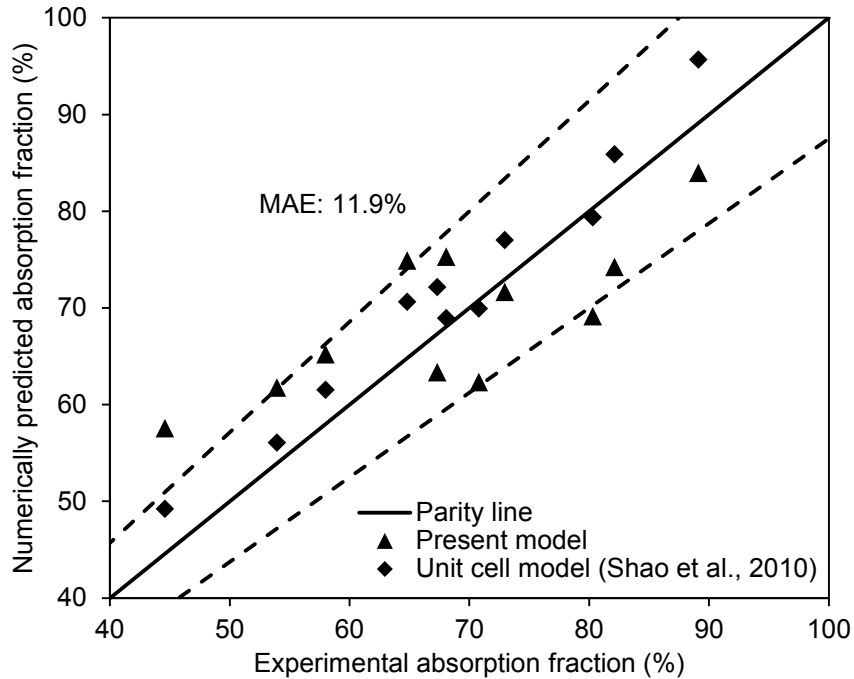
Figure 5.4: Comparison of numerical predictions of absorption fraction with the experimental data of Shao et al. (2010).

A characteristic unit cell obtained from the present simulations is shown in Figure 5.5 from which the recirculating velocity components, which are a characteristic feature of the Taylor flow regime, can be observed. Subsequently, parametric studies were performed with the validated model which are reported and discussed below.
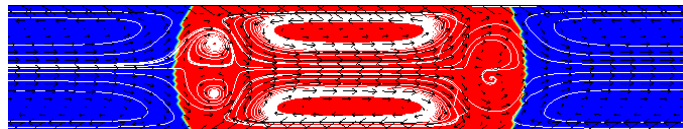
Figure 5.5: Characteristic unit cell obtained from simulations with relative velocity vectors and streamlines (contours of gas phase volume fraction are in red).

5.3.2   Effect of phase concentration

The effect of initial concentration of the gas and liquid phase was studied for a channel having a characteristic dimension of 500 μm and cross-flow inlet configuration. The superficial velocities of the liquid and gaseous phases were both 0.1 m/s. Three sets of studies were conducted.

First, the initial concentration of the gaseous phase was varied from 1% to 10% by volume of CO_2 with constant initial concentration of NaOH equaling 0.2 M. The results reported in Figure 5.6 indicate that with higher initial gas concentration levels, the absorption fraction decreases for a certain residence time (or channel length). This is a result of the increased consumption of the NaOH at the interface at higher gas concentration levels which decreases the potential for mass transfer.

Second, the molar concentration of the NaOH solution was varied from 0.05 M to 1 M with a constant initial gas phase concentration equaling 5% by volume, for all cases. As seen in Figure 5.7, the absorption fraction achieved for a certain residence time (or channel length) steadily increases with increasing levels of liquid reactant concentration. This is because the increased liquid phase concentration, in addition to influencing the reaction rate (Eq. 5.16), also affects the ionic strength of the solution and therefore the rate constant (Eqs. 5.17 and 5.18).
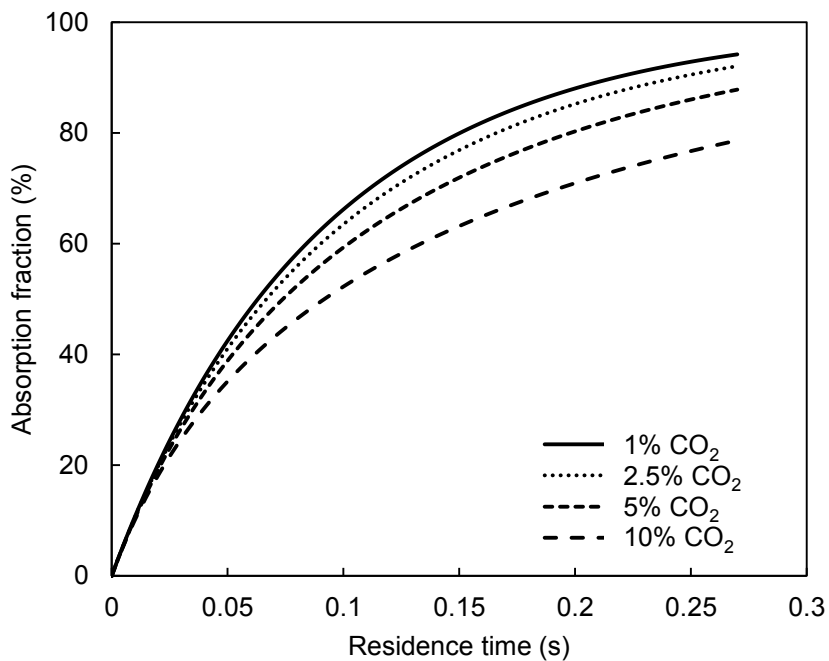
Figure 5.6: Effect of gas phase concentration on absorption fraction (D: 500 μm; U_G: 0.1 m/s; U_L: 0.1 m/s; C_{NaOH}: 0.2 M; T: 298 K).
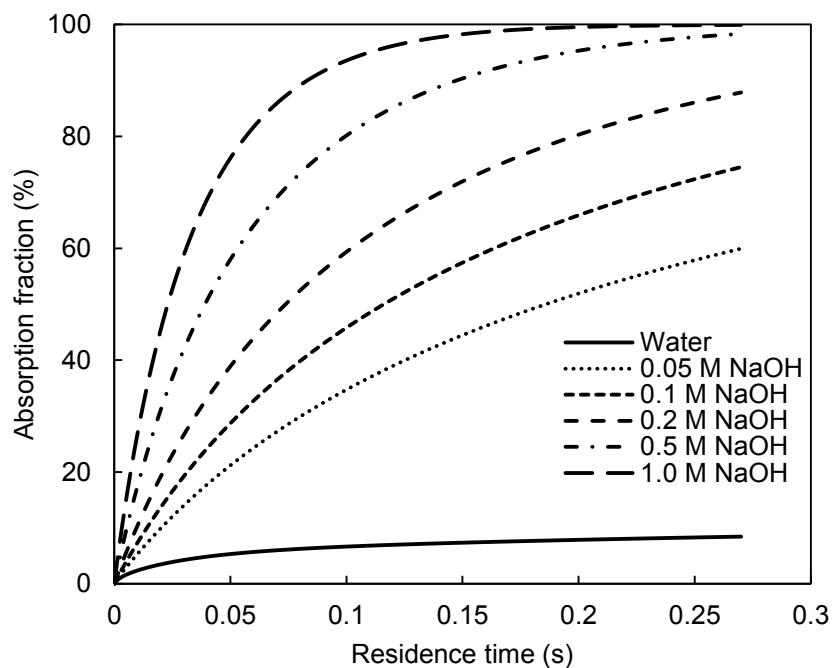
Figure 5.7: Effect of liquid phase concentration on absorption fraction (D: 500 μm; U_G: 0.1 m/s; U_L: 0.1 m/s; C_{CO2}: 5% by volume; T: 298 K).

Third, the gas to liquid concentration ratio was maintained at a constant value while the individual concentration levels were simultaneously varied. Characteristic results reported in Figure 5.8 for a ratio of 10 indicate that higher concentration levels of the liquid reactant were found to yield improved mass transfer characteristics. Similar findings were also reported by Zanfir et al. (2005) in a comparable experimental analysis of a falling film microreactor.
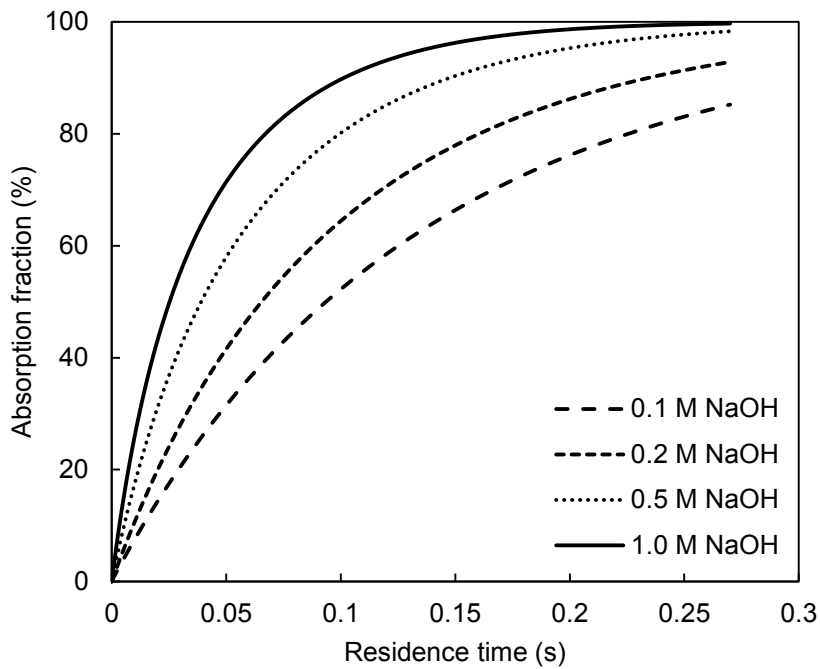
Figure 5.8: Variation of absorption fraction with liquid phase concentration and constant gas-liquid concentration ratio (*D*: 500 μm; C_{gas}/C_{liquid}=10; *T*: 298 K).

5.3.3   Effect of channel size

The effect of channel size was studied for characteristic dimensions ranging from 100 to 750 μm in channels having cross flow inlet configuration. The superficial velocities of the liquid and gaseous phases were both 0.1 m/s. The concentration of the gas phase was 5% by volume CO_2 and that of the liquid phase was 0.2 M NaOH. The

189

results shown in Figure 5.9 indicate that shorter residence times (or channel lengths) were required to achieve a certain level of absorption fraction as the channel size decreases. In comparison to a 750 μm channel, the residence time required to attain a 95% absorption fraction level, was lower by around 40%, 60% and 85% for the 500, 300 and 100 μm channels, respectively. Clearly, any reduction in the residence time translates into a linear decrease in the channel length and therefore the overall size of the microreactor.
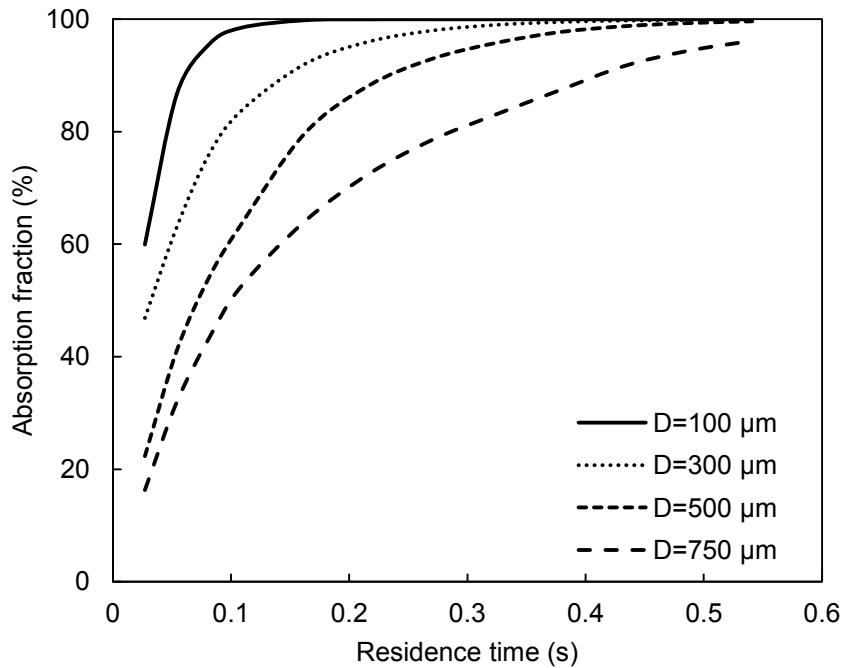
Figure 5.9: Effect of channel size on absorption fraction (U_G: 0.1 m/s; U_L: 0.1 m/s; C_{CO2}: 5% by volume; C_{NaOH}: 0.2 M; T: 298 K).

For the same flow conditions, the smaller channels were found to have longer bubbles than the larger channels. This is consistent with the physics of the flow, since the gas void fraction does not change with the characteristic dimension of the channel (Armand correlation, Eq. 5.22). Hence the enhanced mass transfer characteristics of

the smaller channels are attributed to the larger interfacial areas present as a result of the longer bubbles. It should be noted that these results are not in contradiction with those of Shao et al. (2010) in which an increase in the bubble length was found to adversely affect the absorption fraction, since their study was seemingly performed by arbitrarily varying the bubble length while maintaining a constant channel size. This would have led to an increase in the gas void fraction and hence resulted in deteriorated absorption performance.

5.3.4   Effect of modeling the inlet mixing region

A main advantage of the present model is its ability to account for the mass transfer that occurs in the inlet mixing region. However, it was necessary to quantify the mass transfer that occurs in the region in detail in order to better understand its significance.

It was shown in Figure 5.6 that the initial concentration of CO_2 in the gas bubble affected the predicted value of the absorption fraction at any residence time. Hence, prior to modeling the mass transfer in the gas bubble after it detached itself from the free stream flow at the inlet we attempted to quantify the mass transfer that occurred during the bubble formation period in the inlet mixing region. This mass transfer was considered to occur over the duration of a bubble formation cycle, t_{cycle}. The value t_{cycle} was obtained from the two-phase flow model detailed in Section 5.2.1. The change in concentration was accounted for at intervals of 1 ms such that each transient simulation run yielded a reduced level of CO_2 concentration in the gas bubble. The value obtained at the end of each transient simulation run was used to

define the concentration in the subsequent, further evolved gas bubble. Since the mass transfer in the inlet mixing region was modeled for duration of t_{cycle}, the reaction time in the channel length, $t_{channel}$ was quantified as the difference between the total residence time in the reactor, t_{res}, and bubble formation time, t_{cycle}.

$$t_{channel} = t_{res} - t_{cycle} \tag{5.26}$$

Figure 5.10 and Figure 5.11 show the results obtained by the above procedure, denoted as "Inlet modeled." The curves denoted as "Inlet not modeled" were obtained using the conventional method followed in the unit cell-based approaches wherein the bubble evolution in the inlet mixing region is completely neglected. Rather, the mass transfer from the detached bubble was assumed to occur over the entire residence time.

Figure 5.10 compares the numerically predicted absorption fraction obtained by the two methods over a residence time t_{cycle}. This corresponded to the time spent by a bubble in the channel prior to detachment. The initial concentration of the gas phase was 5% by volume CO_2 and that of the liquid phase was 0.2 M NaOH. For the 100 μm channel, the simulation performed without considering the inlet mixing region was found to over predict the absorption fraction by nearly 16%. In the cases with characteristic dimensions of 300 μm and 500 μm, the absorption fraction was over-predicted by nearly 9% and 8% respectively. In terms of CO_2 concentration, this corresponded to differences of nearly 19%, 10% and 8.5% for the 100, 300 and 500 μm channels, respectively. These discrepancies can be explained as follows. The cases that did not consider the inlet mixing region were associated with large, constant value of bubble length for the entire duration of t_{cycle}, thereby resulting in a

higher value of absorption fraction due to the higher interfacial area. On the other

hand, with the cases that did model the inlet mixing region, the value of bubble

length, and therefore interfacial area for mass transfer, gradually increases as the

bubble develops and emerges. Further, the discrepancies are more dominant for

smaller channels since they are associated with longer bubbles and therefore larger

interfacial areas.
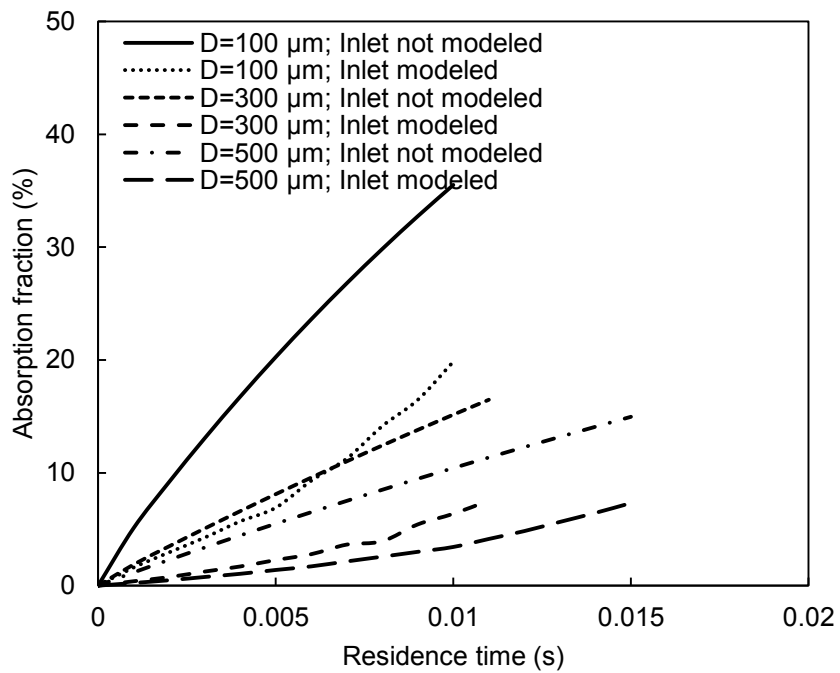
Figure 5.10: Effect of modeling inlet mixing region on absorption fraction for a residence time of t_{cycle} (*D*: 500 μm; U_G: 0.1 m/s; U_L: 0.1 m/s; C_{CO2}: 5% by volume; C_{NaOH}: 0.2 M; *T*: 298 K).

This study described above, which was performed for a relatively short residence

time, t_{cycle}, demonstrated the importance of modeling the inlet mixing region,

especially for smaller diameter channels. Subsequently, the effect of modeling the

inlet mixing region was analyzed for a longer residence time. As can be seen in

Figure 5.11, there is a continuous discrepancy in absorption fraction throughout the channel length for the 500 µm channel. This suggests that even for long residence times, it is essential to accurately account for the mass transfer that occurs in the inlet mixing region. It is worth noting that the relatively smaller discrepancies observed with smaller diameter channels in Figure 5.11 can be attributed to the improved mass transfer characteristics associated with smaller channels.
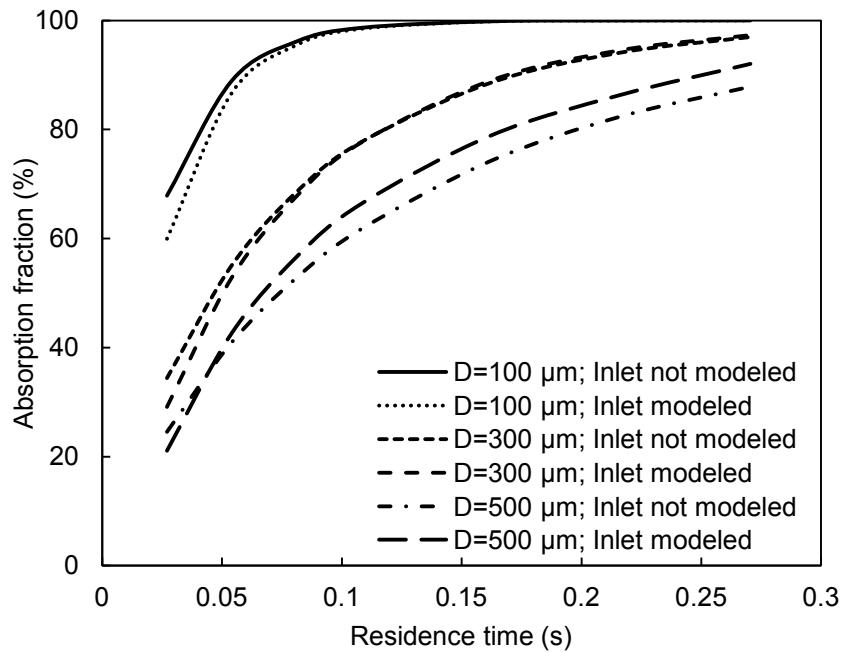
Figure 5.11: Effect of modeling inlet mixing region on absorption fraction for a residence time of $t_{channel}$ (D: 500 µm; U_G: 0.1 m/s; U_L: 0.1 m/s; C_{CO2}: 5% by volume; C_{NaOH}: 0.2 M; T: 298 K).

Based on the above discussion, it is clear that the present observations are in agreement with earlier findings in the literature (Fries and von Rohr, 2009; Tan et al., 2012b) and accordingly, it is recommended that numerical modeling of gas-liquid mass transport phenomena in mini/microchannels should account for the mass

194

transfer that occurs in the inlet mixing region, in addition to that which occurs in the channel length. It is worth noting that the present study used a simplified 2-D domain, as against a more realistic 3-D domain. Nonetheless, based on the present results, it is believed that even with a 3-D domain, numerical simulations that do not model the inlet region will result in erroneous predictions. However, the magnitude of discrepancy associated with 3-D domain-based results could be different from that associated with 2-D domain-based predictions.

5.3.5   Effect of wall contact angle

In the two-phase flow model, a wetted wall boundary condition allowed a specification of a contact angle at the wall. Two values of contact angle, 90° and 60°, were compared as shown in Figure 5.12 for phase superficial velocities of 0.1 m/s. The latter, according to Gupta et al. (2009), would result only in a more realistic bubble appearance and would be a "purely numerical artifact." The validity of this statement was tested by comparing the gas void fraction between the two cases which was found to be within 0.8% of each other. Additionally, no significant change in the bubble and slug lengths was observed. While the above does partially verify the statement by Gupta et al. (2009), it is worth noting that the bubble boundary was altered due to the rounded bubble caps (Figure 5.12). The effect of the altered interfacial profile on the mass transfer performance was further investigated.
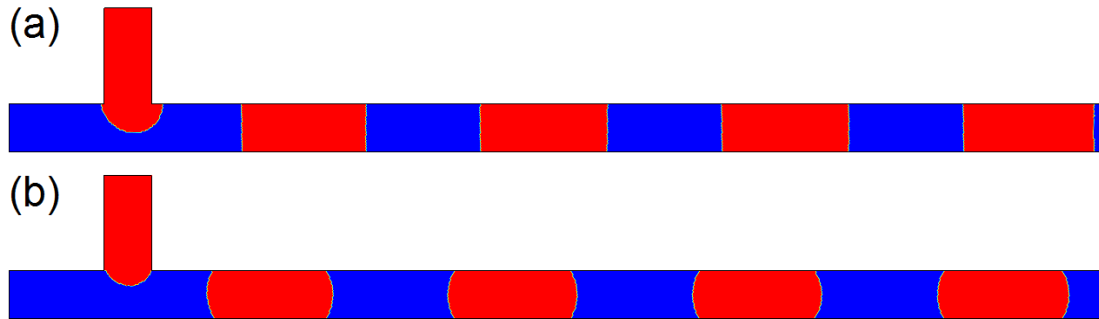
Figure 5.12: Typical image of Taylor flow pattern for wall contact angle (a) 90° and (b) 60° (D: 500 µm; U_G: 0.1 m/s; U_L: 0.1 m/s; C_{CO2}: 5% by volume; C_{NaOH}: 0.2 M; T: 298 K; contours of gas phase volume fraction are in red).

The mass transfer characteristics for contact angles equaling 90° and 60° of the two cases were compared for concentrations of 5% by volume of CO_2 and 0.2 M NaOH. As shown in Figure 5.13, our results generally agree with the findings of Gupta et al. (2009), especially for the smaller channel sizes. The marginal discrepancies of up to 4% that were observed for the 500 µm channel were most likely due to the increasing mass transfer contributions from the bubble caps for larger channels, in which the bubble lengths are also correspondingly less than the smaller channels. Thus it is concluded that while an appropriate definition of the wall contact angle may not generally provide highly improved accuracy for channels having a small characteristic dimension, it could be essential for mass transfer in larger channels.
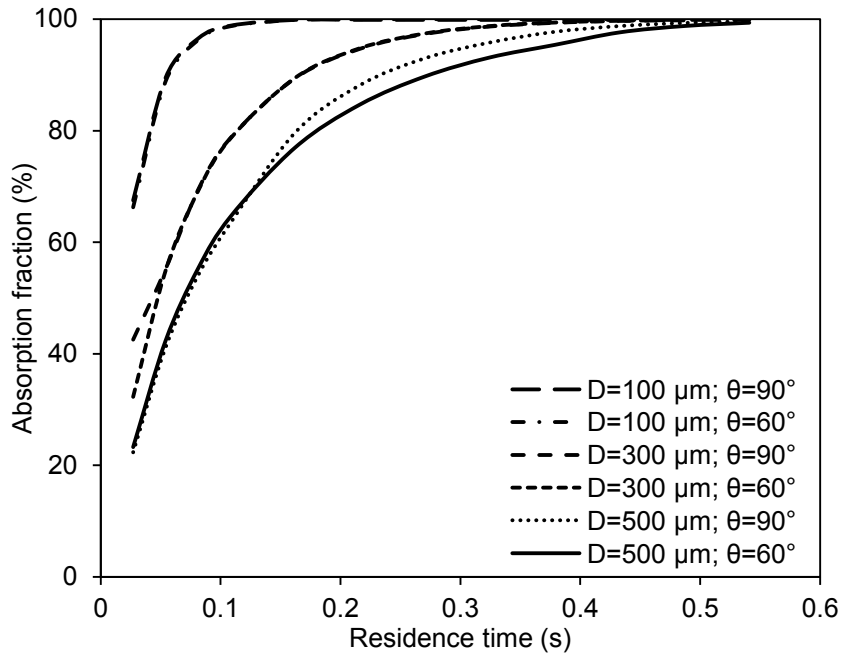
Figure 5.13: Effect of contact angle on absorption fraction (D: 500 μm; U_G: 0.1 m/s; U_L: 0.1 m/s; C_{CO2}: 5% by volume; C_{NaOH}: 0.2 M; T: 298 K).

5.3.6 Effect of temperature

Shao commented on the sensitivity of the reaction rate to temperature, due to which they maintained their test section at isothermal conditions. Likewise, Zanfir et al. (2005), Yue et al. (2007a) and Su et al. (2010) performed their experiments at ambient temperatures only. In the present study, the temperature was found to have a significant effect on the mass transfer, as shown in Figure 5.14 for a 500 μm channel in which the phase superficial velocities were 0.1 m/s and concentrations were 5% by volume of CO_2 and 0.2 M NaOH.
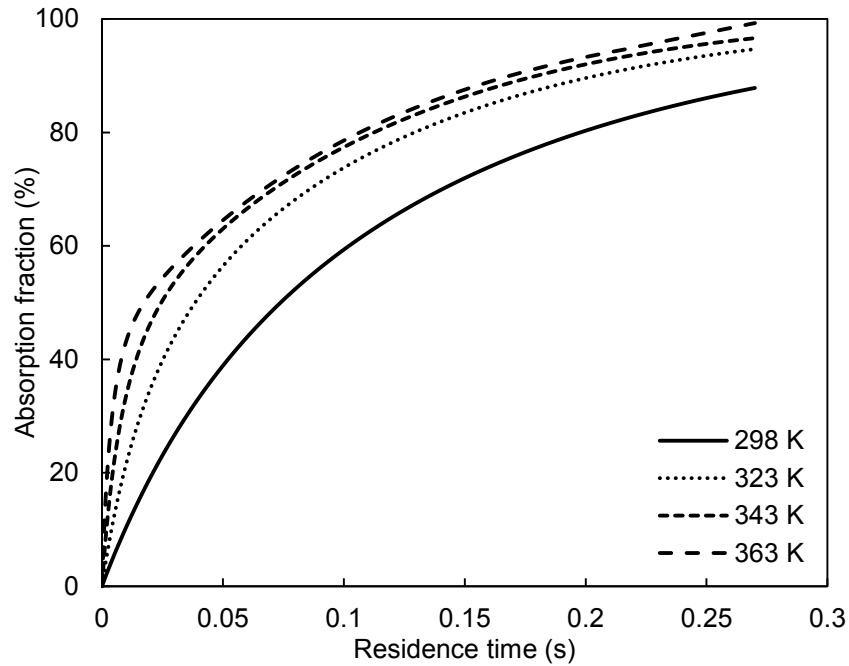
Figure 5.14: Effect of temperature on absorption fraction (D: 500 μm; U_G: 0.1 m/s; U_L: 0.1 m/s; C_{CO2}: 5% by volume; C_{NaOH}: 0.2 M).

The enhancement is more prominent between an increase from ambient conditions of 298 K and that of 323 K, as compared to further increases in temperature. This observed enhancement is attributed to the relationship between temperature and the reaction rate constant (Figure 5.15) as given by Eq. 5.17. The effect of temperature is more pronounced at higher liquid phase concentration levels.
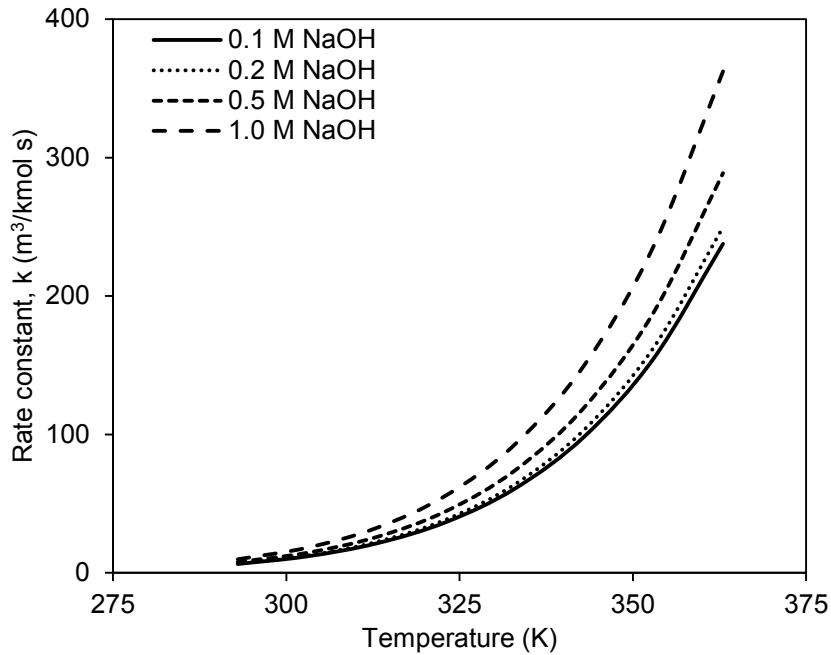
Figure 5.15: Variation of rate constant with temperature at different levels of liquid phase concentration.

5.4 Chapter conclusions

This chapter reports a numerical model to predict the mass transfer characteristics during Taylor flow in mini/microchannel reactors. The current approach is distinct from existing approaches because it models the entire reactor, including the channel length as well as the inlet mixing region. The computational requirements were reduced by decoupling the hydrodynamics of the two-phase flow from the mass transfer phenomena. Further, the model was derived from a purely theoretical basis in order to permit its application towards the design of scaled-up microscale reactors having complex channel geometries and optimized dimensions. A finite-element implementation of the phase field method was used to predict the hydrodynamics of the two-phase flow. The phase distribution obtained was used to define the

199

computational domain to model the mass transfer. The reaction system of absorption of CO_2 into aqueous NaOH solution was considered. Channels with characteristic dimensions ranging from 100 μm to 750 μm were modeled with flow-focusing and cross-flow types of inlet configurations. The effect of channel length was also studied by varying the residence time in the transient simulation. The numerical predictions were compared with experimental data in the literature and a good agreement was obtained with a mean absolute error of 11.9%. Parametric studies on the effect of the gas and liquid phases concentrations were conducted, and the trends of absorption fraction were consistent with the reaction chemistry. The effect of modeling the inlet mixing region was found to be significant and simulations that did not account for the mass transfer that occurs in the inlet region during the bubble formation stages, were demonstrated to yield discrepancies as high as 19% in terms of CO_2 concentration. This observation is in agreement with previous studies in the literature, and based on the same it is recommended that numerical modeling of gas-liquid mass transport phenomena in microchannels should account for the mass transfer that occurs both in the inlet mixing region and the channel length. The effect of modeling a wall contact angle was found to yield marginal discrepancies only for the larger channels. Substantial reductions, as high as 85% in the residence time and therefore the overall reactor size, were obtained as a result of using channels having a reduced characteristic dimension. These enhancements were found to be further enhanced by higher concentration levels of the liquid reactant and increased temperatures. On the whole, the current model had a reasonably good predictive accuracy and can be used for the designing scaled-up microchannel reactors for reacting two-phase flows.

200

Chapter 6: CFD Modeling of Two-Phase Flow with Heat/Mass Transfer across Deforming (Unsteady) Interfaces

6.1 Introduction

Multiphase flow in microscale systems is associated with several flow regimes. A holistic numerical modeling approach for simulating heat/mass transfer in these systems should be independent of the flow regime. In other words, the model should be capable of predicting all regions of a flow regime map without requiring any regime-specific inputs apart from those typically associated with the operating conditions at which these regimes occur. Furthermore, the model should couple the governing equations for the flow hydrodynamics with those for heat/mass transfer, while continuously tracking/re-constructing the interface. Such a model would be of tremendous application for the development of design and optimization capabilities that are applicable to a wide range of operating conditions and applications. This chapter reports numerical models for simulating two-phase flow with heat/mass transfer across deforming, unsteady interfaces. As a pre-cursor to modeling gas-liquid mass transfer with chemical reactions which is a complex process involving multiple species, a slightly simpler problem of condensation heat transfer is first simulated. Section 6.2 proposes a purely theoretical, transient model for condensation heat transfer. The formulation is not restricted to a single bubble or a specific flow regime, but is targeted at the simulation of all condensation flow patterns. The model has been implemented for a relatively simple geometry, a single microchannel, for which well-established correlations are available in the literature. The predictions of two-phase

pressure drop and Nusselt number have been compared against the correlational data. Additionally, condensation flow patterns have been simulated and compared against available experimental visualization data. Section 6.3 proposes a transient model for gas-liquid absorption with chemical reactions in a microchannel. The model predictions are compared against experimental visualization data as well as mass transfer performance parameters.

6.2 Modeling of condensation

6.2.1 Numerical model

6.2.1.1 Governing equations

The present numerical formulation was implemented in a commercial CFD code, FLUENT version 6.3.26 (Ansys, Inc.). The numerical model for multiphase flow solved the equations for continuity, momentum conservation and energy conservation, as given by Eqs. 6.1-6.3, respectively.

$$\frac{\partial \rho}{\partial t} + \nabla \cdot (\rho \mathbf{V}) = 0 \tag{6.1}$$

$$\frac{\partial}{\partial t}(\rho \mathbf{V}) + \nabla \cdot (\rho \mathbf{V} \, \mathbf{V}) = -\nabla P + \nabla \cdot \left[\mu (\nabla \mathbf{V} + \nabla \mathbf{V}') \right] + \mathbf{F} \tag{6.2}$$

$$\frac{\partial}{\partial t}(\rho E) + \nabla \cdot \left[\mathbf{V}(\rho E + P) \right] = \nabla \cdot \left(k_{eff} \nabla T \right) + S_h \tag{6.3}$$

The multiphase flow was modeled by a finite volume method-based implementation of the VOF approach (Hirt and Nichols, 1981). The surface tension forces were

modeled following the continuum surface force (CSF) formulation of Brackbill et al.

(1992). This approach models the pressure jump across the interface as a volume

force that is included as a source term in the momentum equation. Additionally, the

VOF model solves an equation for volume fraction, α, wherein for a multiphase

system with k phases, Eq. 6.4 is solved for k-1 phases, and the volume fraction of the

excluded phase (termed the primary phase) is determined by the summation

expression in Eq. 6.5.

$$\frac{\partial \rho_i \alpha_i}{\partial t} + \nabla \cdot \left(\rho_i \alpha_i \mathbf{V}_i \right) = S_{\alpha_i} \tag{6.4}$$

$$\sum_{i=1}^{n_{phase}} \alpha_i = 1 \tag{6.5}$$

The effective fluid properties such as density and viscosity were computed as the

average property values of the two phases, weighted by their respective volume

fractions. Interface reconstruction was performed using the explicit piecewise-linear

interface construction (PLIC) scheme of Youngs (1982). A pressure-based solver

with an unsteady first-order implicit formulation was utilized. A pressure-based

coupled approach was found to yield improved stability as against a segregated

approach for the pressure-velocity coupling, and hence this approach was used along

with the PRESTO (pressure staggering option) scheme. Following the

recommendations of Krishnan et al. (2010), based on a detailed assessment on the

performance of various numerical schemes for similar two-phase applications, a first-

order upwind scheme for discretizing the momentum equation and a Green-Gauss

node-based scheme for calculating the gradients of scalar variables were utilized.

203

Our modeling methodology aimed at avoiding the common assumption in several earlier works, which is to utilize a fixed interfacial profile between the liquid and vapor phase. This assumption is usually justified by considering the rate of mass transferred from one phase, say the vapor phase in the case of condensation, to exactly equal the mass flow rate of vapor entering the domain. However, such approaches are generally applicable only to certain flow regimes such as annular flow, where the profile of the interface is well established. Hence, it is believed that such models are not suitable for all flow regimes, and therefore developing a generic approach was one of the goals of the present study. In order to accomplish this, the phase change phenomenon was modeled in a manner that simultaneously considered the equations for fluid flow, heat transfer and the associated mass transfer. The use of an interface tracking algorithm allowed us to model both the gas and liquid phases, and hence interfacial motions resulting from the phase change process were successfully simulated. The latent heat associated with the phase change phenomena was modeled as an energy source and was represented by the term S_h in Eq. 6.3. Likewise, the source term accounting for mass transfer between the gas and liquid phases was given by the term S_{α_i} in Eq. 6.4. The heat flux associated with the phase change process in the interfacial region was estimated by applying Fourier's law (Eq. 6.6). The same heat flux also relates the mass flux due to phase change and the latent heat (Eq. 6.7).

$$\left(q'' \right)_{\text{local, interface}} = -k_{\textit{eff}} \times \left(\nabla T \right)_{\text{local, interface}} \tag{6.6}$$

204

$$(q'')_{\text{local, interface}} = (m'')_{\text{local, interface}} \times h_{LV} \tag{6.7}$$

Based on the above, the expressions for the mass source terms for the liquid and vapor phases were defined as given by Eqs. 6.8 and 6.9, respectively. The energy source term is given by Eq. 6.10.

$$(S_{\alpha_L})_{\text{local, interface}} = + \frac{(q'' \cdot \nabla \alpha)_{\text{local, interface}}}{h_{LV}} \tag{6.8}$$

$$S_{\alpha_V} = -S_{\alpha_L} = - \frac{(q'' \cdot \nabla \alpha)_{\text{local, interface}}}{h_{LV}} \tag{6.9}$$

$$S_h = + (S_{\alpha_L})_{\text{local, interface}} \times h_{LV} \tag{6.10}$$

It should be noted that the above expressions defining the mass and energy source terms were not part of the CFD code and were programmed into the numerical model by defining additional routines in C language as follows. The effective thermal conductivity, k_{eff}, was calculated as the average of thermal conductivities of the liquid and vapor phases, weighted by their respective volume fractions. The gradients of temperature and volume fraction were calculated using divergence theory, and were used to determine the three source terms given by Eqs. 6.8-6.10. The source terms were evaluated throughout the computational domain. However, their value is evaluated to equal zero everywhere, except in the vicinity of the liquid-vapor interface where the gradient of volume fraction is non-zero.

6.2.1.2 Computational domain

Since the present study was aimed at developing a numerical model and validating the predictions with known correlations for condensation phenomena, a relatively simple geometry was chosen for this purpose. A single microchannel was modeled as a two-dimensional geometry in the form of a rectangular domain, a schematic of which is presented in Figure 6.1.

The microchannel had a characteristic dimension, D, equaling 100 μm and a length of 0.03 m. A velocity boundary condition was specified at the channel inlet for the superheated vapor phase, and a pressure-based boundary condition was specified at the channel outlet. A constant heat flux was specified at the channel walls. In order to simplify the analysis, the solid microchannel wall was not modeled, and therefore the effects of wall conduction were not accounted for in the present study.
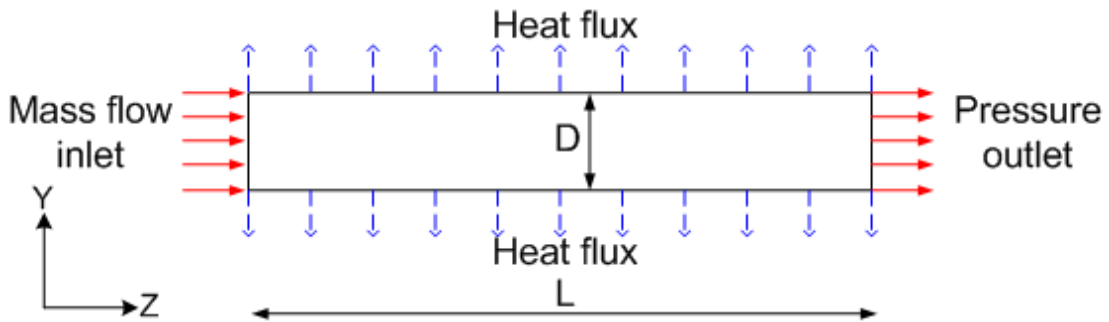
Figure 6.1: Schematic of computational domain.

The entire domain was discretized with a homogeneous structured grid consisting of quadrilateral elements with a size of 2 μm (D/50). The use of a locally refined grid near the channel wall was considered since this could potentially assist in capturing

206

thin liquid films during certain flow conditions such as that involving slug and annular flow patterns. While several previous studies on modeling of two-phase flow phenomena have used non-uniform grids (Taha and Cui, 2004; Liu and Wang, 2008; Kumar et al., 2007; Shao et al., 2008), certain others have preferred to use uniform element sizes throughout the computational domain (Mukherjee and Kandlikar, 2005; Qian and Lawal, 2006; Chen et al., 2009; Gupta et al., 2009; Krishnan et al., 2010; Santos and Kawaji, 2010; Zhuan and Wang, 2010; Zhuan and Wang, 2011; Zhuan and Wang, 2012; Chapter 4; Chapter 5). One of the reasons for the same is to maintain a constant resolution of the liquid-vapor interface throughout the computational domain. Further, this strategy does not facilitate capturing the spatially fine flow features that occur in regions away from the channel wall. For these reasons, a uniform grid was utilized in the present study.

6.2.1.3 Simulation conditions

1,1,1,2-Tetrafluoroethane, more commonly referred to as R-134a or HFC-134a was used as the working fluid, whose thermo-physical properties were obtained from the program REFPROP 9.0 (Lemmon et al., 2010) at the saturation temperature corresponding to a system pressure of 1 MPa. The pressure drop across the channel was relatively small compared to the system pressure for the channel length under consideration in the present work. Hence, the variation in thermo-physical properties across the channel length was neglected. The constant values, taken at the saturation temperature corresponding to 1 MPa system pressure are summarized in Table 6.1. The incoming vapor was superheated by 10 K, and the magnitude of negative heat

flux (heat removal during condensation) applied to the channel wall ranged between 200 to 800 kW/m^2. The vapor mass flux at the inlet ranged from 246 to 615 kg/m^{2}s.

Table 6.1: Thermo-physical properties of R134a at system pressure of 1 MPa corresponding to saturation temperature of 312.54 K.

Property	Liquid phase	Gas phase	Two-phase
Density (kg/m^3)	1149.3	49.22	-
Dynamic viscosity (μPa s)	162.7	12.34	-
Thermal conductivity (W/m K)	0.0749	0.0154	-
Enthalpy (kJ/kg)	255.50	419.16	-
Specific heat capacity (J/kg K)	1494.8	1139.1	-
Latent heat (kJ/kg)	-	-	163.66
Surface tension (N/m)	-	-	0.0062

The Bond number criterion of Brauner and Moalem-Maron (1992), Bo $< (2\pi)^2$, was used to verify that at the present length scale, the surface tension forces were indeed dominant over gravitational forces and hence the latter could be neglected. Additionally, gravitational head-based pressure drops were not present.

Wang et al. (2011) reported that Marangoni convection currents do arise during phase change heat transfer in similar microscale geometries due to non-uniform interfacial temperatures. However, they demonstrated that the effect of the same on heat transfer was relatively negligible. Following their analysis and the assumptions made in other modeling studies (Mukherjee and Kandlikar, 2005; Fang et al. 2010a), the effects of Marangoni convection have been neglected in the present simulations.

6.2.1.4   Surface wettability

The surface wettability can influence the fluid flow and heat transfer characteristics during condensation in microchannels. The experimental study of Fang et al. (2010c) demonstrated that channels with hydrophobic surfaces yield better thermal performances as compared to those with hydrophilic surfaces. The same was attributed to the differences in flow patterns and hence the heat transfer mechanisms. The present VOF formulation can account for surface wetting by altering the interface normal in the near-wall cells based on the specified value of contact angle, and such an approach has been followed in several works (Qian and Lawal, 2006; Kumar et al., 2007; Shao et al., 2008; Gupta et al., 2009; Santos and Kawaji, 2010; Chapter 4). However, various deficiencies in the above approach were identified by Santos and Kawaji (2010), Fang et al. (2008), and in Chapter 4, which include the inability to account for contact angle hysteresis, the lack calculation of dynamic contact angles, the lack of modeling of contact line slip, and use of a constant pre-determined value of contact angle. Addressing these deficiencies is an active area of research and numerous techniques for the same have been suggested in the literature (Renardy et al., 2001; Fang et al., 2008; Thomas et al., 2010). However, the inclusion of these approaches significantly adds to the complexity of the present problem and hence, the effects of surface wettability were not considered in the present simulations. It is recommended that future efforts account for the surface wettability effects and overcome the corresponding deficiencies otherwise.

6.2.1.5 Transient solver settings

The transient solution for the governing equations was obtained using an explicit scheme for which the Courant number was used to adopt a variable time-stepping strategy. The Courant number, C, is a non-dimensional quantity defined by Eq. 6.11 as the ratio of the time step size used by the transient solver, Δt, to the characteristic time required for a fluid element to transit a control volume. The latter is calculated based on the cell volume and the sum of the outgoing fluxes, thereby yielding the duration it takes for fluid to empty out of any given cell. The smallest time associated with all the cells in the control volume is used to determine the appropriate size of the time step to be chosen in order to remain within the specified value of Courant number.

$$C = \frac{\Delta t}{\Delta x_{cell} / V_{fluid}}$$
(6.11)

An exceedingly low value of Courant number corresponds to a very small time-step size and is associated with a high computational cost. However, this case yields high predictive accuracy with respect to being able to capture all physical flow features. An unphysical high Courant number may result in poor simulation of the transient flow features and possibly divergence of the solution.

In the present study, the Courant number for solving the volume fraction equation (Eq. 6.4) was restricted to 0.25, while that for the remaining transport equations (Eqs. 6.1-6.3) was restricted to a higher value of 5. With these settings multiple flow patterns were captured which was considered an indication of the appropriateness of

the above solver settings (Krishnan et al., 2010). Similar values have been reported by Qian and Lawal (2006), Liu and Wang (2008), and Gupta et al. (2009).

6.2.2 Results and discussion

Domain discretization was performed at a coarse level having an element size of 20 μm and was sequentially refined to a fine level having an element size of 2 μm. The average wall temperature was monitored over the condensing region of the computational domain for these levels of domain discretization. The results of the grid independence analysis are reported in Figure 6.2, for an inlet vapor mass flux of 492.2 kg/m²s. The average deviation in wall temperature between the results for the 5 μm and 2 μm, for the four levels of heat flux reported in Figure 6.2, was only 0.79%. While our initial conclusion was that 5 μm elements could be satisfactorily utilized, the ability of the discretized domain to capture thin liquid films typically associated with microscale flows was further assessed using the methodology proposed by Gupta et al. (2009). The capillary number ranged from 0.13 to 0.32 in the present study. Correlations to estimate the thickness of the liquid film as a function of capillary number have been reported in the literature, including Eqs. 6.12 and 6.13, by Bretherton (1961) and Aussillous and Quere (2000), respectively.

$$\frac{2\delta}{D} = 1.34 Ca^{2/3} \tag{6.12}$$

$$\frac{2\delta}{D} = \frac{1.34 Ca^{2/3}}{1 + 2.5\left(1.34 Ca^{2/3}\right)} \tag{6.13}$$
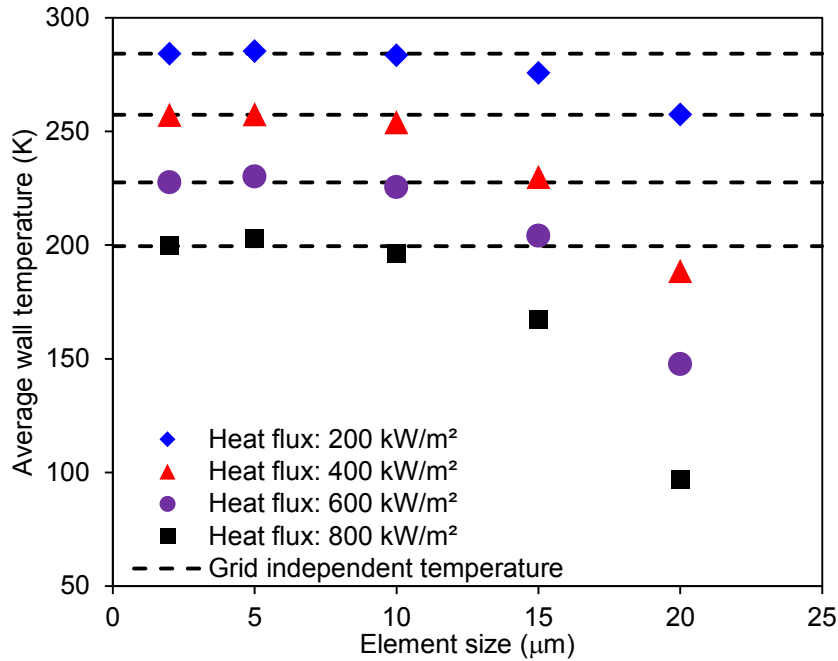
Figure 6.2: Analysis of average wall temperature to determine grid independence.

Gupta et al. (2009) stated that these expressions could be used to estimate the thickness of typical liquid films and thereby ensure that the computational domain is resolved such that sufficient computational cells are present across the above-obtained value of film thickness. Eq. 6.13 was found to yield a more conservative prediction and therefore, was used in the present study. Characteristic results of the same for an inlet vapor mass flux of 492.2 kg/m^{2}s and wall heat flux of 400 kW/m^2 are reported in Table 6.2. As can be seen, a 5 μm element size yields less than 5 mesh elements across a typical liquid film and therefore was concluded to be insufficient. An element size of 2 μm corresponds to a thin film resolution factor of 12 and so was employed for the remainder of the study. It is worth noting that this selection alone resulted in a six-fold increase in the number of computational cells and therefore significantly longer simulation times.

Table 6.2: Characteristic results from grid independence studies for inlet vapor mass flux of 492.2 kg/m^{2}s and wall heat flux of 400 kW/m^2.

Element size (μm)	Computational cells (-)	Average wall temperature (K)	Discrepancy[1] (%)	Resolution of thin film[2] (-)
2	750,000	257.37	-	12.0
5	120,000	257.55	0.07	4.8
10	30,000	254.07	1.28	2.4
15	13,333	230.00	10.63	1.6
20	7,500	188.57	26.73	1.2
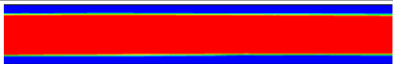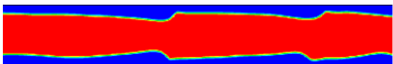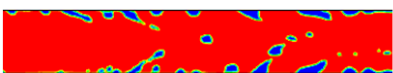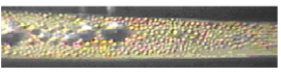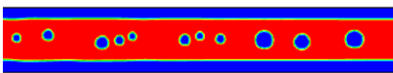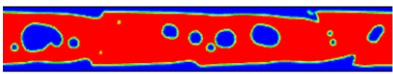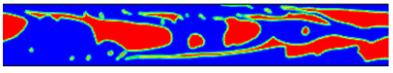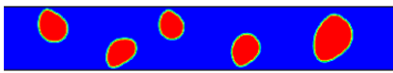
[1]Discrepancy between current case and 2 μm case. [2]Calculated as the ratio of least thickness of thin liquid film in current range of operating conditions (as estimated by Aussillous and Quere, 2000) to the element size.

6.2.2.1   Analysis of condensation flow regimes

Gas-liquid two-phase flow at the microscale is associated with several flow patterns that have been visualized in numerous past experimental works (Coleman and Garimella, 2003; Wu and Cheng, 2005; Hu and Chao, 2007; Wu et al., 2007a; Zhang et al., 2008; Fang et al., 2010b). In the present work, various condensation flow regimes were observed at various locations along the channel length at different operating conditions. The predicted flow regimes were compared with experimental visualization data from the literature for condensing flows and are reported in Figure 6.3. It is noted that this comparison is qualitative in nature and that the channel geometry and operating conditions used to obtain the present simulation-based results do not correspond to the conditions under which the experimental data was obtained.

The condensation flow regimes have been classified into three major categories as described below.

1. Annular flow: This is typically characterized by a core of vapor flowing through the center of the channel surrounded by a thin film of liquid along the channel wall. Smooth and wavy annular flow regimes are reported in Figure 6.3a and Figure 6.3b, respectively. Both have been compared against the visualization data of Kim et al. (2012), and a good resemblance was obtained. While smooth annular flow comprises a relatively straight/flat interface profile, the wavy annular flow regime is characterized by a wavy interfacial profile comprising crests and troughs. Coleman and Garimella (2003) noted that the liquid and vapor phases can move at different velocities, and when this is a dominant occurrence, the resulting shear forces at the interface lead to the formation of waves. Fang et al. (2010) used an optical interference technique to obtain the topology of the interface and the above-described wave-like instabilities were reported to have amplitude on the order of a few microns. Mist/droplet flow is reported in Figure 6.3c and favorably compared against the experimental data of Wu and Cheng (2005). This regime is characterized by numerous tiny droplets of liquid entrained in the bulk vapor phase.

Flow regime classification		Experimental visualization	Numerical simulation
Annular	(a) Smooth annular flow		
	(b) Wavy annular flow		
	(c) Mist/droplet flow		
Transition	(d) Smooth discrete flow		
	(e) Wavy discrete flow		
	(f) Dispersed flow		
Intermittent	(g) Slug flow		
	(h) Bubbly flow		

Legend for numerical simulations: ■ Gas phase ■ Liquid phase

Figure 6.3: Comparison of numerically predicted condensation flow regimes in the microchannel with experimental visualization data in the literature from the studies by (a) smooth annular flow (Kim et al., 2012); (b) wavy annular flow (Kim et al., 2012); (c) mist/droplet flow (Wu and Cheng, 2005); (d) smooth discrete flow (Hu and Chao, 2007); (e) wavy discrete flow (Coleman and Garimella, 2003); (f) dispersed flow (Coleman and Garimella, 2003); (g) slug flow (Kim et al., 2012), (h) bubbly flow (Kim et al., 2012).

2. Transitional flow patterns: These are comprised of four sub-types. Smooth discrete and wavy discrete flows are reported in Figure 6.3d and Figure 6.3e, and have been compared against the experimental visualization data of Hu and Chao (2007) and Coleman and Garimella (2003), respectively. Both of these are very similar to the previously discussed annular flow regimes, except for the presence of numerous liquid droplets entrained in the central vapor core. The

dispersed/churn flow regime was characterized by a seemingly random distribution of the unstable vapor phase surrounded by the liquid phase. Figure 6.3f compares the predicted flow pattern against the experimental visualization of Coleman and Garimella (2003), who classified it as disperse wavy flow with a high intensity of secondary waves. They attributed the occurrence of this regime to an increase in the intensity of the waves discussed above, which results in the surface of the wavy interface contacting the channel wall, causing a dispersion of the waves. At higher wave intensities, multiple waves may be superimposed on each other, making the liquid-vapor interface indistinguishable.

3. Intermittent flow patterns: These are characterized by alternating regions composed of predominantly either the liquid or vapor phase only. Slug flow and bubbly flow are reported by Figure 6.3g and Figure 6.3h, respectively, and both were compared with the experimental visualization data of Kim et al. (2012). Slug flow is characterized by alternating regions of elongated vapor bubbles and liquid slugs. The vapor bubbles are typically longer than the channel width and are separated from the channel wall by a thin film of liquid. On the other hand, bubbly flow is characterized by numerous vapor bubbles present in the bulk liquid phase wherein the bubble lengths are typically only a fraction of the channel width.

The mechanism of bubble formation and detachment which subsequently results in the formation of vapor bubbles and liquid slugs is termed as injection flow. The results reported in Figure 6.4a-Figure 6.4d from the numerical simulations and those in Figure 6.4e from Wu et al. (2007a) indicate the various stages of formation of a

216

neck region between the emerging vapor bubble and the upstream bulk vapor phase, leading to detachment of the bubble.
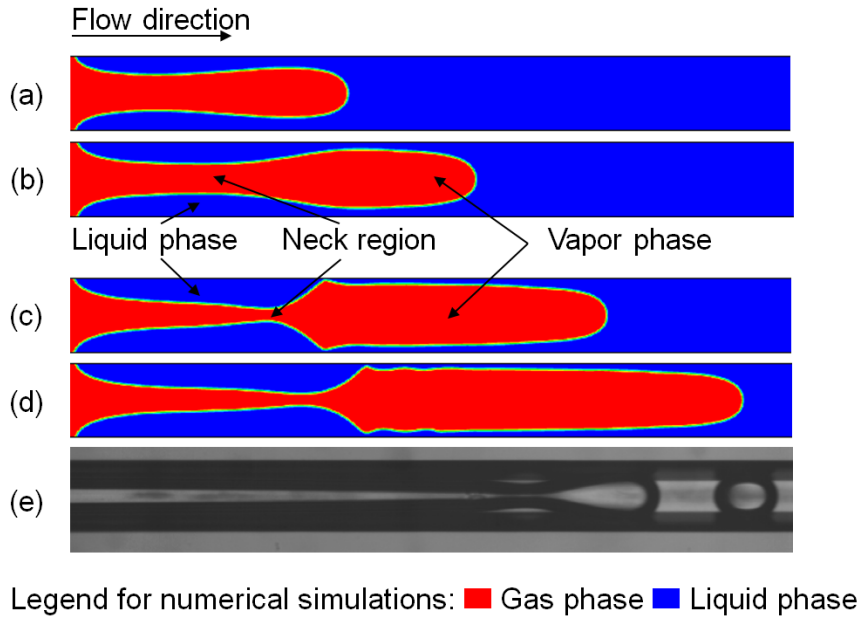
Figure 6.4: (a-d) Numerically predicted contours of vapor void fraction of various stages of bubble growth during injection flow; (e) experimental visualization image from Wu et al. (2007a).

The above results indicate that the numerical model proposed in the present work has a high qualitative accuracy with respect to the simulation of condensation flow patterns. A more detailed effort to analyze quantitative flow regime transition criteria is underway and will be reported in the future. Quantitative validation of the numerical model with respect to two-phase frictional pressure drop and two-phase Nusselt number is reported subsequently.

6.2.2.2   Data reduction: pressure drop and temperature

The pressure drop in the channel was observed to fluctuate in a periodic manner, and the average value was obtained by determining the mean pressure drop over multiple cycles for a given operating condition. The average wall temperature was observed to be relatively constant with respect to time. Figure 6.5 reports the transient variation of pressure drop and surface temperature for a typical case of condensation heat transfer with a heat flux of 600 kW/m^2 and inlet vapor mass flux of 492 kg/m^{2}s. The fluctuations in pressure drop were attributed to the phenomena occurring within the computational domain pertaining to the flow patterns reported in Figure 6.3. These include the formation of liquid droplets in mist, smooth discrete and wavy discrete flow patterns (Figure 6.3c, Figure 6.3d and Figure 6.3e), and the formation of intermittent vapor bubbles in slug and bubbly flow patterns (Figure 6.3g, Figure 6.3h). Similar pressure fluctuations during phase change heat transfer, albeit for boiling mode, were reported by Zhang et al. (2005) and Fang et al. (2010a). However, the observed frequencies are dependent on the time step size and sampling rate and hence, are not expected to have any physical significance.
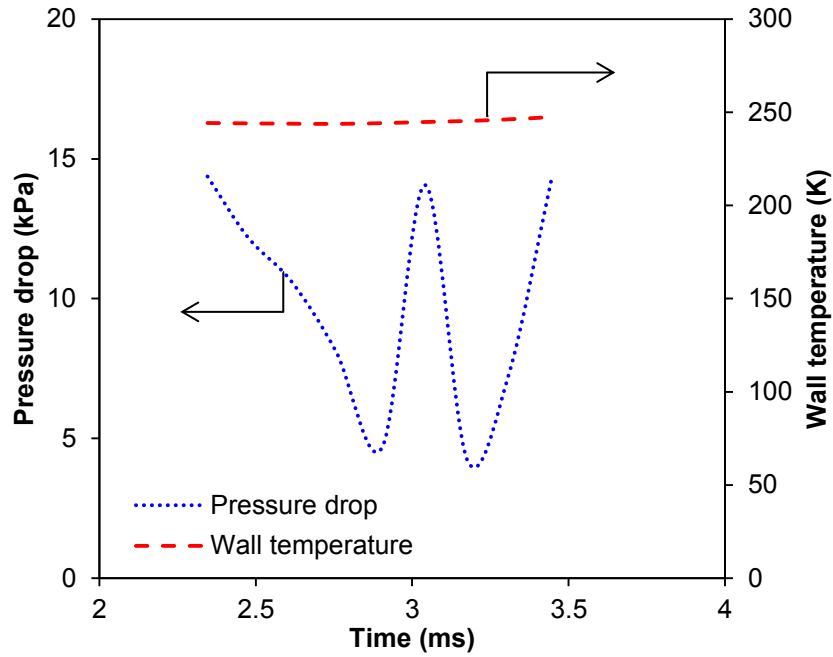
Figure 6.5: Transient variation of pressure drop and wall temperature in microchannel for heat flux of 600 kW/m^2 and inlet vapor mass flux of 492 kg/m^{2}s (average pressure is 9.98 kPa and average temperature is 244.89 K).

6.2.2.3 *Two-phase pressure drop*

The two-phase pressure drop predicted by the numerical model was a summation of the components due to friction and acceleration effects. As per the assumption stated previously, gravitational pressure losses were not considered in the present simulations. The acceleration pressure drop was estimated from Eq. 6.14 and subtracted from the total two-phase pressure drop predicted by the numerical model to yield the frictional pressure drop.

$$\left(-\frac{dP}{dZ}\right)_{TP,A} = G^2 \frac{d}{dZ}\left[\left(\frac{x^2}{\alpha\rho_V}\right)+\left(\frac{(1-x)^2}{(1-\alpha)\rho_L}\right)\right] \tag{6.14}$$

An analysis of the two-phase frictional pressure drop was performed using the separated flow approach, which involves the use of two-phase multipliers. Eq. 6.15 defines ϕ_L^2 and ϕ_V^2 which pertain to cases when either pure liquid or pure vapor flows in the channel at a mass flux of $G(1-x)$ or Gx, respectively. An alternative definition for the two-phase multiplier is provided by Eq. 6.16. Here ϕ_{LO}^2 and ϕ_{VO}^2 pertain to the cases when all the mixture in the channel is either only liquid or only vapor, at a mass flux of G.

$$\left(-\frac{dP}{dZ}\right)_{TP,F} = \phi_L^2 \cdot \left(-\frac{dP}{dZ}\right)_{L,F} = \phi_V^2 \cdot \left(-\frac{dP}{dZ}\right)_{V,F} \tag{6.15}$$

$$\left(-\frac{dP}{dZ}\right)_{TP,F} = \phi_{LO}^2 \cdot \left(-\frac{dP}{dZ}\right)_{LO,F} = \phi_{VO}^2 \cdot \left(-\frac{dP}{dZ}\right)_{VO,F} \tag{6.16}$$

The definitions of the corresponding single-phase pressure drops for the above cases are given by Eqs. 6.17 and 6.18 for the liquid phase, and by Eqs. 6.19 and 6.20 for vapor phase, respectively. The Martinelli parameter, X, is the ratio of the single-phase pressure drop in the liquid phase to that in the gas phase (Eq. 6.21).

$$\left(-\frac{dP}{dZ}\right)_{L,F} = \frac{f_L \left[G(1-x)\right]^2}{2\rho_L D_h} \tag{6.17}$$

$$\left(-\frac{dP}{dZ}\right)_{LO,F} = \frac{f_{LO}G^2}{2\rho_L D_h} \tag{6.18}$$

$$\left(-\frac{dP}{dZ}\right)_{V,F} = \frac{f_V\left[Gx\right]^2}{2\rho_V D_h} \tag{6.19}$$

$$\left(-\frac{dP}{dZ}\right)_{VO,F} = \frac{f_{VO}G^2}{2\rho_V D_h} \tag{6.20}$$

$$X^2 = \left(-\frac{dP}{dZ}\right)_{L,F}\Bigg/\left(-\frac{dP}{dZ}\right)_{V,F} = \phi_V^2/\phi_L^2 \tag{6.21}$$

The numerically predicted pressure drop was used to calculate the non-dimensional two-phase multiplier. The vapor quality in the present study was estimated from the numerically predicted void fraction, in conjunction with the homogeneous flow model expression given by Eq. 6.22.

$$\alpha = \left[1+\left(\frac{1-x}{x}\right)\cdot\left(\frac{\rho_V}{\rho_L}\right)\right]^{-1} \tag{6.22}$$

The two-phase viscosity, which is a function of the vapor quality, was calculated using the correlation of McAdams et al. (1942), given by Eq. 6.23. The mixture density was determined from Eq. 6.24. μ_{TP} and ρ_{TP} were used to determine the total mass flux of the two-phase flow.

$$\mu_{TP} = \left(\frac{x}{\mu_V}+\frac{1-x}{\mu_L}\right)^{-1} \tag{6.23}$$

$$\rho_{TP} = \left(\frac{x}{\rho_V}+\frac{1-x}{\rho_L}\right)^{-1} \tag{6.24}$$

221

The variation of the two-phase multiplier, ϕ_L^2, with the Martinelli parameter, X, as obtained from the present numerical simulations and available empirical correlations in the literature, is reported in Figure 6.6. Additionally, a parity plot comparing the numerical and empirical values of ϕ_L^2, for various values of X, is reported in Figure 6.7. The mean absolute error (MAE) was estimated from Eq. 6.25 and the values are summarized in Table 6.3 along with a brief description of the expressions.

$$\left(\text{MAE}\right)_{\phi_L^2} = \frac{1}{N}\sum_N \frac{\left|\left(\phi_L^2\right)_{numerical} - \left(\phi_L^2\right)_{correlation}\right|}{\left(\phi_L^2\right)_{correlation}} \times 100\% \qquad (6.25)$$
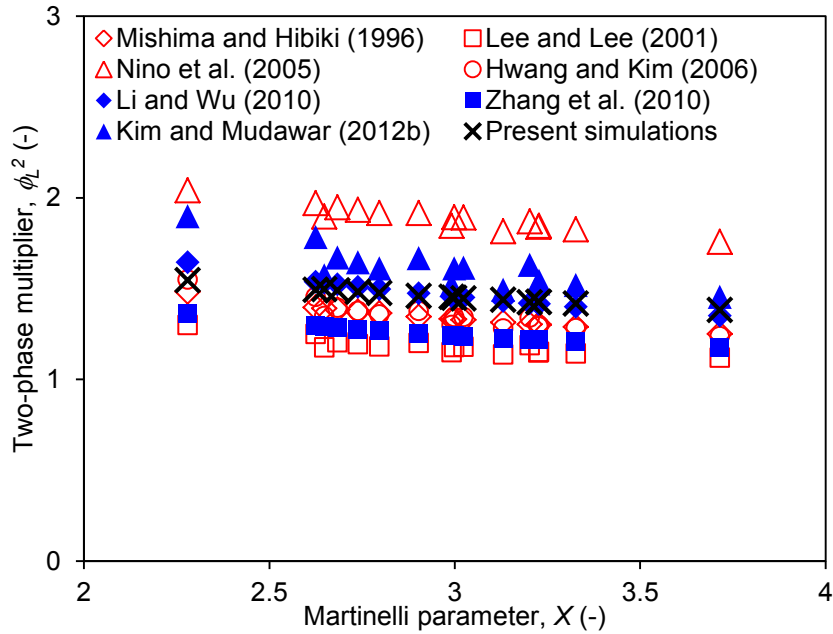
Figure 6.6: Variation of empirical and numerically predicted two-phase multiplier, ϕ_L^2, with Martinelli parameter, X.

Table 6.3: Comparison of numerically predicted two-phase frictional pressure drop with empirical correlations.

Authors	Characteristic dimensions	Working fluid(s)	MAE (%)
Mishima and Hibiki (1996)	1.05-4.08 mm	Air/water	8.5
Lee and Lee (2001)	0.78-6.67 mm	Air/water	24.9
Nino et al. (2005)	1.02-1.54 mm	Air/water, R134a, R410A	21.9
Hwang and Kim (2006)	0.244-0.792 mm	R134a	9.6
Li and Wu (2010)	0.148-3.25 mm	769 data points obtained from the literature involving 12 working fluids (55% of the data based on R134a)	1.5
Zhang et al. (2010)	0.007–6.25 mm	2201 data points obtained from the literature involving 10 working fluids	16.5
Kim and Mudawar (2012b)	0.0695–6.22 mm	7115 data points obtained from the literature involving 17 working fluids	8.1
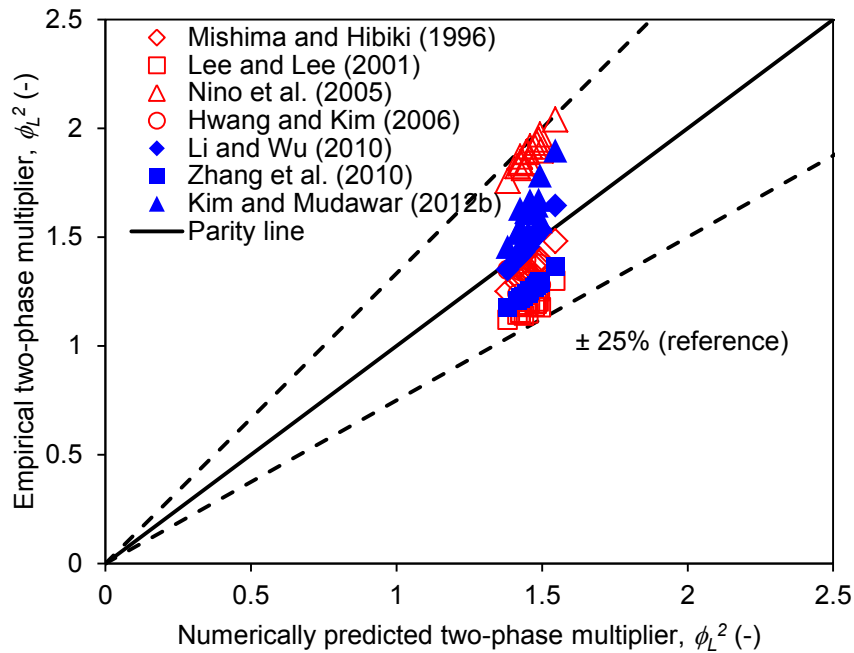
Figure 6.7: Validation of two-phase frictional pressure drop by comparing numerically predicted two-phase multiplier, ϕ_L^2, with empirical correlations. All predictions are within an MAE of 25%.

A good agreement, with an MAE less than 25%, was obtained with the correlations by Mishima and Hibiki (1996), Lee and Lee (2001), Nino et al. (2005), Hwang and Kim (2006), Li and Wu (2010), Zhang et al. (2010) and Kim and Mudawar (2012b). Particularly, it is worth mentioning the recent expression by Kim and Mudawar (2012b) which was proposed as a universal approach for two-phase frictional pressure drop. The same was developed based on a large database comprising 7115 experimental data points from the literature for adiabatic and condensing flows largely in minichannels and microchannels (69.5 μm to 6.22 mm) involving 17 working fluids. The present simulations yielded an MAE of 8.1% with the above-described universal approach. All of the above were considered indicative of the

reasonably good predictive accuracy of the current numerical model with respect to pressure drop.

6.2.2.4   Two-phase Nusselt number

The two-phase heat transfer coefficient was estimated from Eq. 6.26 and subsequently used to calculate the Nusselt number from Eq. 6.27. The calculated Nusselt number was compared against the empirical correlations listed in Table 6.4 by Shah (1979), Dobson and Chato (1998), and Shah (2009) where the MAE values were estimated from Eq. 6.28.

$$h_{TP} = \frac{q''}{T_{sat} - T_{wall}} \tag{6.26}$$

$$Nu_{TP} = \frac{h_{TP}D}{k_L} \tag{6.27}$$

$$\left(\text{MAE}\right)_{Nu_{TP}} = \frac{1}{N}\sum_{N} \frac{\left|\left(Nu_{TP}\right)_{numerical} - \left(Nu_{TP}\right)_{correlation}\right|}{\left(Nu_{TP}\right)_{correlation}} \times 100\% \tag{6.28}$$

The results are reported in Figure 6.8, and MAE values of 19.1%, 16.6% and 20.2% were obtained with the correlations of Shah (1979), Dobson and Chato (1998), and Shah (2009), respectively. While these expressions do have their own accuracy when compared to various sources of experimental data in the literature, the presently obtained values of MAE were considered to be indicative of a reasonably acceptable level of predictive accuracy of the current numerical formulation with respect to heat transfer characteristics during condensation in microchannels. Additionally, it is worth noting that the expressions listed in Table 6.4 were predominantly developed

225

for conventional channel sizes only. Given this fact, it is interesting to observe the

good predictive accuracy of these expressions for the present 100 μm channel.
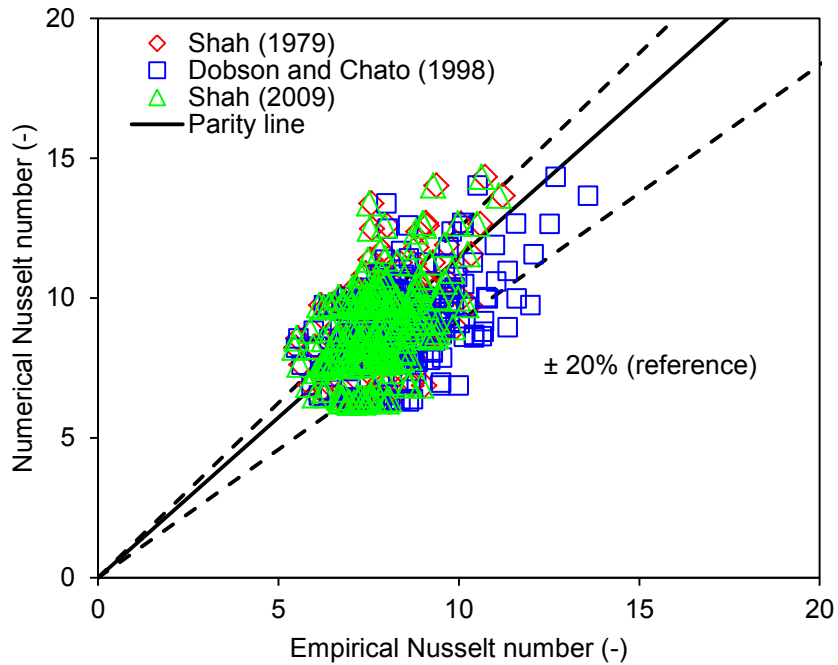
Figure 6.8: Validation of numerically predicted two-phase Nusselt number by comparison with empirical correlations.

Table 6.4: Comparison of numerically predicted two-phase Nusselt number with empirical correlations.

Author(s)	Characteristic dimension	Working fluids	MAE (%)
Shah (1979)	7.4-40 mm	473 data points obtained from the literature involving 10 working fluids	19.1
Dobson and Chato (1998)	3.14-7.04 mm	R12, R22, R134a, R32/R125	16.6
Shah (2009)	2-49 mm	1189 data points obtained from the literature involving 22 working fluids	20.2

However, numerous recent works have found the same expressions to be suitable for mini/microchannel applications. The correlation by Shah (1979) compared well against the experimental data of Shin and Kim (2004) for condensation in a 690 μm channel. Likewise, Derby et al. (2012) studied square, triangular and semi-circular cross-sections in a 1 mm channel and reported that their experimental condensation data for all cross-sections were in best agreement with the expressions by Shah (1979) and Shah (2009), as compared to certain available alternatives. Kim and Mudawar (2012a) have demonstrated the effectiveness of the correlations by Shah (1979) and Dobson and Chato (1998) in predicting their experimental data for condensation in a 1 mm channel. The current results serve as additional verification of the suitability of the presently tested conventional channel correlations for micro-level length scales as well.

The variation of Nusselt number with inlet vapor mass flux for various levels of wall heat flux is reported in Figure 6.9. The trend indicating an increase in Nusselt number with increasing mass flux can be attributed to the relative dominance of certain flow regimes over a larger portion of the channel length at different mass flux levels. Additionally, the Nusselt number curves have a steep positive slope with respect to increasing mass fluxes, which is a characteristic feature of condensation associated with high levels of vapor quality (Wang et al., 2002), as was the case in the present study, which considered superheated vapor at the inlet.
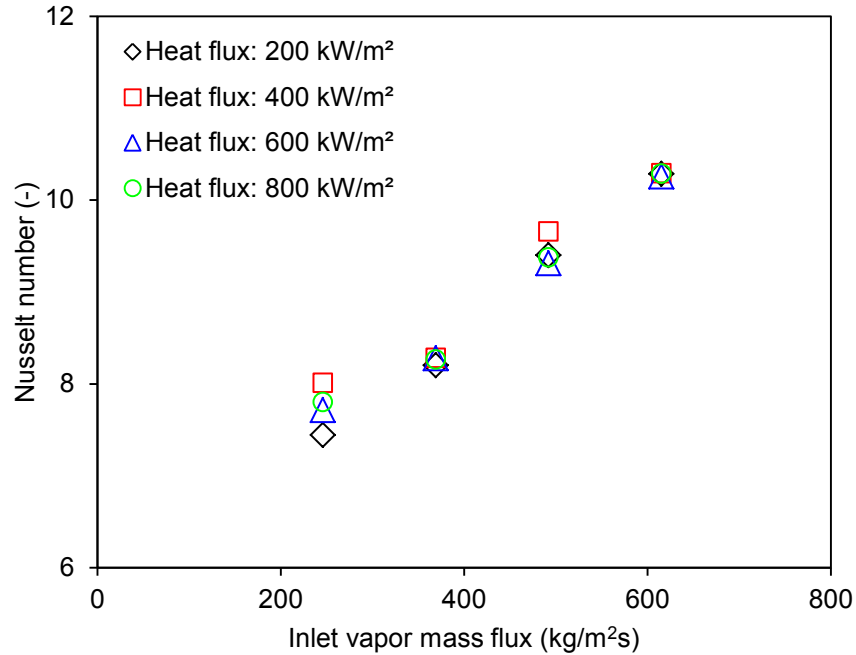
Figure 6.9: Variation of two-phase Nusselt number with inlet vapor mass flux for different levels of wall heat flux.

6.2.3 Inferences from modeling of condensation

The current section proposed a purely theoretical modeling approach for the simulation of condensation heat transfer in microchannels. The developed model was based on the volume of fluid method for governing the hydrodynamics of the liquid and vapor phases. Source terms were defined in the governing equations for volume fraction and energy in order to account for the heat and mass transfer due to condensation. All simulations were based on a channel with characteristic dimension of 100 μm and R134a as the working fluid. The numerically simulated condensation flow regimes were qualitatively compared against available experimental visualization data, and a favorable agreement was obtained. Further, the quantitative predictive accuracy of the proposed model was assessed by comparing the two-phase

frictional pressure drop and two-phase Nusselt number against numerous empirical correlations in the literature, and a reasonably good agreement was obtained. The two-phase pressure drop was predicted within an MAE of 8.1% with a recent universal predictive approach reported in the literature. The Nusselt number was predicted within an MAE of 16.6% with an empirical correlation available in the literature. Based on the validation studies performed in the present work, the proposed numerical formulation was concluded to have a reasonable level of predictive accuracy that supports its potential application towards the simulation of condensation heat transfer in more complex microscale geometries as a design tool for the development of next-generation, ultra-compact, phase-change heat exchangers.

6.3 Modeling of reactive gas-liquid absorption

6.3.1   Numerical model

6.3.1.1   Governing equations

The model was implemented in a commercial CFD code, ANSYS FLUENT version 14.5.7 (Ansys, Inc.). The numerical model for multiphase flow solved the equations for continuity, momentum conservation and energy conservation, as given by Eqs. 6.29-6.31, respectively.

$$\frac{\partial \rho}{\partial t} + \nabla \cdot (\rho \mathbf{V}) = 0 \qquad (6.29)$$

$$\frac{\partial}{\partial t}(\rho \mathbf{V}) + \nabla \cdot (\rho \mathbf{V} \ \mathbf{V}) = -\nabla P + \nabla \cdot \left[\mu \left(\nabla \mathbf{V} + \nabla \mathbf{V'} \right) \right] + \mathbf{F} \qquad (6.30)$$

$$\frac{\partial}{\partial t}(\rho E) + \nabla \cdot \left[\mathbf{V} (\rho E + P) \right] = \nabla \cdot \left(k_{eff} \nabla T \right) + S_h \qquad (6.31)$$

The multiphase flow was modeled by a finite volume method-based implementation of the VOF approach (Hirt and Nichols, 1981). The surface tension forces were modeled following the continuum surface force (CSF) formulation of Brackbill et al (1992). This approach models the pressure jump across the interface as a volume force that is included as a source term in the momentum equation. Additionally, the VOF model solves an equation for volume fraction, α, wherein for a multiphase system with k phases, Eq. 6.32 is solved for n-1 phases, and the volume fraction of the excluded phase (termed the primary phase) is determined by the summation expression in Eq. 6.33. The right-side terms in Eq. 6.32 correspond to the net mass transfer to the ith phase from all other phases.

$$\frac{\partial \rho_i \alpha_i}{\partial t} + \nabla \cdot \left(\rho_i \alpha_i \mathbf{V}_i \right) = \sum_{j=1}^{n_{phase}} \left(i^{\cdot} \qquad \cdot \right) \qquad (6.32)$$

$$\sum_{i=1}^{n_{phase}} \alpha_i = 1 \qquad (6.33)$$

The convection-diffusion equation is solved for all, but one of the reaction species and is given by Eq. 6.34 for the kth specie. The summation equation given by Eq. 6.35 is used to calculate the mass fraction of the excluded specie. Here, J_k represents the diffusion flux and R_k represents the net rate of production of the kth specie by chemical reaction. The rate of the heterogeneous chemical reaction (Eq. 6.36) was

specified by a user-defined function written in C language and compiled by the

ANSYS FLUENT code. It follows the reaction kinetics detailed in Section 3.2.4 for

the CO_2-DEA mass transfer system. The nature of Eq. 6.36 is such that the reaction

rate is negligible throughout the computational domain, except at the gas-liquid

interface. The concentration of CO_2 at the interface is based on Henry's law. The

reaction rate is scaled by a regression-based grid resolution factor, α, to accurately

capture the effect of interfacial concentration gradients (Eq. 6.37). This was derived

as a function of the liquid phase Reynolds number since the present mass transfer

system (CO_2-DEA) is dominated by mass transfer resistances on the liquid side,

whereas the gas-side resistances are negligible. The constants k_2, k_2K_{H2O}/k_{-1}, k_2k_{DEA}/k_{-1}

equal 3.24, 1.71×10^{-6}, 7.07×10^{-4}, respectively (Versteeg and Oyevaar, 1989). The

constants ϕ_1 and ϕ_2 were determined to equal 0.12 and 0.18, respectively.

$$\frac{\partial}{\partial t}(\rho Y_k) + \nabla \cdot (\rho \mathbf{V} Y_k) = -\nabla \cdot (J_k) + R_k \tag{6.34}$$

$$\sum_{k=1}^{n_{specie}} Y_k = 1 \tag{6.35}$$

$$R_{CO_2} = \frac{\left[(CH_2CH_2OH)_2 \, NH\right][CO_2]}{\dfrac{1}{k_2} + \dfrac{k_{-1}}{k_2k_{H_2O}[H_2O] + k_2k_{(CH_2CH_2OH)_2 \, NH}\left[(CH_2CH_2OH)_2 \, NH\right]}} \tag{6.36}$$

$$\alpha = \phi_1 \, \mathrm{Re}_L^{\phi_2} \tag{6.37}$$

The effective fluid properties such as density and viscosity were computed as the

average property values of the two phases, weighted by their respective volume

fractions. Interface reconstruction was performed using the explicit piecewise-linear

interface construction (PLIC) scheme of Youngs (1982). A pressure-based solver

with an unsteady first-order implicit formulation was utilized. The SIMPLE algorithm

was used for the pressure-velocity coupling along with the PRESTO (pressure

staggering option) scheme. The momentum equation was discretized using a second-

order upwind scheme and a least square cell-based scheme for calculating the

gradients of scalar variables were utilized. Any increase in temperature due to the

exothermic nature of the reaction was deemed negligible as understood from

experimental measurements, and hence not modeled in this work.

6.3.1.2 Computational domain

A single channel microreactor was modeled with a three-dimensional domain. The

hydraulic diameter was 762 μm and reactor lengths of 0.01 m and 0.02 m were

studied. A velocity boundary condition was specified at the channel inlets for the gas

and liquid phases, and a pressure-based boundary condition was specified at the

channel outlet. The effects of surface wetting at the channel wall were modeled by

specifying a contact angle (0°) to ensure complete wetting as suggested by Killion

and Garimella (2005).

The entire domain was discretized with a homogeneous structured grid consisting of

quadrilateral elements with a size of 40 μm (D/20). The use of a locally refined grid

near the channel wall was not considered in order to enable maintaining a constant

resolution of the gas-liquid interface throughout the computational domain.

Furthermore, this strategy does not facilitate capturing the spatially fine flow features

that occur in regions away from the channel wall. For these reasons, a uniform grid was utilized in the present study.

6.3.1.3   Simulation conditions

The gas phase comprised CO_2 mixed with N_2 at a concentration of 10% by mass. The liquid solvent was aqueous diethanolamine at 20% concentration by mass. The gas phase inlet velocity ranged from 1.8-9.1 m/s, while that of the liquid phase ranged between 0.04-0.4 m/s. The Bond number criterion of Brauner and Moalem-Maron (1992), $Bo < (2\pi)^2$, was used to verify that at the present length scale, the surface tension forces were indeed dominant over gravitational forces and hence the latter could be neglected.

6.3.1.4   Solver settings

The transient solution for the governing equations was obtained using an explicit scheme for which the Courant number was used to adopt a variable time-stepping strategy. The Courant number for solving the volume fraction equation was restricted to 0.25, while that for the remaining governing equations was restricted to a higher value of 2. With these settings multiple flow patterns were captured which was considered an indication of the appropriateness of the above solver settings (Krishnan et al., 2010). Similar values have been reported by Qian and Lawal (2006), Liu and Wang (2008), and Gupta et al. (2010).

6.3.2 Results and discussion

6.3.2.1 Model validation

Grid independent was verifying by based on non-dimensions bubble lengths obtained using a range of element sizes. As seen in Figure 6.10, the discrepancy between the 40 μm (D/20) and the 15 (D/50) μm cases was 9.1%. Given the computationally intensive nature of the present simulations, the 40 μm case was deemed to be sufficiently accurate and utilized for subsequent simulation cases. Next, the numerically predicted mass transfer performance parameters, namely the absorption efficiency and mass transfer coefficient, were compared using data derived from the experiments reported in Chapter 3. The time-averaged concentration obtained from the numerically predicted results was used to calculate these parameters for which a sufficiently large set of transient data points were considered. A wide range of operating conditions were considered that included variations in the gas and liquid phase velocities, as well as the channel length. Data points with close to 100% absorption efficiency were not considered since such cases do not give any significant insight into the predictive accuracy of the model.

As can be seen in Figure 6.11, the absorption efficiencies were in good agreement with an MAE of 8.3%. Likewise, the mass transfer coefficient data in Figure 6.12 was predicted within an MAE of 9.5%. These results were considered an indication of the successful ability of the present numerical model to simulate reactive gas-liquid absorption in microreactors.
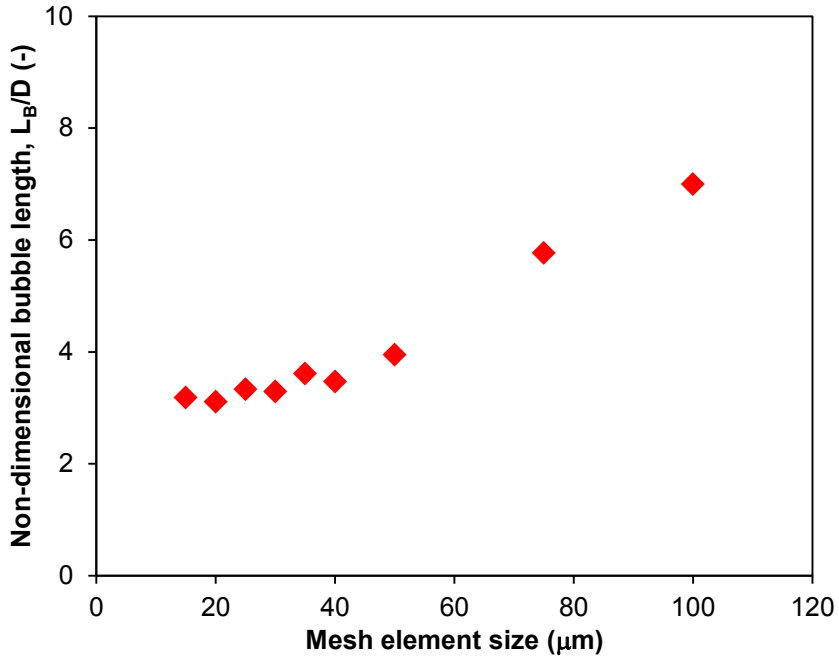
Figure 6.10: Analysis of grid independence.
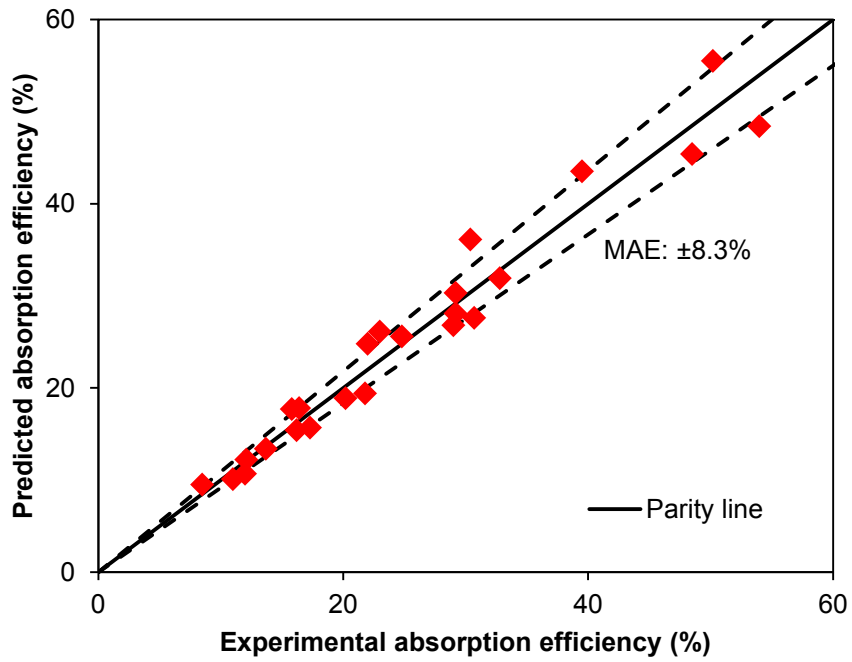
Figure 6.11: Comparison of experimental absorption efficiencies with model
predictions.
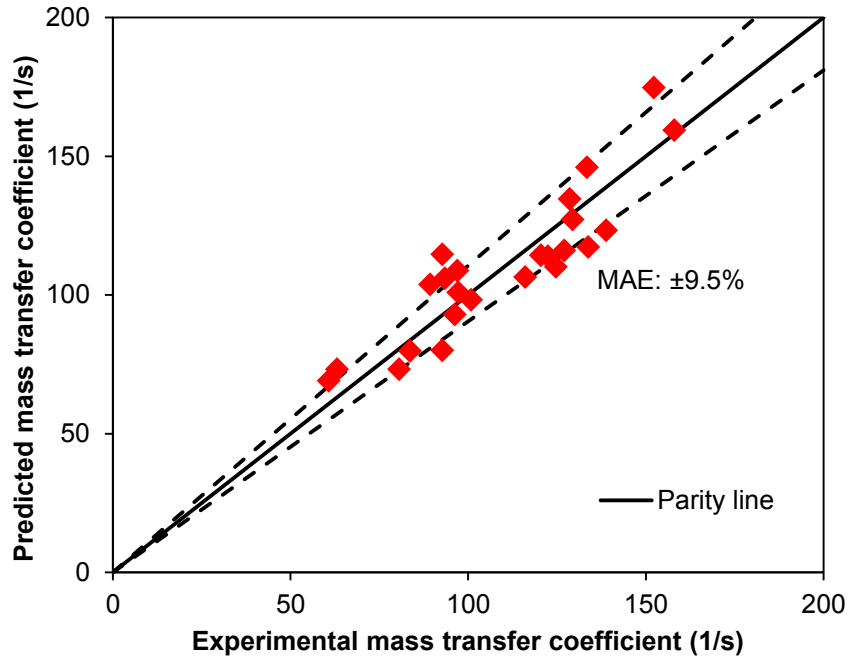
Figure 6.12: Comparison of experimental mass transfer coefficients with model predictions.

6.3.2.2 Flow patterns

Depending upon the relative magnitudes of gas and liquid phase superficial velocities, a range of two-phase flow regimes were predicted by the numerical model including bubbly flow, slug flow, slug-annular flow, annular flow, and churn flow. Detailed descriptions of these regimes were already provided in Chapter 3. A qualitative comparison of these with experimental visualization data is reported in Figure 6.13. Additionally, the transition lines between the regimes were compared against available data in the literature and a reasonably good agreement was obtained (Figure 6.14). The minor differences in transition criteria can be attributed to the difference in hydraulic diameter (762 μm presently versus 530 μm in Chung and Kawaji, 2004).

Figure 6.13: Qualitative comparison of numerically predicted flow regimes with high-speed visualization images (a) bubbly flow (U_G: 5 m/s, U_L: 0.5 m/s); (b) slug flow (U_G: 0.1 m/s, U_L: 0.1 m/s); (c) slug-annular flow (U_G: 0.11 m/s, U_L: 1.8 m/s); (d) annular flow (U_G: 9.1 m/s, U_L: 0.04 m/s); (e) churn flow (U_G: 9.1 m/s, U_L: 0.4 m/s).
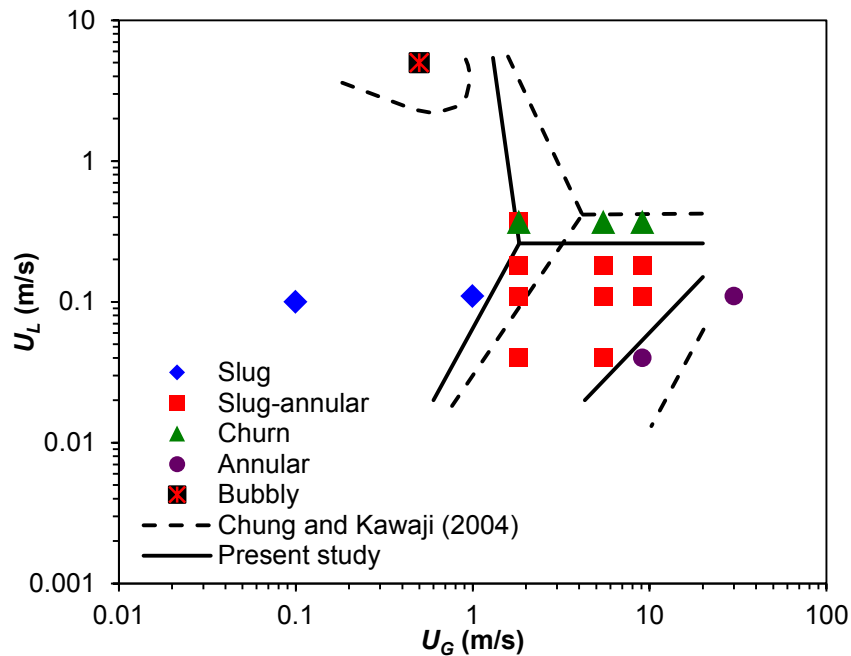
Figure 6.14: Flow regime map.

6.3.2.3 Parametric studies

The first set of parametric studies varied the gas and liquid flow rates. Accordingly, the superficial velocity was varied between 1.8-9.1 m/s for the gas phase and between 0.04-0.4 m/s for the liquid phase. As can be seen in Figure 6.15, the absorption efficiency is larger at small gas velocities and high liquid velocities. The corresponding results of mass transfer coefficient reported in Figure 6.16 indicate higher values at larger gas and liquid flow rates.
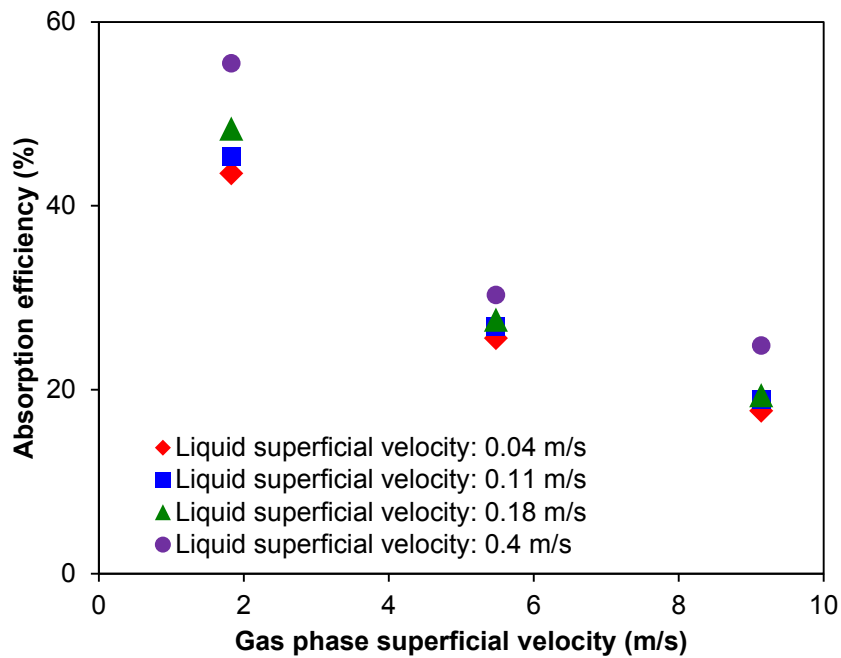
Figure 6.15: Effect of phase velocity on absorption efficiency.
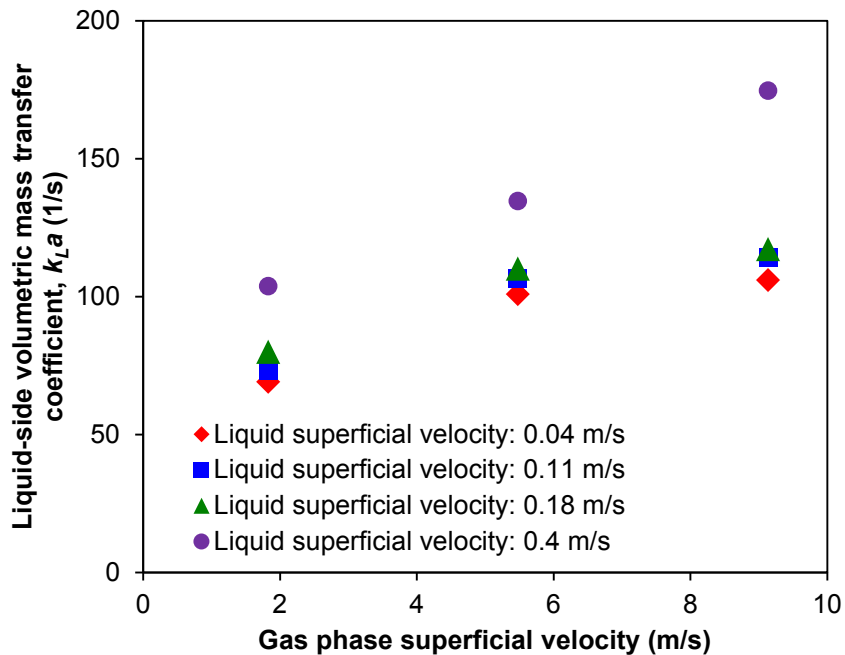
Figure 6.16: Effect of phase velocity on liquid-side volumetric mass transfer coefficient.

Next, the effect of reactor length was studied. As can be seen in Figure 6.17, the higher residence time associated with longer reactors resulted in higher absorption efficiencies. However, the decreased utilization of the absorption capacity of the amine solution per unit volume of the reactor resulted in lower mass transfer coefficients (Figure 6.18). All of the above-described trends are in agreement with the previously reported experimental analyses and serve as an indication of the potential applicability of the presently proposed model for design and scaling-up of microreactors.
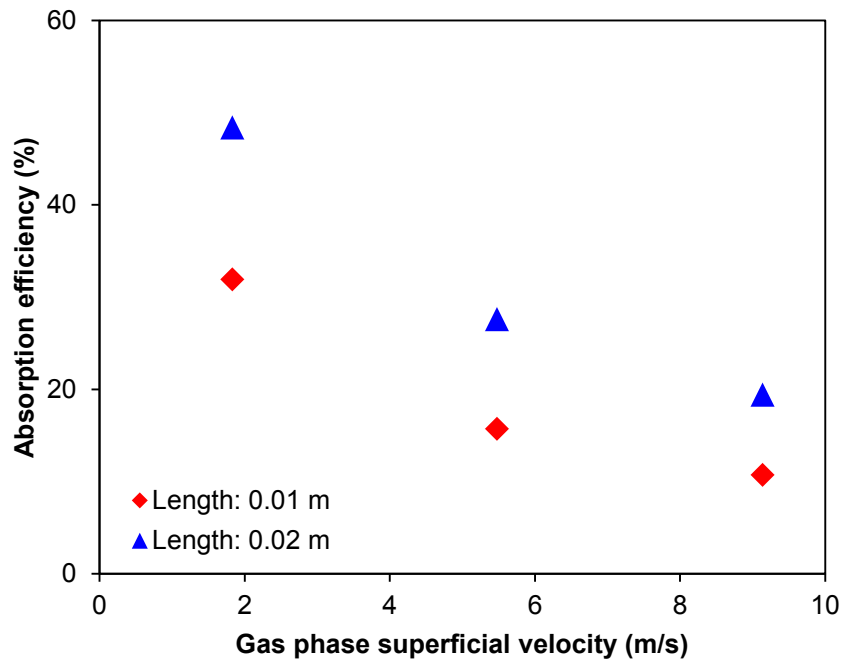
Figure 6.17: Effect of reactor length on absorption efficiency.
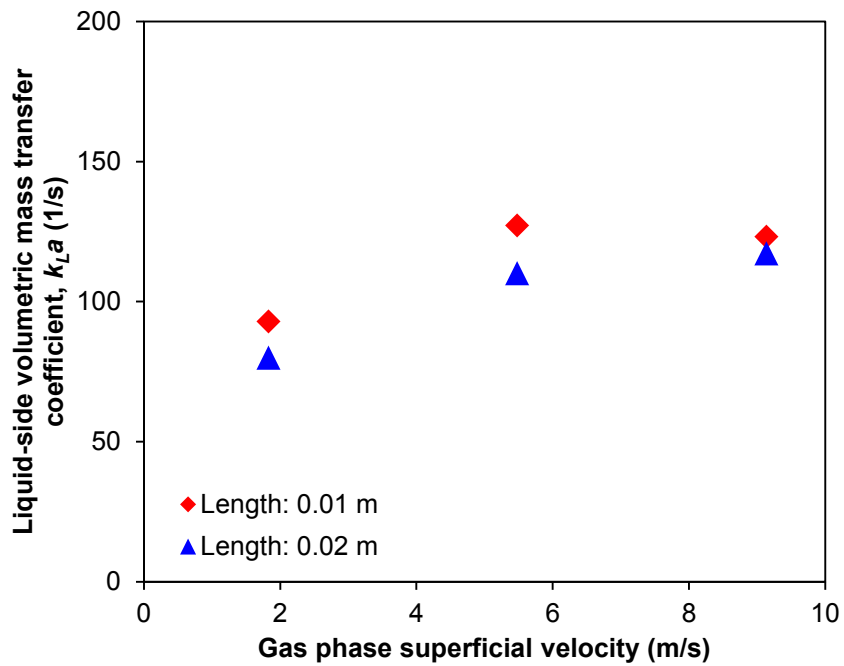
Figure 6.18: Effect of reactor length on liquid-side volumetric mass transfer coefficient.

240

6.3.3   Inferences from modeling of reactive gas-liquid absorption

The current section proposed a numerical model for reactive gas-liquid absorption in a microreactor. The approach implemented the volume of fluid method for governing the two-phase flow, and a heterogeneous reaction was defined to model the mass transfer. A single channel microreactor having hydraulic diameter of 762 μm was considered with CO_2 mixed with N_2 as the gas phase and aqueous DEA as the liquid phase. The numerically simulated two-phase flow regimes were favorably compared against experimental visualization data and a regime transition map was developed. Two mass transfer performance parameters, namely the absorption efficiency and mass transfer coefficient, were determined and compared against experimental data. A good agreement was obtained for both cases within an MAE of 8.3% and 9.5%, respectively. Additionally, parametric studies varying the phase flow rate and reactor length (residence time) were conducted. The observed trends were found to be in good agreement with presently obtained experimental data, as well as the literature. On the whole, the proposed numerical formulation was concluded to have a reasonable level of predictive accuracy that supports its potential application for the design and scaling up of microreactors for enhanced gas-liquid absorption processes.

6.4 Chapter conclusions

This chapter focused on the modeling of flow regime, heat and mass transfer in microchannel geometries. The ability to simulate unsteady two-phase interfaces was investigated. First, the condensation process was modeled which involved mass transfer due to a temperature gradient. This model was based on the volume of fluid

method, and involved defining source terms to simulate the heat/mass transfer due to the condensation phenomena. It was based on a channel with characteristic dimension of 100 μm and with R134a as the working fluid. Various flow regimes were simulated and favorably compared against available experimental visualization data. The two-phase pressure drop and Nusselt number were predicted within MAEs of 8.1% and 16.6% with empirical correlations.

Second, gas-liquid absorption driven by a chemical reaction was modeled. This approach was also based on the volume of fluid method, and involved modeling the mass transfer by defining a heterogeneous chemical reaction. It was based on a channel with characteristic dimension of 762 μm and for the CO_2-DEA mass transfer system. Numerically simulated flow regimes were compared against experimental visualization data and a good agreement was obtained. Subsequently, a flow regime map was developed, and the presently observed regime transition lines were compared against those previously reported in the literature. The absorption efficiency and mass transfer coefficient were predicted within MAEs of 8.3% and 9.5%, respectively, as compared to experimental results. Parametric studies varying the gas and liquid flow rates, as well as the reactor length were performed, and the results were found to be consistent with the physics of the process. In conclusion, the presently proposed models for heat/mass transfer across unsteady interfaces in two-phase flow have good predictive accuracy and can be potentially applied towards the design and optimization of scaled up microscale heat/mass transport systems featuring enhanced transport phenomena.

Chapter 7: Experimental Study of Multiport Microreactors

7.1 Introduction

This chapter reports an experimental analysis of the fluid flow and mass transfer characteristics during the absorption of CO_2 mixed with N_2 in aqueous DEA in multiport microreactors which represent an order of magnitude increase in the scale of the system over the reactors studied in Chapter 3. Three types of analyses were conducted to characterize the absorber performance. Section 7.2 focuses on open-loop testing wherein only the absorber was present in the test loop and fresh amine solution was supplied to characterize its performance. Section 7.3 focuses on closed-loop testing wherein a regeneration system is incorporated to strip CO_2 from the loaded amine solution leaving the absorber in order to permit its re-use, as is done in practical industrial systems. Section 7.4 focuses on studying the effect of residence time (channel length) using a closed-loop experimental setup configuration. In all cases, the performance is characterized with respect to absorption efficiency, mass transfer coefficient, and pressure drop. Parametric studies varying the flow rates of the gas and liquid phases, liquid phase reactant concentration, and gas phase concentration are conducted.

7.2 Absorber performance characterization: open-loop testing

7.2.1 Description of experiments

7.2.1.1 Experimental setup

The multiport minichannel channel absorber comprised 15 straight, parallel channels machined on an aluminum substrate (Figure 7.1). This material was chosen on account of its ease of machining. The CNC machining process was designed to produce channels having square cross-sectional geometry corresponding to an aspect ratio of unity, and the length of the channels equaled 0.455 m. The targeted hydraulic diameter during the machining process was 500 μm.

The gas and liquid phases were supplied to the absorber at their respective manifolds shown in Figure 7.1a. A single port was used to supply the liquid phase to all the channels, while 15 separate ports were present to supply the gas phase to each channel. The two-phase mixture exited the absorber through a common outlet port. A circumferential groove for a gasket was machined on the aluminum substrate for a gasket. Multiple threaded holes were tapped along the edges of the aluminum substrate and along that of a similar-sized block of polymethyl methacrylate (PMMA), as shown in Figure 7.1a. Accordingly, each channel had a metallic wall on three sides, and a PMMA surface on the top. As can be seen from Figure 7.1, the present absorber had a cross-flow inlet configuration with liquid being admitted along the main channel.
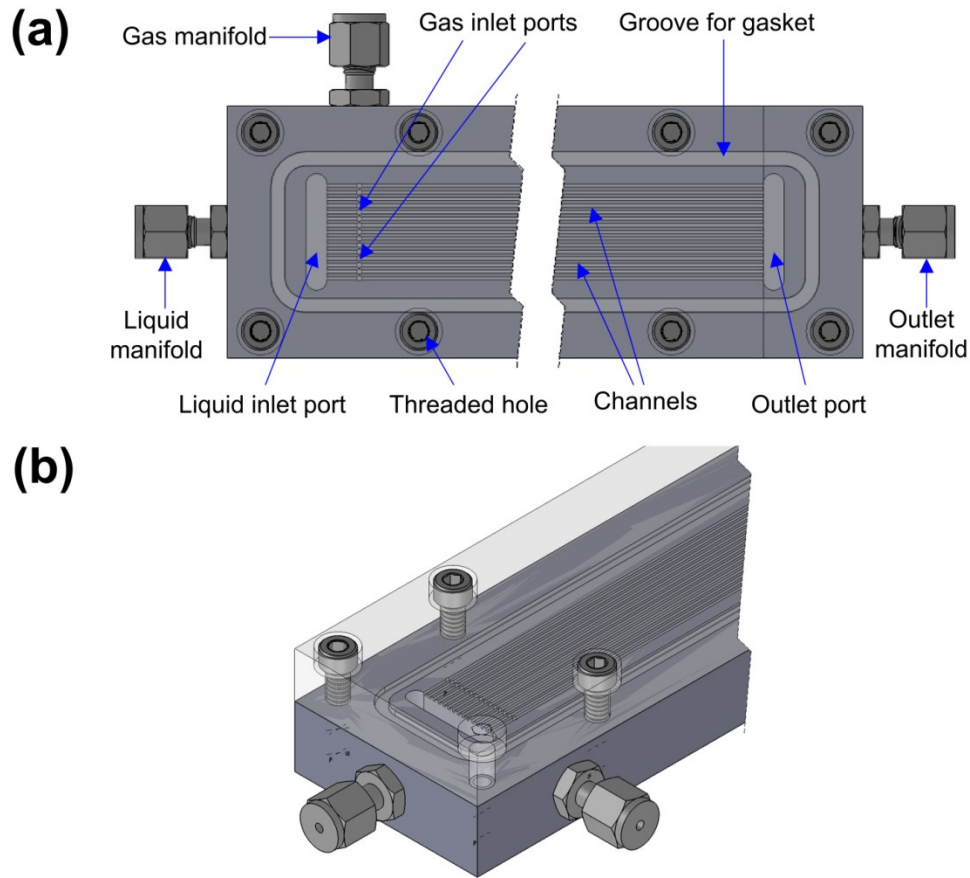
Figure 7.1: Schematic diagram of reactor (a) top view of reactor without cover (b) isometric view of reactor with cover.

On account of the extremely small values of cross-sectional dimensions of the channel, it was not feasible to obtain an accurate verification of the design values (500 μm for both the channel width and height) by using the conventional measurement techniques available to the authors. Further, it is quite plausible to conceive that clearance spacing, albeit marginal in magnitude, could exist between the metallic base of the absorber and the PMMA cover that would not be measurable when the absorber is sealed. Hence, the effective hydraulic diameter of the channels were determined by obtaining measurements of single-phase pressure drop separately for gas and liquid flow, and comparing the same with an established theoretical

correlation in the literature. A thorough experimental procedure was followed for the same, as detailed subsequently, that accounted for the effects of the inlet regions, and accordingly, a hydraulic diameter of 456 μm was obtained.
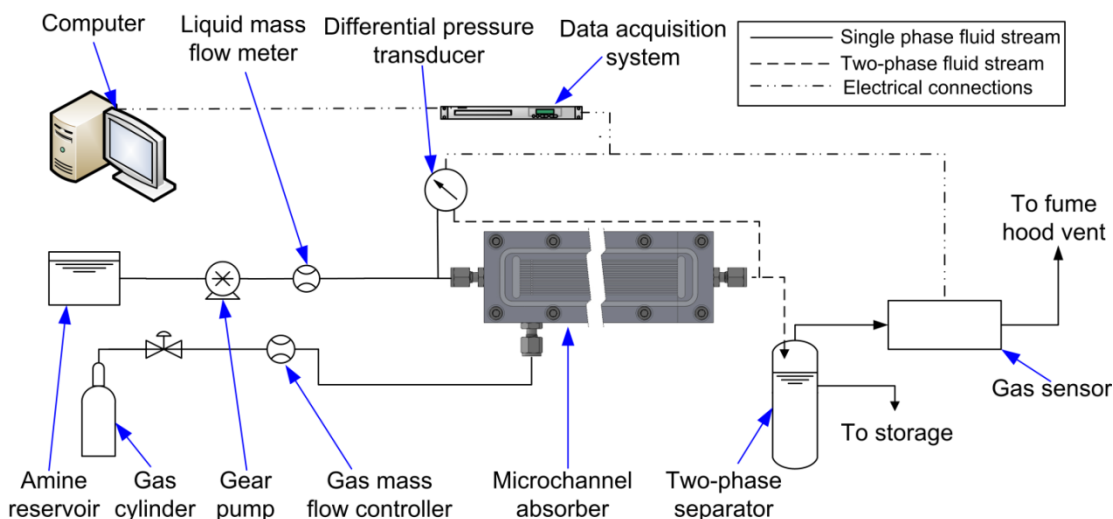
Figure 7.2: Layout of experimental test loop.

The layout of the test loop is reported in Figure 7.2. A variable speed gear pump (Micropump Inc., USA) was used to control the liquid flow rate which was subsequently measured by a Coriolis mass flow meter (Endress+Hauser Inc., USA). The gas flow rate was measured and controlled by a differential pressure-based mass flow controller (Cole-Parmer, USA). A differential pressure transducer (Honeywell International Inc., USA) was connected across the liquid inlet and the channel outlet. The two-phase mixture leaving the absorber entered a two-phase separating column. The column comprised of vertically installed tubing (ID: 10 mm) that performed gravity-based separation of the loaded amine solution from the unabsorbed gas stream. Further, a level-control mechanism was incorporated in order to maintain a relatively constant level of liquid in the separation column. This arrangement resulted

in unabsorbed gaseous stream entering the gas sensor for analysis, while the loaded

amine solution was continuously removed from the experimental setup. The CO_2

concentration was measured continuously in-line with the fluid flow, by a non-

dispersive infrared (NDIR) sensor (Vaisala Inc., USA). Based on the difference in

concentration levels at the inlet and outlet of the absorber, the absorption efficiency

was defined as given by Eq. 7.1.

$$\eta_{abs} = \frac{C_{CO_2,in} - C_{CO_2,out}}{C_{CO_2,in}} \times 100\% \qquad (7.1)$$

7.2.1.2 Operating conditions

The gas phase was CO_2 mixed with N_2 at concentration levels of 2.5-10% by mass,

and was of industrial grade purity. The liquid phase was aqueous amine solution

prepared using laboratory grade DEA (99% purity). The amine was diluted with

distilled water to concentration levels ranging from 5-20% by mass. The gas and

liquid flow rates were varied such that the range of Reynolds numbers for each phase

varied between 15 to 151, and 19 to 93, respectively. All experiments were conducted

at an ambient temperature of 298 K and at atmospheric pressure.

7.2.1.3 Uncertainty analysis

The uncertainty in the measurement of CO_2 concentration was ±3% of the reading

and ±1.5% of the full scale range of the device (20% concentration of CO_2 by mass).

The gas flow rate was measured with an uncertainty of ±0.8% of the reading and

±0.2% of the full scale range of the device (8.33×10^{-5} m^3/s). The uncertainty in liquid

flow rate and pressure drop equaled ±0.1% and ±0.25% of the readings, respectively.

By following the error propagation method, the average uncertainty in absorption

efficiency was determined to equal ±16.7%. The results were repeatable within ±2.3.

7.2.2   Results and discussion

7.2.2.1   *Analysis of pressure drop*

The experimental test setup was validated by measuring the single-phase pressure

drop. The Darcy friction factor obtained from the measurements for nitrogen (gas)

and water (liquid) flow were compared against the theoretical predictions from Eq.

7.2 for laminar flow in rectangular channels (Shah and London, 1978) where β is the

aspect ratio equaling unity in the present study.

$$f \times \mathrm{Re} = 56\left(1 - 1.3553\beta + 1.9467\beta^2 - 1.7012\beta^3 + 0.9564\beta^4 - 0.2537\beta^5\right) \quad (7.2)$$

Since the above expression does not account for the pressure drop across the inlets

and outlet, it was required to determine the contributions due to the same, prior to

utilizing Eq. 7.2. The same was accomplished by measuring the pressure drop during

single-phase fluid flow of both gas and liquid, separately, for the three configurations

detailed in Figure 7.3 by selectively closing certain ports and permitting the fluid to

flow through the remaining ports. Here, inlets 1 and 2 refer to the phase inlets along

and perpendicular to the channel length, respectively. The components of the total

pressure drop for the configurations in Figure 7.3a, Figure 7.3b, and Figure 7.3c are

given by Eqs. 7.3, 7.4, and 7.5, respectively. While, it was not possible to

experimentally account for the expansion losses at the channel outlet, given the

substantially larger characteristic dimension of the outlet manifold, as compared to the channels, the associated loss was deemed to represent a negligibly small fraction of the total pressure drop and hence was ignored.
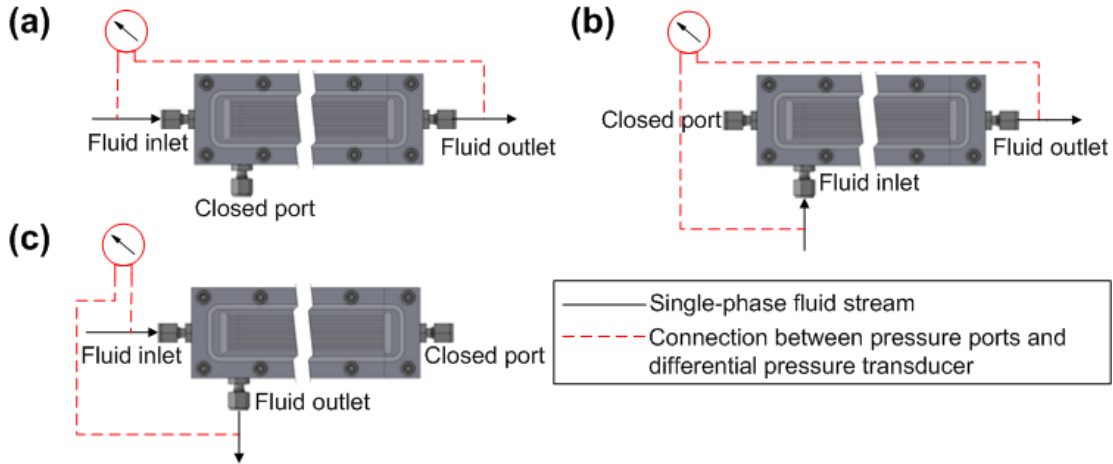
Figure 7.3: Arrangements for measurement of single phase pressure drop across (a) liquid inlet, channel, and outlet (b) gas inlet, channel, and outlet (c) liquid inlet and gas inlet.

$$\Delta P_{case1} = \Delta P_{inlet-1} + \Delta P_{channel} + \Delta P_{outlet} \tag{7.3}$$

$$\Delta P_{case2} = \Delta P_{inlet-2} + \Delta P_{channel} + \Delta P_{outlet} \tag{7.4}$$

$$\Delta P_{case3} = \Delta P_{inlet-1} + \Delta P_{inlet-2} \tag{7.5}$$

The final pressure drop in the channel is given by Eq. 7.6 and this value was used to determine the experimental Darcy friction factor (Eq. 7.7) for comparison against Eq. 7.2. With the objective of minimizing the discrepancy between the two friction factors, the hydraulic diameter of the absorber was determined to equal 456 µm.

$$\Delta P_{channel} = \frac{1}{2}\left(\Delta P_{case1} + \Delta P_{case2} - \Delta P_{case3}\right) \tag{7.6}$$

$$f = \frac{2D_h \Delta P_{channel}}{\rho L U^2} \tag{7.7}$$

As can be observed from Figure 7.4, the experimental measurements for frictional

pressure drop are in excellent agreement with the theoretical predictions, with an

MAE of only 3.2%. This established the validity of the current test loop with respect

to single-phase frictional pressure drop. It is worth noting that the pressure drop

through the inlets were less than 5% of the channel pressure drop for liquid flow and

less than 3% for gas flow. Hence, in the subsequent analysis of two-phase frictional

pressure drop, the effects of the inlet region have been safely neglected.
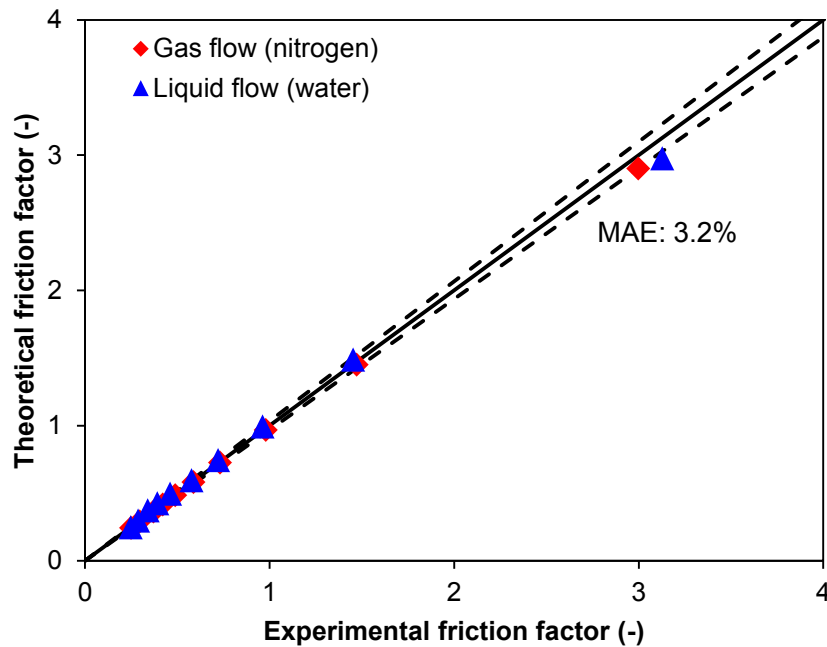
Figure 7.4: Comparison of experimental friction factor data with theoretical
predictions for single-phase flow.

The measured value, ΔP_{TP}, comprised the pressure drop due to the effects of friction and acceleration. Previous analyses have shown that the acceleration component, under the present conditions, is negligibly small, and can be neglected. Accordingly, the two-phase frictional pressure drop, $\Delta P_{TP,F}$, was used to calculate the two-phase friction multiplier, $\phi_L{}^2$. The experimental value of $\phi_L{}^2$ was compared against the predictions of Eq. 7.8. Several models exist in the literature for the Chisolm parameter, c. In the present work, a reasonably good agreement was obtained with the piecewise model proposed by Eq. 7.9 which adopts the model of Li and Wu (2010) for $Re_{TP} \le 70$, and that of Mishima and Hibiki (1996) for $Re_{TP} > 70$. The results reported in Figure 7.5 indicate a reasonably good agreement with an MAE of 9.8%.

$$\phi_L^2 = 1 + \frac{c}{X} + \frac{1}{X^2} \qquad (7.8)$$

$$c = \begin{cases} 11.9 \left[\dfrac{(\rho_L - \rho_G) g D_h^2}{\sigma} \right]^{0.45} & : \quad \mathrm{Re}_{TP} \le 70 \\ 21 \left(1 - e^{-0.319 D_h} \right) & : \quad \mathrm{Re}_{TP} > 70 \end{cases} \qquad (7.9)$$

7.2.2.2   Repeatability of mass transfer results

In order to assess the repeatability of the present setup, a typical set of measurements were repeated three times. For a fixed liquid phase Reynolds number equaling 62, the gas phase Reynolds number was varied from 15 to 151. The concentrations of the gaseous and liquid phases were 10% by mass of CO_2 in N_2, and 5% by mass of DEA in water. The results of the above analysis reported in Figure 7.6 indicate that the present measurements of absorption efficiency were repeatable within $\pm 2.3\%$.

251
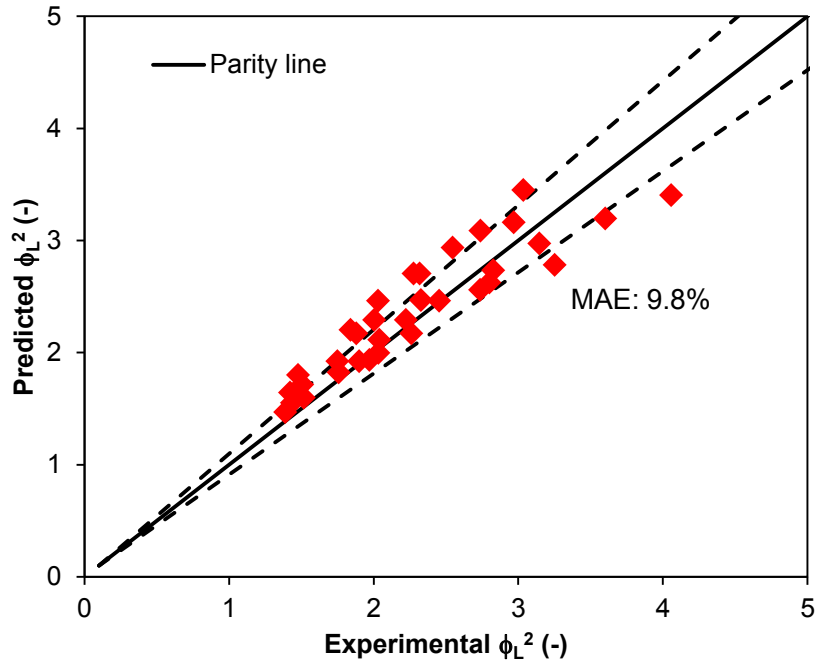
Figure 7.5: Comparison of experimental pressure drop data with theoretical predictions (a) single-phase flow (b) two-phase flow.
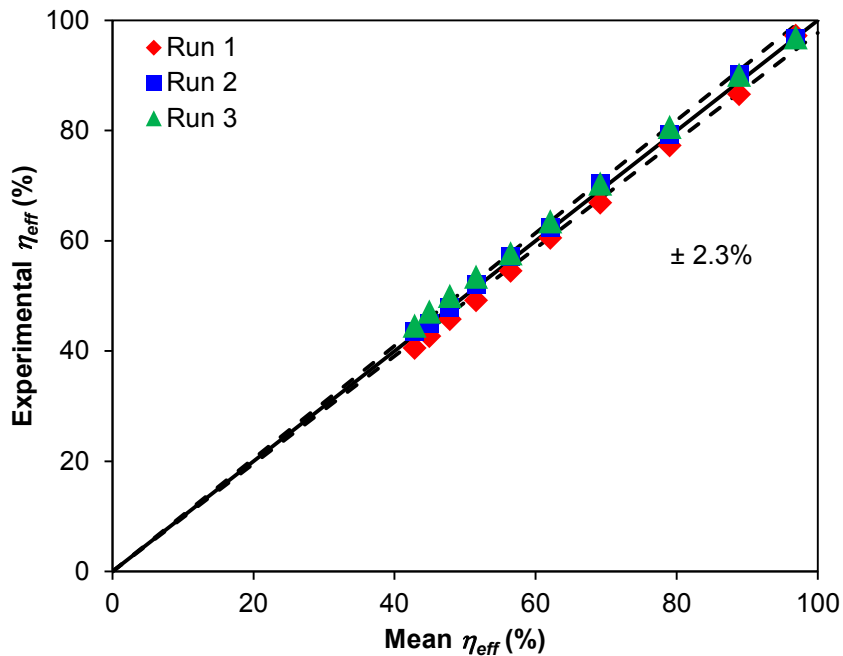
Figure 7.6: Repeatability of measurements of absorption efficiency during absorption of CO_2/N_2 mixture (10% by mass) in aqueous DEA (5% by mass) for constant liquid phase Reynolds number of 62 and gas phase Reynolds number ranging from 15 to 151.

7.2.2.3   Effect of gas and liquid flow rate

A parametric study was performed by varying the gas phase Reynolds number between 15 and 151 and the liquid phase Reynolds number between 19 and 93. These results correspond to a gas concentration of 10% by mass of CO_2 in N_2 and an aqueous amine concentration of 5% by mass of DEA in water. It is noted that for the highest value of $Re_L = 93$, it was not possible to obtain measurements for $Re_G > 75$ on account of the lack of sufficient gas pressure under these conditions to sustain two-phase flow.

The phase distribution in the channel is determined by the relative magnitudes of gas and liquid phase superficial velocities. Based on the same, different two-phase flow regimes can occur in the channel which in turn influences the mass transfer characteristics. Hence, a flow pattern map was developed using the regime transition criteria reported in the literature by Chung and Kawaji (2004). As can be seen in Figure 7.7, the dominant regimes under the present operating conditions were slug and slug-annular flow. Slug flow is characterized by an alternating arrangement of elongated, cylindrical gas bubbles and liquid slugs. A thin film of liquid separates the gas bubble from the channel wall. Convective mixing within the gas bubbles and liquids slugs is enhanced by recirculating velocity currents as observed experimentally using particle image velocimetry (King et al., 2007; Malsch et al., 2008), and by numerical simulations (He and Kasagi, 2008; Chapter 4). For a constant liquid velocity, the bubble length increases with an increase in gas velocity. Simultaneously, the forces responsible for bubble detachment become weaker until a

point when bubble detachment no longer occurs. This corresponds to the onset of slug-annular flow which is characterized by a continuous central gas core surrounded by a liquid film having periodic interfacial waves. The frequency of occurrence of these interfacial waves decreases with an increase in the gas velocity. It is also noted that with an increase in liquid velocity, the transition between slug and slug-annular regimes occurs at higher gas velocities.
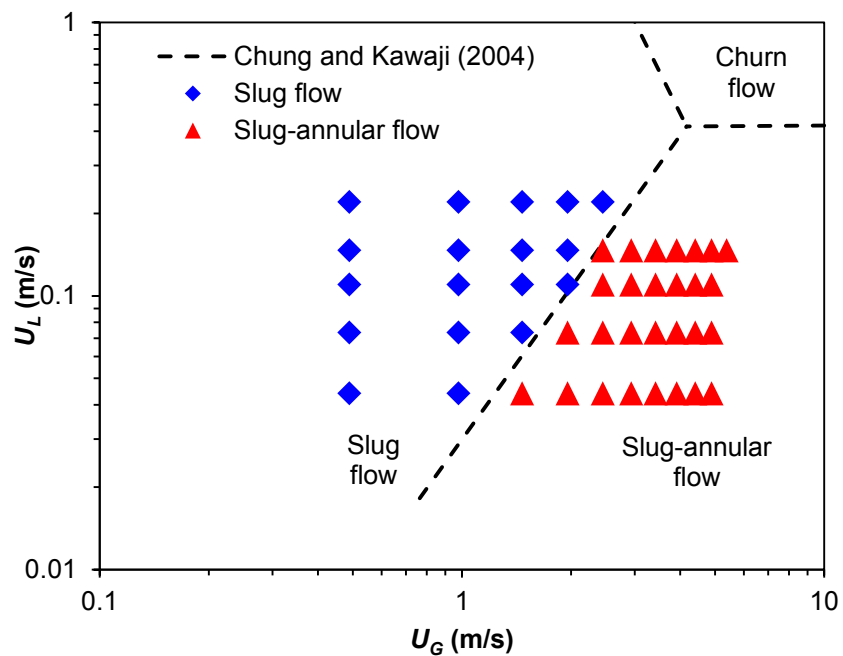
Figure 7.7: Flow pattern map with regime transition lines.

The two-phase pressure drop is reported in Figure 7.8. The pressure drop was observed to increase with an increase in either the gas or liquid flow rate, which is consistent with the physics of the phenomena.
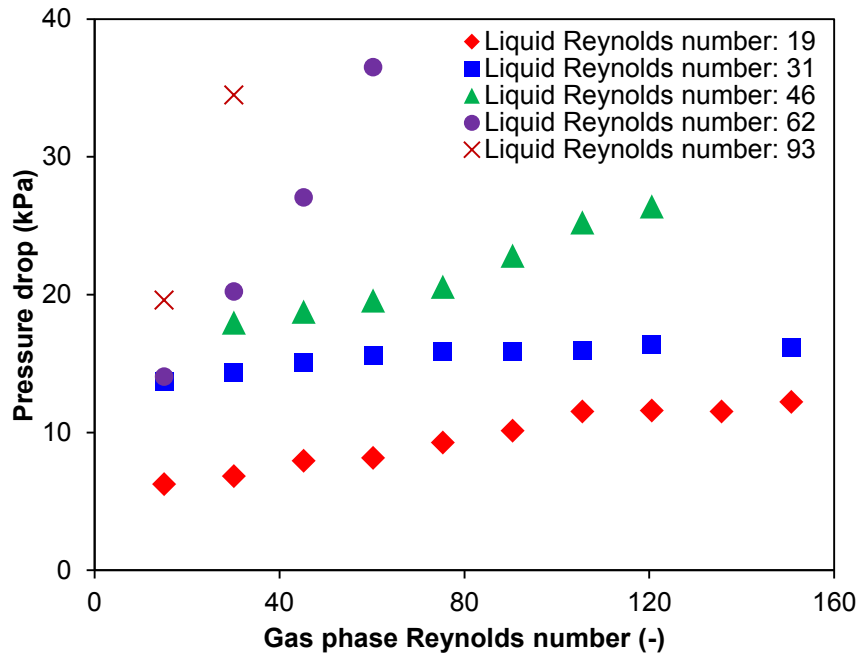
Figure 7.8: Effect of gas and liquid flow rate on two-phase pressure drop (C_{CO2}: 10% by mass of CO_2 in N_2; C_{DEA}: 5% by mass of DEA in water; Re_L: 19-93; Re_G: 15-151).

Figure 7.9 indicates that for a constant liquid Reynolds number, an increase in gas flow rate resulted in a decrease in the absorption efficiency and the reasons for this behavior are explained based upon the prevalent flow regime. With slug flow, although higher gas flow rates result in larger magnitudes of recirculating velocity currents within the gas bubbles and thus creating additional convective mixing, the impact of the same is relatively minimal since the present mass transfer system has negligible resistance on the gas side. Instead, the dominant mass transfer resistance is present on the liquid side wherein the magnitude of mixing currents is reduced which results in lower fractions of CO_2 being absorbed by the liquid reactant. With slug-annular flow, higher gas velocities result in larger gas void fractions and therefore less thick liquid films. This results in rapid saturation of the liquid reactant adjacent to

255

the gas core which explains the observed trend of decreasing absorption efficiency. On the other hand, higher absorption efficiencies were achieved with larger liquid flow rates. This can be attributed to increased convective mixing within the liquid slugs during slug flow, and lower gas void fractions resulting in thicker liquid films in slug-annular flow. Previous studies (Zanfir et al., 2005; Niu et al., 2009; Su et al., 2010; Ye et al., 2012) for gas-liquid absorption in single channels have also reported similar trends.
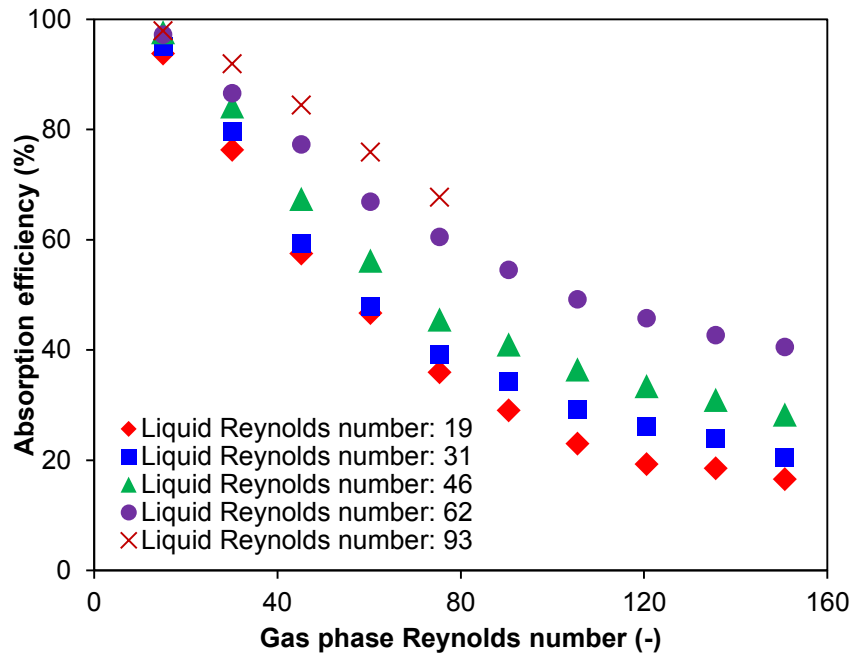
Figure 7.9: Effect of gas and liquid flow rate on absorption efficiency (C_{CO2}: 10% by mass of CO_2 in N_2; C_{DEA}: 5% by mass of DEA in water; Re_L: 19-93; Re_G: 15-151).

The results of liquid-side volumetric mass transfer coefficient, k_La, are reported in Figure 7.10. As can be seen, an increase in the liquid flow rate results in a higher value of mass transfer coefficient on account of the higher level of absorption that occurs at larger liquid flow rates as observed in Figure 7.9. An analysis of the effect

256

of gas flow rate indicates two contrasting trends. At high liquid flow rates ($Re_L > 46$), an increase the gas flow rate resulted in a monotonous increase in k_La on account of the increased consumption of the liquid reactants' absorption capacity. In other words, the difference in molar flow rate, Δn_{CO_2}, is higher, as a result of which k_La increases. However, at low liquid flow rates ($Re_L \leq 46$) an increase the gas flow rate resulted in a barely discernible initial increase followed largely by decreasing values of k_La. This can be attributed to extremely rapid saturation of the liquid film under these operating conditions. The effect is particularly dominant for low liquid velocities which are inherently associated with very thin liquid films containing minimal volume of liquid reactant, and further thinning occurs when increasing the gas velocity due to the higher gas void fractions. Due to these factors, the liquid reactant contained in the film is rapidly consumed following which minimal absorption occurs. It is expected that a similar situation (i.e. decreasing k_La with increasing gas velocity) would occur for $Re_L > 46$ too, provided the gas flow rates are increased beyond the present ranges. However, such extreme operating conditions were not tested on account of excessively high pressure drop. Among previous works on systems dominated by liquid-side mass transfer resistances, similar trends have been reported elsewhere (Luo and Ghiaasiaan, 1997; Yue et al., 2007a).
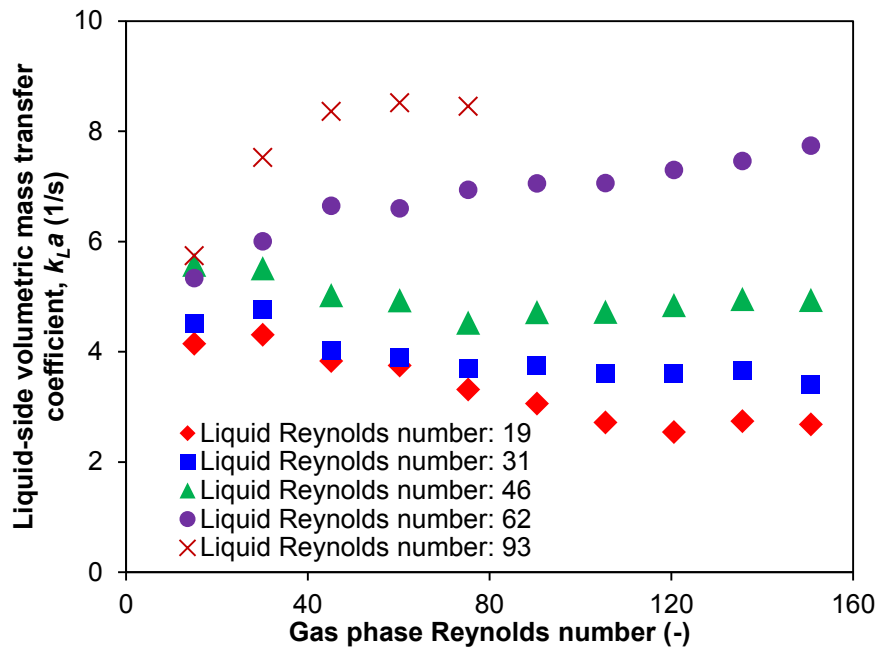
Figure 7.10: Effect of gas and liquid flow rate on liquid-side volumetric mass transfer coefficient (C_{CO2}: 10% by mass of CO_2 in N_2; C_{DEA}: 5% by mass of DEA in water; Re_L: 19-93; Re_G: 15-151).

The acid gas loading ratio was defined as the moles of CO_2 absorbed in a single mole of DEA, and the results are reported in Figure 7.11. An increase in this ratio represents an improvement in the operating performance of the system. Based on the definition, the highest values of the loading ratio are expected to be achieved at low liquid flow rates and high gas flow rates, and indeed this is the observed trend for Re_L ranging from 31 to 93. However, for Re_L=19, the previously discussed phenomenon of rapid saturation of the liquid film appeared to be dominant, and as a result the loading ratio did not have a monotonic trend. More specifically, lesser absorption occurred at high gas flow rates and this resulted in a decrease in the loading ratio.
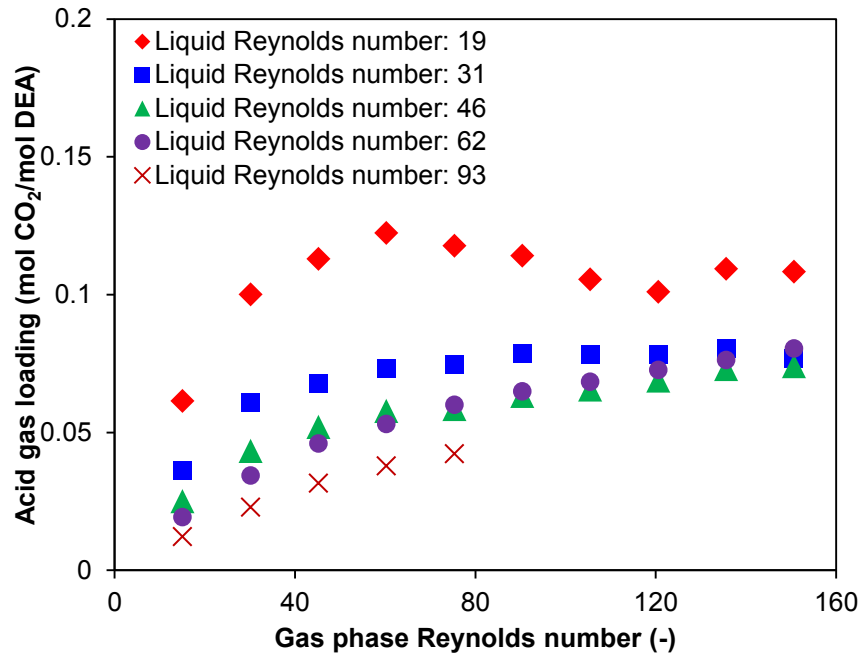
Figure 7.11: Effect of gas and liquid flow rate on acid gas loading (C_{CO2}: 10% by mass of CO_2 in N_2; C_{DEA}: 5% by mass of DEA in water; Re_L: 19-93; Re_G: 15-151).

7.2.2.4 *Effect of gas and liquid phase concentration on mass transfer*

To study the effect of gas phase concentration, its concentration was varied between 2.5-10% by mass of CO_2 in N_2 while the concentration of the liquid phase was constant at 5% by mass of DEA in water. The liquid phase Reynolds number was fixed at 31, while the gas phase Reynolds number ranged from 15 to 151. Increased fraction of CO_2 in the gas phase clearly results in higher acid gas loading ratios (Figure 7.12). However, there was a slight decrease in the absorption efficiency due to the fact that the residence time remained constant for all these cases (Figure 7.13). As a result, smaller values of mass transfer coefficient were observed (Figure 7.14). In comparison to the 10% concentration case, the average enhancement in k_La with the 7.5%, 5%, and 2.5% cases were 12%, 13% and 26%, respectively. These results

are in agreement with the data of Niu et al. (2009) and the single channel analysis

reported in Section 3.3.6.
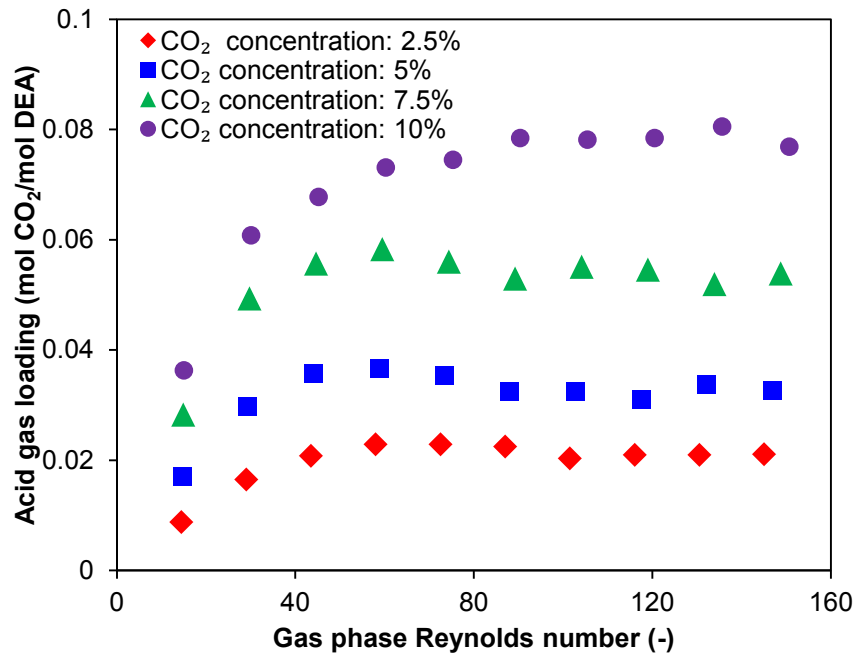
Figure 7.12: Effect of gas phase concentration on acid gas loading (C_{DEA}: 5% by mass of DEA in water; Re_L: 31; Re_G: 15-151).
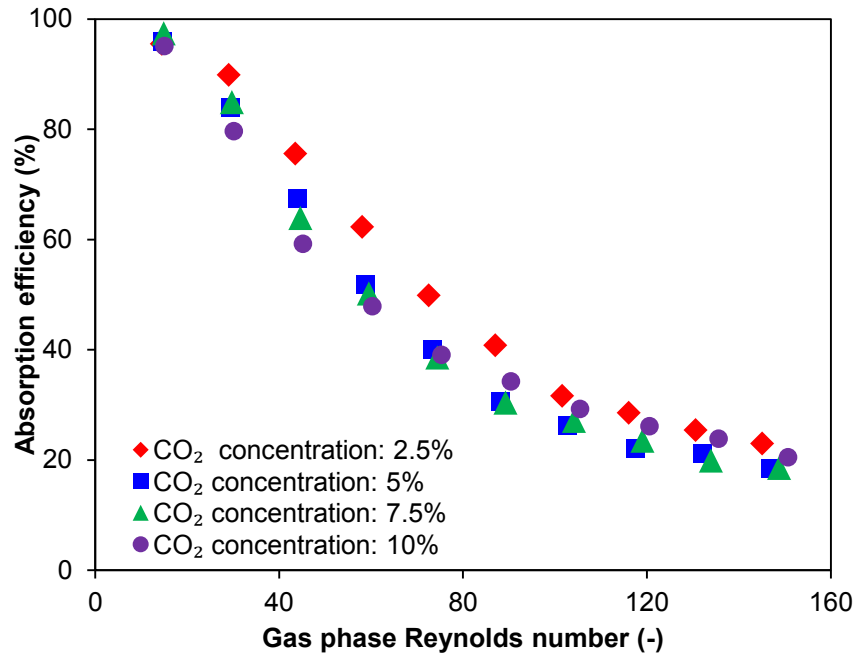
Figure 7.13: Effect of gas phase concentration on absorption efficiency (C_{DEA}: 5% by mass of DEA in water; Re_L: 31; Re_G: 15-151).
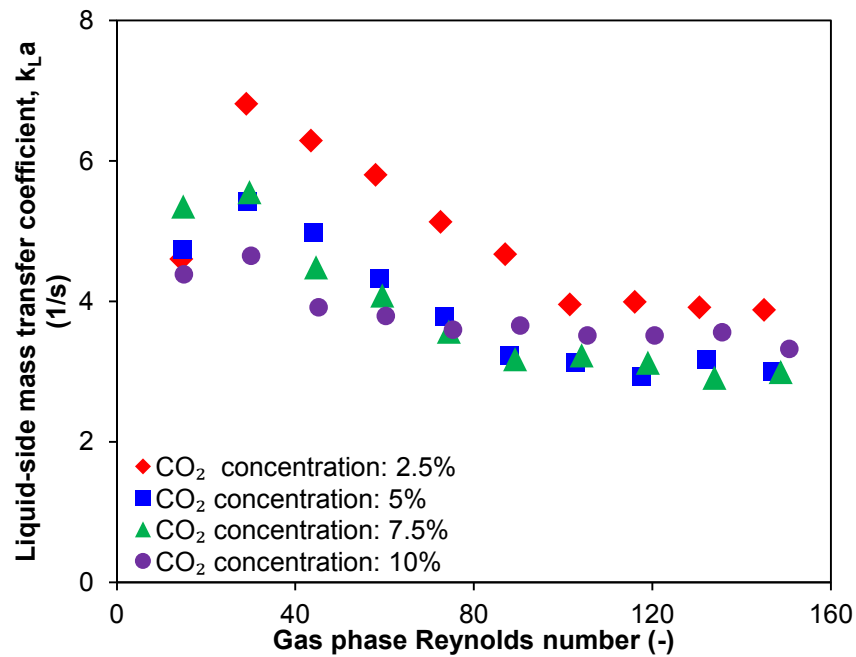
Figure 7.14: Effect of gas phase concentration on liquid-side volumetric mass transfer coefficient (C_{DEA}: 5% by mass of DEA in water; Re_L: 31; Re_G: 15-151).

Next, the effect of liquid phase concentration was investigated. The concentration of the aqueous amine solution was varied between 5-20% by mass of DEA in water, while that of the gas phase was constant at 10% by mass of CO_2 in N_2. The gas phase Reynolds number varied between 15 and 136. The liquid phase mass flow rate was selected as 1 g/s. The results reported in Figure 7.15 indicate an enhancement in absorption efficiency with increasing amine concentration levels and this behavior can be attributed to the reaction kinetics previously. For the same reason, the liquid-side volumetric mass transfer coefficient (Figure 7.16) was observed to be higher with an increase in the amine concentration. In comparison to the 5% concentration case, the average enhancement in $k_L a$ with the 10% and 20% concentration cases were 62% and 125%, respectively. However, the increased amount of DEA present in the liquid phase resulted in a decrease in the acid gas loading ratio (Figure 7.17). The decrease was quantified to equal 39% and 66% on an average for the 10% and 20% amine concentration cases, respectively, as compared to the 5% case. These results are a clear indication that a more concentrated gas stream or a higher gas flow rate can be utilized. Alternatively, the amine solution can be reused prior to regeneration, in order to achieve a higher value of the acid gas loading ratio that is closer to the theoretical limit of the mass transfer system. In particular, the amine reuse strategy is expected to be incorporated during subsequent scaling-up stages of microreactor technology by designing multiple pass configurations. Successive passes could possibly employ longer residence times and/or shorter hydraulic diameters. It is noted that most industrial systems typically operate at high levels of solvent loading close to their theoretical limit.
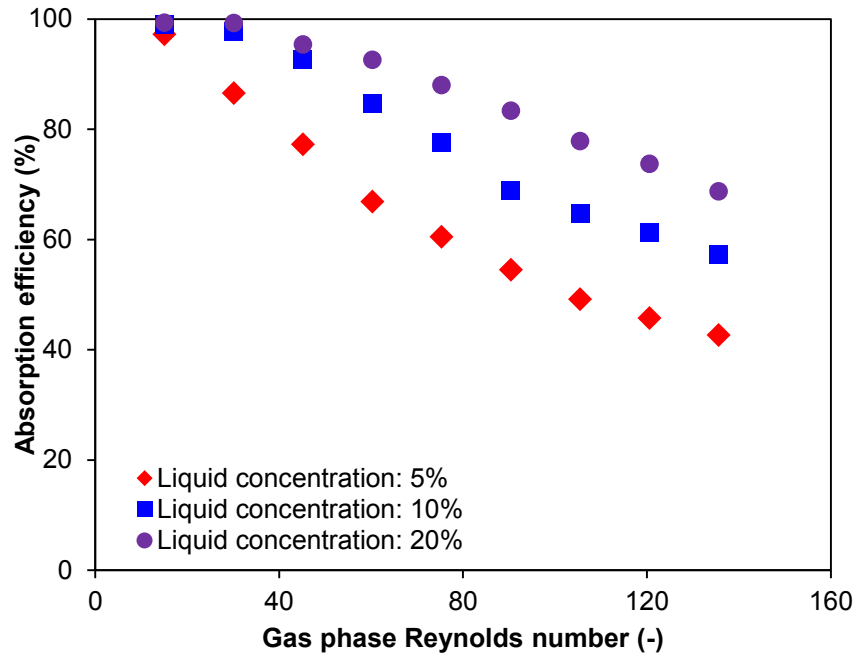
Figure 7.15: Effect of liquid phase concentration on absorption efficiency (C_{CO2}: 10% by mass of CO_2 in N_2; Re_L: 44-62; Re_G: 15-151).
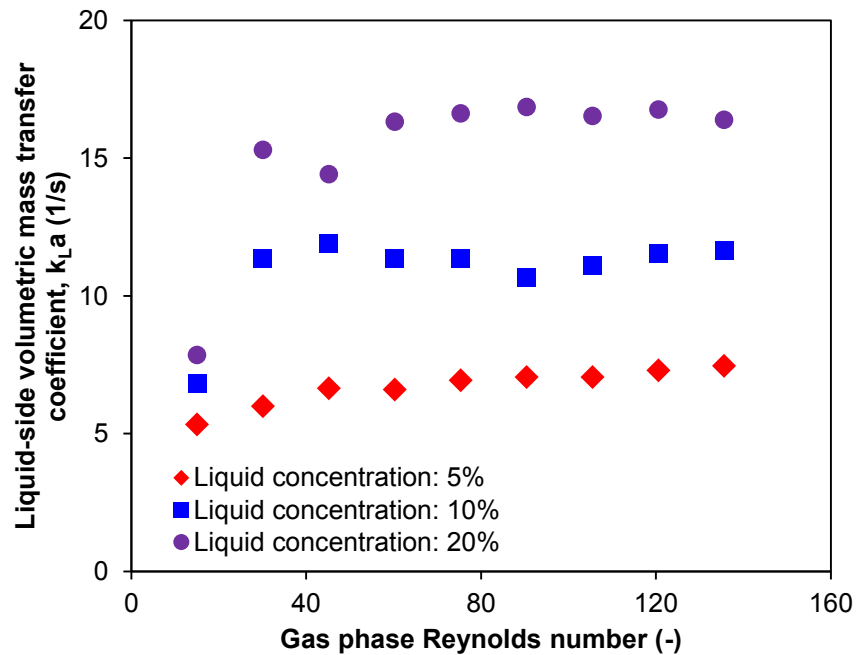
Figure 7.16: Effect of liquid phase concentration on liquid-side volumetric mass transfer coefficient (C_{CO2}: 10% by mass of CO_2 in N_2; Re_L: 44-62; Re_G: 15-151).
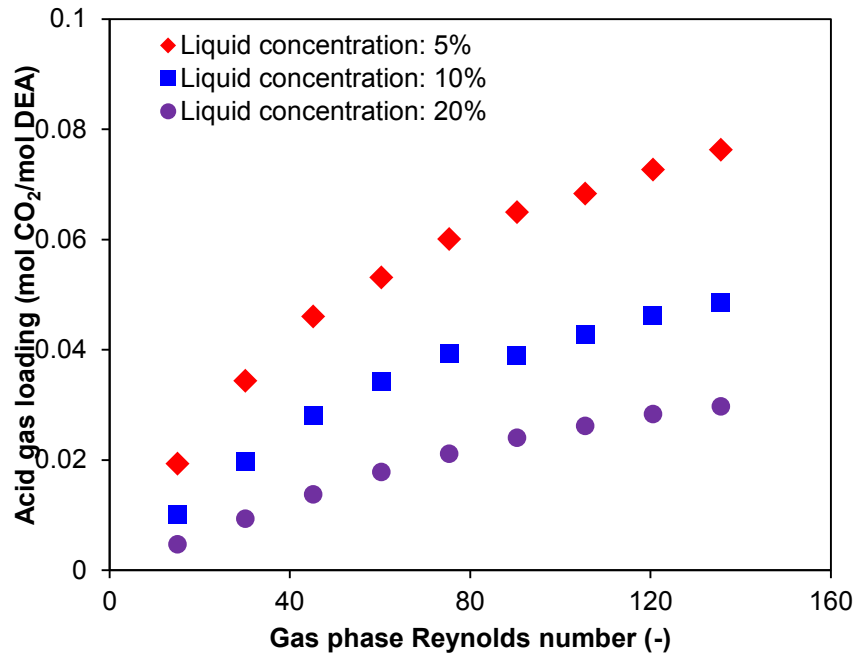
Figure 7.17: Effect of liquid phase concentration on acid gas loading (C_{CO2}: 10% by mass of CO_2 in N_2; Re_L: 44-62; Re_G: 15-151).

7.2.3   Inferences from open-loop tests

This section investigated the fluid flow and mass transfer characteristics during the absorption of CO_2 into diethanolamine in a micro-structured absorber. An open-loop experimental testing configuration was utilized. The performance of the absorber which comprised multiple straight, parallel channels, each having a hydraulic diameter of 456 µm, was studied with respect to the pressure drop, absorption efficiency, mass transfer coefficient, and acid gas loading ratio. Using available flow regime transition criteria, the flow patterns prevalent under the presently tested range of phase superficial velocities were identified to be slug and slug annular flows. The experimental single-phase pressure drop was found to be in agreement with a theoretical correlation for laminar flow with an MAE of 3.2%. The two-phase

264

pressure drop was compared against the predictions of a piecewise model and a reasonably good agreement was obtained within an MAE of 9.8%. Absorption efficiencies close to 100% were observed under certain operating conditions. Higher absorption efficiencies were achieved at larger liquid and smaller gas flow rates, and these trends were explained based upon the magnitude of convective mixing currents during slug flow, and the film thickness in slug-annular flow. Rapid saturation of the liquid reactant contained within the thin film region, particularly at high values of gas void fraction, was found to be avoided at liquid Reynolds numbers greater than 46. Parametric studies varying the gas and liquid phase concentrations were conducted. An enhancement in the mass transfer coefficient, by as much as 125% on average, was observed at higher liquid phase concentration levels. Enhanced absorption efficiencies were observed at lower gas phase concentrations, with the mass transfer coefficient improving by as much as 26%. The present micro-structured absorber yielded mass transfer coefficients as high as 17 s^{-1} which is between 1-3 orders of magnitude higher than those reported for most conventional gas-liquid absorption systems and is an indication of the high level of process intensification and enhancement that can be achieved by using microreactors for gas-liquid absorption applications.

7.3 Absorber performance characterization: closed-loop testing

7.3.1 Description of experiments

7.3.1.1 Experimental setup

The absorber design and its operational details were similar to that described in Section 7.2.1. However, instead of using fresh amine solution to operate the absorber, in the present configuration, the loaded amine solution leaving the absorber was regenerated in a column and re-circulated back to the absorption loop. A gear pump (Micropump Inc., USA) was used to pump the rich amine solution leaving the two-phase separator into a regenerating column. The regenerator was fabricated with stainless steel and was operated in a vertical orientation, as shown in Figure 7.18. The column was externally insulated using polyurethane foam to prevent thermal losses. At steady state the system operated in countercurrent mode with the loaded amine solution (liquid phase) flowing from top to bottom, and the gaseous phase flowing in the opposite direction.
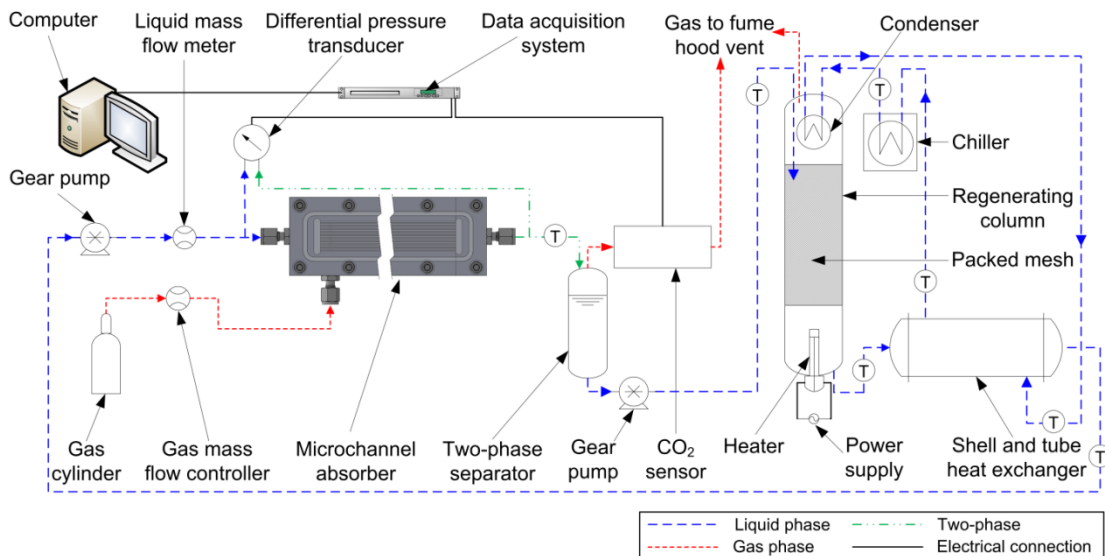
Figure 7.18: Layout of experimental test loop (connections between thermocouples and data acquisition system are not shown for simplicity).

The base of the regenerator was fitted with a tubular heater having a maximum power rating of 800 W. The heater was connected to an AC power source and controlled by an autotransformer. It was used to vaporize the water present in the aqueous amine solution, thereby lowering the partial pressure of CO_2 in the gas phase. This served as a driver to strip CO_2 from rich amine solution. In addition to water, a small fraction of the amine also evaporated in the regenerator. A condenser was placed at the top of the column to condenser the water vapor as well as to minimize amine losses. This arrangement maintained constant concentration of the liquid solvent at the absorber inlet and the same was verified by analyzing the steady-state performance of the absorption process. The mid-region of the regenerating column was packed with stainless steel mesh in order to enhance mass transfer by increasing the contact area. The temperature of the aqueous amine was measured using a T-type thermocouple at

the outlet of the absorber, separator, regenerator, and heat exchanger, while that of the chiller was measured at the outlet of the chiller, condenser, and heat exchanger.

7.3.1.2   Operating conditions

The gas phase was CO_2 mixed with N_2 at a concentration level of 10% by mass, and was of industrial grade purity. The liquid phase was aqueous amine solution prepared using laboratory grade DEA (99% purity). The amine was diluted with water to concentration levels of 5% and 25% by mass. The gas and liquid flow rates were varied such that the range of Reynolds numbers for each phase varied between 15 to 151, and 19 to 62, respectively.

7.3.1.3   Uncertainty analysis

The uncertainty in the measurement of CO_2 concentration was ±3% of the reading and ±1.5% of the full scale range of the device (20% concentration of CO_2 by mass). The gas flow rate was measured with an uncertainty of ±0.8% of the reading and ±0.2% of the full scale range of the device (8.33×10^{-5} m^3/s). The uncertainty in liquid flow rate and pressure drop equaled ±0.1% and ±0.25% of the readings, respectively. By performing an error propagation analysis, the average uncertainties in absorption efficiency and liquid-side volumetric mass transfer coefficient were determined to equal ±10.3% and ±18.5%, respectively. As discussed subsequently, these results were repeatable within ±2.4%.

7.3.2 Results and discussion

7.3.2.1 *Repeatability of mass transfer results*

In order to assess the repeatability of the present setup, a typical set of measurements were repeated three times. For a fixed liquid phase Reynolds number equaling 62, the gas phase Reynolds number was varied from 15 to 151. The results of the above analysis reported in Figure 7.19 indicate that the present measurements of absorption efficiency were repeatable within ±2.4%.
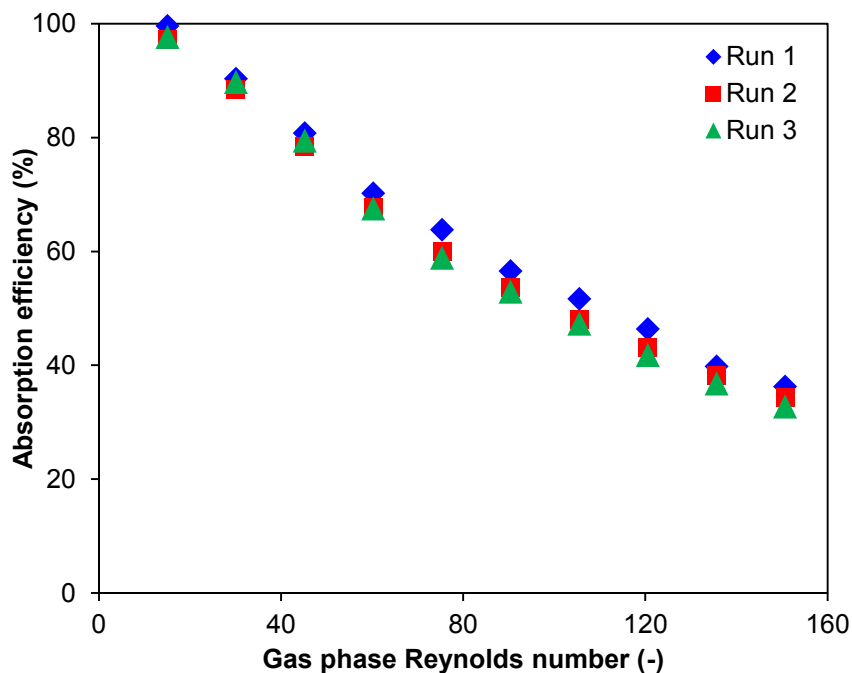
Figure 7.19: Repeatability of measurements of absorption efficiency during absorption of CO_2/N_2 mixture (10% by mass) in aqueous DEA (5% by mass) for constant liquid phase Reynolds number of 62.

7.3.2.2 *Comparison of absorption performance with and without regeneration*

In the present study, the system operated as a closed loop with the absorber receiving regenerated amine solution. Hence, it was essential to ensure that the gas-liquid

269

absorption performance under these conditions is sufficiently close to that achieved when the absorber is supplied with freshly prepared amine solution. The results of the comparison are reported in Figure 7.20, wherein the data was obtained during the absorption of CO_2/N_2 mixture (10% by mass) in aqueous DEA (5% by mass) for gas phase Reynolds number ranging from 15 to 151 and liquid phase Reynolds number ranging from 19 to 93. As can be seen, the presently obtained data during absorption and regeneration is in reasonably good agreement with that obtained without regeneration (fresh amine solution). The mean absolute error (MAE) of this data is 14.1%. Further, there was no discernible bias in the distribution of the data points across either side of the parity line in Figure 7.20.
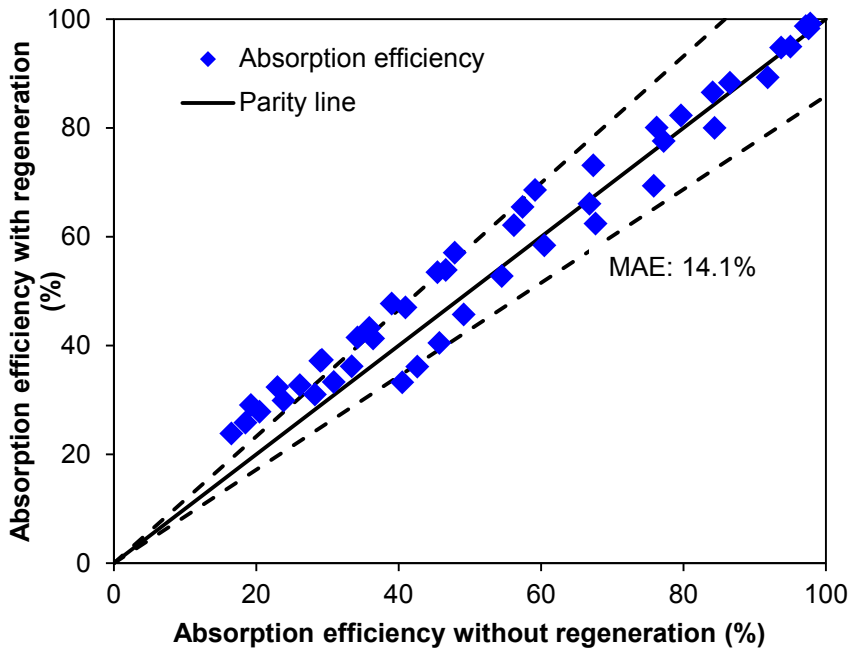
Figure 7.20: Comparison of absorption efficiencies with and without amine regeneration during absorption of CO_2/N_2 mixture (10% by mass) in aqueous DEA (5% by mass) for gas phase Reynolds number ranging from 15 to 151 and liquid phase Reynolds number ranging from 19 to 93.

7.3.2.3   Assessment of steady-state performance

A typical measurement for a given operating condition required between 180 to 300 seconds to attain steady-state conditions. The present section analyzed the system performance over a significantly longer period of 1000 s, in order to verify that the system operates in a similar manner for extended periods of time. For a constant gas phase Reynolds number of 75, the transient variation of absorption efficiency was measured for different liquid phase Reynolds numbers ranging from 31 to 93 (Figure 7.21). For each case, the average variation of absorption efficiency from the mean value over the analyzed period was less than 0.5% and this served as sufficient verification of the ability of the present gas-liquid absorption system to operate efficiently as a closed loop when the amine solution is being constantly regenerated.
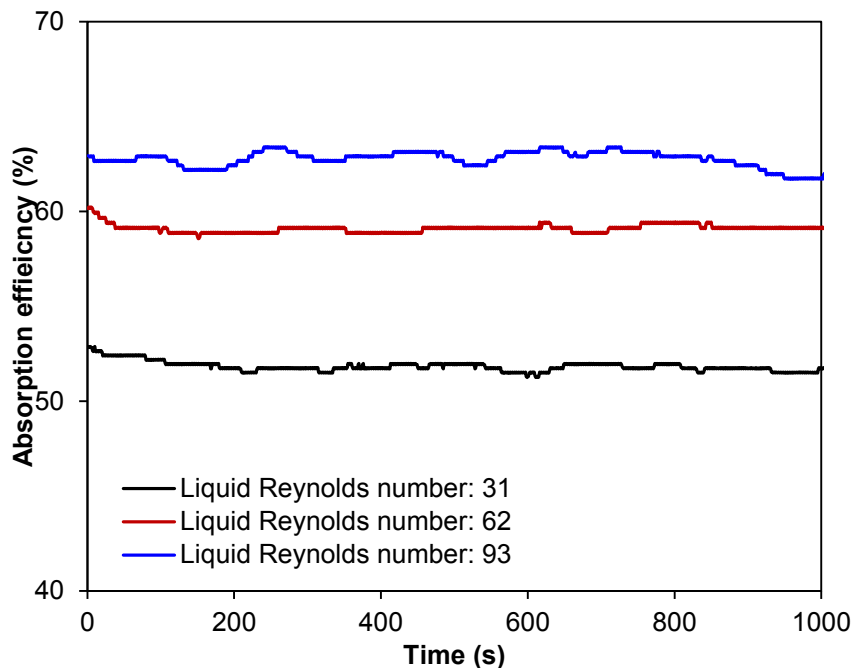
Figure 7.21: Performance of system at steady-state conditions for a duration of 1000 s during absorption of CO_2/N_2 mixture (10% by mass) in aqueous DEA (5% by mass) for constant gas phase Reynolds number of 75.

7.3.2.4 Effect of gas and liquid flow rate

A parametric study was performed by varying the gas phase Reynolds number between 15 and 151 and the liquid phase Reynolds number between 19 and 93. As can be seen from Figure 7.22, for a constant liquid Reynolds number, an increase in the gas phase Reynolds number results in a decrease in the absorption efficiency. On the other hand, higher absorption efficiencies were achieved with larger liquid phase Reynolds number due to the increased contact time of the gas phase with fresh amine solution. The results for liquid-side volumetric mass transfer coefficient and acid gas loading ratio are reported in Figure 7.23 and Figure 7.24, respectively. The interpretation of these trends is similar to the discussion provided previously in Section 7.2.2.3.
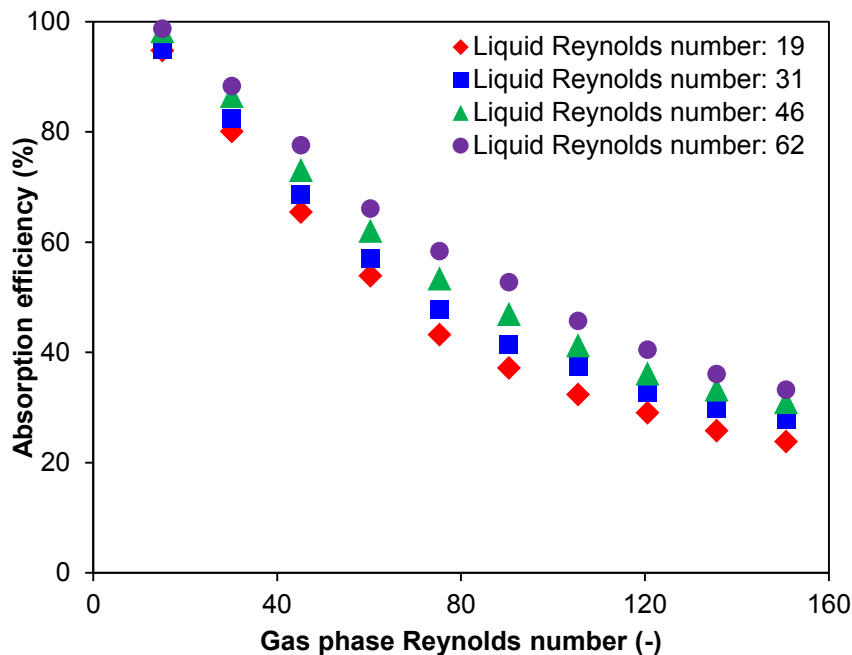
Figure 7.22: Variation of absorption fraction with gas and liquid phase Reynolds number during absorption of CO_2/N_2 mixture (10% by mass) in aqueous DEA (5% by mass).

272
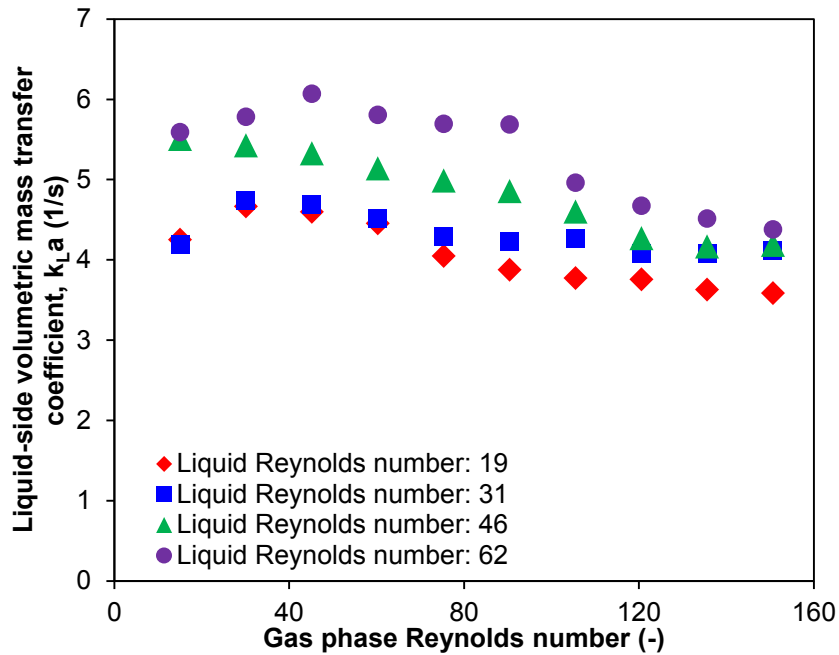
Figure 7.23: Variation of liquid-side volumetric mass transfer coefficient with gas and liquid phase Reynolds number during absorption of CO_2/N_2 mixture (10% by mass) in aqueous DEA (5% by mass).
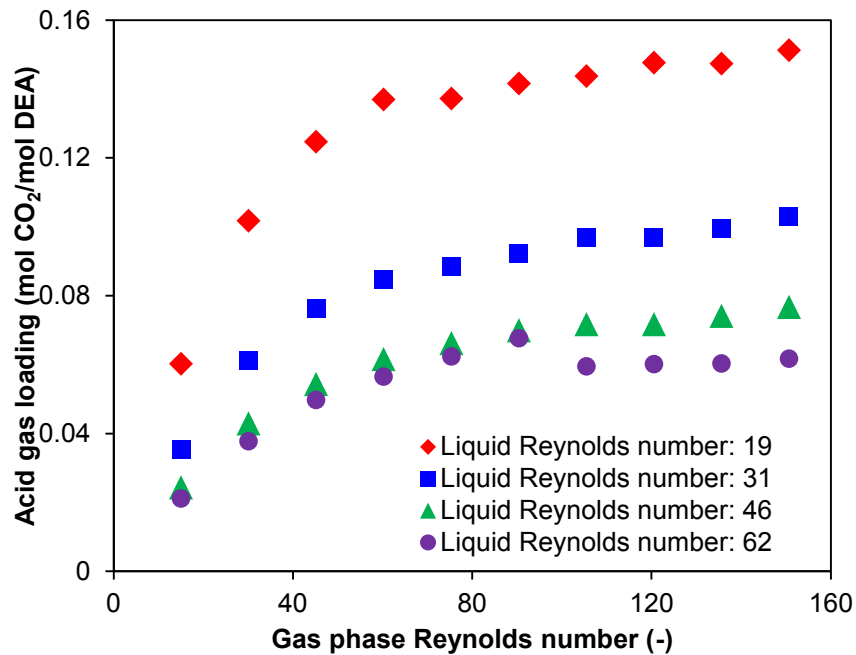
Figure 7.24: Variation of acid gas loading ratio with gas and liquid phase Reynolds number during absorption of CO_2/N_2 mixture (10% by mass) in aqueous DEA (5% by mass).

7.3.2.5 Effect of heater power on performance

The power supplied to the heater in the regenerator was varied and the system performance was assessed. As seen in Figure 7.25, for heater powers in excess of 462 W, the CO_2 concentration in the gas phase at the outlet of the absorber is nearly constant, as is the solution temperature at the outlet of the regenerator. However, when it was decreased to 393 W, there was an increase in CO_2 concentration thereby resulting in deterioration of the mass transfer characteristics. For the same case, there was a decrease in the solution temperature at the outlet of the regenerator which suggested that under these conditions, there is insufficient energy to regenerate the rich amine solution. As a result, partially loaded amine solution enters the absorber thereby resulting in lesser CO_2 being separated in the absorber. It is worth noting that even with low heater power, the absorption process occurs at steady state, only that the system performance is now degraded.

An efficient regenerating system should be designed such that it consumes minimal energy to achieve the desired performance levels at steady-state conditions, and the following factors are of importance in order to improve the overall economics of the gas-liquid absorption process. Excessive heater power, in addition to consuming unnecessary thermal energy, also results in additional cooling loads that have to be met. The load at the condenser will increase in order to minimize amine and water losses, thereby maintaining a constant solution concentration in the test loop. Additionally, the heat exchanger will also require a larger energy input in order to cool the excessively heated amine solution back to the temperature at which the

absorber operates. Lastly, the inclusion of a heat exchanger to recover heat from the lean amine solution leaving the regenerator and use the same to pre-heat rich amine solution entering the regenerator, would also reduce the energy requirements of the system.
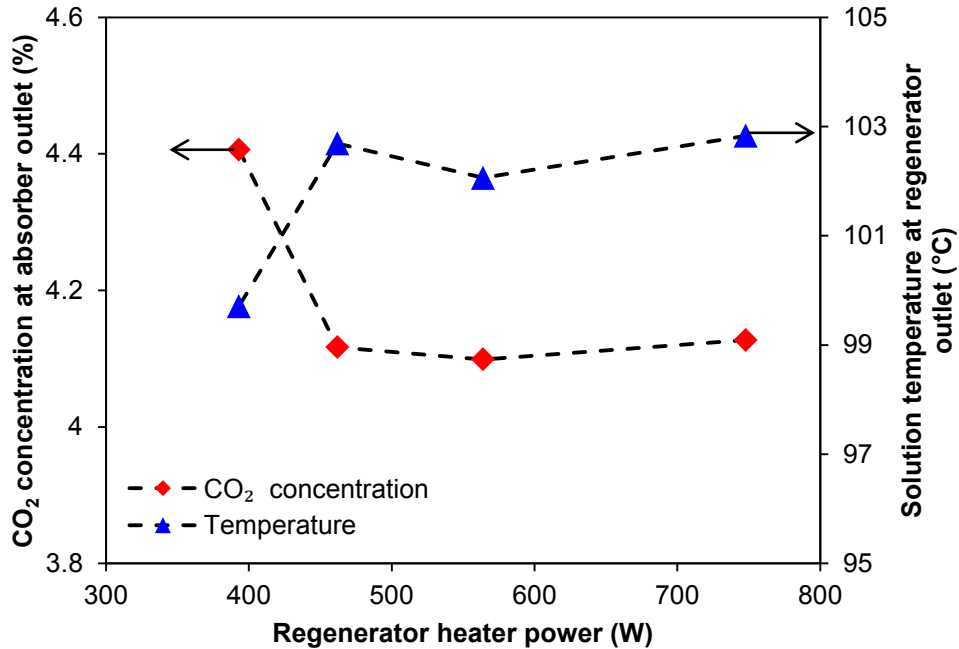
Figure 7.25: Effect of regenerator heater power on CO_2 concentration in gas phase at absorber outlet and aqueous amine solution temperature at regenerator outlet during absorption of CO_2/N_2 mixture (10% by mass) in aqueous DEA (5% by mass) for gas phase Reynolds number of 75 and liquid phase Reynolds number of 62.

7.3.2.6 Effect of amine concentration on mass transfer

All of the previous results discussed in this paper have used dilute amine solutions having a concentration of 5% by mass of DEA in water. The present section investigates the mass transfer characteristics with a significantly concentrated solution having 25% by mass of DEA in water. The gas phase Reynolds number varied between 15 and 151. The liquid phase mass flow rate was selected as 1 g/s.

The results reported in Figure 7.26 indicate an enhancement in the absorption efficiency with increasing amine concentration levels and this behavior can be attributed to the reaction kinetics previously. For the same reason, the liquid-side volumetric mass transfer coefficient (Figure 7.27) was observed to be higher with an increase in the amine concentration.
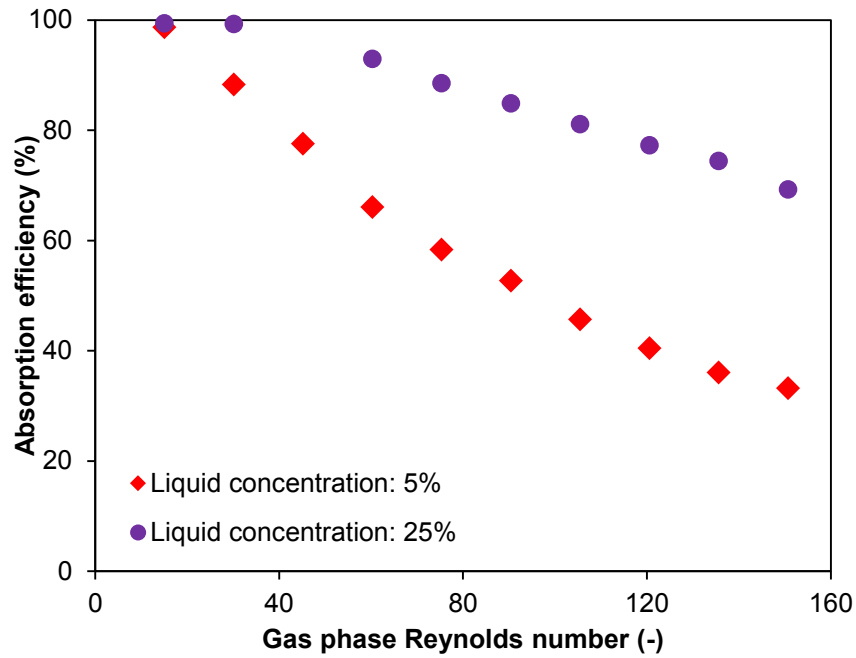
Figure 7.26: Variation of absorption efficiency with liquid reactant concentration for constant gas phase concentration (10% by mass of CO_2 in N_2) and constant liquid mass flow rate of 1 g/s (Re_L: 40-62).
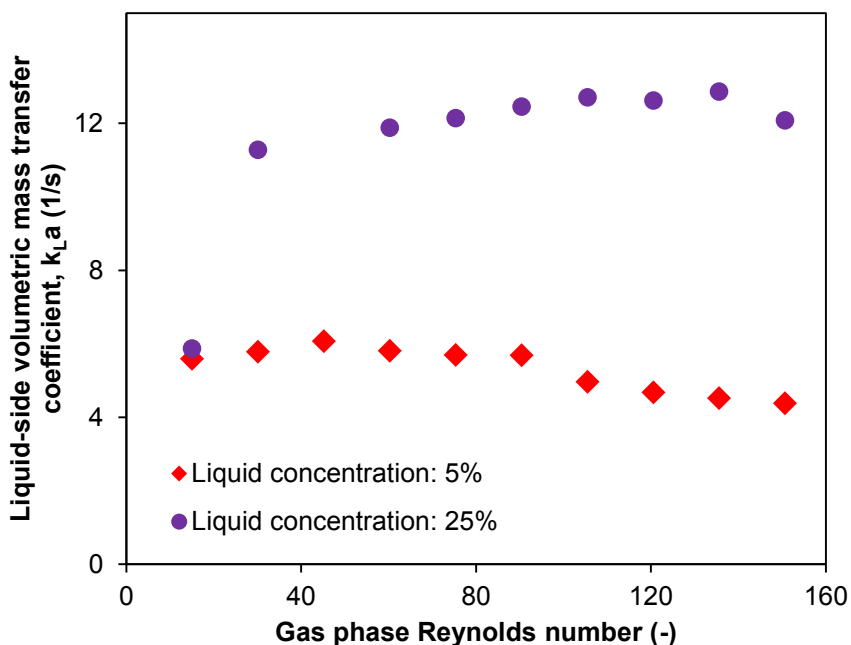
Figure 7.27: Variation of liquid-side mass transfer coefficient with liquid reactant concentration for constant gas phase concentration (10% by mass of CO_2 in N_2) and constant liquid mass flow rate of 1 g/s (Re_L: 40-62).

7.3.3 Inferences from closed-loop tests

This section investigated the fluid flow and mass transfer characteristics during the absorption of CO_2 into diethanolamine in a micro-structured absorber. A closed-loop configuration was utilized wherein absorption and solvent regeneration occurred in the same system. The performance of the absorber which comprised multiple straight, parallel channels, each having a hydraulic diameter of 456 μm, was studied with respect to the absorption efficiency, mass transfer coefficient, and acid gas loading ratio. The system operation at steady state was verified for different operating conditions. The absorber performance with and without amine regeneration was compared and found to be within a MAE of 14.1%. Parametric studies varying the gas and liquid flow rates were conducted and absorption efficiencies close to 100%

were observed under certain operating conditions. The regenerator heater power was optimized to determine an energy efficient operating condition. The optimum power was determined to equal 462 W. Additional parametric studies varying the solvent concentration were conducted and the trends were found to be in agreement with the process chemistry. Parametric studies varying the solvent concentration concentrations were conducted. The subsequent section utilized the present test configuration to study the effect of reactor residence time on mass transfer.

7.4 Closed loop testing with variant residence time

7.4.1   Description of experiments

7.4.1.1   Experimental setup

The microreactor utilized in the present analysis was a modified version of that described in Section 7.2.1.1. The PMMA reactor cover was replaced with an aluminum cover to achieve better sealing using higher compressive forces. A central transparent window was incorporated for visualization purposes. The hydraulic diameter of the reactor was estimated following the method described in Section 7.2.1.1 and determined to equal 716 μm. The remaining details of the test setup are similar to that described in Sections 7.2.1.1 and 7.3.1.1.

7.4.1.2   Operating conditions

The gas phase was CO_2 mixed with N_2 at concentration levels of 10% and 19% by mass, and was of industrial grade purity. The liquid phase was aqueous amine solution prepared using laboratory grade DEA (99% purity). The amine was diluted

with distilled water to a concentration of 20% by mass. The gas and liquid flow rates were varied such that the range of Reynolds numbers for each phase varied between 30 to 150, and 22 to 52, respectively. All experiments were conducted at an ambient temperature of 298 K and at atmospheric pressure.

7.4.1.3 Uncertainty analysis

The uncertainty in the measurement of CO_2 concentration was $\pm 3\%$ of the reading and $\pm 1.5\%$ of the full scale range of the device (20% concentration of CO_2 by mass). The gas flow rate was measured with an uncertainty of $\pm 0.8\%$ of the reading and $\pm 0.2\%$ of the full scale range of the device (8.33×10^{-5} m^3/s). The uncertainty in liquid flow rate and pressure drop equaled $\pm 0.1\%$ and $\pm 0.25\%$ of the readings, respectively. By performing an error propagation analysis, the average uncertainties in absorption efficiency and liquid-side volumetric mass transfer coefficient were determined to equal $\pm 11.6\%$ and $\pm 20.3\%$, respectively. The results were repeatable within ± 2.4.

7.4.2 Results and discussion

7.4.2.1 Analysis of pressure drop

The operation of the test loop was validated by comparing the experimental pressure drop with theoretical predictions. For single phase flow, the friction factor was compared against the theoretical predictions from Eq. 7.10 for laminar flow in rectangular channels (Shah and London, 1978) where β is the aspect ratio equaling unity in the present study. A good agreement was obtained (Figure 7.28) with an MAE of 5.8%.

279

$$f \times \text{Re} = 56 \left(1 - 1.3553\beta + 1.9467\beta^2 - 1.7012\beta^3 + 0.9564\beta^4 - 0.2537\beta^5 \right) \quad (7.10)$$
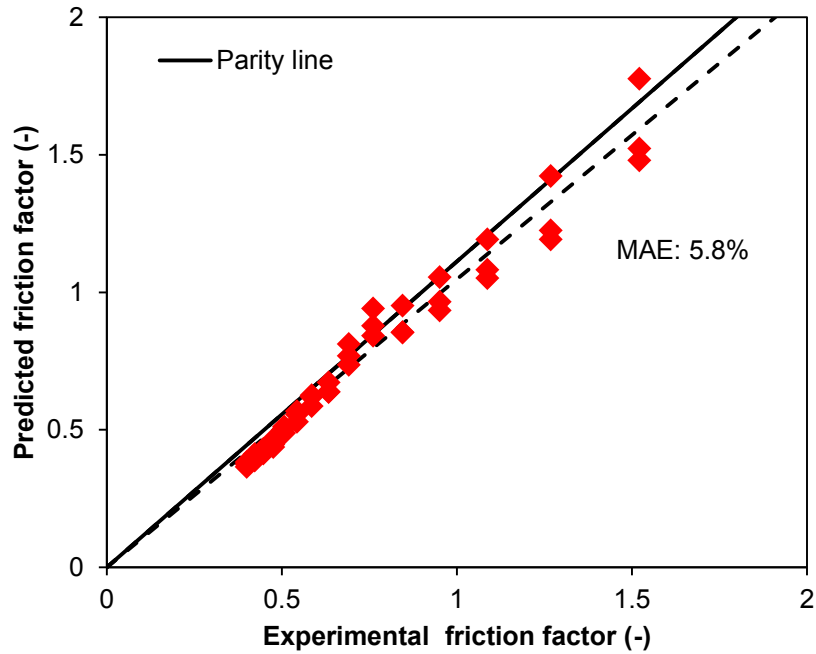
Figure 7.28: Comparison of experimental single phase friction factor with theoretical predictions.

The experimental two-phase pressure drop was used to calculate the two-phase friction multiplier, $\phi_L{}^2$. The same was compared against the predictions of the models by Li and Wu (2010) and Kim and Mudawar (2012b). The former is given by Eqs. 7.11-7.13 and yielded an MAE of 10.5%. The latter is given by Eq. 7.11 and Eqs. 7.14-7.16, with which an MAE of 16% was obtained. These results are reported in Figure 7.29.

$$\phi_L^2 = 1 + \frac{c}{X} + \frac{1}{X^2} \quad (7.11)$$

$$c = \begin{cases} Bo \leq 1.5 & 11.9 Bo^{0.45} \\ 1.5 < Bo \leq 11 & 109.4 \left(Bo \, \mathrm{Re}_L^{0.5} \right)^{-0.56} \end{cases} \tag{7.12}$$

$$Bo = \frac{(\rho_L - \rho_G) g D^2}{\sigma} \tag{7.13}$$

$$c = 0.0015 \, \mathrm{Re}_{LO}^{0.59} \, Su_{GO}^{0.19} \left(\frac{\rho_L}{\rho_G} \right)^{0.36} \tag{7.14}$$

$$\mathrm{Re}_{LO} = \frac{G D_h}{\mu_L} \tag{7.15}$$

$$Su_{GO} = \frac{\rho_G \sigma D_h}{\mu_G^2} \tag{7.16}$$
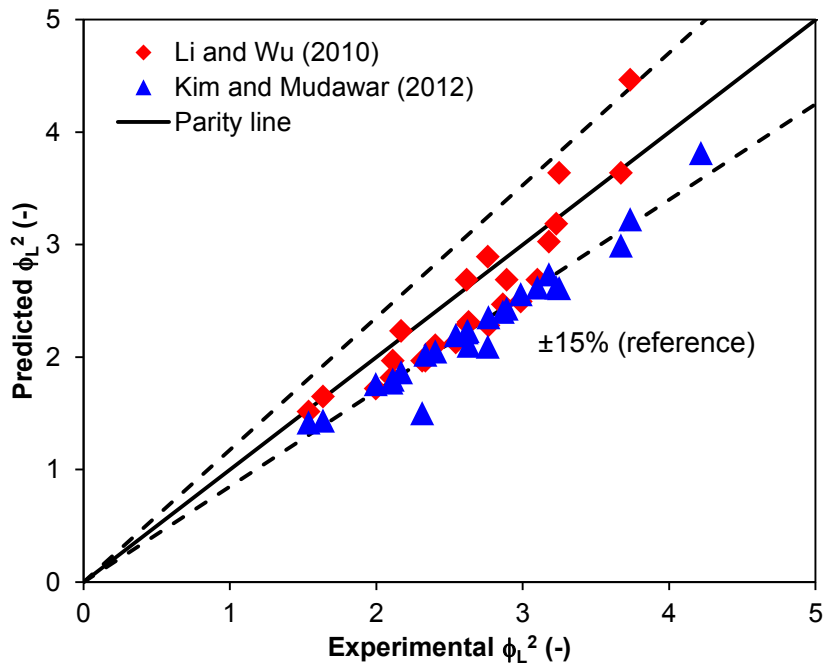
Figure 7.29: Comparison of experimental two-phase friction multiplier with empirical models.

7.4.2.2 *Effect of gas and liquid flow rate*

A parametric study was performed by varying the gas phase Reynolds number between 30 and 150 and the liquid phase Reynolds number between 22 and 54. The reactor length was 0.1 m. As can be seen from Figure 7.30, for a constant liquid Reynolds number, an increase in the gas phase Reynolds number results in a decrease in the absorption efficiency. On the other hand, higher absorption efficiencies were achieved with larger liquid phase Reynolds number due to the increased contact time of the gas phase with fresh amine solution. The results for liquid-side volumetric mass transfer coefficient are reported in Figure 7.31. The interpretation of these trends is similar to the discussion provided previously in Section 7.2.2.3.
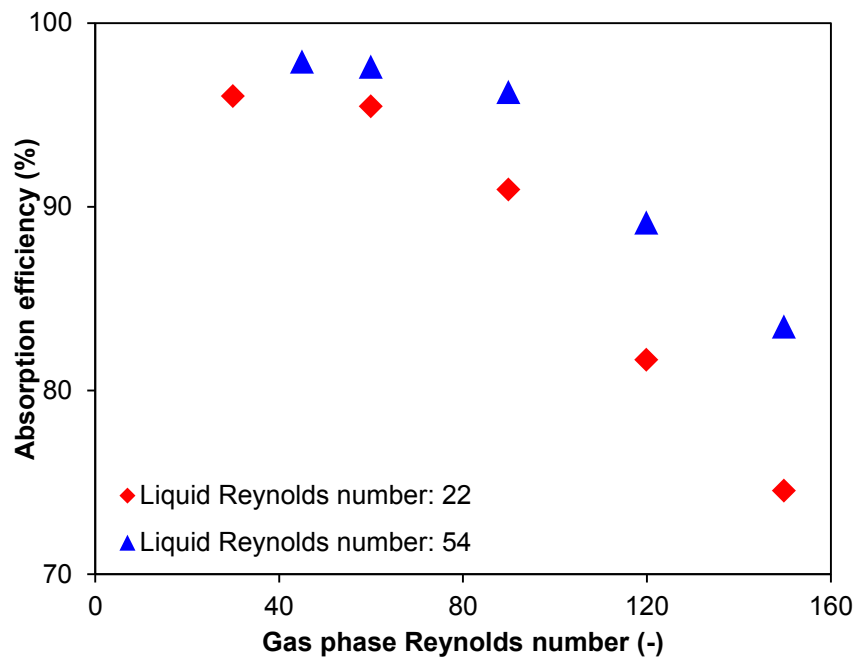
Figure 7.30: Effect of flow rate on absorption efficiency (C_{CO2}: 10% by mass of CO_2 in N_2; C_{DEA}: 20% by mass of DEA in water; *L*: 0.1 m; Re_G: 30-150; Re_L: 22-52).
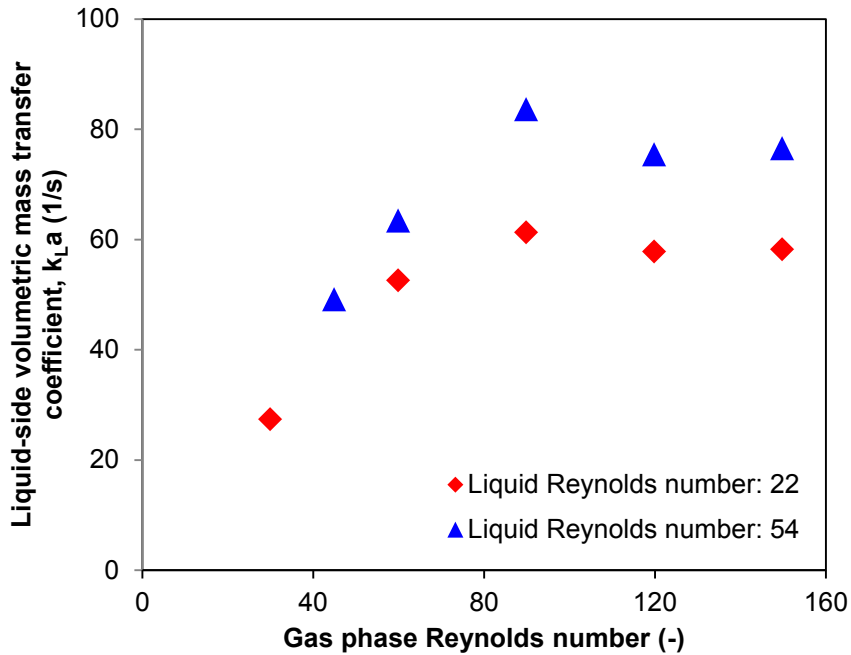
Figure 7.31: Effect of flow rate on liquid-side volumetric mass transfer coefficient (C_{CO2}: 10% by mass of CO_2 in N_2; C_{DEA}: 20% by mass of DEA in water; L: 0.1 m; Re_G: 30-150; Re_L: 22-54).

7.4.2.3 Effect of reactor length (residence time)

To study the effect of reactor length (residence time) the channel length was varied to 0.05, 0.1, and 0.45 m. The gas phase Reynolds number was varied between 30 and 150, while the liquid phase Reynolds number was constant at 54. The gas phase concentration was 10% by mass of CO_2 in N_2, and the liquid phase concentration was 20% by mass of DEA in water.

As seen in Figure 7.32, the increased residence time with longer reactors resulted in slightly higher absorption efficiencies. In comparison to the 0.05 m channel, the absorption efficiency with the 0.1 m and 0.45 m channels was higher on average by 3% and 8%, respectively. However, the mass transfer coefficients were lower by 43%

and 84%, respectively (Figure 7.33). This was attributed to the improved utilization of the absorption capacity of the amine solution for a given reactor volume. Short channel lengths prevent localized interfacial saturation of the liquid reactant, thereby yielding higher values of mass transfer coefficient. The trends are in agreement with the single channel analysis reported in Section 3.3.4.
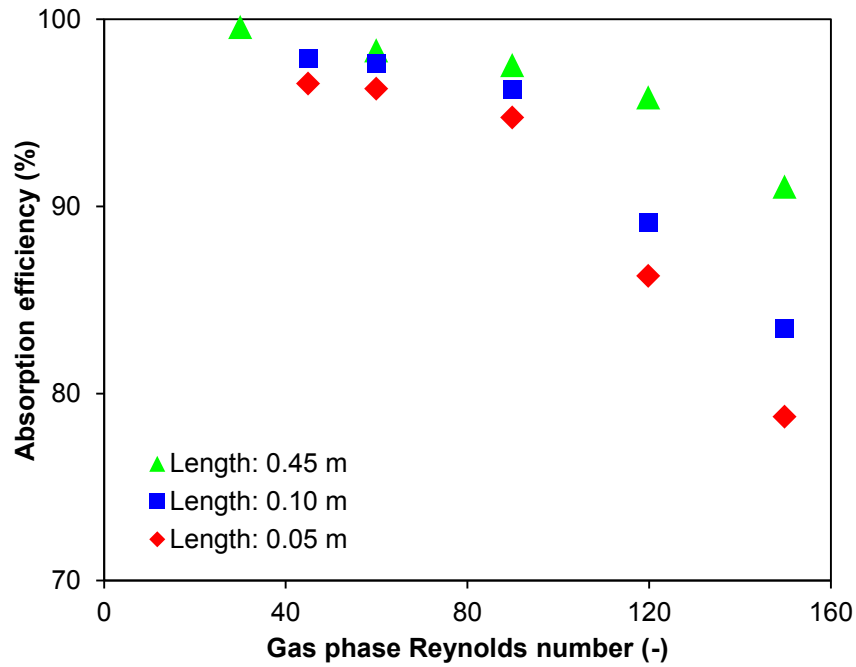
Figure 7.32: Effect of channel length (residence time) on absorption efficiency (C_{CO2}: 10% by mass of CO_2 in N_2; C_{DEA}: 20% by mass of DEA in water; Re_G: 30-150; Re_L: 54).
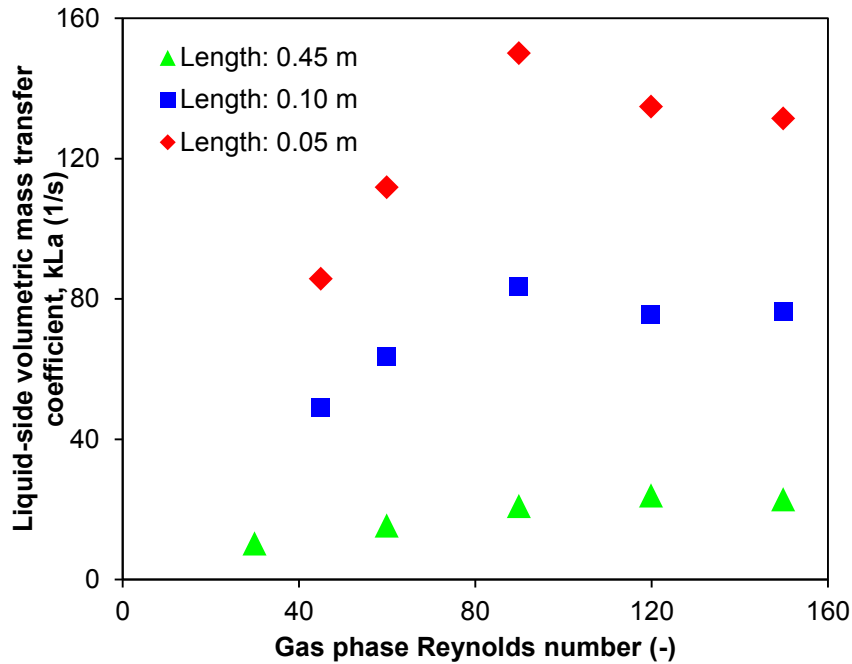
Figure 7.33: Effect of channel length (residence time) on liquid-side volumetric mass transfer coefficient (C_{CO2}: 10% by mass of CO_2 in N_2; C_{DEA}: 20% by mass of DEA in water; Re_G: 30-150; Re_L: 54).

7.4.2.4   Effect of gas phase concentration

To study the effect of gas phase concentration, the same was varied to 10% and 19% by mass of CO_2 in N_2 while the concentration of the liquid phase was constant at 20% by mass of DEA in water. The reactor length was 0.05 m, the liquid phase Reynolds number was fixed at 54, and the gas phase Reynolds number ranged from 45 to 150. Higher CO_2 concentrations resulted in lower absorption efficiencies since the residence time remained constant for all these cases (Figure 7.34). As a result, smaller values of mass transfer coefficient were observed (Figure 7.35). These trends are similar to that observed in previous analyses.
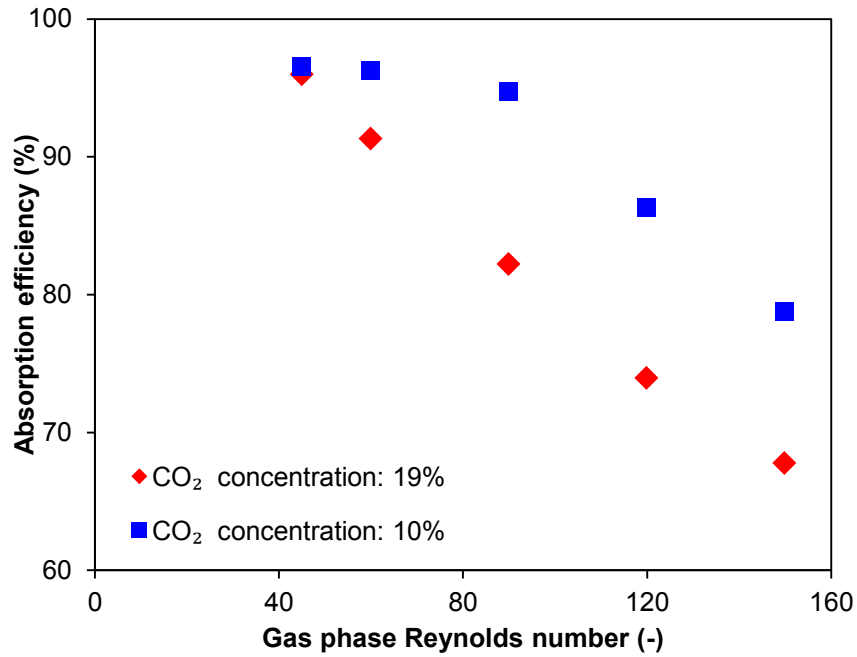
Figure 7.34: Effect of gas concentration on absorption efficiency (C_{DEA}: 20% by mass of DEA in water; L: 0.05 m; Re_G: 45-150; Re_L: 54).
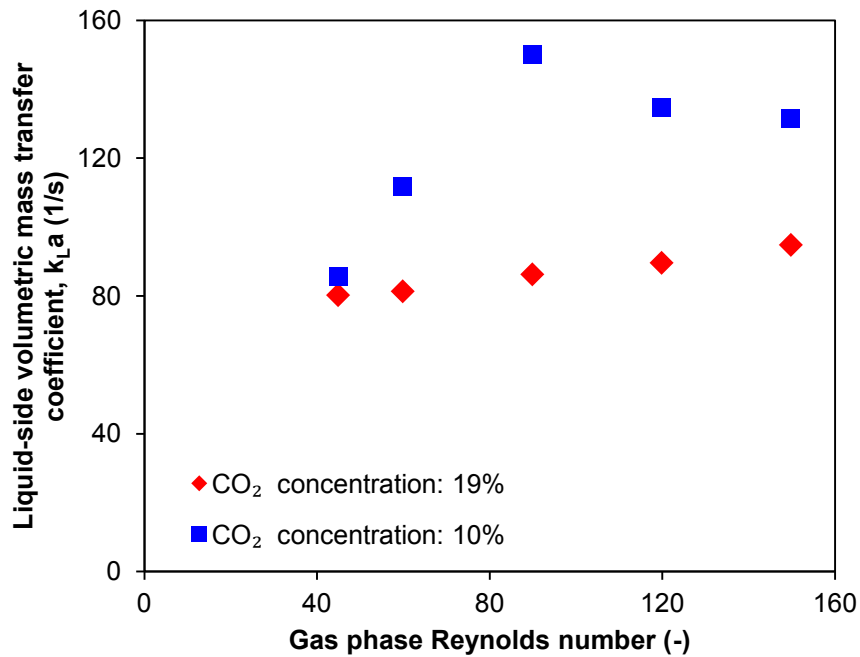
Figure 7.35: Effect of gas concentration on liquid-side volumetric mass transfer coefficient (C_{DEA}: 20% by mass of DEA in water; L: 0.05 m; Re_G: 45-150; Re_L: 54).

7.4.3 Inferences from closed loop testing with variant residence time

This section investigated the fluid flow and mass transfer characteristics during the absorption of CO_2 into diethanolamine in a micro-structured absorber. A closed-loop configuration was utilized wherein absorption and solvent regeneration occurred in the same system. The performance of the absorber was studied with respect to the pressure drop, absorption efficiency, and mass transfer coefficient. The single-phase and two-phase pressure drops were compared against available models and a good agreement was obtained. Parametric studies varying the gas and liquid flow rates, as well as the gas phase concentration, were conducted. The effect of channel length (residence time) was investigated for cases of 0.05, 0.1, and 0.45 m. In comparison to the 0.05 m channel, the absorption efficiency with the 0.1 m and 0.45 m channels was higher on average by 3% and 8%, respectively, while the mass transfer coefficients were lower by 43% and 84%, respectively. These trends are in conformance with that observed during the single channel analysis in Chapter 3 and are an indication of the scalability of the microreactor technology proposed therein.

7.5 Comparison with conventional systems

The performance of the multiport microreactor studied in this chapter was compared with several conventional absorption systems in order to determine the magnitude of process enhancement that was achieved. The performance parameter data for conventional systems was obtained from Charpentier (1981). As can be seen in Figure 7.36, the presently achieved liquid-side volumetric mass transfer coefficients, k_La, are higher by 2-4 orders of magnitude. These results are an indication of both the

tremendous intensification in mass transfer that can be achieved with microreactors, as well as the potential for successful scaling-up from single channel microreaction systems.
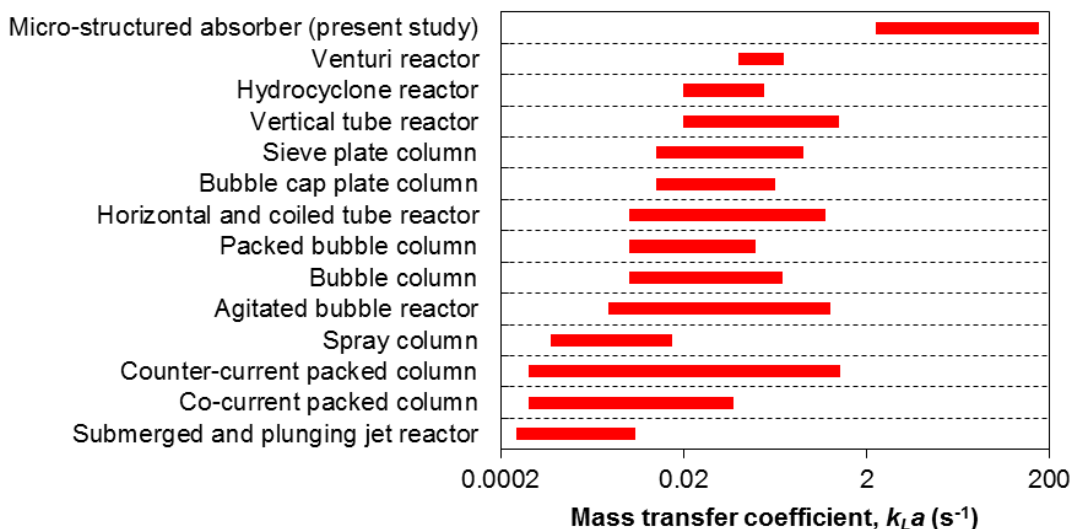
Figure 7.36: Comparison of performance parameters with conventional technologies.

7.6 Chapter conclusions

This chapter reported an experimental investigation of the gas-liquid absorption of CO_2 into aqueous DEA in multiport microreactors having 15 straight, parallel channels. The performance of the reactor was studied with respect to the absorption efficiency, mass transfer coefficient, acid gas loading ratio, and pressure drop. Open-loop and closed-loop configurations were developed, validated, and tested. Parametric studies investigating the effects of gas and liquid flow rates, gas and liquid phase concentration, and reactor length, were performed and discussed. A flow map based on gas and liquid phase superficial velocities was generated based on available transition criteria in the literature. High levels of absorption efficiency, close to

288

100%, were observed under certain operating conditions. The mass transfer coefficient was found to be higher with short residence times, which was attributed to improved utilization of the absorption capacity of the amine solution for a given reactor volume. Enhanced mass transfer characteristics were obtained at higher liquid phase concentration levels.

In general, the trends observed with the present multiport microreactor were found to be in agreement with the previously discussed single channel microreactor analysis. Furthermore, liquid-side volumetric mass transfer coefficients as high as 150 s^{-1} were achieved with the present multiport microreactor which is between 2-4 orders of magnitude higher than that reported using most conventional gas-liquid absorption systems. The same was considered an indication of both the high levels of intensification of the absorption process that can be achieved with microreactors, as well as the potential for successful scaling-up from single channel microreaction systems.

Chapter 8: Experimental study of Stacked Multiport Microreactor

8.1 Introduction

Microreactors have been demonstrated to yield several orders of magnitude enhancement in performance as compared to conventional mass transfer systems. Laboratory-scale single channel microreactors were investigated in Chapter 3, following which an order of magnitude increase in scaled was achieved with a 15 channel multiport microreactor in Chapter 7. One of the challenges associated with scaling up is to design a suitable inlet design that achieved optimum flow distribution without excessive pressure drop and/or complexity. The present chapter goes further in scaling up with a two orders of magnitude increase in the scale of the system over the laboratory-scale reactors studied in Chapter 3 by developing and testing a bench-scale stacked multiport microreactor for the absorption of CO_2 mixed with N_2 in aqueous DEA.

8.2 Description of experiments

8.2.1 Experimental setup

The present microreactor was fabricated out of aluminum. It comprised 105 channels compactly arranged in 7 stacked layers, with each layer comprising 15 straight, parallel channels. The channels were fabricated by extrusion process and had a hydraulic diameter of 1 mm, length of 25 cm, circular cross-sectional geometry. For

thermal management purposes, adjacent layers were separated by a gap of 1 mm to facilitate natural convection cooling using ambient air.

A primary concern when designing scaled-up microreactors for two-phase flows is to achieve optimum mixing of the gas and liquid phase at the reactor inlet such that the gas void fraction in every channel is relatively similar. For this reason, an annular-type inlet configuration was designed which ensured that the first point of contact or mixing between the gas and liquid phases occurred inside individual channels. In this configuration, a two-phase inlet header was utilized which contained one inlet port for the gas phase and two inlet ports for the liquid phase, as shown in Figure 8.1. The gas stream supplied to the microreactor through the gas inlet port flowed into a reservoir having volume of ~1400 mm^3. From here, the gas stream was fed to each microreactor channel, individually, through a network of gas manifolds having internal and external diameters equaling 0.413 mm and 0.718 mm, respectively. Accordingly, the circular cross-section of each microreactor channel in the inlet region was partially obstructed by a gas manifold, thus creating an annular space having width of 0.141 mm. The liquid phase stream being supplied to the microreactor was split and directed into two inlet ports, flowed past the external surfaces of the network of gas manifolds, and entered each microreactor channel through the aforementioned annular space. The above arrangement, albeit its complexity, ensured that individual phases and not a two-phase mixture were delivered to each microreactor channel, and mixing of the two-phases occurred separately within each channel, thus achieving optimum flow distribution and

291

minimal maldistribution. Finally, the two-phase mixture leaving individual

microreactor channels was directed towards a single outlet port.

Schematic diagrams of the microreactor in exploded view are shown in Figure 8.1and

an assembled image of the same is reported in Figure 8.2. The height and width of the

microreactor equaled 47 mm, while the length (or height depending on orientation)

equaled 292 mm.
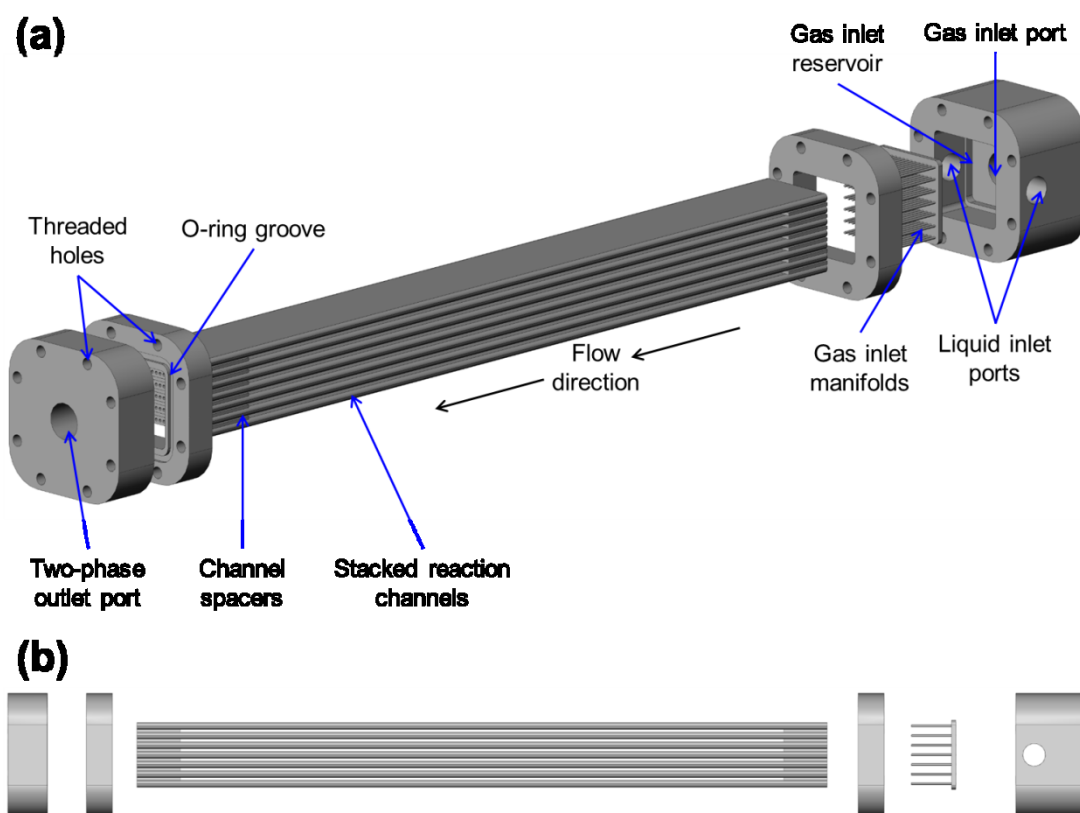
Figure 8.1: Schematic exploded diagram of microreactor in (a) isometric view (b) front view.
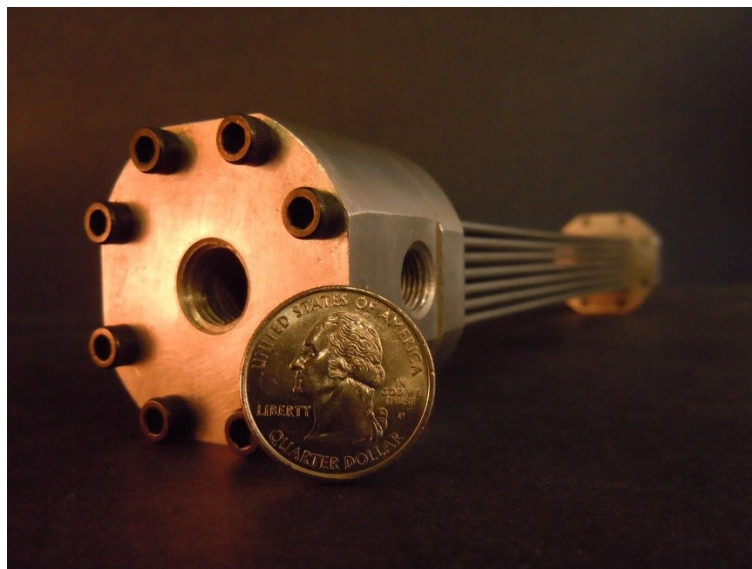
Figure 8.2: Image of assembled microreactor with reference scale.

The layout of the test loop is reported in Figure 8.3. A variable speed gear pump (Micropump Inc., USA) was used to control the liquid flow rate which was subsequently measured by a Coriolis mass flow meter (Endress+Hauser Inc., USA). The gas flow rate was measured and controlled by a differential pressure-based mass flow controller (Cole-Parmer, USA). A differential pressure transducer (OMEGA Engineering Inc., USA) was connected across the liquid inlet (prior to the splitting the liquid stream for the two microreactor inlet ports), and the channel outlet. The two-phase mixture leaving the absorber entered a two-phase separating column. The column comprised of vertically installed tubing (ID: 10 mm) that performed gravity-based separation of the loaded amine solution from the unabsorbed gas stream. Further, a level-control mechanism was incorporated in order to maintain a relatively constant level of liquid in the separation column. This arrangement resulted in unabsorbed gaseous stream entering the gas sensor for analysis, while the loaded amine solution was continuously removed from the experimental setup. The CO_2

concentration was measured continuously in-line with the fluid flow, by a non-dispersive infrared (NDIR) sensor (Vaisala Inc., USA). Based on the difference in concentration levels at the inlet and outlet of the absorber, the absorption efficiency was defined as given by Eq. 8.1.

$$\eta_{abs} = \frac{C_{CO_2,in} - C_{CO_2,out}}{C_{CO_2,in}} \times 100\% \qquad (8.1)$$
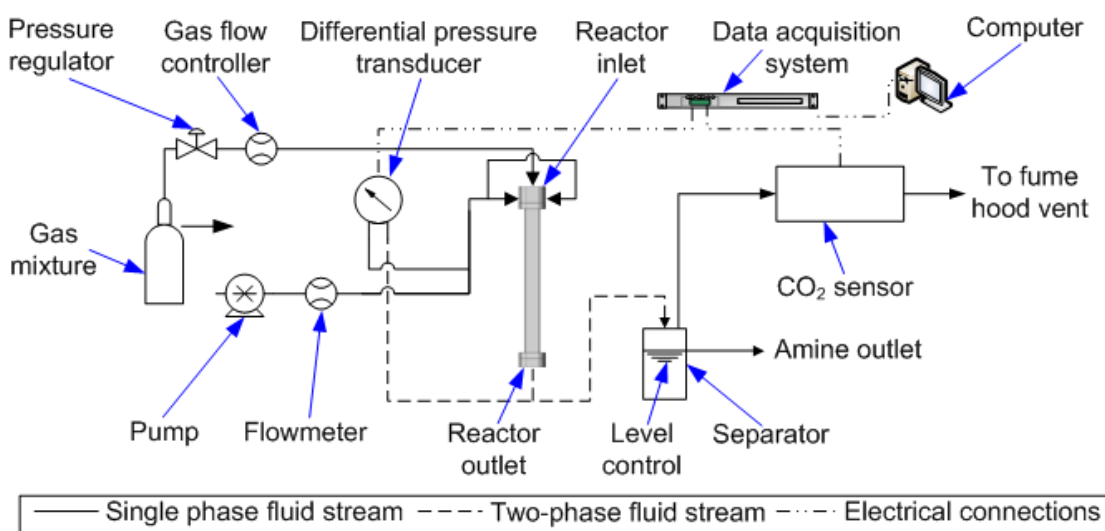
Figure 8.3: Layout of experimental test loop.

8.2.2 Operating conditions

The gas phase was CO_2 mixed with N_2 at concentration levels of 10% by volume, and was of industrial grade purity. The liquid phase was aqueous amine solution prepared using laboratory grade DEA (99% purity). The amine was diluted with distilled water to 20% concentration by mass. The gas and liquid flow rates were varied such that the range of Reynolds numbers for each phase varied between 28 to 195, and 26 to 66, respectively. All experiments were conducted at an ambient temperature of 298 K and at atmospheric pressure.

294

8.2.3 Uncertainty analysis

The uncertainty in the measurement of CO_2 concentration was ±3% of the reading and ±1.5% of the full scale range of the device (20% concentration of CO_2 by mass). The gas flow rate was measured with an uncertainty of ±0.8% of the reading and ±0.2% of the full scale range of the device (8.33×10^{-5} m^3/s). The uncertainty in liquid flow rate and pressure drop equaled ±0.1% and ±0.25% of the readings, respectively. By following the error propagation method, the average uncertainty in absorption efficiency and liquid-side volumetric mass transfer coefficient were determined to equal ±6.5% and ±16.9%, respectively.

8.3 Performance characterization

To characterize the performance of the reactor, the gas phase Reynolds number was varied between 28 and 195 and the liquid phase Reynolds number was varied between 26 and 66. The concentrations of the gas and liquid phases were 10% by volume of CO_2 in N_2, and 20% by mass of DEA in water, respectively.

The phase distribution in the channel is determined by the relative magnitudes of gas and liquid phase superficial velocities. Based on the same, different two-phase flow regimes can occur in the channel which in turn influences the mass transfer characteristics. Hence, a flow pattern map was developed using the regime transition criteria reported in the literature by Chung and Kawaji (2004). As can be seen in Figure 8.4, the dominant regimes under the present operating conditions were slug and slug-annular flow. Detailed descriptions of these regimes have been reported in previous chapters.
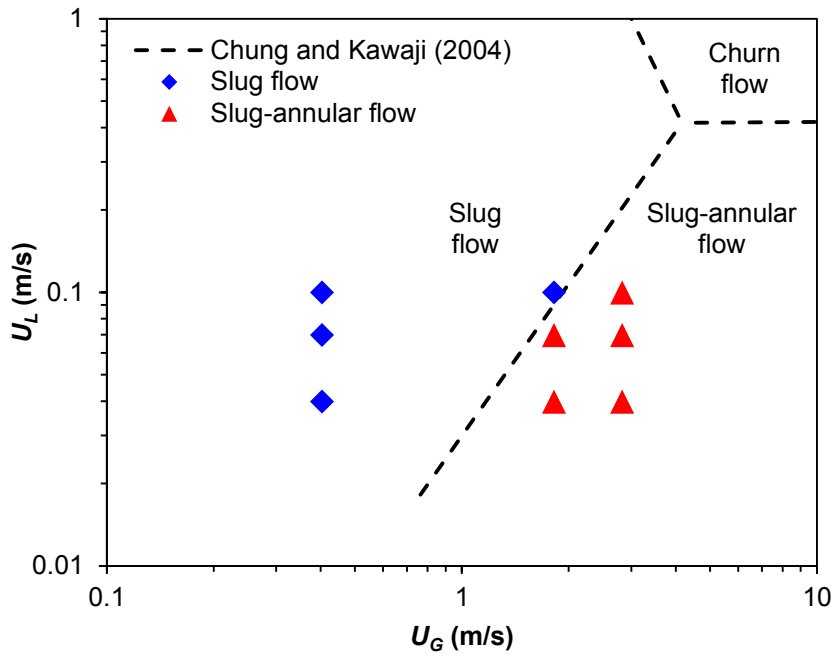
Figure 8.4: Flow pattern map with regime transition lines.
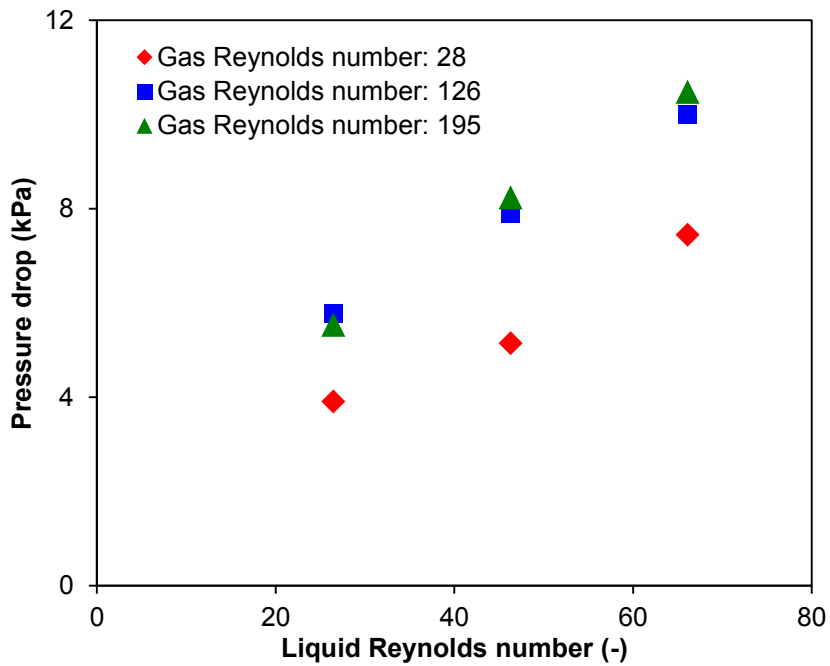
Figure 8.5: Effect of gas and liquid flow rate on two-phase pressure drop (C_{CO2}: 10% by volume of CO_2 in N_2; C_{DEA}: 20% by mass of DEA in water; Re_L: 26-66; Re_G: 28-195).

The results of two-phase pressure drop reported in Figure 8.5 indicate higher pressure drops with increasing gas/liquid flow rate and this behavior is consistent with the physics of fluid flow. Figure 8.6 indicates that for a constant gas Reynolds number, an increase in the liquid Reynolds number results in higher absorption efficiencies. Additionally, higher gas Reynolds numbers resulted in a decrease in absorption efficiency. The reasons for the above-described trends depend upon the prevalent flow regime as detailed in Chapter 3. Furthermore, the current trends are in agreement with previously reported single channel analyses in Chapter 3, thus demonstrating the successful scalability of the single channel microreactor studied therein.
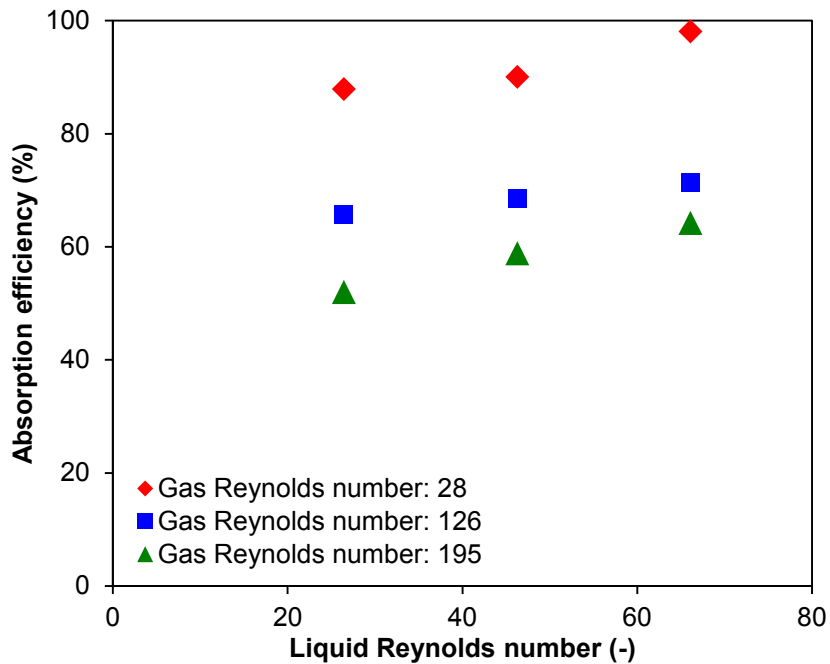
Figure 8.6: Effect of gas and liquid flow rate on absorption efficiency (C_{CO2}: 10% by volume of CO_2 in N_2; C_{DEA}: 20% by mass of DEA in water; Re_L: 26-66; Re_G: 28-195).

The results for liquid-side volumetric mass transfer coefficient are reported in Figure 8.7. As can be seen, higher mass transfer coefficients were obtained at higher liquid

phase Reynolds numbers on account of the increased absorption occurring under these conditions. Likewise, higher gas phase Reynolds numbers also resulted in higher mass transfer coefficients and this can be attributed to higher molar fluxes. The interpretation of these trends is similar to the discussion provided previously in Chapter 3.
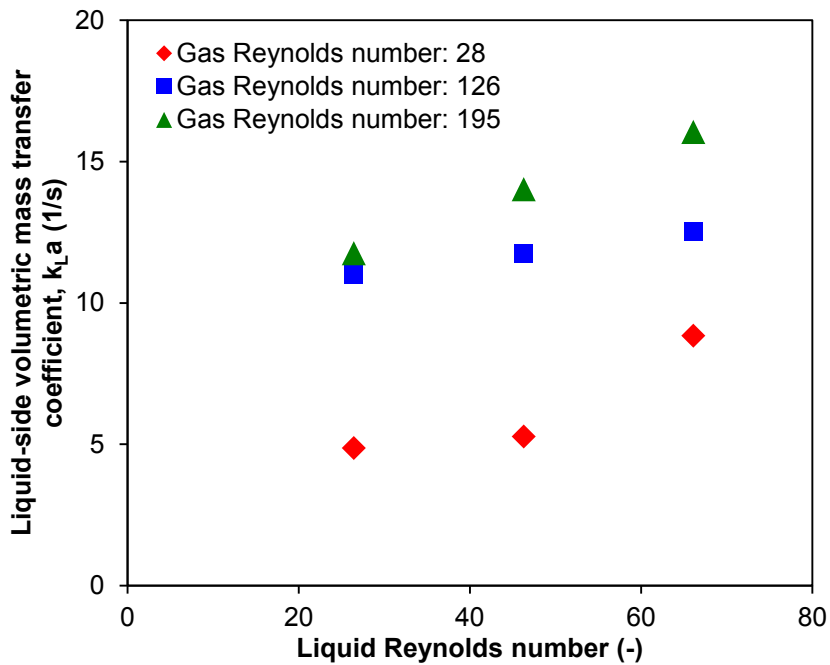
Figure 8.7: Effect of gas and liquid flow rate on liquid-side volumetric mass transfer coefficient (C_{CO2}: 10% by volume of CO_2 in N_2; C_{DEA}: 20% by mass of DEA in water; Re_L: 26-66; Re_G: 28-195).

The acid gas loading ratio was defined as the moles of CO_2 absorbed in a single mole of DEA, and the results are reported in Figure 8.8. An increase in this ratio represents an improvement in the operating performance of the system. Based on the definition, the highest values of the loading ratio are expected to be achieved at low liquid flow rates and high gas flow rates, and indeed this is the observed trend in Figure 8.8. It is

worth noting that although the present values of acid gas loading are relatively low when compared to the theoretical loading potential of the liquid solvent, this can be easily addressed by using multiple pass configurations and/or re-using the amine solution prior to regeneration.
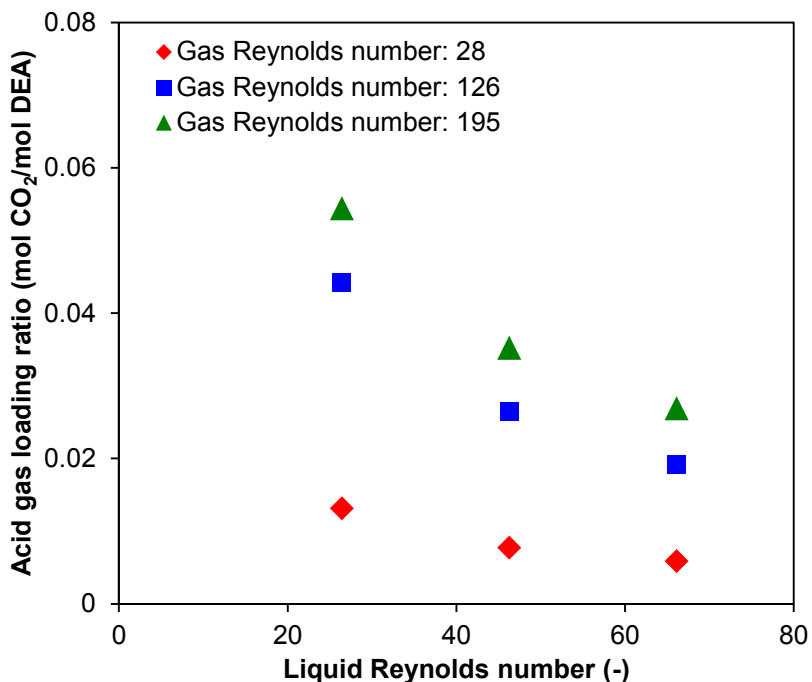
Figure 8.8: Effect of gas and liquid flow rate on acid gas loading ratio (C_{CO2}: 10% by volume of CO_2 in N_2; C_{DEA}: 20% by mass of DEA in water; Re_L: 26-66; Re_G: 28-195).

8.4 Comparison with conventional technologies

The performance of the stacked multiport microreactor studied in this chapter was compared with several conventional absorption systems in order to determine the magnitude of process enhancement that was achieved. The performance parameter data for conventional systems was obtained from Charpentier (1981). As can be seen in Figure 8.9, the presently achieved liquid-side volumetric mass transfer coefficients,

$k_L a$, are higher by 1-3 orders of magnitude. These results are an indication of both the tremendous intensification in mass transfer that can be achieved with microreactors, as well as the potential for successful scaling-up from single channel microreaction systems.
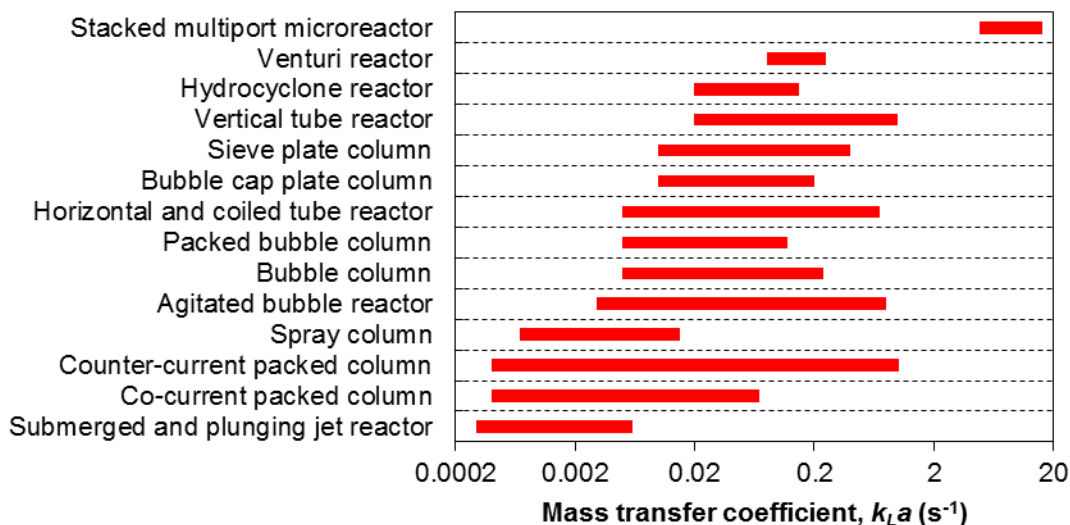
Figure 8.9: Comparison of mass transfer performance of present microreactor with conventional technologies.

8.5 Chapter conclusions

This chapter reported an experimental investigation of the gas-liquid absorption of CO_2 into aqueous DEA in a stacked multiport microreactor comprising 105 channels in 7 stacked layers. This represents an increase in system size by two orders of magnitude as compared to the single channel microreactors studied in Chapter 3. The performance of the reactor was studied with respect to the absorption efficiency, mass transfer coefficient, acid gas loading ratio, and pressure drop. Parametric studies investigating the effects of gas and liquid flow rates were performed and discussed. A

flow map based on gas and liquid phase superficial velocities was generated based on available transition criteria in the literature. High levels of absorption efficiency, close to 100%, were observed under certain operating conditions. Liquid-side volumetric mass transfer coefficients that were between 1-3 orders of magnitude higher than those reported using most conventional gas-liquid absorption systems were achieved with the present microreactor. The same was considered an indication of both the high levels of intensification of the absorption process that can be achieved with microreactors, as well as the potential for successful scaling-up from single channel microreaction systems.

Chapter 9: Dissertation Conclusions and Future Work

Recommendations

9.1 Conclusions from dissertation

This dissertation reported an experimental and computational analysis of enhanced gas-liquid absorption in microreactor systems. Based on the experimental analysis of various types of microreactors, the following conclusions are drawn.

1. Microreactors can offer substantial process intensification and enhancement of gas-liquid absorption phenomena. Mass transfer coefficients as high as 400 s^{-1} were demonstrated in this study which corresponds to 2-4 orders of magnitude enhancement when compared to conventional technologies. This can be attributed to a 1-2 order of magnitude enhancement in the specific interfacial area, which can be as high as 15,000 m^2/m^3. High levels of absorption efficiency, close to 100%, can be achieved under optimum operating conditions.

2. Microscale two-phase flow is characterized by various flow regimes depending upon the relative magnitudes of surface tension and inertial forces including slug, slug-annular, annular, churn, and bubbly flow. Low gas phase superficial velocities and high liquid phase superficial velocities are optimum for achieving high absorption efficiency. High gas phase superficial velocities and high liquid phase superficial velocities are largely the most suited conditions for achieving high mass transfer coefficients. Rapid saturation of

the liquid solvent contained within the film region occurs at low liquid and high gas phase velocities. The reasons for these trends depend upon various factors including the prevalent flow regime, the magnitude of convective mixing currents, the phase associated with the dominant resistance to mass transfer, the thickness of thin liquid films, and the frequency of intense mixing/churning zones, among others.

3. Smaller diameter microreactors yield improved mass transfer characteristics. The specific interfacial area for 254 and 508 μm microreactors was on average 183% and 50% higher than that of a 762 μm microreactor, as a result of which the mass transfer coefficient was 256% and 53% higher, respectively. Microreactors with shorter residence times yield higher mass transfer coefficients on account of improved utilization of the absorption potential of the liquid solvent for a unit reactor volume. Multiple pass configuration systems are recommended to achieve the required absorption efficiency and/or solvent loading ratio metrics.

4. During the Taylor/slug flow regime, bubble formation by the dripping mechanism is characterized by marginal pressure forces and stronger shear forces. The squeezing mechanism is primarily driven by pressure forces, wherein multiple pressure fluctuations were observed as against a singular rise in pressure followed by a drop in pressure. With increasing mobility in the phase field model, the surface tension force field is suitably altered to yield increasingly longer bubbles while conforming to the physics of homogeneous two-phase flow. Capturing the thin liquid film at the channel wall can be best

303

accomplished using a highly resolved, three-dimensional domain. The numerically predicted flow fields from the phase field model are free of unphysical parasitic currents, while the corresponding VOF-based results are adversely affected by unphysical recirculations with the gas bubble. Likewise, the pressure distribution in the channel predicted by the phase field model does not involve any unphysical interfacial oscillations in pressure.

5. Microreactor technologies can be successfully scaled up from laboratory-scale systems to bench-scale systems. The scaling up process can achieve multiple orders of magnitude enhancement in system size. Potential future scaling up to capacities/throughputs of industrial relevance/significance is indeed feasible. Appropriate design of the inlet mixing region is essential to minimize maldistribution of the gas and liquid phases. Additionally, microreactors are compatible for operation in a closed loop with absorption and solvent regeneration occurring simultaneously.

6. A stationary interface numerical model was proposed to model gas-liquid absorption during Taylor flow in microreactors. This approach models the entire reactor, including the channel length as well as the inlet mixing region. The computational requirements are reduced by decoupling the hydrodynamics of the two-phase flow from the mass transfer phenomena. The model uses the phase field method to simulate the phase distribution during two-phase flow. The approach is purely theoretical in order to permit its application towards unconventional channel geometries. The model features good predictive accuracy with an MAE of 11.9% with respect to absorption

efficiency. While stationary interface models are more computationally efficient than unsteady interface models, their application is inherently limited to only those gas-liquid absorption applications that involve low gas phase concentration levels.

7. A volume of fluid-based unsteady interface formulation was developed to simulate the condensation process in microchannels. This model involves mass transfer driven by a temperature gradient. The model utilizes user-defined functions to specify the condensation heat and mass fluxes. The approach is completely independent of operating conditions and simulates all condensation flow regimes that occur depending upon the heat flux, mass flux and vapor quality. The model features good predictive accuracy with MAEs of 8.1% and 16.6% with respect to pressure drop and heat transfer coefficient.

8. A volume of fluid-based unsteady interface formulation was proposed to simulate the gas-liquid absorption in a microreactor driven by chemical reactions. The model simulates all two-phase flow regimes that are in occurrence depending upon the relative magnitudes of gas and liquid phase velocities. The model features good predictive accuracy with MAEs of 8.3% and 9.5% with respect to the absorption efficiency and mass transfer coefficient.

9.2 Recommendations for future work

Microscale devices are quickly penetrating new application areas in diverse engineering applications due to their proven potential to intensify processes, improve

process control, increase safety, and reduce the overall size. While the focus of this dissertation was on gas-liquid absorption processes driven by chemical reactions, the outcomes which indicate the benefits of microreactor technologies can be directed towards various other applications in the energy, chemical, process, biomedical, and aerospace sectors. The following recommendations are made to further advance the research reported in this dissertation.

1. Microreactor designs employing short residence times to achieve high utilization of the absorption potential of the liquid solvent per unit volume of the reactor are recommended to achieve high mass transfer coefficients, and multiple pass configurations are recommended to achieve the desired absorption efficiency and solvent loading metrics. Future work could design and test such a system in order to increase the potential to implement the proposed technology in industrial applications.

2. This dissertation demonstrated microreactor scaling up by two orders of magnitude from laboratory-scale to bench-scale systems. Appropriate design of the inlet mixing region with multiple channel systems was found to be essential. The present annular-type inlet mixing region employed for the stacked multiport microreactor was relatively complex in design. Subsequent scaling-up would likely involve the development of a system for testing in a pilot plant. When designing and manufacturing the associated large-size inlet mixing region, in addition to considering the performance as it relates to optimum gas/liquid phase distribution, the costs associated with the

manufacturing technique as well as the required materials could be considered.

3. The potential use of emerging advanced manufacturing techniques such as additive manufacturing or subtractive manufacturing should be considered, particularly if they are shown to have the capability to produce unconventional high-performance channel geometries that are not feasible with conventional manufacturing techniques. Likewise, the use of novel materials including various polymer-based substances should be investigated.

4. Most industrial gas separation processes do not deal with highly pure gas streams and are likely to contain significant particulate content in the millimeter/sub-millimeter range, that is assuming the filtration systems associated with the conventional absorption system are sufficient to remove large particulate content. This particulate content can cause fouling and eventual clogging of microreactor systems, which have channel diameters in the range of a few hundred micrometers. The mere deployment of micron/sub-micron level filters will result in a high pressure drop and will also necessitate frequent maintenance of the filters, resulting in increased costs and downtime. The development of more efficient anti-fouling/anti-clogging technologies based on mechanical separation processes is strongly warranted in order to facilitate higher adoption rates of microreactor systems for industrial applications.

5. Despite the significant progress that has been made in CFD modeling of two-phase flow without heat/mass transfer in recent years, much remains to be

accomplished, particularly with respect to emerging microscale computational domains, which are quite different from conventional macroscale domains. This includes the capability to simulate thin liquid films, as well as to realistically model the channel wall wetting behavior.

6. Optimization tools need to be developed for the design of large-scale gas-liquid absorption systems utilizing micro-structured surfaces. There are numerous dependent variables that influence the key objective functions, namely pressure drop, absorption efficiency, and mass transfer coefficient. Related research on high-performance heat exchangers has shown that optimum channel geometries are typically complex in design and have high aspect ratios. Similar analyses are needed for mass transfer applications as well, and the presently developed CFD models can be applied towards this effort.

Publications Thus Far Generated From This Work

At this time, a total of 13 peer-reviewed publications have been published based on the research reported in this dissertation. These include five peer-reviewed journal publications, seven peer-reviewed conference publications, and one peer-reviewed conference presentation. A list of these publications is reported below.

Peer-reviewed journal publications

1. H. Ganapathy, A. Shooshtari, S. Dessiatoun, M. Alshehhi, M. Ohadi, 2014, Fluid flow and mass transfer characteristics during enhanced CO_2 capture in a minichannel contactor, Applied Energy, 119, 43-56.

2. H. Ganapathy, A. Shooshtari, K. Choo, S. Dessiatoun, M. Alshehhi, M. Ohadi, 2013, Numerical simulation of condensation heat transfer in microchannels, International Journal of Heat and Mass Transfer, 65, 62-72.

3. H. Ganapathy, E. Al-Hajri, M. Ohadi, 2013, Mass transfer characteristics of gas-liquid absorption in a Taylor flow mini/microchannel reactors, Chemical Engineering Science, 101, 69-80.

4. H. Ganapathy, E. Al-Hajri, M.M. Ohadi, 2013, Phase field modeling of Taylor flow in mini/micro channels, Part I: Bubble formation mechanisms and phase field parameters, Chemical Engineering Science, 94, 138-149.

5. H. Ganapathy, E. Al-Hajri, M.M. Ohadi, 2013, Phase field modeling of Taylor flow in mini/micro channels, Part II: Hydrodynamics of Taylor flow, Chemical Engineering Science, 94, 156-165.

Peer-reviewed conference publications

1. H. Ganapathy, A. Shooshtari, S. Dessiatoun, M. Alshehhi, M.M. Ohadi, 2013, Enhanced carbon capture in a multiport microscale absorber, International Mechanical Engineering Congress & Exposition, San Diego, USA.

2. H. Ganapathy, A. Shooshtari, S. Dessiatoun, M. Alshehhi, M.M. Ohadi, 2013, Experimental investigation of advanced microscale reactors for enhanced carbon capture and natural gas sweetening applications, 7th International Conference on Energy Sustainability, Minneapolis USA.

3. H. Ganapathy, A. Shooshtari, S. Dessiatoun, M. Alshehhi, M.M. Ohadi, 2013, Experimental investigation of enhanced absorption of carbon dioxide in diethanolamine in a microreactor, 11th International Conference on Nanochannels, Microchannels and Minichannels, Sapporo, Japan.

4. H. Ganapathy, A. Shooshtari, K. Choo, S. Dessiatoun, M. Alshehhi, M.M. Ohadi, 2012, Numerical analysis of condensation of R134a in a single microchannel, International Mechanical Engineering Congress & Exposition, Houston, USA.

5. H. Ganapathy, E. Al-Hajri, M.M. Ohadi, 2011, Analysis of Taylor flow in microchannels by the phase field method, International Mechanical Engineering Congress & Exposition, Denver, USA.

6. H. Ganapathy, E. Al-Hajri, M.M. Ohadi, 2011, Phase field method for simulation of multiphase flow, International Mechanical Engineering Congress & Exposition, Denver, USA.

7. H. Ganapathy, E. Al-Hajri, M.M. Ohadi, 2011, Numerical simulation of mass transfer characteristics in a Taylor flow microreactor, 9th International Conference on Nanochannels, Microchannels and Minichannels, Edmonton, Canada.

Peer-reviewed conference presentations

1. H. Ganapathy, A. Shooshtari, S. Dessiatoun, M. Alshehhi, M. Ohadi, 2013, High efficiency carbon capture technology utilizing advanced micro-structured surfaces, Carbon Management Technology Conference 2013, Alexandria, USA.

Bibliography

[1]   Aaron D., Tsouris C., 2005. Separation of CO_2 from flue gas: a review. Separation Science and Technology 40, 321-348.

[2]   Abiev R.Sh., Lavretson I.V., 2012. Hydrodynamics and mass exchange in gas-liquid slug flow in microchannels. Russian Journal of General Chemistry 82, 2088-2099.

[3]   Aboulhasanzadeh B., Hosoda S., Tomiyama A., Tryggvason G., 2013. A validation of an embedded analytical description approach for the computations of high Schmidt number mass transfer from bubbles in liquids. Chemical Engineering Science 101, 165-174.

[4]   Aboulhasanzadeh B., Thomas S., Taeibi-Rahni M., Tryggvason G., 2012. Multiscale computations of mass transfer from buoyant bubbles. Chemical Engineering Science 75, 456-467.

[5]   Akanksha, Pant K.K., Srivastava V.K., 2008. Mass transport correlation for CO2 absorption in aqueous monoethanolamine in a continuous film contactor. Chemical Engineering and Processing: Process Intensification 47, 920-928.

[6]   Akbar M.K., Ghiaasiaan S.M., 2006. Simulation of Taylor flow in capillaries based on the volume-of-fluid technique. Industrial & Engineering Chemistry Research 45, 5396–5403.

[7]   Akhtar F., Andersson L., Keshavarzi N., Bergström L., 2012. Colloidal processing and CO_2 capture performance of sacrificially template zeolite monoliths. Applied Energy 97, 289-296.

[8]   Al Hosn Gas, 2012. Al Hosn news. 1(3).

[9]   Alonso T.V., 2010. High efficiency on CO2 removal in natural gas with UCARSOL solvents. Proceedings of the Rio Oil & Gas Expo and Conference, IBP 2778_10.

[10]   Angeli P., Gavriilidis A., 2008. Hydrodynamics of Taylor flow in small channels: a review. Proceedings of the IMechE Part C Journal of Mechanical Engineering Science 222, 737–750.

[11]   Armand A.A., Treschev G.G., 1946. The resistance during the movement of a two-phase system in horizontal pipes. Izvestya Vsesoyuznogo Teplotekhnicheskogo Instituta 1, 16–23.

[12]   Asadolahi A.N., Gupta R., Fletcher, D.F., Haynes, B.S., 2011. CFD approaches for the simulation of hydrodynamics and heat transfer in Taylor flow. Chemical Engineering Science 66, 5575-5584.

[13]   Asadolahi A.N., Gupta R., Leung S.S.Y., Fletcher D.F., Haynes B.S., 2012. Validation of a CFD model of Taylor flow hydrodynamics and heat transfer. Chemical Engineering Science 69, 541-552.

[14] Aussillous P., Quere D., 2000. Quick deposition of a fluid on the wall of a tube. Physics of Fluids 12, 2367–2371.

[15] Balasubramanian P., Kandlikar S.G., 2004. An experimental study of flow patterns, pressure drop and flow instabilities in parallel rectangular minichannels. In: Proceedings of the 2nd International Conference on Microchannels and Minichannels, Rochester, New York, 475-481.

[16] Baummer T., Cetegen E., Ohadi M., Dessiatoun S., 2008. Force-fed evaporation and condensation utilizing advanced micro-structured surfaces and micro-channels. Microelectronics Journal 39, 975-980.

[17] Berčič G., Pintar A., 1997. The role of gas bubbles and liquid slug lengths on mass transport in the Taylor flow through capillaries. Chemical Engineering Science 52, 3709-3719.

[18] Bin H., Shisen X., Shiwang G., Lianbo L., Jiye T., Hongwei N., Cai M., Cheng J., 2010. Industrial test and techno-economic analysis of CO_2 capture in Huaneng Beijing coal-fired power station. Applied Energy 87, 3347-3354.

[19] Blaszczak R.J., Zerbonia R.A., Spivey J.J., Agarwal S.K., Damle A.S., Sanford C.W., 1995. Survey of control technologies for low concentration organic vapor gas streams. U.S. Environmental Protection Agency EPA-456/R-95-003, pp. 93-103.

[20] Blauwhoff P.M.M., Versteeg G.F., van Swaaij W.P.M., 1984. A study on the reaction between CO2 and alkanolamines in aqueous solutions. Chemical Engineering Science 39, 207-225.

[21] Bothe D., Kroger M., Warnecke H.-J., 2011. A VOF-based conservative method for the simulation of reactive mass transfer from rising bubbles. Fluid Dynamics and Materials Processing 7, 303-316.

[22] Bounaceur R., Lape N., Roizard D., Vallieres C., Favre E., 2006. Membrane processes for post-combustion carbon dioxide capture: a parametric study. Energy 31, 2256-2270.

[23] Brackbill J.U., Kothe D.B., Zemach C., 1992. A continuum method for modeling surface tension. Journal of Computational Physics 100, 335-354.

[24] Brauner N., Moalem-Maron D., 1992. Identification of the range of 'small diameter' conduits regarding two-phase flow pattern transition. International Communications in Heat and Mass Transfer 19, 29-39.

[25] Bretherton F.P., 1961. The motion of long bubbles in tubes. Journal of Fluid Mechanics 10, 166–188.

[26] Browning G.J., Weiland R.H., 1994. Physical solubility of carbon dioxide in aqueous alkanolamines via nitrous oxide analogy. Journal of Chemical Engineering Data 39, 817-822.

[27] Cahn J.W., Hilliard J.E., 1959. Free energy of a non-uniform system. III. Nucleation in a two-component incompressible fluid. The Journal of Chemical Physics 31 (3), 688-699.

[28] Carlson A., Kudinov P., Narayanan C., 2008. Prediction of two-phase flow in small tubes: a systematic comparison of state-of-the-art CMFD codes, in: Proceedings of 5th European Thermal-Sciences Conference, Eindhoven, The Netherlands.

[29] Cetegen E., 2010. Force fed microchannel high heat flux cooling utilizing microgrooved surfaces. Ph.D. Dissertation, University of Maryland College Park.

[30] Chambers R.D., Holling D., Spink R.C.H., Sandford G., 2001. Elemental fluorine part 13. Gas-liquid thin film microreactors for selective direct fluorination. Lab on a Chip 1, 132-137.

[31] Charpentier J.C., 1981. Mass-transfer rates in gas-liquid absorbers and reactors. In: Drew TB, Cokelet GR, Hoopes JW, Vermeulen T, editors. Advances in Chemical Engineering, New York: Academic Press, Inc., 11, 1-133.

[32] Chen J.F., Chen G.Z., Wang J.X., Shao L., Li P.F., 2011. High-throughput microporous tube-in-tube microreactor as novel gas-liquid contactor: mass transfer study. AiCHE Journal 57, 239-249.

[33] Chen Y., Kulenovic R.., Mertz R., 2009. Numerical study on the formation of Taylor bubbles in capillary tubes. International Journal of Thermal Sciences 48, 234-242.

[34] Cheung O., Bacsik Z., Liu Q., Mace A., Hedin N., 2013. Adsorption kinetics for CO_2 on highly selective zeolites NaKA and nano-NaKa. Applied Energy 112, 1326-1336.

[35] Chevron Australia, 2014. Gorgon project overview. http://www.chevronaustralia.com/docs/default-source/default-document-library/fact-sheet-gorgon-project-overview--jan-2014.pdf?sfvrsn=0, Retrieved on February 26, 2014.

[36] Chevron Corporation, 2014. http://www.chevron.com, Retrieved on February 26, 2014.

[37] Chiesa P., Campanari S., Manzolini G., 2011. CO_2 cryogenic separation from combined cycles integrated with molten carbonate fuel cells. International Journal of Hydrogen Energy 36, 10355-10365.

[38] Chung P.M.-Y., Kawaji M., 2004. The effect of channel diameter on adiabatic two-phase flow characteristics in microchannels. International Journal of Multiphase Flow 30, 735–761.

[39] Coleman J.W., Garimella S., 2003. Two-phase flow regimes in round, square and rectangular tubes during condensation of refrigerant R134a. International Journal of Refrigeration 26, 117-128.

[40] ConocoPhillips, 2012. Natural gas, sour (Canada). http://www.conocophillips.com/EN/products/safetydata/Documents/MSDS%20Canada/791785%20Natural%20Gas,%20Sour%20_Canada_.pdf, Retrieved on 31st March 2013.

[41] Constantinou A., Barrass S., Pronk F., Bril T., Wenn D.A., Shaw J.E.A., Gavriilidis A., 2012. CO_2 absorption in a high efficiency silicon nitride mesh contractor. Chemical Engineering Journal 207-208, 766-771.

[42] Constantinou A., Gavriilidis A., 2009. CO_2 absorption in a microstructured mesh reactor. Industrial & Engineering Chemistry Research 49, 1041-1049.

[43] Crovetto R., 1991. Evaluation of solubility data of the system CO_2-H_2O from 273 K to the critical point of water. Journal of Physical and Chemical Reference Data 20, 575-589.

[44] Danckwerts P.V., 1970. Gas-Liquid Reactions. McGraw Hill: New York.

[45] David M.P., Miler J., Steinbrenner J.E., Yang Y., Touzelbaev M., Goodson K.E., 2011. Hydraulic and thermal characteristics of a vapor venting two-phase microchannel heat exchanger. International Journal of Heat and Mass Transfer 54, 5504-5516.

[46] Davies R.M., Taylor G., 1950. The mechanics of large bubbles rising through extended liquids and through liquids in tubes, in: Proceedings of the Royal Society of London, Series A, Mathematical and Physical Sciences 200 (1062), 375-390.

[47] de Mas N., Jackman R. J., Schmidt,M. A., Jensen K. F., 2001. Microchemical systems for direct fluorination of aromatics. In: Microreaction Technology. IMRET 5: Proceedings of the Fifth International Microreaction Technology, Springer Berlin Heidelberg, pp. 60-67.

[48] De Menech M., 2006. Modeling of droplet breakup in a microfluidic T-shaped junction with a phase field model. Physical Review E 73, 031515.

[49] De Menech M., Garstecki P., Jousse F., Stone H.A., 2008. Transition from squeezing to dripping in a microfluidic T-shaped junction. Journal of Fluid Mechanics 595, 141-161.

[50] Derby M., Lee H.J., Peles Y., Jensen M.K., 2012. Condensation heat transfer in square, triangular, and semi-circular mini-channels. International Journal of Heat and Mass Transfer 55, 187-197.

[51] Dobson M.K., Chato J.C., 1998. Condensation in smooth horizontal tubes. Journal of Heat Transfer 120, 193-213

[52] Donaldson A.A., Kirpalani D.M., Macchi A., 2011. Diffuse interface tracking of immiscible fluids: improving phase continuity through free energy density selection. International Journal of Multiphase Flow 37, 777-787.

[53] Ehrfeld W., Hessel V., Löwe H., 2000. Microreactors: new technology for modern chemistry. 1st ed. Weinheim: Wiley-VCH.

[54] Esmaeeli A., Tryggvason G., 2004a. Computations of film boiling. part I: numerical method. International Journal of Heat and Mass Transfer 47, 5451-5461.

[55] Esmaeeli A., Tryggvason G., 2004b. Computations of film boiling. part II: multi-mode film boiling. International Journal of Heat and Mass Transfer 47, 5463-5476.

[56] Fairbrother F., Stubbs A.E., 1935. Studies in electro-endosmosis. Part VI. The bubble-tube method of measurement. Journal of the Chemical Society 1, 527-529.

[57] Fang C., David M., Rogacs A, Goodson K., 2010a. Volume of fluid simulation of boiling two-phase flow in a vapor venting microchannel. Frontiers in Heat and Mass Transfer 1, 013002.

[58] Fang C., David M., Wang F., Goodson K.E., 2010b, Influence of film thickness and cross-sectional geometry on hydrophilic microchannel condensation. International Journal of Multiphase Flow 36, 608-619.

[59] Fang C., Hidrovo C., Wang F., Eaton J., Goodson K., 2008. 3-D numerical simulation of contact angle hysteresis for microscale two phase flow. International Journal of Multiphase Flow 34, 690-705.

[60] Fang C., Steinbrenner J.E., Wang F., Goodson K.E., 2010c. Impact of wall hydrophobicity on condensation flow and heat transfer in silicon microchannels. Journal of Micromechanics and Microengineering 20, 0405018.

[61] Fries D.M., von Rohr P.R., 2009. Impact of inlet design on mass transfer in gas-liquid rectangular microchannels. Microfluid Nanofluid 6, 27-35.

[62] Ganapathy H., Al-Hajri E., Ohadi M., 2013a. Mass transfer characteristics of gas-liquid absorption in a Taylor flow mini/microchannel reactors. Chemical Engineering Science 101, 69-80.

[63] Ganapathy H., Al-Hajri E., Ohadi M.M., 2011a. Analysis of Taylor flow in microchannels by the phase field method. In: Proceedings of the International Mechanical Engineering Congress & Exposition, Denver, USA.

[64] Ganapathy H., Al-Hajri E., Ohadi M.M., 2011b. Numerical simulation of mass transfer characteristics in a Taylor flow microreactor. In: Proceedings

of the 9th International Conference on Nanochannels, Microchannels and Minichannels, Edmonton, Canada.

[65] Ganapathy H., Al-Hajri E., Ohadi M.M., 2011c. Phase field method for simulation of multiphase flow. In: Proceedings of the International Mechanical Engineering Congress & Exposition, Denver, USA.

[66] Ganapathy H., Al-Hajri E., Ohadi M.M., 2013b. Phase field modeling of Taylor flow in mini/micro channels, Part I: Bubble formation mechanisms and phase field parameters. Chemical Engineering Science 94, 138-149.

[67] Ganapathy H., Al-Hajri E., Ohadi M.M., 2013c. Phase field modeling of Taylor flow in mini/micro channels, Part II: Hydrodynamics of Taylor flow. Chemical Engineering Science 94, 156-165.

[68] Ganapathy H., Emlin V., Parikh A.N., Sajith V., 2011d. Experimental investigation on surface particle interactions during pool boiling of nanofluids. In: 9th International Conference on Nanochannels, Microchannels and Minichannels, Edmonton, Canada.

[69] Ganapathy H., Sajith V., 2013. Semi-analytical model for pool boiling of nanofluids. International Journal of Heat and Mass Transfer 57, 32-47.

[70] Ganapathy H., Shooshtari A., Choo K., Dessiatoun S., Alshehhi M., Ohadi M., 2013d, Numerical simulation of condensation heat transfer in microchannels, International Journal of Heat and Mass Transfer, 65, 62-72.

[71] Ganapathy H., Shooshtari A., Choo K., Dessiatoun S., Alshehhi M., Ohadi M.M., 2012. Numerical analysis of condensation of R134a in a single microchannel. In: Proceedings of the International Mechanical Engineering Congress & Exposition, Houston, USA.

[72] Ganapathy H., Shooshtari A., Dessiatoun S., Alshehhi M., Ohadi M., 2014. Fluid flow and mass transfer characteristics during enhanced CO_2 capture in a minichannel contactor. Applied Energy 119, 43-56.

[73] Ganapathy H., Shooshtari A., Dessiatoun S., Alshehhi M., Ohadi M.M., 2013e. Enhanced carbon capture in a multiport microscale absorber. In: Proceedings of the International Mechanical Engineering Congress & Exposition, San Diego, USA.

[74] Ganapathy H., Shooshtari A., Dessiatoun S., Alshehhi M., Ohadi M.M., 2013f. Experimental investigation of advanced microscale reactors for enhanced carbon capture and natural gas sweetening applications. In: Proceedings of the 7th International Conference on Energy Sustainability, Minneapolis USA.

[75] Ganapathy H., Shooshtari A., Dessiatoun S., Alshehhi M., Ohadi M.M., 2013g. Experimental investigation of enhanced absorption of carbon dioxide in diethanolamine in a microreactor. In: Proceedings of the 11th

International Conference on Nanochannels, Microchannels and Minichannels, Sapporo, Japan.

[76] Ganapathy H., Shooshtari A., Dessiatoun S., Alshehhi M., Ohadi M.M., 2013h. High efficiency carbon capture technology utilizing advanced micro-structured surfaces. In: Proceedings of the Carbon Management Technology Conference 2013, Alexandria, USA.

[77] Gao N.N., Wang J.X., Shao L., Chen J.F., 2011. Removal of carbon dioxide by absorption in microporous tube-in-tube microchannel reactor. Industrial & Engineering Chemistry Research 50, 6369-6374.

[78] Garstecki P., Fuerstman M.J., Stone H.A., Whitesides G.M., 2006. Formation of droplets and bubbles in a microfluidic T-junction-scaling and mechanism of break-up. Lab Chip 6, 437-446.

[79] Ghiaasiaan S.M., Abdel-Khalik S.I., 2001. Two-phase flow in microchannels. Advances in Heat Transfer 34, 145-254.

[80] Giuffrida A., Bonalumi D., Lozza G., 2013. Amine-based post-combustion CO_2 capture in air-blown IGCC systems with cold and hot gas clean-up. Applied Energy 110, 44-54.

[81] Global CCS Institute, 2014. Gorgon carbon dioxide injection project. http://www.globalccsinstitute.com/project/gorgon-carbon-dioxide-injection-project, Retrieved on February 26, 2014

[82] Guangwen C., Jun Y., Quan Y., 2008. Gas-liquid microreaction technology: recent developments and future challenges. Chinese Journal of Chemical Engineering 16, 663-669.

[83] Gupta R., Fletcher D.F., Haynes B.S., 2009. On the CFD modeling of Taylor flow in microchannels. Chemical Engineering Science 64, 2941-2950.

[84] Gupta R., Fletcher D.F., Haynes B.S., 2010. Taylor flow in microchannels: A review of experimental and computational work. The Journal of Computational Multiphase Flow 2, 1–31.

[85] Harirchian T., Garimella S.V., 2011. Flow regime-based modeling of heat transfer and pressure drop in microchannel flow boiling. International Journal of Heat and Mass Transfer 55, 1246-1260.

[86] Harish G., Emlin V., Sajith V., 2011. Effect of surface particle interactions on pool boiling of nanofluids. International Journal of Thermal Sciences 50, 2318-2327.

[87] Hart A., Gnanendran N., 2009. Cryogenic CO_2 capture in natural gas. Energy Procedia 1, 697-709.

[88] Hassanvand A., Hashemabadi S.H., 2011. Direct numerical simulation of interphase mass transfer in gas-liquid multiphase systems. International Communications in Heat and Mass Transfer 38, 943-950.

318

[89]   Hassanvand A., Hashemabadi S.H., 2012. Direct numerical simulation of mass transfer from Taylor bubble flow through a circular capillary. International Journal of Heat and Mass Transfer 55, 5959-5971.

[90]   Hayashi S., Kasagi N., Suzuki Y., 2007. The effects of inlet flow conditions on gas-liquid two-phase flow in a microtube. Proceedings of the ASME/JSME 2007 Thermal Engineering Heat Transfer Summer Conference 3, 707-714.

[91]   He Q., Kasagi N., 2008. Phase-field simulation of small capillary-number two-phase flow in a microtube. Fluid Dynamics Research 40, 497-509.

[92]   Hedin N., Andersson L., Bergström L., Yan J., 2013. Adsorbents for the post-combustion capture of CO_2 using rapid temperature swing or vacuum swing adsorption. Applied Energy 104, 418-433.

[93]   Hirt C.W., Nichols B.D., 1981. Volume of fluid (VOF) method for the dynamics of free boundaries. Journal of Computational Physics 39, 201–225.

[94]   Ho M.T., Allinson G.W., Wiley D.E., 2008. Reducing the cost of CO_2 capture from flue gas using membrane technology. Industrial & Engineering Chemistry Research 47, 1562-1568.

[95]   Hu J.S., Chao C.Y.H., 2007. An experimental study of the fluid flow and heat transfer characteristics in micro-condensers with slug bubbly flow. International Journal of Refrigeration 20, 1309-1318.

[96]   Hwang Y.W., Kim M.S., 2006. The pressure drop in microtubes and the correlation development. International Journal of Heat and Mass Transfer 49, 1804-1812.

[97]   In Salah Gas, 2014. http://www.insalahco2.com, Retrieved on February 26, 2014.

[98]   International Energy Agency (IEA), 2009. Carbon Capture and Storage. http://iea.org/publications/freepublications/publication/ccs_g8july09.pdf, Retrieved on 10 May, 2013.

[99]   Irandoust S., Andersson B., 1989. Simulation of flow and mass transfer in Taylor flow through a capillary. Computers and Chemical Engineering 13 (4/5), 519-526.

[100]   Jacqmin D., 1999. Calculation of two-phase Navier-Stokes flows using phase-field modeling. Journal of Computational Physics 155, 96-127.

[101]   Jeon S.S., Kim S.J., Park G.C., 2011. Numerical study of condensing bubble in subcooled boiling flow using volume of fluid model. Chemical Engineering Science 66, 5899-5909.

[102]   Jiang B., Wang X., Gray M.L., Dian Y., Luebke D., Li B., 2013. Development of amino acid and amine acid-complex based solid sorbents for CO_2 capture. Applied Energy 109, 112-118.

[103] Juric D., Tryggvason G., 1998. Computations of boiling flows. International Journal of Multiphase Flow 24, 387-410.

[104] Kandlikar S.G., Grande W.J., 2003. Evolution of microchannel flow passages-thermohydraulic performance and fabrication technology. Heat Transfer Engineering 24 (1), 3-17.

[105] Katzer J., Ansolabehere S., Beer J., Deutch J., Ellerman A.D., Friedmann S.J., Herzog H., Jacoby H.D., Joskow P.L., McRae G., Lester R., Moniz E.J., Steinfeld E., 2007. The future of coal. Massachusetts Institute of Technology, 17-42.

[106] Kawahara A., Chung P.M.-Y., Kawaji, M., 2002. Investigation of two-phase flow pattern, void fraction and pressure drop in a microchannel. International Journal of Multiphase Flow 28, 1411–1435.

[107] Kawaji M., Mori K., Bolintineanu D., 2009. The effects of inlet geometry and gas-liquid mixing on two-phase flow in microchannels. Journal of Fluids Engineering 131, 041302-1.

[108] Kececi S., Worner M., Onea A., Soyhan H.S., 2009. Recirculation time and liquid slug mass transfer in co-current upward and downward Taylor flow. Catalysis Today 147S, S125-S131.

[109] Killion J.D., Garimella S., 2004. Simulation of pendant droplets and falling films in horizontal tube absorbers. Journal of Heat Transfer 126, 1003-1013.

[110] Kim S.J., Park G.C., 2011. Interfacial heat transfer of condensing bubble in subcooled boiling flow at low pressure. International Journal of Heat and Mass Transfer 54, 2962-2974.

[111] Kim S.-M., Kim J., Mudawar I., 2012. Flow condensation in parallel micro-channels – part 1: experimental results and assessment of pressure drop correlations. International Journal of Heat and Mass Transfer 55, 971-983.

[112] Kim S.-M., Mudawar I., 2012a. Flow condensation in parallel micro-channels – part 2: heat transfer results and correlation technique. International Journal of Heat and Mass Transfer 55, 984-994.

[113] Kim S.-M., Mudawar I., 2012b. Universal approach to predicting two-phase frictional pressure drop for adiabatic and condensing mini/micro-channel flows. International Journal of Heat and Mass Transfer 55, 3246-3261.

[114] Kim Y.J., Joshi Y.K., Fedorov A.G., 2008. An absorption based miniature heat pump system for electronics cooling. International Journal of Refrigeration 31, 23-33.

[115] King C., Walsh E., Grimes R, 2007. PIV measurements of flow within plugs in a microchannel. Microfluid Nanofluid 3, 463-472.

[116] King C., Walsh E., Grimes R., 2007. PIV measurements of flow within plugs in a microchannel. Microfluid Nanofluid 3, 463-472.

[117] Kohl A., Nielsen R., 1997. Gas purification. 5th ed. Houston: Gulf Publishing Company.

[118] Kovvali A.S., Sirkar K.K., 2002. Carbon dioxide separation with novel solvents as liquid membranes. Industrial & Engineering Chemistry Research 41, 2287-2295.

[119] Kreutzer M.T., 2003. Hydrodynamics of Taylor flow in capillaries and monolith reactors. Ph.D. Dissertation, Technische Universiteit Delft, The Netherlands.

[120] Kreutzer M.T., Kapteijn F., Moulijn J.A., Heiszwolf J.J., 2005. Multiphase monolith reactors: chemical reaction engineering of segmented flow in microchannels. Chemical Engineering Science 60, 5895–5916.

[121] Krishna K.H., Ganapathy H., Sateesh G., Das S.K., 2011. Pool boiling characteristics of metallic nanofluids. Journal of Heat Transfer 133, 111501.

[122] Krishnan R.N., Vivek S., Chatterjee D., Das S.K., 2010. Performance of numerical schemes in the simulation of two-phase free flows and wall bounded mini channel flows. Chemical Engineering Science 65, 5117 – 5136.

[123] Kumar V., Vashisth S., Hoarau Y., Nigam K.D.P., 2007. Slug flow in curved microreactors: hydrodynamic study. Chemical Engineering Science 62, 7494-7504.

[124] Kundu A., Basu J.K., Das G., 2012. A novel gas-liquid contactor for chemisorption of CO_2. Separation and Purification Technology 94, 115-123.

[125] Kunze C., Spliethoff H., 2012. Assessment of oxy-fuel, pre- and post-combustion-based carbon capture for future IGCC plants. Applied Energy 94, 109-116.

[126] Kuzmin A., Januszewski M., Eskin D., Mostowfi F., Derksen J.J., 2013. Lattice Boltzmann study of mass transfer for two-dimensional Bretherton/Taylor bubble train flow. Chemical Engineering Journal 225, 580-596.

[127] Laborie S., Cabassud C., Durand-Bourlier L., Laine J.M., 1999. Characterization of gas–liquid two-phase flow inside capillaries. Chemical Engineering Science 54 (23), 5723–5735.

[128] Lafaurie B., Nardone C., Scardovelli R., Zaleski S., Zanetti G., 1994. Modelling merging and fragmentation in multiphase flows with SURFER. Journal of Computational Physics 113, 134–147.

[129] Lakhehal D., Larrignon G., Narayanan C., 2008. Computational heat transfer and two-phase flow topology in miniature tubes. Microfluid Nanofluid 4, 261-271.

[130] Leal O., Bolivar C., Ovalles C., Urbina A., Revette J., Garcia, J.J., 1996. Carbon dioxide removal from natural gas using amine surface bonded adsorbents. Proceedings of Symposium on the Capture, Utilization and Disposal of CO_2, American Chemical Society, pp. 1332-1336.

[131] Lee H.J., Lee S.Y., 2001. Pressure drop correlations for two-phase flow within horizontal rectangular channels with small heights. International Journal of Multiphase Flow 27, 783-796.

[132] Lee W.H., 1980. A pressure iteration scheme for two-phase flow modeling, in: T.N. Veziroglu (Ed.). Multiphase Transport Fundamentals, Reactor Safety, Applications, vol. 1, Hemisphere Publishing, Washington, DC.

[133] Lemmon E.W., Huber M.L., McLinden M.O., 2010. NIST Standard Reference Database 23: Reference Fluid Thermodynamic and Transport Properties-REFPROP, Version 9.0. National Institute of Standards and Technology, Standard Reference Data Program, Gaithersburg.

[134] Li B., Duan Y., Luebke D., Morreale B., 2013. Advances in CO_2 capture technology: a patent review. Applied Energy 102, 1439-1447.

[135] Li W., Wu Z., 2010. A general correlation for adiabatic two-phase pressure drop micro/mini-channels. International Journal of Heat and Mass Transfer 53, 2732–2739.

[136] Liu D., Wang S., 2008. Hydrodynamics of Taylor flow in noncircular capillaries. Chemical Engineering and Processing: Process Intensification 47, 2098-2106.

[137] Liu H., Vandu C.O., Krishna, R., 2005. Hydrodynamics of Taylor flow in vertical capillaries: flow regimes, bubble rise velocity, liquid slug length and pressure drop. Industrial and Engineering Chemistry Research 44, 4884–4897.

[138] Liu H., Zhang Y., 2009. Droplet formation in a T-shaped microfluidic junction. Journal of Applied Physics 106, 034906.

[139] Lockhart R.W., Martinelli R.C., 1949. Proposed correlation of data for isothermal two-phase, two-component flow in pipes. Chemical Engineering Progress 45, 39–48.

[140] Luo D., Ghiaasiaan S.M., 1997. Liquid-side interphase mass transfer in cocurrent vertical two-phase channel flows. International Journal of Heat and Mass Transfer 40, 641-655.

[141] Lv Y., Yu X., Jia J., Tu S.T., Yan J., Dahlquist E., 2012a. Fabrication and characterization of superhydrophobic hollow fiber membranes for carbon dioxide absorption. Applied Energy 90, 167-174.

322

[142] Lv Y., Yu X., Tu S.T., Yan J., Dahlquist E., 2012b. Experimental studies on simultaneous removal of CO_2 and SO_2 in a polypropylene hollow fiber membrane contactor. Applied Energy 97, 283-288.

[143] Malsch D., Kielpinski M., Merthan R., Albert J., Mayer G., Köhler J.M., Süße H., Stahl M., Henkel T., 2008. µPIV-analysis of Taylor flow in micro channels. Chemical Engineering Journal 135, S166-S172.

[144] Mandel R.K., Ohadi M.M., Shooshtari A., Dessiatoun S.V., 2011. Thin film evaporation on microstructured surfaces-application to cooling high heat flux electronics, In: Proceedings of 27th Annual IEEE Semiconductor Thermal Measurement and Management Symposium (SEMI-THERM), 138-145.

[145] Marschall H., Hinterberger K., Schuler C., Habla F., Hinrichsen O., 2012. Numerical simulation of species transfer across fluid interfaces in free-surface flows using OpenFOAM. Chemical Engineering Science 78, 111-127.

[146] McAdams W.H., Woods W.K., Heroman L.C., 1942. Vaporization inside horizontal tubes. II: benzene-oil mixture. Transactions ASME 64, 193–200.

[147] Merkel T.C., Lin H., Wei X., Baker R., 2010. Power plant post-combustion carbon dioxide capture: an opportunity for membranes. Journal of Membrane Science 359, 126-139.

[148] Metz B., Davidson O., de Coninck H., Loos M., Meyer L., 2005. IPCC special report on carbon dioxide capture and storage. Prepared by Working Group III of the Intergovernmental Panel on Climate Change, Cambridge and New York: Cambridge University Press.

[149] Mills A.D., 1995. Heat and mass transfer. Chicago: Richard D. Irwin, Inc.

[150] Mishima K., Hibiki T., 1995. Some characteristics of air-water two-phase flow in small diameter vertical tubes. International Journal of Multiphase Flow 22, 703-712.

[151] Mokhtar M., Ali M.T., Khalilpour R., Abbas A., Shah N., Hajaj A.A., Armstrong P., Chiesa M., Sgouridis S., 2012. Solar-assisted post-combustion carbon capture feasibility study. Applied Energy 92, 668-676.

[152] Mukherjee A., Kandlikar S.G., 2005. Numerical simulation of growth of a vapor bubble during flow boiling of water in a microchannel. Microfluid Nanofluid 1, 137-145.

[153] National Oceanic and Atmospheric Administration (NOAA), 2013. Carbon dioxide at NOAA's Mauna Loa observatory reaches new milestone: tops 400 ppm. http://research.noaa.gov/News/NewsArchive/LatestNews/TabId/684/ArtMID/1768/ArticleID/10061/Carbon-Dioxide-at-NOAA%E2%80%99s-

Mauna-Loa-Observatory-reaches-new-milestone-Tops-400-ppm.aspx, Retrieved on 20 July, 2013.

[154] National Oceanic and Atmospheric Administration (NOAA), 2013. Trends in Atmospheric Carbon Dioxide. http://www.esrl.noaa.gov/gmd/ccgg/trends, Retrieved on April 7, 2014.

[155] Nino V.G., Jassim E.W., Hrnjak P.S., Newell T.A., 2005. Flow regime based model for pressure drop predictions in microchannels. University of Illinois at Urbana-Champaign, ACRC TR-242.

[156] Niu H., Pan L., Su H., Wang S., 2009. Effects of design and operating parameters on CO_2 absorption in microchannel contactors. Industrial & Engineering Chemistry Research 48, 8629-8634.

[157] Ohadi M., Choo K.., Dessiatoun S., Cetegen E., 2012. Next generation microchannel heat exchangers. 1st ed. New York: Springer.

[158] Ohadi M.M., Ganapathy H., Qi J., 2015. Alternative energy technologies: price effects. In: Encyclopedia of Energy Engineering and Technology, 2nd Ed., Taylor and Francis.

[159] Onea A., Worner M., Cacuci D.G., 2009. A qualitative computational study of mass transfer in upward bubble train flow through square and rectangular mini-channels. Chemical Engineering Science 64, 1416-1435.

[160] Ong C.L., Thome J.R., 2011. Macro-to-microchannel transition in two-phase flow: part 1 – two-phase flow patterns and film thickness measurements. Experimental Thermal and Fluid Science 35, 37-47.

[161] Osher S., Sethian J.A., 1988. Fronts propagating with curvature-dependent speed: algorithms based on Hamilton–Jacobi formulations. Journal of Computational Physics 79, 12–49.

[162] Ozturk B., Yilmaz D., 2006. Absorptive removal of volatile organic compounds from flue gas streams. Process Safety and Environmental Protection 84, 391-398.

[163] Park C.Y., Jang Y., Kim B., Kim Y., 2012. Flow boiling heat transfer coefficients and pressure drop of FC-72 in microchannels. International Journal of Multiphase Flow 39, 45-54.

[164] Pires J.C.M., Martins F.G., Alvim-Ferraz M.C.M., Simões M., 2011. Recent developments on carbon capture and storage: an overview. Chemical Engineering Research and Design 89, 1446-1460.

[165] Pohorecki R., Moniuk W., 1988. Kinetics of reaction between carbon dioxide and hydroxyl ions in aqueous electrolyte solutions. Chemical Engineering Science 43, 1677-1684.

[166] Qian D., Lawal A., 2006. Numerical study on gas and liquid slugs for Taylor flow in a T-junction microchannel. Chemical Engineering Science 61, 7609-7625.

[167] Raimondi N.D.M., Prat L., Gourdon C., Cognet P., 2008. Direct numerical simulations of mass transfer in square microchannels for liquid-liquid slug flow. Chemical Engineering Science 53, 5522-5530.

[168] Ranjan R., Murthy J.Y., Garimella S.V., 2011. A microscale model for thin-film evaporation in capillary wick structures. International Journal of Heat and Mass Transfer 54, 169-179.

[169] Renardy M., Renardy Y., Li J., 2001. Numerical simulation of moving contact line problems using a volume-of-fluid method. Journal of Computational Physics 171, 243-263.

[170] Rochelle G.T., 2009. Amine scrubbing for CO_2 capture. Science 325:1652-1654.

[171] Rodosta T.D., 2013. Carbon storage: developing and validating technologies, In: Proceedings of the Carbon Management Technology Conference 2013.

[172] Rubin E.S., Mantripragada H., Marks A., Versteeg P., Kitchin J., 2012. The outlook for improved carbon capture technology. Progress in Energy and Combustion Science 38, 630-71.

[173] Salman W., Gavriilidis A., Angeli P., 2004. A model for predicting axial mixing during gas-liquid Taylor flow in microchannels at low Bodenstein numbers. Chemical Engineering Journal 101, 391-396.

[174] Salman W., Gavriilidis A., Angeli P., 2006. On the formation of Taylor bubbles in small tubes. Chemical Engineering Science 61, 6653-6666.

[175] Santos R.M., Kawaji M., 2010. Numerical modeling and experimental investigation of gas-liquid slug formation in a microchannel T-junction. International Journal of Multiphase Flow 36, 314-323.

[176] Schumpe A., 1993. The estimation of gas solubilities in salt solutions. Chemical Engineering Science 48, 153-158.

[177] Serizawa A., Feng Z., Kawara Z., 2002. Two-phase flow in microchannels. Experimental Thermal and Fluid Science 26, 703–714.

[178] Shah M.M., 1979. A general correlation for heat transfer during film condensation inside pipes. International Journal of Heat and Mass Transfer 22, 547-556.

[179] Shah M.M., 2009. An improved and extended general correlation for heat transfer during condensation in plain tubes. HVAC&R Research 15, 889-913.

[180] Shao N., 2010. Gas-liquid two-phase flow and reaction in microstructured reactors. Ph.D. Dissertation, University College London.

[181] Shao N., Gavriilidis A., Angeli P., 2009. Flow regimes for adiabatic gas–liquid flow in microchannels. Chemical Engineering Science 64, 2749-2761.

[182] Shao N., Gavriilidis A., Angeli P., 2010. Mass transfer during Taylor flow in microchannels with and without chemical reaction. Chemical Engineering Journal. 160, 873–881.

[183] Shao N., Salman W., Gavriilidis A., Angeli P., 2008. CFD simulations of the effect of inlet conditions on Taylor flow formation. International Journal of Heat and Fluid Flow 29, 1603–1611.

[184] Shin J.S., Kim M.H., 2004. An experimental study of condensation heat transfer inside a mini-channel with a new measurement technique. International Journal of Multiphase Flow 30, 311-325.

[185] Shooshtari A., Kuzmicki R., Dessiatoun S., Alshehhi M., Al-Hajri E., Ohadi M., 2012. Enhancement of CO_2 absorption in aqueous diethanolamine using microchannel contactors. In: Proceedings of Carbon Management Technology Conference 2012, CMTC 151732.

[186] Sobhan C.B., Garimella S.V., 2001. A comparative analysis of studies on heat transfer and fluid flow in microchannels. Microscale Thermophysical Engineering 5, 293-311.

[187] Socolow R., Desmond M., Aines R., Blackstock J., Bolland O., Kaarsberg T., Lewis N., Mazzotti M., Pfeffer A., Sawyer K., Siirola J., Smit B., Wilcox J., 2011. Direct air capture of CO_2 with chemicals. American Physical Society, 4-44.

[188] Son S., Dhir V.K., 1998. Numerical simulation of film boiling near critical pressures with a level set method. Journal of Heat Transfer 120, 183-192.

[189] Song C.F., Kitamura Y., Li S.H., 2012a. Evaluation of Stirling cooler system for cryogenic CO_2 capture. Applied Energy 98, 491-501.

[190] Song C.F., Kitamura Y., Li S.H., Ogasawara K., 2012b. Design of a cryogenic CO_2 capture system based on Stirling Coolers. International Journal of Greenhouse Gas Control 7, 107-114.

[191] Su H., Wang S., Niu H., Pan L., Wang A., Hu Y., 2010. Mass transfer characteristics of H_2S absorption from gaseous mixture into methyldiethanolamine solution in a T-junction microchannel. Separation and Purification Technology 72, 326-334.

[192] Sussman M., Smereka P., Osher S., 1994. A level set approach for computing solutions to incompressible two-phase flow. Journal of Computational Physics 114, 146-159.

[193] Taha T., Cui Z.F., 2004. Hydrodynamics of slug flow inside capillaries. Chemical Engineering Science 59, 1181-1190.

[194] Tan J., Lu Y.C., Xu J.H., Luo G.S., 2012a. Mass transfer performance of gas-liquid segmented flow in microchannels. Chemical Engineering Journal 181-182, 229-235.

[195] Tan J., Lu Y.C., Xu J.H., Luo G.S., 2012b. Mass transfer characteristic in the formation stage of gas-liquid segmented flow in microchannel. Chemical Engineering Journal, 185-186, 314-320.

[196] Taylor G.I., 1961. Deposition of a viscous fluid on the wall of a tube. Journal of Fluid Mechanics 10, 161–165.

[197] The Cooperative Research Center for Greenhouse Gas Technologies (CO2CRC), 2014. www.co2crc.com.au, Retrieved on February 26, 2014.

[198] Thomas S., Esmaeeli A., Tryggvason G., 2010. Multiscale computations of thin films in multiphase flows. International Journal of Multiphase Flow 36, 71-77.

[199] Thorsen T., Roberts R.W., Arnold F.H., Quake S.R., 2001. Dynamic pattern formation in a vesicle-generating microfluidic device. Physical Review Letters 86 (18), 4163-4166.

[200] Total S.A., 2007. Sour gas- a history of expertise.

[201] Tryggvason G., Esmaeeli A., Al-Rawahi N., 2005. Direct numerical simulations of flows with phase change. Computers and Structures 83, 445-453.

[202] Tuckerman D.B., Pease R.F.W., 1981. High-performance heat sinking for VLSI. IEEE Electron Device Letters 2, 126-129.

[203] Tuinier M.J., Annaland M.S., Kramer G.J., Juipers J.A.M., 2010. Cryogenic CO_2 capture using dynamically operated packed beds. Chemical Engineering Science 65, 114-119.

[204] U.S. Department of Energy, 2014. Enhanced oil recovery. http://energy.gov/fe/science-innovation/oil-gas/enhanced-oil-recovery, Retrieved on February 26, 2014.

[205] U.S. Energy Information Administration, 2013. International Energy Outlook.

[206] U.S. Environmental Protection Agency, 2014. Standards of performance for greenhouse gas emissions from new stationary sources: electric utility generating units, Proposed Rule 79 Federal Register 5, 1430-1519.

[207] Unverdi S.O., Tryggvason G., 1992. A front-tracking method for viscous, incompressible, multi-fluid flows. Journal of Computational Physics 100, 25-37.

[208] van Baten J.M., Krishna R., 2004. CFD simulations of mass transfer from Taylor bubbles rising in circular capillaries. Chemical Engineering Science 59, 2535-2545.

[209] van der Waals J.D., 1893. The thermodynamic theory of capillarity flow under the hypothesis of a continuous variation of density. Journal of Statistical Physics 20, 197-244.

[210] Vandu C.O., Liu H., Krishna R., 2005. Mass transfer from Taylor bubbles rising in single capillaries. Chemical Engineering Science 60, 6430-6437.

[211] Versteeg G.F., Oyevaar M.H., 1989. The reaction between CO_2 and diethanolamine at 298 K. Chemical Engineering Science 44, 1264-1268.

[212] Versteeg G.F., van Swaaij W.P.M., 1988a. On the kinetics between CO_2, and alkanolamines both in aqueous and non-aqueous solutions-I. primary and secondary amines. Chemical Engineering Science 43, 573-585.

[213] Versteeg G.F., van Swaaij W.P.M., 1988b. Solubility and diffusivity of acid gases (CO_2, N_2O) in aqueous alkanolamine solutions. Journal of Chemical Engineering Data 33, 29-34.

[214] Walsh E., Muzychka Y., Walsh P., Egan V., Punch J., 2009. Pressure drop in two phase slug/bubble flows in mini scale capillaries. International Journal of Multiphase Flow 35, 879-884.

[215] Wang E.N., Zhang L., Jiang L., Koo J., Maveety J.G., Sanchez E.A., Goodson K.E., 2004. Micromachined jets for liquid impingement cooling of VLSI chips. Journal of Microelectromechanical Systems 13, 833-842.

[216] Wang H., Garimella S.V., Murthy J.Y., 2007a. An analytical solution for the total heat transfer in the thin-film region of an evaporating meniscus. International Journal of Heat and Mass Transfer 51, 6317-6322.

[217] Wang H., Garimella S.V., Murthy J.Y., 2007b. Characteristics of an evaporating thin film in a microchannel. International Journal of Heat and Mass Transfer 50, 3933-3942.

[218] Wang H., Pan Z., Garimella S.V., 2011. Numerical investigation of heat and mass transfer from an evaporating meniscus in a heated open groove. International Journal of Heat and Mass Transfer 54, 3015-3023.

[219] Wang H.S., Rose J.R., 2005. A theory of film condensation in horizontal noncircular section microchannels. Journal of Heat Transfer 127, 1096-1104.

[220] Wang H.S., Rose J.R., 2006. Film condensation in horizontal microchannels: effect of channel shape. International Journal of Thermal Sciences 45, 1205-1212.

[221] Wang H.S., Rose J.R., 2011. Theory of heat transfer during condensation in microchannels. International Journal of Heat and Mass Transfer 54, 2525-2534.

[222] Wang W., Zhuan R., 2008. Numerical simulation of micro scale flowing and boiling. Frontiers of Energy and Power Engineering in China 3(4), 396-401.

[223] Wang W.-W.W., Radcliff T.D., Christensen R.N., 2002. A condensation heat transfer correlation for millimeter-scale tubing with flow regime transition. Experimental Thermal and Fluid Science 26, 473-485.

[224] Warnier M.J.F., Rebrob E.V., de Croon M.H.J.M., Hessel V. Schoten, J.C., 2008. Gas hold-up and liquid film thickness in Taylor flow in rectangular microchannels. Chemical Engineering Journal 135S, S153-S158.

[225] Welch S.W.J., Wilson J., 2000. A volume of fluid based method for fluid flows with phase change. Journal of Computational Physics 160, 662-682.

[226] Wood Mackenzie, 2013. Upstream insight.

[227] Wu H., Yu M., Cheng P., Wu X., 2007a. Injection flow during steam condensation in silicon microchannels. Journal of Micromechanics and Microengineering 17, 1618-1627.

[228] Wu H.L., Peng X.F., Ye P., Gong Y.E., 2007b. Simulation of refrigerant flow boiling in serpentine tubes. International Journal of Heat and Mass Transfer 50, 1186-1195.

[229] Wu H.Y., Cheng P., 2005. Condensation flow patterns in silicon microchannels. International Journal of Heat and Mass Transfer 48, 2186-2197.

[230] Wu J., Chen Y., Shi M., Fu P., Peterson G.P., 2009. Three-dimensional numerical simulation for annular condensation in rectangular microchannels. Nanoscale and Microscale Thermophysical Engineering 13, 13-29.

[231] Xu X., Carey P., 1990. Film evaporation from a micro-grooved surface-an approximate heat transfer model and its comparison with experimental data. Journal of Thermophysics 4, 512-520.

[232] Yang H., Xu Z., Fan M., Gupta R., Slimane R.B., Bland A.E., Wright I., 2008a. Progress in carbon dioxide separation and capture: a review. Journal of Environmental Sciences 20, 14-27.

[233] Yang Z., Peng X.F., Ye P., 2008b. Numerical and experimental investigation of two phase flow during boiling in a coiled tube. International Journal of Heat and Mass Transfer 51, 1003-1016.

[234] Yasuda M., Tsugita N., Ito K., Yamauchi S., Glomm W.R., Tsuji I., Asano H., 2011. High-efficiency NO_X absorption in water using equipment packed with a glass fiber filter. Environmental Science & Technology 45, 1840-1846.

[235] Ye C., Chen G., Yuan Q., 2012. Process characteristics of CO_2 absorption by aqueous monoethanolamine in a microchannel reactor. Chinese Journal of Chemical Engineering 20, 111-119.

[236] Youngs D.L., 1982. Time-Dependent multi-material flow with large fluid distortion. In: K.W. Morton, M.J. Baines (Eds.), Numerical Methods for Fluid Dynamics, Academic Press, New York, 273–285.

[237] Yu Z., Hemminger O., Fan L, 2007. Experimental and lattice Boltzmann simulation of two-phase gas-liquid flows in microchannels. Chemical Engineering Science 62, 7172-7183.

[238] Yue J., Boichot R., Luo L., Gonthier Y., Chen G., Yuan Q., 2010. Flow distribution and mass transfer in a parallel microchannel contactor integrated with constructal distributors. AiCHE Journal 56, 298-317.

[239] Yue J., Chen G., Yuan Q., Luo L., Gonthier Y., 2007a. Hydrodynamics and mass transfer characteristics in gas-liquid flow through a rectangular microchannel. Chemical Engineering Science 62, 2096-2108.

[240] Yue J., Luo L., Gonthier Y., Chen G., Yuan Q., 2008. An experimental investigation of gas–liquid two- phase flow in single microchannel contactors. Chemical Engineering Science 63, 4189–4202.

[241] Yue J., Luo L., Gonthier Y., Chen G., Yuan Q., 2009. An experimental study of air-water Taylor flow and mass transfer inside square microchannels. Chemical Engineering Science 64, 3697-3708.

[242] Yue P., Feng J.J., Liu C., Shen J., 2004. A diffuse-interface method for simulating two-phase flows of complex fluids. Journal of Fluid Mechanics 515, 293-317.

[243] Yue P., Zhou C., Feng J.J., 2007b. Spontaneous shrinkage of drops and mass conservation in phase-field simulations. Journal of Computational Physics 223, 1-9.

[244] Yue P., Zhou C., Feng J.J., Ollivier-Gooch C.F., Hu, H.H., 2006. Phase-field simulations of interfacial dynamics in viscoelastic fluids using finite elements with adaptive meshing. Journal of Computational Physics 219, 47-67.

[245] Zanfir M., Gavriilidis A., Wille Ch., Hessel V., 2005. Carbon dioxide absorption in a falling film microstructured reactor: experiments and modeling. Industrial & Engineering Chemistry Research 44, 1742-1751.

[246] Zhang L., Wang E.N., Goodson K.E., Kenny T.W., 2005. Phase change phenomena in silicon microchannels. International Journal of Heat and Mass Transfer 48, 1572-1582.

[247] Zhang W., Hibiki T., Mishima K., 2010. Correlations of two-phase frictional pressure drop and void fraction in mini-channel. International Journal of Heat and Mass Transfer 53, 453–465.

[248] Zhang W., Xu J., Thome J.R., 2008. Periodic bubble emission and appearance of an ordered bubble sequence (train) during condensation in a single microchannel. International Journal of Heat and Mass Transfer 51, 3420-3433.

[249] Zhang Y., Faghri A., Shafii M.B., 2001. Capillary blocking in forced convective condensation in horizontal miniature channels. Journal of Heat Transfer 123, 501-511.

[250] Zhao G., Aziz B., Hedin N., 2010. Carbon dioxide adsorption on mesoporous silica surfaces containing amine-like motifs. Applied Energy 87, 2907-2913.

[251] Zhao T.S., Bi Q.C., 2001. Pressure drop characteristics of gas-liquid two-phase flow in vertical miniature triangular channels. International Journal of Heat and Mass Transfer 44, 2523-2534.

[252] Zhuan R., Wang W., 2010. Simulation on nucleate boiling in micro-channel, International Journal of Heat and Mass Transfer 53, 502-512.

[253] Zhuan R., Wang W., 2011. Simulation of subcooled flow boiling in a micro-channel. International Journal of Refrigeration 34, 781-795.

[254] Zhuan R., Wang W., 2012. Flow pattern of boiling in micro-channel by numerical simulation. International Journal of Heat and Mass Transfer 55, 1741-1753.